Experimental and Modeling of Pneumatic Tire Performance on Ice

Emilio Jimenez

Dissertation submitted to the Faculty of the
Virginia Polytechnic Institute and State University
in partial fulfillment of the requirements for the degree of

Doctor of Philosophy
in
Mechanical Engineering

Corina Sandu, Chair
Saied Taheri
John B. Ferris
Jan Terziyski
Ricardo A. Burdisso

March 15^{th}, 2018
Blacksburg, Virginia

Keywords: Advanced Tire-Ice Interface Model, Indoor Testing, Water Film Height, Model Validation, Tire Tractive Performance on Ice

Experimental and Modeling of Pneumatic Tire Performance on Ice

Emilio Jimenez

ABSTRACT

The tire-ice interaction is a highly complex phenomenon, which has a direct influence on the overall performance of the pneumatic tire. From tire-terrain interaction dynamics, it is evident that icy road conditions and tire operational parameters play a vital role in determining the overall performance of the vehicle. With the reduction of traction available at the surface in icy conditions, the dynamics of the vehicle becomes more unpredictable, as the system can become unstable. In order to design an appropriate safety system, the tire-ice interaction must be closely investigated. Since the tire is the part of the vehicle that is in direct contact with the terrain during operation, it is critical to have an in-depth understanding of the contact mechanics at the contact patch.

This study has led to the development and validation of an existing tire-ice model to further improve the understanding of the contact phenomena at the tire-ice interface. Experimental investigations led to a novel measurement technique in order to validate the semi-empirical based tire-ice contact model.

The Advanced Tire-Ice Interface Model serves to simulate the temperature rise at the contact patch based on the pressure distribution in the contact patch, thermal properties of the tread compound and of the ice surface. Since its initial development, the advanced model is now capable of simulating the thin water film created from the melted ice, the prediction of tractive performance, the estimation of the viscous friction due to the water layer, and the influence of braking operations including the locked wheel condition.

Experimental studies, carried out at the Terramechanics, Multibody, and Vehicle Systems (TMVS) Laboratory, were performed on the Terramechanics Rig. The investigation included measuring the bulk temperature distribution at the contact patch in order to validate the temperature rise simulations of the original Tire-Ice Model. The tractive performance of a P225/60R16 97S Standard Reference Test Tire and a 235/55R-19 Pirelli Scorpion Verde All-Season Plus XL were also investigated during this study. A design of experiment was prepared to capture the tire tractive performance under various controlled operating conditions.

This study has been partially supported by the Center for Tire Research (CenTiRe), an NSF-I/UCRC at Virginia Tech, and by the Terramechanics, Multibody, and Vehicle Systems (TMVS) Laboratory. We would like to thank all of the CenTiRe Industrial Advisory Board members that serve as mentors for this project for their suggestions and feedback on this study.

Experimental and Modeling of Pneumatic Tire Performance on Ice

Emilio Jimenez

GENERAL AUDIENCE ABSTRACT

Icy road conditions and tire performance play a vital role in determining the overall performance of a vehicle. With the reduction of traction available at the surface in icy conditions, the vehicle becomes more unpredictable and can become uncontrollable. In order to design an appropriate safety system, the tire-ice interaction must be closely investigated. This research aims at enhancing the understanding of the tire-ice contact interaction at the contact patch through modeling and experimental studies for a pneumatic tire traversing over solid ice.

Prior work in the laboratory produced a Tire-Ice Model (TIM) with the purpose of estimating the friction at the tire-ice interface. The current work builds on that study, resulting in the Advanced Tire-Ice Interface Model (ATIIM). This model predicts the temperature rise at the tire-ice interface based on the measured pressure distribution and the thermal properties of the tire and of the ice surface. This model allows a more thorough investigation of the tire-ice interface, being capable of predicting the height of the thin water film created from the melted ice, the prediction of tractive performance of the tire, the estimation of the viscous friction due to the water layer at the contact interface, and the influence of braking operations, including the locked wheel (skid) condition.

Experimental studies were carried out at Terramechanics, Multibody, and Vehicle Systems (TMVS) Laboratory on the Terramechanics Rig. The experimental investigation included measuring the temperature at various points at the tire-ice interface in order to compare the temperature rise predicted using the ATIIM. Furthermore, the tractive performance of the tire was also investigated by examining different conditions of vertical tire load, tire inflation pressure, and ice surface temperatures as well as various steering configurations set by the user.

In addition to investigating the performance at the tire-ice interface, a vehicle model in which the front wheels are considered as one (and the same for the rear wheels), often referred to as the bicycle model, is studied while traveling over smooth ice. To ensure the accuracy of the vehicle simulation, the tire model chosen must account for the actual conditions in which the model will operate. In this study, the ATIIM is incorporated in empirical tire models commonly used in industry and used in conjunction with a vehicle model to accurately predict the behavior of the vehicle when operating on smooth ice.

Dedication

It is with deepest gratitude and warmest affection that this thesis is dedicated to our Professor Dr. Corina Sandu who has been a constant source of knowledge and inspiration.

Dedicated to those that gave me life and grew me up. Those angels who were always my support and guidance. I owe them each moments of my life and praise them in every breath. Dedicated to the most holy person, Mother and the dearest person, Father.

All my love to them for finding me the light, whenever it was far away.

Acknowledgments

I would like to begin by expressing my sincere gratitude to my advisor Professor Dr. Corina Sandu. With her guidance and continuous support, it would not have had been possible for me to reach the point where I am now in my career. Her guidance helped me in all the time of research and writing of this thesis. I could not have imagined having a better advisor and mentor for my Ph.D study.

I am also grateful to the members of my committee. To Professor Dr. Saied Taheri, Professor Dr. John Ferris, Dr. Jan Terziyski, and Professor Dr. Ricardo Burdisso, thank you for not only serving in my committee and for the insightful comments and encouragement, but also for the hard question which incented me to widen my research from various perspectives.

Many thanks to my colleagues at the Terramechanics, Multibody, and Vehicle Systems (TMVS) Laboratory at Virginia Tech. Firstly, Dr. Anudeep Bhoopalam for the fruitful and inspiring conversations pertaining to all aspects in life. I express my gratitude to Aamir Khan, Rui He, Tan Li, Sebastien Corner, and Hoda Mousavi for their discussions and support of my work to help me get further in my education. I also am thankful for the support which Dr. Qing Li was able to provide. With this knowledge and support, the extension of our testing capabilities would not have come to light.

Also I thank my professors at James Madison University. In particular, I am grateful to Professor Dr. Kyle Gipson for enlightening me the first glance of research at Clemson University.

I would like to thank those of the Vehicle Dynamics Group at the University of Pretoria. To Professor Dr. Schalk Els, thank you for further expanding my knowledge base in this ever-changing topic. To Glenn Guthrie, Joachim Stallmann and Jacob Grobler, I thank you for supporting me and providing guidance to me while I continued my studies at the University of Pretoria. Also, a thank you to my colleagues in Germany, Professor Dr. Valentin Ivanov, Dzmitry Savitski, and Dmitrij Schleinin for their efforts to improve upon existing technologies using experimental and modeling techniques for the European Unions Horizon 2020 research and innovation program under the Marie Sklodowska-Curie grant agreement No. 645736.

Lastly, to the members of CenTiRe, we thank our colleagues who provided insight and expertise that greatly assisted the research. To Dr. Shayrar Taheri thank you for your initial discussion pertaining to tire modeling. To Eric Pierce thank you always being supportive and helpful in the laboratory. And finally to Ashlin Jackson for her program support of CenTiRe.

This study has been partially supported by the NSF I/UCRC Center for Tire Research (CenTiRe) and by the Terramechanics, Multibody, and Vehicle Systems (TMVS) Laboratory at Virginia Tech. We would like to thank all of the CenTiRe Industrial Advisory Board members that serve as mentors for this project for their suggestions and feedback on this study.

We are grateful to the authors of the reprints included in this thesis for the permission that they have given for reproduction here, and to many other authors for allowing us to use figures from their publications.

Contents

List of Figures

List of Tables

Nomenclature

α	Heat Transfer Coefficient
α	Slip Angle
β	Bulk Water Properties
ΔT	Temperature Rise in the Contact Patch
η	Viscosity of Water
κ	Relative Contact Area Ratio
λ	Contact Patch Deformation
h	Water Film Height
V	Translational Velocity of Wheel
μ_d	Dynamic Friction
μ_F	Saturated Friction Coefficient from Wet Film
ω	Wheel Rotational Velocity
ρ	Density of Ice
ρ_{avg}	Average Pressure Distribution at Contact Patch
τ	Shear Stress at the Contact Interface
$ATIIM$	Advanced Tire-Ice Interface Model
DP	Drawbar Pull
F_z	Normal Load at Wheel Center
k_t	Thermal Conductivity of Tread

R_0	Undeflected Rolling Radius of Tire
R_e	Effective Rolling Radius of Tire
R_0	Undeflected Radius of Pneumatic Tire
R_e	Effecive Rolling Radius of Pneumatic Tire
s	Slip Ratio
SAE	Society of Automotive Engineering
$SRTT$	Standard Reference Test Tire
T_m	Melting Temperature of Ice Surface
TIM	Tire−Ice Model
V	Translational Velocity of Wheel
NR	Natural Rubber of Tire
SR	Synthetic Rubber of Tire
Treaded SRTT	Standard Reference Test Tire with full tread depth of 7.97 mm

Chapter 1

Introduction

1.1 Motivation

This investigation is motivated by the need for performance improvement for pneumatic tires in icy conditions. The pneumatic tire is the only force transmitting component between the terrain and the vehicle under normal operation. Therefore, it is critical to grasp the understanding of the contact mechanics at the contact patch under various surfaces and operating conditions. Pneumatic tire designers are thus faced with many conflicting goals. For example, the requirements for reduced noise, increased tread life, and reduced power loss all conflict with the goal of improved traction performance.

From 1995 to 2005 there were 193,899 crashes due to adverse weather and pavement conditions directly related to ice. The average accident data [16] presented that out of 193,899 crashes, 34% of those resulted in injuries to a person. In order to traverse over icy terrain, which has a low level of friction, vehicles need several characteristics including proper brake applications, increased friction at the contact patch to provide better traction,

and a uniform temperature distribution around the contact patch in order to reduce melting of the ice at the surface.

In certain geographical locations, as seen in Figure 1.1, there are higher chances of icy conditions which shapes the lifestyle of many individuals. Over 70% of the nation's roads are covered in snowy regions. Therefore, it is imperative to fully characterize the pneumatic tire in such conditions in order to provide improvements to the tire regarding its performance on ice.

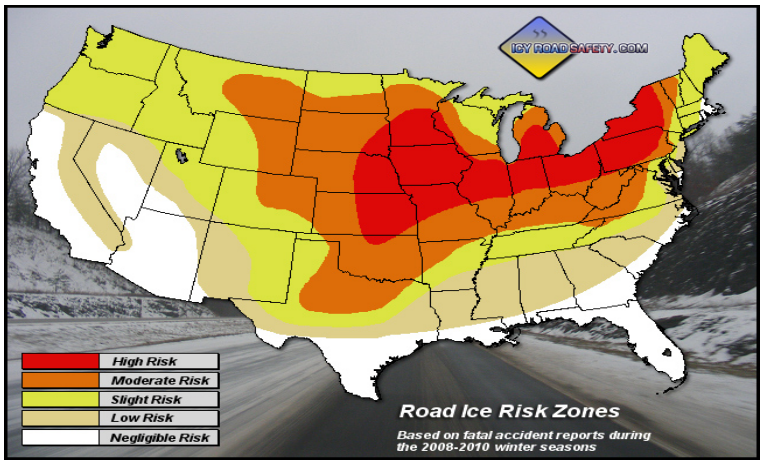

Figure 1.1: Road ice risk zones. Based on fatal accident reports during the 2008 - 2010 Winter seasons. Adapted from [1] under fair use; Fair use determination attached.

1.2 Problem Statement

In order to provide an improvement to the existing technologies, it is imperative to first understand the underlying physics behind the problem. The purpose of this study is to enhance the understanding of the tire-ice contact interaction at the contact patch through experimental studies and a semi-empirical Advanced Tire-Ice Interface Model (*ATIIM*). An early version (named the Tire-Ice Model (*TIM*)) was developed in our research group by Bhoopalam [17] for a pneumatic tire traversing over solid ice.

The first objective of this research is to validate the existing Tire-Ice Model for the various simulations investigated. This included using a different tire than what the original model was developed for, to investigate the fidelity of the model. An additional objective is to also extend the current model by developing modules to account for new scenarios thus providing an Advanced Tire-Ice Interface Model (*ATIIM*)

The second objective of this research is to perform a comparative analysis between Winter Tires and All−Season Tires in order to further expand our knowledge base of tire traction on ice. This will be done through experimental investigations at the Terramechanics, Multibody, and Vehicle Systems (TMVS) Laboratory following the proposed design of experiment, as seen in Table 3.1.

The third objective of this research is to investigate the effect of different rubber compounds on the tire-ice friction. This will provide insight into the traction performance of tires manufactured with various rubber compounds.

The final objective of this research is to implement the Advanced Tire-Ice Interface Model into an existing tire model in order to further expand that tire model's capabilities and accuracy. The tire model thus enhanced will then be employed in a vehicle model to illustrate its advanced capabilities.

1.3 Main Contributions of this Research

The research conducted in this study was intended to improve the Tire-Ice Model and to investigate the tractive performance of tires on ice with various operational parameters. The parameters included the effect of toe and camber angles, the effect of varying the inflation pressure, the effect of the normal load, the effect of ice surface temperature, and the

effect of the slip ratio at the contact patch. This experimental study was conducted at the Terramechanics, Multibody, and Vehicle Systems (TMVS) Laboratory using the single-wheel Terramechanics Rig.

Several tires were used for this study, one being the Standard Reference Test Tire ($SRTT$). This tire was chosen to develop, validate, and further improve upon the Advanced Tire-Ice Interface Model. This specific tire was chosen to be the test tire because it is widely used in industry for benchmarking and comparing experimental results. Other tires were chosen to test the limits of the Advanced Tire-Ice Interface Model.

The Tire-Ice Model (TIM), developed by [17], is to be validated for tires of different sizes, types, and tread pattern during this study. Other modules were developed to accompany (TIM) and provide further details of the temperature rise phenomena at the contact patch. This includes the drawbar pull performance, the height of the thin water film at the contact patch due to the temperature rise and its resultant viscous friction, and the rise in temperature at the contact patch during braking operating.

The overall efforts of this research study provide insight into the friction interaction at the tire-ice interface and enhances the understanding of the effect of the temperature rise during operation. The results of the study provide significant information necessary to improve the tire design in order to increase safety on icy roads.

1.4 Outline of the Dissertation

The dissertation will follow the following outline:

Chapter 2 presents a comprehensive literature review on the experimental methodologies and modeling techniques used to characterize a pneumatic tire, primarily on ice. This

chapter begins by reviewing parameters which effects the ice surface conditions and is followed by tire design and construction. The mechanics of the pneumatic tire is also reviewed in this section The latter portion of the chapter will focus on existing technologies used to test tires on ice.

In Chapter 3, the test procedure used for the experimental portion of the study is described. A design of experiment is presented to capture the dynamics of the pneumatic tires under investigation. The results from the test program, which includes the friction versus slip ratio curves for the different test conditions are presented and interpreted.

Chapter 4 presents the original and extended versions of the Advanced Tire-Ice Interface Model. A brief overview is given followed by the governing equations dictating the simulations. The results of the simulations are then presented and discussed. Finally, validation results are shown for simulations of different tires.

Chapter 5 presents the findings of implementing the Advanced Tire-Ice Interface Model into a more comprehensive tire and vehicle model. Existing tire models are briefly discussed followed by the mechanism in which ($ATIIM$) can be employed into an existing tire model.

Chapter 6 discusses the development of the bicycle model and presents qualitative and quantitative results which could be compared to experimental data from vehicles. Results from a CarSim simulation are also presented in this chapter.

Finally, chapter 7 presents the conclusions and discusses the contribution of this work and recommendations for future research.

Chapter 2

Literature Review

In this chapter, a comprehensive literature review on the experimental methodologies and modeling techniques used to characterize a pneumatic tire, primarily on ice, is presented. The chapter is sectioned in the following manner:

- Discussion of factors influencing the friction at the ice surface
- Tire design variables affecting the traction performance
- Existing technologies used for investigating the tire-ice interface
- Discussion of existing tire-ice models

The literature review should suggest some theoretical framework to be explained further. The review thus describes and analyzes previous research on the topic. This chapter, however, will not merely string together what other researchers have found. Rather, it will discuss and analyze the body of knowledge, with the ultimate goal of determining what is known and is not known about the topic.

2.1 Previous Work

Experimental data on ice friction are not enough for a detailed interpretation of the physics of ice friction since the frictional heating depends on the relative sliding velocity between the contact patch and the ice surface [18]. For this reason, an in-house Tire-Ice Model (*TIM*) was developed in order to simulate the temperature rise due to the pressure distribution at the contact patch [19]. To study the temperature rise of the contact patch under normal operating conditions, the Tire-Ice Model uses the principle of heat balance to identify the rise in temperature at the contact patch as well as to identify areas of dry and wet regions in the contact patch [19], as seen in Figure 2.1. Once the temperature rise is determined, the dynamic friction coefficient is obtained at the tire-ice interface. Numerical formulations are used to estimate the temperature under various moving scenarios according to the formulation developed by Jaeger [20]. Further details are presented in Section 4.1.

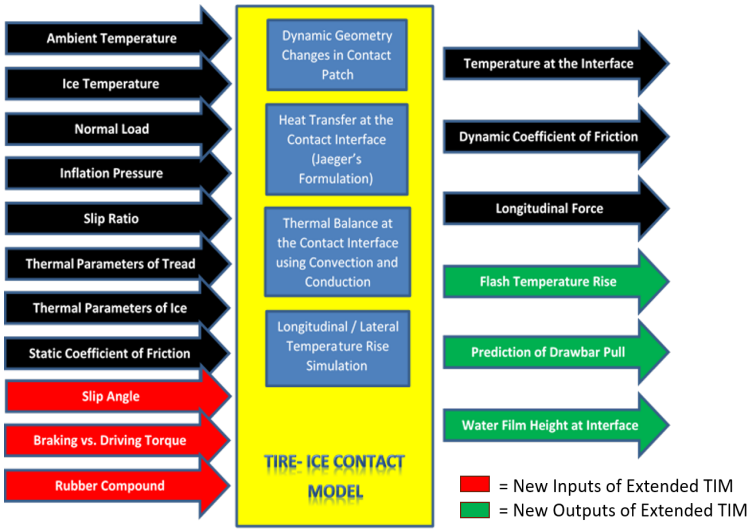

Figure 2.1: Inputs and outputs representing the structure of the Advanced Tire-Ice Inteface Model. Items in red and green represent the extension of the model since its initial development.

As the temperature rise causes the temperature distribution to reach the melting

point of the ice surface, wet regions in the contact patch begin to form. This thin water film results in low levels of friction. Therefore, in order to quantify the performance of the pneumatic tire, both dry and wet regions must be taken into account. *ATIIM* uses the relative ice surface temperature to determine if the temperature rise is sufficient enough to melt the ice.

2.2 Investigation of Ice Surface Characteristics

The tire-ice interaction is a highly complex phenomenon which has a direct influence in the overall performance of the pneumatic tire. From tire-terrain interaction dynamics, it is evident that icy road conditions and tire operational parameters play a vital role in determining the overall performance of the vehicle, including the drawbar pull. The friction at the tire-ice contact is changing over time as the ice surface conditions may vary during normal operation. Various factors contributing to the tire-ice friction include: ambient and ice temperatures, growth rate of the ice surface, impurities present in the ice itself, effect of ice texture, and the age of the surface.

2.2.1 Ambient and Ice Surface Temperature

The ambient and the ice temperature are two of the most difficult variables to control to ensure consistent testing conditions. Geissler et al., [2], studied their effect on tire performance on ice. The purpose of their investigation was to capture the transient temperature rise using experimental results and a theoretical approach, to the problem regarding tire traction on ice and snow. An internal drum test bench was employed during this study to allow tire performance measurements, under controllable conditions. As a major result of

these experiments, a strong correlation of thermal conditions and transmittable forces were discovered. Furthermore, a high-speed infrared camera was used to monitor the temperature increase of the tire surfaces under operation. An increase in ambient temperature was found to lead to an increase in the surface temperature [2]. Once the surface reaches the melting point, a thin water film can be observed, which results in a lower coefficient of friction. Therefore, it was found that at low temperatures the traction transmissibility was increased at the contact patch, as seen in Figure 2.2. The reduction of force available, due to increase in temperature, is higher for longitudinal loading than for lateral loading. On the other hand, the longitudinal traction force coefficient is lower at the same ambient temperature compared to maximum lateral force coefficient [2].

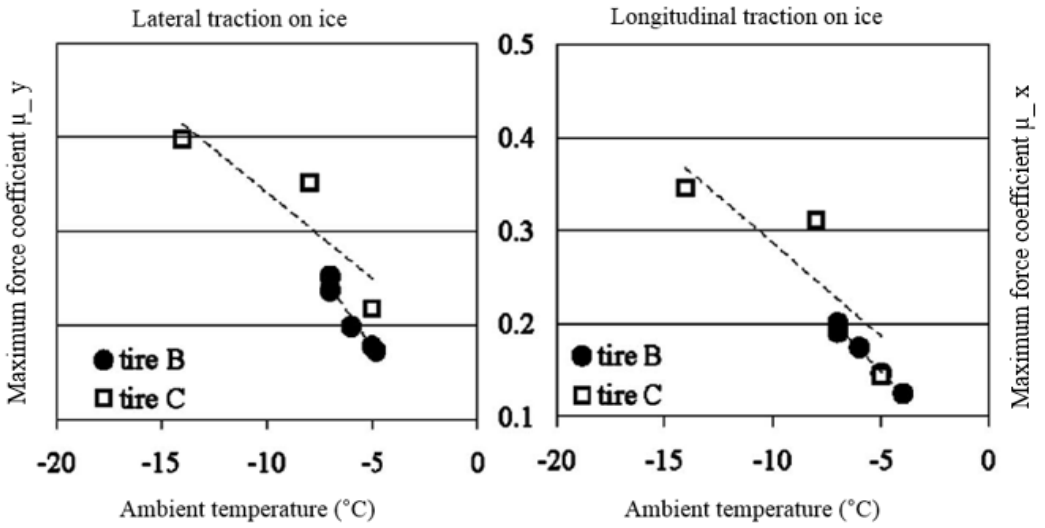

Figure 2.2: Lateral and longitudinal maximum coefficient of friction versus ambient temperature. The results show a decrease in the available friction as the ambient temperature reaches the melting point. Adapted from [2] under fair use; Fair use determination attached.

Force transmission between the tire and track leads to frictional heat, which produces a liquid layer at the contact interface. In most cases, this thin water film serves as a source of friction forces from the viscosity of a sheared intermediate thin liquid layer of melted ice. The design of the tread patterns of the tire must be such that the liquid is rapidly pushed

out of the contact patch in order to promote rubber adhesion at the interface.

2.2.2 Effect of Ice Surface Growth Rate and Track Age

The rate at which the ice is formed contributes to the overall strength of the ice surface. Shimizu et al., [3], found the overall yield strength of the ice to have a direct correlation to the rate at which the ice is made. In order to clarify the effect of micro texture, iced roads composed of different ices (different in shape and size of crystals) were made by means of controlling the growth rate of ice.

Stronger ice is obtained when the ice surface is created at a rate of $3 - 5$ mm/hr. Therefore, the rate of growth directly impacts the texture of the ice. The strength of the ice must be taken into consideration when creating ice for testing. The pressure exerted on the ground due to carcass stiffness is not a constant, and its value varies with inflation pressure and load. Therefore, the ice used for testing must be strong enough to handle the extreme loading caused during a test.

The temperature of the water used to form the ice surface also has a direct influence in the overall texture of the ice. If the temperature of water is reduced, the growth rate of ice increases, leading to the formation of cloudy ice [3]. As these conditions are met, the ice is composed of mostly granular crystals, and the air bubbles remaining between the crystals causes cloudiness. Therefore cloudiness of ice increases with an increase in growth rate, but excessive growth rate causes a "rough" or non-smooth ice surface [3].

Roberts [21] studied the effect of the age of the ice track. As the track ages, the ionic impurities which are created with time eventually break-down the top layer of the ice as seen in Figure 2.3.

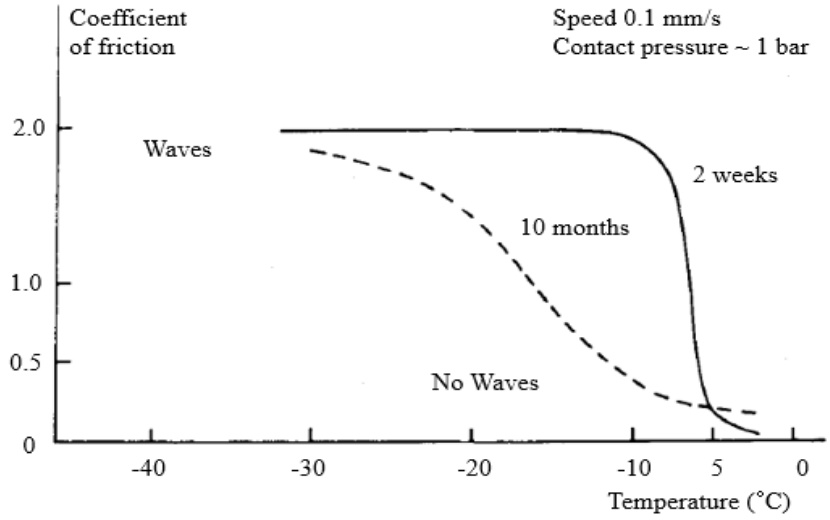

Figure 2.3: Comparison of friction levels made with a rubber lens sliding on a new and old ice track. The tracks are polished in the same manner before testing to ensure consistent testing conditions. Adapted from [3] under fair use; Fair use determination attached.

2.2.3 Effect of Impurities in the Ice Surface

In real-world conditions, impurities are also present in the ice; they play a role in the friction at the ice surface. It was found that salt and impurities in the ice cause a reduction in friction [22]. Impurities are formed over time in the ice. The way the ice is produced is critical. At the Terramechanics, Multibody, and Vehicle Systems (TMVS) Laboratory, ice is formed by freezing thin layers of water on top of an existing ice surface. This can directly impact the location of any impurities. This results in freezing that starts from the bottom of the layer (at the ice−water interface) and progresses upwards. Such freezing may have a tendency to reject impurities towards the top surface, as well concentrating impurities at grain boundaries [22]. As the impurities accumulate, the layer of the ice weakens due to the lack of bonds being formed in the micro-surface of the ice. This weakening of the ice surface leads to a reduction in the available friction [21], which has a direct effect on the temperature rise at the contact patch during operation. Therefore, it is important to note that within the temperature range -20° C to 0° C, which is of considerable practical importance, it is

the ice behavior rather than that of the rubber that sets the general level of friction.

2.2.4 Effect of Ice Surface Texture

Referring back to 2.2.2, the size of the crystals are influenced by the growth rate of the ice surface. The size of the crystals define the overall texture of the ice which has an effect on the tire longitudinal characteristics on ice. Shimizu et al., [3] found that the maximum friction coefficient has a tendency to increase when the size of the ice crystals increases, and it is very much dependent on the temperature as shown in Figure 2.4

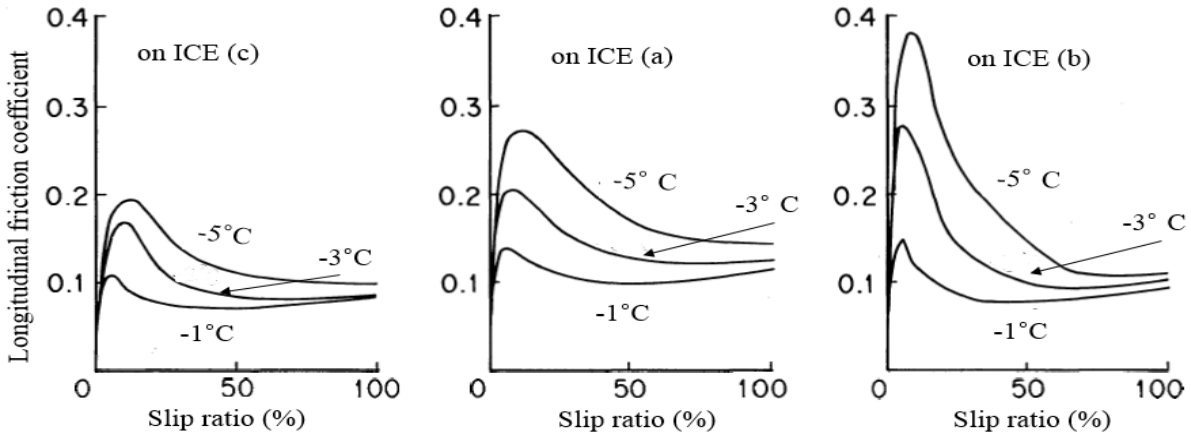

Figure 2.4: Comparison of friction levels made with different tires on two different ice surfaces. Ice (b) has crystal grain diameter size which is larger than Ice (c). As the ice temperature is decreased, the longitudinal friction coefficient is increased. Adapted from [3] under fair use; Fair use determination attached.

In Figure 2.4, the results show that the effect of crystal size increases as the capacity for adhesion of the tire at the contact patch increases. When the effect of the different types of tires are studied, the results also show that the overall level of friction coefficient on more granular ices at high temperatures, increases with the density of edges in the tread design [3]. This edge produces "biting" and is responsible for promoting traction in icy and snow conditions.

2.2.5 Discussion on the Effect of Various Ice Conditions

The main factors of ice parameters which directly influence the amount of friction available at the tire-ice interface are:

1. The ambient and ice surface temperatures
2. The effect of ice surface growth rate and track age
3. The effect of impurities in the ice surface
4. The effect of ice surface texture

In most cases, the lowest ambient and ice surface temperature resulted in the highest levels of friction as the low temperatures promote bonding between the tire and ice surfaces. This was investigated by Geissler et al., and Roberts in [2] and [21] respectively.

The effect ice surface growth rate was investigated by Shimizu et al., [3]. In this study, it was found that the size of the crystals in the ice, are influenced by the growth rate of the ice surface. The size of the crystals define the overall texture of the ice which in turn, has an effect on the tire longitudinal characteristics on ice. Roberts [21] also investigated the influence of the age of the ice track and how that affects the available friction levels. The investigation determined that as the track ages, the ionic impurities which are created with time eventually break-down the top layer of the ice as seen in Figure 2.3. As the impurities accumulate, the layer of the ice weakens due to the lack of bonds being formed in the micro-surface of the ice. This weakening of the ice surface leads to a reduction in the available friction [21], which has a direct effect on the temperature rise at the contact patch during operation.

Finally, the ice surface texture also plays a critical role in the contribution of friction available. In Figure 2.4, the results show that the effect of crystal size increases as the capacity for adhesion of the tire at the contact patch increases.

The mechanical properties of ice, i.e., the capacity of ice to resist the influences of external forces, change considerably depending on temperature. The closer the temperature of the ice is to the melting point, the more dominant are the effects of the plastic properties of the ice and the lower its overall strength. This phenomenon is explained by the weakening of the cohesion of the ice molecules in the lattice of the crystals. On the other hand, the lower the temperature is, the more difficult it is for the atoms to become rearranged in the space lattice of ice and the more apparent are the elastic and brittle properties of ice.

2.3 Tire Design Characteristics

To study the characteristics of a tire and the forces and moments acting on the contact patch, an axis system must be defined in order to reference specific parameters. A common axis systems provided by the Society of Automotive Engineers is presented in Figure 2.5 (*SAE* J670e, 1978).

The center of the contact patch is the origin of the coordinate system, as shown in Figure 2.5. The Z axis is perpendicular to the ground plane and is chosen to be positive in the downward direction to make the axis system orthogonal. The X axis represents the direction of travel. It is tangential to the direction of the velocity vector in the wheel heading direction at the center of the contact patch. The Y axis follows the right-hand rule and is perpendicular to the direction of the wheel heading. All forces and moments investigated originate at the contact patch.

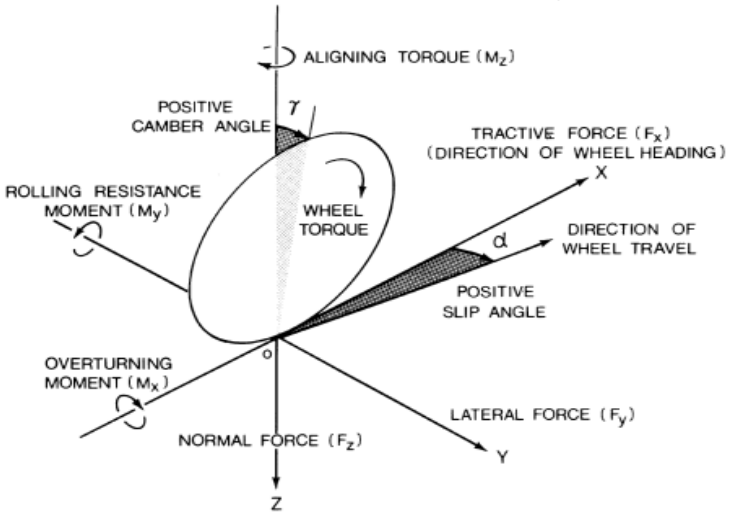

Figure 2.5: Axis System of a Tire according to *SAE* J670e & *SAE* J2047. Adapted from [4] under fair use; Fair use determination attached.

The tire is a high performance composite structure which resembles a doubly curved surface that is relatively soft and flexible. The tire has three boundary regions: one is the zone of contact with the terrain and the other two are with the rim. In the zone of contact with the terrain, friction affects the tire deformation and footprint. In conjunction, the three boundary zones work together to provide a diverse range of performance qualities such as:

- Carry Load
- Transmit Drive / Braking torque
- Produce Cornering Force
- Provide Steering Response
- Cushion Road Inputs
- Dimensional Stability
- Consume Minimum Power
- Low Noise / Vibration
- Tolerate Poor Maintenance
- Durable and Safe Performance
- Long Wear Life

During driving operation, the driving torque on the wheel produces a tractive force

which moves the footprint forwards relative to the center of the wheel axle ($\lambda < l$) as seen in Figure 2.6. This action causes the tread blocks entering the contact patch to be compressed which leads to the tire deforming with respect to the circumference in order to accommodate the tread displacements. Therefore, the circumferential speed drops from ωR_0 relative to the wheel center, to ωR_e [5]. R_e is the effective rolling radius of the pneumatic tire. As more tread elements progress through the contact patch under increasing load, the longitudinal shear force will build up linearly as seen in Figure 2.6.

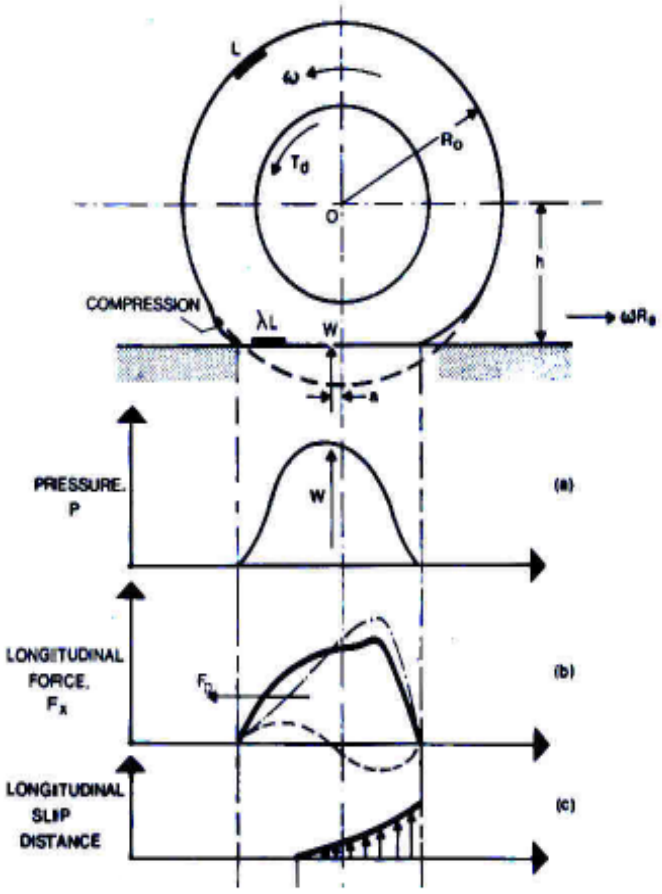

Figure 2.6: Longitudinal characteristics of a pneumatic tire under driving torque applied at the wheel center. The figure shows the compression of the tread elements at the leading edge of the contact patch. Adapted from [5] under fair use; Fair use determination attached.

During braking, the braking torque applied from the brake calipers at the wheel

produces a braking force from the terrain to the tire, as seen in Figure 2.7. The force moves the footprint of the contact interface back relative to the axle, stretching the tread blocks of the footprint. This causes the tread blocks to pull and stretch ahead of the nominal footprint. These elements will adhere to the surface upon entering the footprint and will be bent backward by the rearward shear stress, thus decelerating the tire [5]. This braking force causes the effective rolling radius to be larger than the undeflected rolling radius.

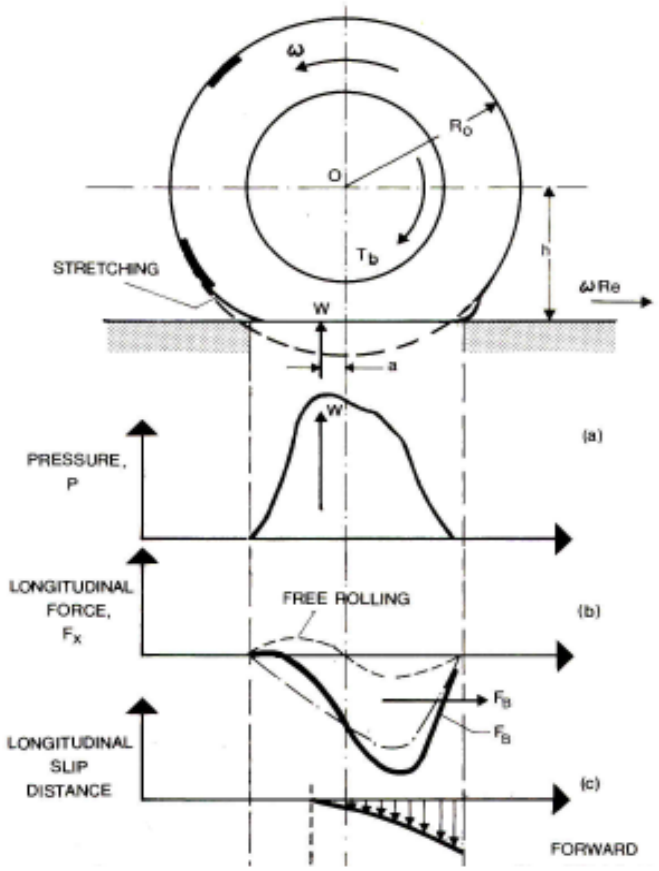

Figure 2.7: Longitudinal characteristics of a pneumatic tire under braking torque applied at the wheel center. The figure shows the stretching of the tread elements at the leading edge of the contact patch. Adapted from [5] under fair use; Fair use determination attached.

2.3.1 Effect of Tread Pattern

The tread is designed to serve various important functions in the operation of the wheel. The tread must provide the necessary grip capacity for driving, braking and cornering operations. It is designed to provide uniform wear, to channel water out of the footprint, and to minimize pattern noise on a variety of terrains.

The tread rubber compound also has its own function. It is specially formulated to provide a balance between wear, traction, handling and low rolling resistance. This is done by using different compounds to alter the tread mechanical properties such as stiffness [23].

The manufacturing of the pattern onto the tire tread is done during vulcanization or curing. The tread can be separated into two categories, namely subtread and undertread:

1. The subtread, is typically a lower hysteresis, formed under the tread compound to improve rolling resistance in order to meet the manufacturer's goals for fuel economy [23]. It also can be used to fine-tune other aspects of the tire such as ride quality, noise, and handling.

2. The undertread is a thin layer of rubber layered under the extruded subtread to promote adhesion of the tread to the plies during tire assembly and manufacturing.

There are four general types of tread designs which are commonly employed by the tire industry. These include, but are not limited to:

1. *Symmetric Tread Patterns*

   A symmetric tread pattern is the most common tread design used on non-high-performance passenger cars because it is typically quiet and long-lasting. The pattern is made of continuous ribs or independent tread blocks across the entire tread face where both the

inside and outside of the contact patch exhibit the same pattern as seen in Figure 2.8a. The figure shows how the tire tread has the same symmetrical pattern using continuous grooves and/or independent lugs across the whole tire [6]. Tires featuring symmetric tread patterns allow using multiple tire rotation patterns [24].

2. *Asymmetric Tread Patterns*

   An asymmetric pattern is designed to blend the specific requirements of both dry and wet grip through water dispersal where the tread pattern varies across the face of the tread, as seen in Figure 2.8b. Typically the inside and middle parts of the tread pattern will be designed for wet or winter traction. The outboard side of the tread pattern will have larger tread ribs to increase cornering stability on dry terrains by offering greater contact area. This also helps to reduce tread squirm and heat buildup on the outside shoulder [6].

   To ensure that the tires are positioned correctly on the car (to maximize handling capabilities), the sidewalls are marked outside only and inside only. Tires featuring asymmetric tread patterns also allow using multiple tire rotation patterns.

3. *Directional (Unidirectional) Tread Patterns*

   A directional (also called a unidirectional) tread pattern is designed to roll in only one direction, which is indicated by an arrow on the sidewall of the tire. It incorporates lateral grooves on both sides of the tire's centerline that point in the same direction and results in V-shaped tread blocks, as seen in Figure 2.8c. This V-shaped tread improve hydroplaning resistance at high speeds by siphoning water more efficiently through the tread making these tires ideal for performance and ultra-high performance applications [24].

   Unless they are dismounted and remounted on their wheels to accommodate use on

(a) Symmetric

(b) Asymmetric

(c) Directional

(d) Asymmetric and Directional

Figure 2.8: Four basic tread patterns which are commonly used in industry. Adapted from [6] under fair use; Fair use determination attached.

the other side of the vehicle, directional tires are to be used on one side of the vehicle and are intended to be rotated from the front axle to the rear axle. If different tire sizes are used on the front vs. rear axle, the tires become location-specific and prohibit tire rotation unless remounted.

4. *Asymmetric and Directional Tread Patterns*

   Tires which are asymmetric and directional simultaneously are also designed by the tire industry. The tread patterns have V-shaped tread grooves that are offset compared to the centerline of the tire, as seen in Figure 2.8d. Directional and asymmetrical tire treads are the best of both worlds as it is composed of the V-shaped pattern of the directional tread design for discharging water away from the contact patch and the dry grip of the asymmetrical tread for high performance traction on dry surfaces [6].

   Tires featuring asymmetric and directional tread patterns must be treated as directional tires for tire rotation. However, if different tire sizes are used on the front vs. rear axle, they become location-specific and prohibit any tire rotation possibilities.

For driving in severe winter conditions such as ice, winter tires with increased tread depth such as with the asymmetrical and directional tread pattern and a specially formulated soft tread compound, are recommended.

2.3.2 Effect of Tire Construction

Rubber is a viscoelastic material which can be defined as a deformable material with a behavior which lies between that of a viscous liquid and an elastic solid. This definition leads to the origin of tire grip mechanics which is produced from the hysteresis. Hysteresis is when a viscoelastic material which has been deformed, reverts back to its original shape

after some time [7]. For grip purposes, the composition of rubbers in tires should be selected so that their modulus is moderate and their hysteresis is maximum [23]. In winter and icy conditions, the modulus of rubber is high which causes the material to be brittle. Therefore specific types of rubber must be used for winter tires. In general, there are four main types of rubber used [7]:

1. Natural Rubber (NR): This rubber serves as the main component of the tread layers.
2. Synthetic Rubber (SR): This rubber forms part of the treads of cars, vans and 4 X 4 tires.
3. Carbon Black and Silica: The function of this rubber type is to serve as a reinforcing agent in order to reduce wear and noise.
4. Metallic and Textile Reinforcement Cables: This is the skeleton of the tire. It forms the geometric shape and provides rigidity for the pneumatic tire.
5. Numerous Chemical Agents: These agents provide unique properties like low rolling resistance or ultra-high grip depending on the requirements of the tire.

The radial tire is made up of eight major components which work in union to handle the interaction of the terrain, as seen in Figure 2.9:

1. *Inner Liner*

   The inner liner serves to retain the air inside the tire and is typically composed of Bromobutyl (SR) to help improve durability.

2. *Carcass Ply*

   This is the layer above the inner line which serves as a key structural component of the tire [23]. It is used to maintain the size and shape of the tire and to provide strength

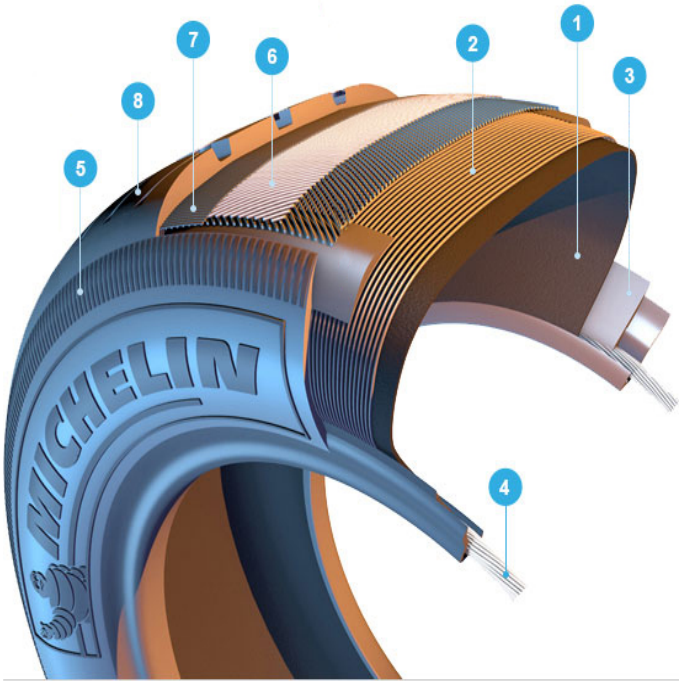

Figure 2.9: Highlights the eight major components of a radial tire. Adapted from [7] under fair use; Fair use determination attached.

to the sidewalls. Eventually this component transfers forces from the tread to the bead and rim of the tire.

The ply is made up of thin polyester cables typically in layers of one, two, or three. Standard tires contain about 1,400 cords, each one of which can resist a force of 33 lbs. [7].

3. *Lower Bead Area*

   This is the part of the tire which is in direct contact with the rim. The power from the engine and braking effort is transmitted from the rim of the tire to the contact area with the road's surface [25]. It is made of tear resistant rubber to protect liners during mounting.

4. *Beads*

The beads provide a chamber seal around the rim by using a wire to ensure that the tire is properly seated on the rim. There are several wires per tire, and each wire can take a load of up to 3,968 lbs. without risk of breaking.

5. *Sidewall*

   The sidewalls are made of weather resistant rubbers which are flexible in nature to protect the side of the tire from impact with curbs and debris. They are mainly exposed to various weather conditions and are designed to protect the inner construction from weather, sun, abrasion, scuffing, and ozone.

6. *Crown Plies*

   The crown plies or belts is the key components of the tire which determines the strength of the tire. It's made up of very fine resistant steel cords bonded into the rubber [25]. This allows the tire to limit its deformation during driving operations such as cornering, acceleration, and braking. It helps to stabilize the tire treads and resists penetration into the inner liner.

7. *Cap ply (Overlay)*

   The overlay or "zero degree" belt is a safety layer which reduces frictional heating and helps maintain the shape of the tire during high speeds [23]. It is usually composed of a nylon fabric, flat or spiral in shape, that is wound at 0°. To prevent centrifugal stretching of the tire, reinforced nylon based cords are embedded in a layer of rubber and placed around the circumference of the tire [7].

8. *Tread*

   The tread is in direct contact with the terrain and serves to:

- Carry load efficiently
- Provide traction
- Promote low rolling resistance
- Resist tread wear
- Resist cutting or puncturing
- Resist heat buildup
- Absorb road irregularities
- Respond to cornering and steering inputs

2.3.3 Effect of Tire Type- All-Season, Summer, and Winter Tires

Depending on the ambient and ice surface temperature, the tire may encounter wet or dry conditions. Therefore, winter tires must be able to accommodate both types of traction requirements [7].

Design elements that impact wet grip include groove ratio, sipes, and the overall shape and layout of the tread design. The larger the grooves of the tire, the more efficient it is at pumping water away from the contact patch. The sipes work in conjunction with the grooves and are thin slits on the tread block which improve traction in wet and icy conditions.

Design elements that impact dry grip are the tire's profile. For example, a flat profile with square shoulders provides good support in turns [7]. Under dry conditions, to have the highest available friction, it is desired to have more rubber in direct contact with the terrain. Therefore, the smaller the percentage of grooves in the tread pattern, the better traction capabilities the tire has. When the individual tread block are large in size, the better the traction is, but this eventually leads to the trade-off of excessive noise. Therefore a variation of sipes are introduced to reduce the rigidity of the tread blocks [25].

Running all-season tires all year may seem like a smart way to save money however it is a bad compromise for safety [26]. On snow, ice, or cold pavement the stopping distance of

a car can be up to 30% - 40% longer if you have all-season tires compared to winter tires [24]. While many people focus solely on the tread of a tire when it comes to winter tires what should actually be considered is what the rubber compound it made out of. The soft rubber treads of a winter tire are able to splay and wrap themselves around minute imperfections on cold pavement, or even what may appear to be perfectly smooth ice. On the opposite end of the spectrum summer tires harden as temperatures begin to fall. All-season tires lie somewhere in the middle. They do not necessarily harden but they do not soften like a true winter tire to provide the additional grip on the road. Winter tires should be put on once temperatures are expected to drop below 7°C. As the temperature falls, the rubber in summer and all-season tires becomes inflexible.

Winter tires should be narrower than summer models. Reducing the width of a tire increases the pressure it exerts on the surface beneath it, which helps the tire traverse through winter conditions and reduces hydroplaning. In the old days, winter tires came with deep, aggressive treads designed to paddle through deep snow. This made for a noisy ride and compromised stability, since the treads deflect under acceleration, braking and cornering loads [27]. Current winter tire technology focuses on shallower treads with closely spaced grooves that carry away the water film created when the tire presses down on ice or snow. Some manufacturers offer winter tires that use rubber mixed with hard materials; e.g., crushed walnut shells and chopped nylon strands. This helps to give increased bite at the contact patch. Although these can offer improved traction in some conditions, the most important factors contributing to a winter tire's all-around grip are the quality of its rubber compound and its tread design [28].

2.3.4 Discussion on Tire Design

The tire grip is a general safety requirement for any vehicle, whatever the condition might be. This includes summer and winter weather conditions along with smooth and rough on-road and off-road terrains. The tire is a high performance composite structure that is relatively soft and flexible in nature. At the contact patch, friction affects the tire deformation and footprint. The three boundary zones of the tire and rim work together to provide a diverse range of performance qualities such as:

- Carry Load
- Transmit torque
- Produce Cornering Force
- Provide Steering response
- Cushion Road Inputs
- Dimensional Stability
- Consume Minimum Power
- Low Noise / Vibration
- Tolerate Poor Maintenance
- Durable and Safe Performance
- Long Wear Life

The tread is designed to serve various important functions in the operation of the wheel. The tread must provide the necessary grip capacity for driving, braking and cornering operations. It is designed to provide uniform wear, to channel water out of the footprint, and to minimize pattern noise on a variety of terrains. In general, the radial tire is made up of eight major components which work in union to handle the interaction of the terrain, as seen in Figure 2.9.

The performance of winter tires has been significantly improved over the past decade by advanced rubber compounds that allow designs to make tires softer without sacrificing other critical properties, including wear and heat buildup as temperatures climb. Major manufacturers spend a lot of money on R&D. Although testing makes it easy to see the performance advantages of a winter tire, the technology behind it is deceptively complex. Tire designers must consider a long list of factors including tread stability and hysteresis to

ensure high performance.

2.4 Existing Technologies for Experimental Investigations of a Pneumatic Tire

Experimental methods are common methods of investigation for evaluating tractive performance. The experiments are usually a result of a direct evaluation conducted in the field. Therefore, the data collected is only valid for the particular terrain and it is hard to extrapolate for other types of terrain. Furthermore, such results are dependent on the tire tested, and this also makes extrapolating the results to other types of tires difficult. There are relatively few studies that investigate experimentally the effect of the temperature distribution at the contact patch with an imposed slip and under various steering configurations. Moreover, no study exists that provides direct validation of the tire-ice contact model [19].

A tire manufacturer should have a comprehensive array of grip tests that effectively include the full spectrum of end-user conditions [7]. In addition, these tests must be reproducible and unbiased. The results of these tests are used for the development of new tires and their certification by vehicle manufacturers and the authorities. The parameters taken into account in a grip test procedure are as follows:

1. The stress imposed on the tire:
   (a) Stress mode (Longitudinal, Transversal, or Composite)
   (b) Slippage rate (Braking conditions and during driving operation)
   (c) Slip angle and Camber angle

(d) Vehicle speed (Acceleration or Deceleration)

(e) Tire parameters (Normal Load, Inflation Pressure)

1. The test conditions:

   (a) Surface Type (Macro-roughness, Micro-roughness, Thermal properties)

   (b) Surface Condition (Dry, damp, wet, flooded, snow, ice, as well as surface temperature)

   (c) Type of Vehicle or Test Machine (Weight, Load Transfers, and Steering Configurations)

   (d) Mode of Measurement (Speed, Braking Distance, Traveling time, Acceleration and deceleration rates, forces, etc.)

2.4.1 Laboratory Tire Testing

Analytical testing are tests in which stress is applied on the tire isolated from the vehicle body, thus having the tire run on a road simulator or roller rig. A popular testing equipment used is the roller rig. A roller rig may come in all shapes and sizes which allows the movement to be either rotational, translational, or both [29]. A roller rig consists of a drum or flat test bed which is composed of an artificial surface dependent on the desired investigation. In some context, the rig is designed to have the wheel rotate on the outside of the rig, as seen in Figure 2.10. This provide a concave surface for the tire to roll on. Other rigs have the tire rolling inside the drum or on a flat track, such as the Terramechanics Rig in $TMVS$ at Virginia Tech.

Tests on a laboratory rig have a major advantage of controlling a certain number of parameters which cannot be controlled on a test track or outside of a laboratory setting.

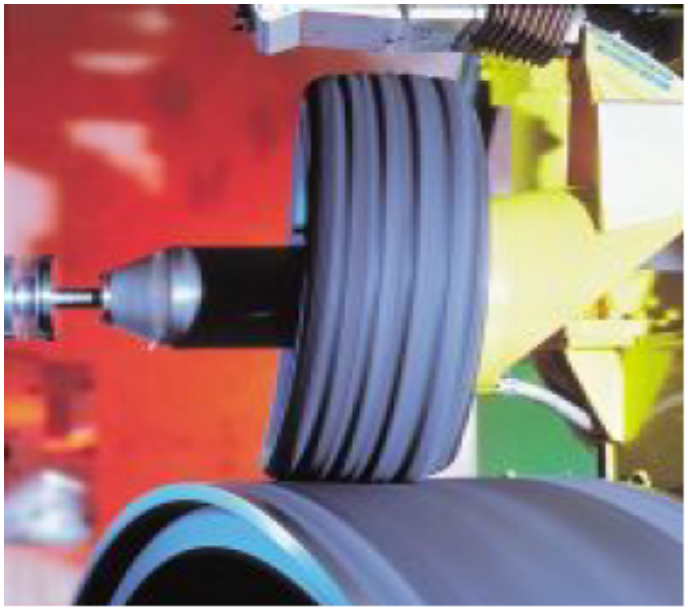

Figure 2.10: Road simulator in operation. The tire is running on the outside of the drum for this specific study. Adapted from [8] under fair use; Fair use determination attached.

These include parameters such as ambient or tire temperature, atmospheric conditions, wheel load, and drive or brake torque at the wheel. These tests are to produce graphs of the coefficient of grip as a function of the load, slip angle, slippage rate, speed and temperature.

2.4.2 Laboratory Vehicle Testing

Laboratory vehicles are used on test tracks or other terrains and are fitted with instrumentation connected to an additional wheel operating independently of others as seen in Figure 2.11.

The principle of the test is composed of the vehicle traveling at a constant speed, in a straight line and over a surface considered to be regular [8]. The tire on the measurement wheel is subjected to a given load and inflated to a specific pressure. During analytical tests, the force measuring equipment captures the longitudinal and lateral forces on the hub along with the respective slip ratios.

Figure 2.11: Laboratory vehicle that has been equipped with a measurement wheel. This wheel is located at the center of the vehicle. It operates independently of the other four wheels allowing for its dynamics to be investigated. Adapted from [8] under fair use; Fair use determination attached.

By determining all the parameters selected and the measurements made, the longitudinal and lateral tractive performance can be investigated as a function of the slip ratio. Analytical tests are essential to the understanding of the operating mechanisms of tires. However, they are not representative of the combined stresses to which the vehicle tires are subjected to on the road. To reproduce these real stress conditions, vehicle track tests are necessary.

2.4.3 Outdoor Test Tracks

Another form of testing pneumatic tires are on outdoor test tracks, as seen in Figure 2.12. Various test can be performed on test tracks, such as: aquaplaning test in a bend, testing longitudinal and lateral grip, and testing on a combination circuit to test different parameters simultaneously.

What characterizes these tests is the number of parameters over which there is little control over, for example: wind, sunshine, rain, ambient temperature, track temperature

Figure 2.12: Combination circuit at the Ladoux test center, France. The track is refereed to as the Duck (Canard) circuit because of its distinctive shape. This circuit alternates between wide bends, tight bends and straight stretches. Adapted from [9] under fair use; Fair use determination attached.

and the differences between vehicles [23]. In order to obtain usable results, track tests are always performed against a set of reference tires. In addition, each test is usually run with several different types or versions of the tire, thus providing not only measurements but also a classification of the tire's performance.

2.4.4 Discussion on Existing Technologies Related to Tire-Ice Testing

A tire manufacturer should have a comprehensive array of grip tests that effectively include the full spectrum of end-user conditions [7]. Several techniques are employed by researchers and manufacturers in order to accomplish this. These include laboratory testing and field testing.

The unique capabilities of laboratory testing are used to help innovators measure

and understand tire performance and characteristics for all types of tires. Vehicles are also instrumented with an additional wheel which is capable of collecting information, such as forces at the contact patch during operation. Finally, test tracks also serve the purpose of providing a comparative analysis between tire performance based on subjective opinions.

2.5 Tire-Ice Interaction

The tire-ice interaction is a highly complex phenomenon which is dictated by various parameters, some of which can be controlled and others that are a direct result of the dynamics of a tire. In order to understand the interaction, it is important to study the effect of various conditions such as:

- Friction Mechanism
- Effect of Temperature rise
- Effect of Thin Water Film in Contact Patch
- Effect of Slip Ratio

Friction at the contact patch is continuously changing as a result of the ambient and ice surface conditions. When the ambient temperature is low enough, the friction is predominantly from a dry surface which causes the tire to have increased tire grip. At higher temperatures, the contact patch dynamics causes the tire-ice interface to reach a temperature appropriate enough to allow melting. This thin liquid layer that is formed provides a new surface for which the tire will operate on and will ultimately lead to lower friction.

2.5.1 Friction Mechanism

Rubber friction on smooth surfaces has two contributions, namely an adhesive (surface) and a hysteresis (bulk) contribution [30]. The adhesive portion results from the attractive bonding forces between the rubber tread block and the surface which causes the tread block to deform accordingly. Surface forces are often dominated by weak attractive van der Waals interactions [31]. For very smooth surfaces, due to the low elastic moduli of rubber-like materials, this weak attraction may still result in a nearly complete contact at the interface, leading to the large sliding friction force usually observed in dry conditions on ice [21]. On the other side of the spectrum, for rough surfaces, the adhesive contribution to rubber friction will be much smaller because of the small contact area. In this case, the bulk (hysteresis) friction mechanism is believed to dominate at the tire-ice interface.

Quite early in the 1970s Gnörich [32] introduced some of the first tribometers which dealt with rubber-ice friction and developed some of the original techniques for laboratory ice surface preparation and experimental investigations. A few years later, Roberts proved the existence of an apparent "switch" between friction mechanisms dependent on the ambient temperature and ice surface temperature [21]. He also noted that at lower temperatures, where the measured friction is surprisingly high, the properties of the rubber compound also plays an important role.

The frictional behavior of a sliding rubber block on a surface is characterized by different mechanisms that are generally classified as [13] follows:

- Hysteresis friction due to viscoelastic energy losses in the deformed and excited rubber during operation.
- Adhesive friction due to interaction between the rubber and the surface on an atomic scale.

- Viscous friction due to water or another liquid in the gap between surface and rubber tread block.
- Frictional effects related to the geometry and dynamics of the rubber tread block.

2.5.2 Effect of Temperature Rise

During normal tire operation, the tire will build up heat due to its energy losses. This rise in temperature has been experimentally investigated as the bulk temperature distribution at the contact patch. The heat that is built up is eventually transferred to surfaces through the intermediate interaction between the two interfaces in contact. In icy surfaces when the melting point is approached, the tire grip capacity is lowered as the overall friction which is available is decreased. At lower temperatures, where the measured friction is surprisingly high, the properties of the rubber compound play the important role in the friction available [33].

At low temperatures, the tire tends to have a higher grip capacity on the smooth ice surface as compared to temperatures near the melting point. Schallamach investigated this scenarios [31] using various experimental studies and eventually concluded with what is now identified as "Schallamach Waves." When the contact patch remains dry, and if the temperature of the ice is low enough, the tire tread adheres to the ice surface and, as the tire rotates, microscopic parts of the tread blocks are left behind in the track. At low ice temperatures, this was observed as the tire skipped along its path during travel. The phenomenon occurred when the tread block deflected towards the trailing edge and snapped back to equilibrium causing increased wear and a peel-stick condition which was visualized as waves. The Schallamach waves, which can be visualized using microscopic instruments, indicate a peel-stick condition at the contact patch which leads to wear in the tire. The

areas of the contact patch where the waves are present are considered to have a coefficient of friction greater than unity [31].

When the ambient temperature is high enough, a thin liquid layer is formed at the tire-ice interface as the tire is operated. The phase transition as the ice melts into water must be taken into account when performing a heat balance to properly model the tire-ice interaction. The decisive factor which limits the amount of friction available at the interface is the height of the fluid at the medium [13]. As the height is increased, the direct contact between the ice and the tire is reduced and leads to the tire ultimately riding on a thin liquid layer leading to a decrease in the friction.

The temperature distribution in the contact patch needs to be established in order to properly characterize a pneumatic tire, since thermo-mechanical properties of rubber materials are strongly dependent on temperature [34]. The temperature rise at the contact patch is due to various factors influencing the tire during operation. A large fraction of the total work done in rolling tires under normal operation conditions is made up of hysteresis heat distributed throughout the tire, where most of the heat generation is found to be located near the tread of the tire [35]. To acquire sufficient temperature information in a rolling tire, a new wireless temperature measurement system was set up for this study.

2.5.3 Effect of Thin Water Film in Contact Patch

It was proposed as early as 1939 that frictional heating might be the main contributor to ice slipperiness [36]. Heat is generated by friction which gives rise to a boundary condition of constant heat flux (the rate at which heat is transferred across any surface at a given point per unit area per unit time).

For the special situation of an ice surface, the contact between rubber and ice is

lubricated by a thin liquid water layer since the induced frictional energy leads to continuous ice melting. The existence of this water layer is even proven experimentally for high ice temperatures [37]. Viscous friction is therefore one of the main friction mechanisms for a rubber block sliding on ice. Further research showed this phenomenon was most prevalent at surfaces temperatures between 0°C and -6°C (32°F and 21.2°F) [33].

The layer of water that ensues between the ice and tire acts like a lubricant, reducing the traction which the tire can achieve. The height of the fluid is due to the weight of the car and the friction of the rubber on ice [13]. There exist a critical height of the thin water film at which the friction value is reduced to 25% of the original value. This is when the tire operating directly on the water film and the friction is reduced to a saturated value, much lower than the initial friction level as shown in Figure 2.13.

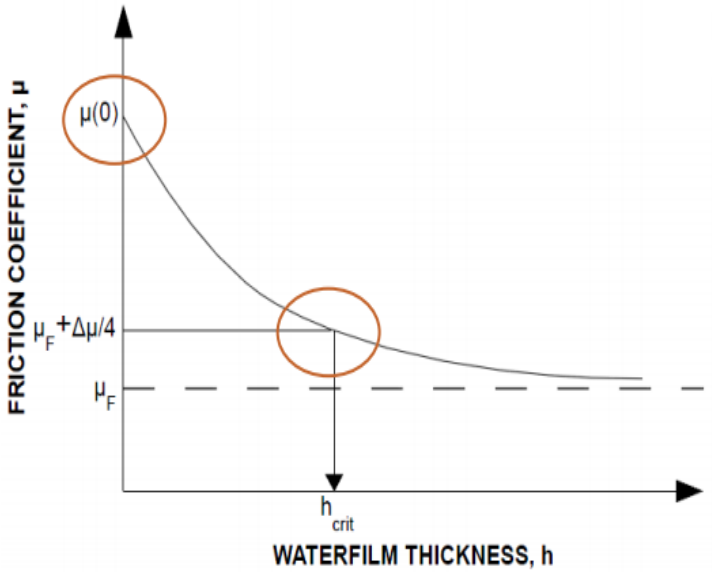

Figure 2.13: Friction level as a function of water film thickness. There exist a critical height in the fluid film for which the friction drops to 25% of the original value. Adapted from [10] under fair use; Fair use determination attached.

In order to determine the friction based off of the fluid height, Kulakowski and Hardwood developed an equation in 1990 [10] which computes the friction as shown in Equa-

tion (2.1):

$$\mu = \Delta\mu \cdot e^{-\beta h} + \mu_F \tag{2.1}$$

In Equation (2.1) h is the height of the fluid layer, μ is the friction coefficient, and β refers to the properties of the water.

2.5.4 Effect of Slip Ratio

An important observation, later confirmed by several studies [35], was that the sliding speed and the temperature have very similar roles. It is well understood that the ice becomes more slippery as the temperature increases, but it is also true if the rubber slides faster. This relation was explained by showing that the main governing factor of rubber-ice friction is the evolution of the temperature in the contact patch [35]. Not only is the sliding speed a factor but also the contact pressure and the ambient temperature influence the friction on ice. As a result, a friction characteristic can be plotted as seen in Figure 2.14. It shows the influence of sliding velocity, contact pressure and temperature on the friction coefficient of rubber on ice. It can be observed that an increasing sliding velocity and an increasing normal pressure causes a decrease in the friction coefficient. An increasing temperature causes a decreasing friction coefficient as well, which are all typical for ice friction mechanisms.

The viscoelastic properties of rubber-type materials are strongly temperature dependent [21]. Therefore, it is necessary to include the local temperature increase in any analysis regarding the friction at the tire-ice interface. At very low sliding velocity the temperature increase is negligible because of heat diffusion [10], but already for velocities of order 10^{-2} m/s the local heating may be very important. The influence of the local heating on the

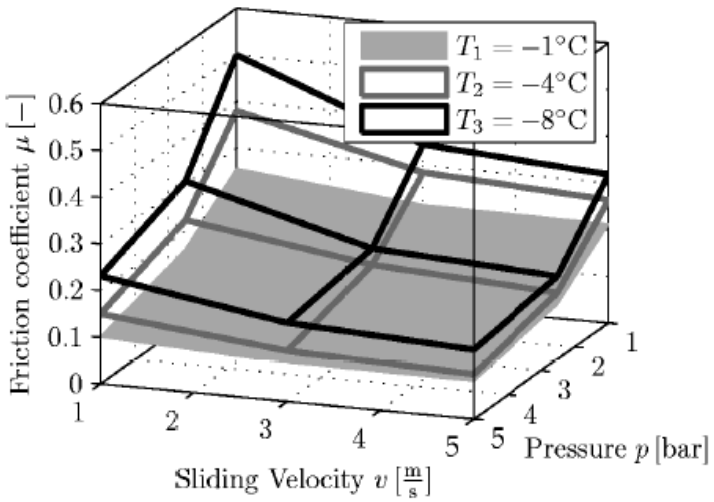

Figure 2.14: Friction characteristic of rubber-ice interface depending on sliding velocity, normal pressure, and temperature. Adapted from [9] under fair use; Fair use determination attached.

rubber friction results in a decrease in rubber friction with increasing sliding velocity for v > 0.01 m/s. This may result in stick-slip instabilities [31], and is of crucial importance in many practical applications in particular for ABS-braking systems. These effects can lead, for example, to velocity-dependent mixed-mode lubricated friction and also fluid-solid interactions [38].

2.5.5 Discussion of Tire-Ice Interaction

The tire-ice interaction is a highly complex phenomenon which is dictated by various parameters, some of which can be controlled and others that are a direct result of the dynamics of the tire. In order to understand the interaction, it is important to understand the effect of various conditions such as those discussed in Section 2.5. In order to fully characterize the friction mechanism at the tire-ice interface, the adhesive and the hysteresis contributions must be understood. The friction at the interface results in local heating at

the contact patch, ultimately leading to a temperature rise. In some cases, depending on the ambient temperature, the temperature rise might lead to a thin water film at the tire-ice interface. This thin water film will lead to a change in the friction mechanism at the contact patch as the viscous forces due to the film will now also have to be taken into consideration. Various models take the friction due to the fluid into consideration, but in most cases these are on wet roads. The novelty in this investigation is to account for the height of the fluid due to the direct tire-ice interaction and to quantify the shear forces the water will induce at the contact patch, under icy conditions.

2.6 Tire-Ice Modeling

The physics behind the tire-ice phenomena must be well understood in order to model this interaction. As stated earlier, tires are a complex composite composed of many layers of materials as seen in Figure 2.9. A tire is very anisotropic, meaning that the mode of operation dictates the performance of the tire. It is for this reason that the tire behavior is not only derived from the material properties and structure of a tire. Simplifications are therefore made in order to create analytical, semi-empirical and empirical models for a tire. Under these simplifications though, some of the real dynamics are not captured as they are ignored.

There are three main contributions to the tire-ice interaction which must be understood to simulate the tire dynamics. These three contributions include the effect of which rubber-ice friction has on the temperature rise, the effect of various tire parameters on the resulting forces at the contact patch, and the ambient conditions in which the tire operates, which may or may not be able to be controlled. If these three contributions can be properly integrated together to model the tire, then it may be possible to characterize the tire-ice in-

teraction. In literature, various researchers have attempted to quantity these varying factors in order to model the tire-ice interaction.

2.6.1 Existing Tire-Ice Models

Tire traction models play a major role in predicting the frictional mechanisms at the tire-ice interface by taking into account various factors. Eventually, these models lead to a better understanding and ultimately to improved vehicle safety on icy road conditions. Various models have been developed to predict the friction coefficient of the tire-ice interface considering different factors.

Peng [11] developed a new method to determine the tire traction on ice. Using the principles of heat balance and Jaeger's conduction theories for solids, Peng is able to quantify the temperature rise at the contact patch for a tire in a state of rolling. The assumptions of the model are:

1. The tread was rigid and its surface was perfectly smooth and remained parallel to the ice surface whether melting or not.

2. The contact pressure distribution was uniform across the interface, or $p_{avg} = Const.$

3. Some of the frictional heat generated at the interface was used to melt the ice and the rest conducted into the tread and bulk ice surfaces. The heat flow was only one dimension normal to the frictional surfaces because the depth of heat penetration was much smaller than the sizes of the interface.

4. Coefficient of friction was constant in the dry sliding region of the interface.

5. Temperature in the melting region was kept at the ice melting point.

6. Initial temperatures of both tire and ice surfaces were equal to the ice bulk temperature.

Peng determined that the frictional heating generated in the dry region of the contact patch during rolling can be quantified by the following Equation (2.2):

$$Q_d = \int_0^{x_m/v} q_d dt = \mu_d \; p_{avg} \; S \; x_m \tag{2.2}$$

where q_d is given by

$$q_d = \mu_d \; p_{avg} \; v_s \tag{2.3}$$

Using Figure 2.15, the total quantity heat transfer from the melting patch into the surfaces of the tire and ice is given by Equation (2.4):

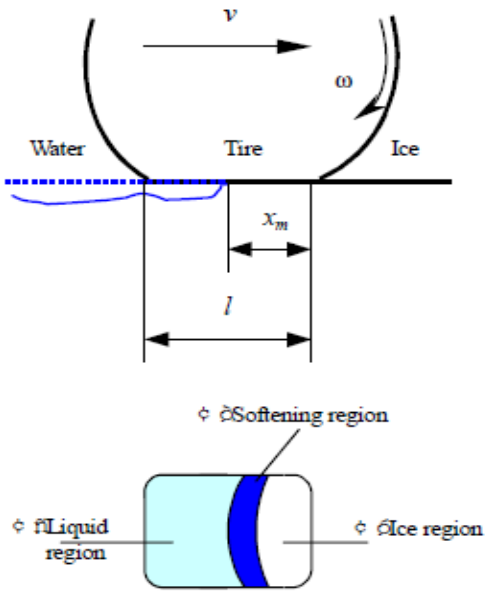

Figure 2.15: Schematic Model for Analyzing Peng's Model. Adapted from [11] under fair use; Fair use determination attached.

$$Q_t = 2k_t(T_m - T_t)(\frac{l - x_m}{\pi\alpha_t v})^{1/2} \tag{2.4}$$

Although the model is able to capture the frictional heating in the dry region, it lacks the capabilities to provide vital information regarding the friction after the ice has melted.

Persson also studied the temperature rise due to local heating caused by friction. The author assumed the ice surface to be as smooth as possible and accounted for the local heating due to the sliding of the rubber. The author introduces the role of flash temperature [39] into the tire-ice modeling. This idea of the flash temperature is a sudden rise in temperature due to the macro-asperities contact at the surface. This is especially evident in locked wheel conditions. In Persson's temperature rise model, the surface is first characterized using a power spectrum which has the power-law behavior seen in Equation (2.5). The law is chosen because the ice surface can be considered to be "self-affine fractural." This means that if part of the surface is magnified, then the statistical properties of the surface are the same [39].

$$C(q) \sim q^{-2(H+1)} \tag{2.5}$$

After the surface has been characterized, the author uses a heat balance to account for the temperature field on a rubber block as:

$$\frac{\partial T}{\partial t} - D\nabla^2 T = \frac{\dot{Q}(x,t)}{\rho C v} \tag{2.6}$$

where $\dot{Q}$ is the energy production per unit volume and unit time as a result of the internal friction in the rubber and D is the heat diffusivity.

In general, the influence of the flash temperature on rubber friction differs depending on if the perturbing frequency $\omega_0 = vq_0$ is smaller or larger than the frequency ω_1 where $ImE(\omega, T_0)/|E(\omega, T_0)$ is maximal [39]. Using the WLF equation, an increase in temperature shifts the viscoelastic spectrum to higher frequencies which results in a decrease in friction when the flash temperature is taken into consideration. This is the case for tire applications. Even though the flash temperature is taken into account, the model fails to take into account the effects of melted ice at higher ambient temperatures.

The third model which was investigated in this comprehensive literature review was developed by Hayhoe and Sahpley [12]. In this study, the authors provide a model to determine the forces generated by a tire on wet ice.

Using a theoretical heat balance, it is shown that the temperature in the contact patch of a tire sliding on ice can reach the melting point, resulting to a thin layer of water at the interface. This allows a mathematical model to be derived which can estimate the traction forces generated in the contact patch using well-known fluid dynamics [12]. The study resulted in the following governing equations which together make up the model for tire traction forces on ice shown in Equation (2.7):

$$\frac{dh}{dx} = \frac{A}{h} - \frac{B}{\sqrt{x}} \tag{2.7}$$

where:

$$A = \frac{Frictional\ Flux}{Melt\ Flux} h \tag{2.8}$$

$$B = \frac{Conduction\ Flux}{Friction\ Flux} \sqrt{x} \tag{2.9}$$

In Equation (2.7), h is the fluid height, and x is the longitudinal distance from the leading edge of the contact patch. Traction forces are calculated from the model for a number of different braking and driving conditions and for different vehicle speeds. These results are then compared to available test results. This model was able to simulate the friction levels at different slip ratio and was relatively close to the experimental results studied, as shown in Figure 2.16.

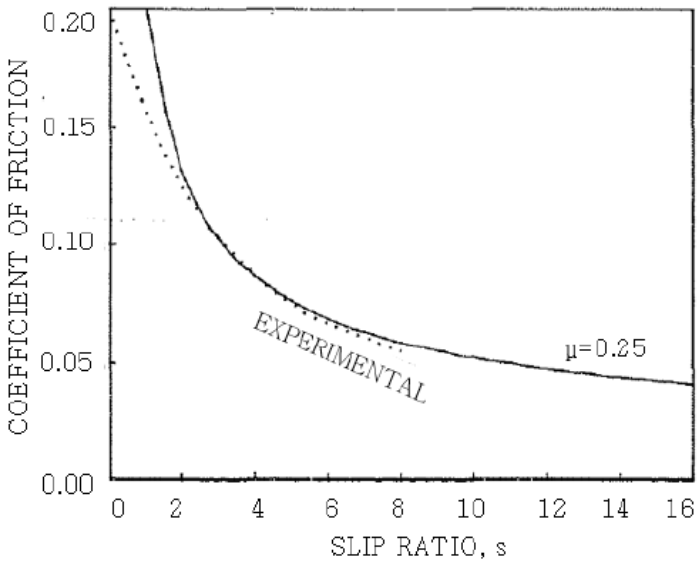

Figure 2.16: Experimental and simulated results representing the friction levels of tires on ice at the contact patch for varying slip ratios. Adapted from [12] under fair use; Fair use determination attached.

Finally, the fourth model which was investigated during this study dealt with the bulk temperature distribution of the tire under steady state conditions. Yavari et al., [40] coupled the mechanical rolling contact problem with a thermo-viscoelasticity problem to come up with a simplified solution to predict the temperature distributions in static and rolling tires. In order to model the temperature distribution in such manner, the power loss of the tire during mechanical loading, serves as the heat source for the heat transfer equations. By employing the first law of thermodynamics, the authors formulated an equation of energy

balance which is based on the change of internal energy being equal to the sum of the total work performed on the system. Using this method, the equation [40] can be written as:

$$\rho \frac{De}{Dt} = \sigma : \nabla \dot{\mathbf{u}} - \nabla \mathbf{q} \tag{2.10}$$

The first term of Equation (2.10) represents the change of internal energy per unit mass using the material derivative, D/Dt. The second term deals with the rate of change in mechanical energy where σ is the Cauchy stress and $\nabla \dot{\mathbf{u}}$ is the rate of the deformation gradient. Finally, the last term represents the rate at which heat is being added by conduction.

2.6.2 Tire-Ice Model (TIM)

The Tire-Ice contact Model was developed at Virginia Tech in order to understand the tire-ice interaction [19]. TIM uses the principle of heat balance, along with information regarding the pressure distribution to identify the rise in temperature during normal driving operations. Depending on the ice surface temperature, the Tire-Ice Model is also capable of determining areas of wet and dry regions. It uses the relative difference between the rise in temperature and the ice surface temperature to determine if the rise in temperature is sufficient enough to induce melting. Further work increasing the capabilities of the model has been the focus of this study and is presented in Chapter 4. The Tire-Ice contact Model (TIM) is validated for two parameters. These include the temperature rise in the contact patch and the friction level generated at the tire-ice interface. With a novel method developed, as shown in Chapter 3, the model was able to be validated.

2.6.3 Temperature Rise under Braking Conditions

On an ice surface, the ABS braking systems equipped on vehicles struggle to maintain control of the vehicle under emergency situations. In order to improve on the current design it is critical to determine the transient temperature distribution of the tread due to the heat generated by sliding friction under conditions of severe cornering and braking.

To account for the temperature rise during severe sliding, the slip between tread surface and the ice must be quantified as this is the main source of frictional heat generation during sliding [41]. The slip ratio can be defined as:

$$s = \frac{V - r\omega}{V} \tag{2.11}$$

Where V is the translational velocity of the wheel, r is the radius of the wheel, and ω is its rotational angular velocity. The frictional force has a component due to hysteresis and one due to the adhesive force. The hysteresis component affects not only the external tread surface, but also the bulk rubber material to a certain depth [41].

Under conditions of severe sliding, due to either the slip angle α or the slip ratio s, the power consumed by the tire is given by the following equation:

$$W = (\sin^2 \alpha + s^2)^{1/2} \mu_d V F_z \tag{2.12}$$

Note that the coefficient of sliding friction is μ_d, the load is F_z, and the translational velocity is V. Equation (2.12) corresponds to the work being done under severe sliding [41].

During severe sliding, the flash temperature phenomena must also be taken into account [37]. During sliding of a tire, the temperature increases rapidly as a result of the

frictional abrasion between the tire tread and the ice surface. In most cases this leads to a thin fluid at the tire-ice interface due to melting.

2.6.4 Modeling the Coefficient of Friction of Smooth Ice

In order to model the friction at the tire-ice interface, the ice surface must be well characterized. At very low surface temperatures, (below -10°C) the ice surface remains dry as a tire rolls over the surface. Under these conditions, the stick-slip scenarios are the most common. This is because the tire rubber tends to stick to the surface as it forms microscopic bonds at the interface [31]. Under these dry conditions, the traction of the tire is the highest as the only source of friction are from the asperities at the ice surface. The typical friction levels of dry ice are in the range of 0.16 to 0.20 [37]. Therefore the design of the tire tread must be able to "cut" into the ice in order to maintain friction with the asperities of the ice surface.

At temperatures close to freezing, the tire rolling on the ice surface typically induces viscous friction due to water or another liquid in the gap between the surface and rubber tread block. In these conditions, the water film must be taken into account when modeling the friction at the tire-ice interface. These effects can lead, for example, to velocity-dependent mixed-mode lubricated friction and also fluid-solid interactions [33]. The existence of this water layer is even proven experimentally for high ice temperatures [13]. Viscous friction is therefore one of the main friction mechanisms for a rubber block sliding on ice and must be considered by all theoretical models in the literature when the ice surface temperature is within range.

2.6.5 Discussion of Tire-Ice Models

In order to model the tire-ice interaction, it must be well understood the physics behind the phenomena. As stated earlier, tires are a complex composite comprising many layers of materials as seen in Figure 2.9. Simplifications are therefore made in order to create analytical, semi-empirical and empirical models for a tire. To develop a comprehensive tire-ice model, the three main contributions to the tire-ice interaction must be understood to simulate the tire dynamics. These three contributions include the effect of which rubber-ice friction has on the temperature rise, the effect of various tire parameters on the resulting forces at the contact patch, and the ambient conditions in which the tire operates which may or may not be able to be controlled.

In this section, existing tire-ice models were discussed. Peng [11] developed a new method to determine the tire traction on ice using the principles of heat balance and Jaeger's conduction theories for solids. Persson also modeled the tire-ice interaction by introducing the phenomena of the flash temperature [39]. Hayhoe and Sahpley [12] used a theoretical heat balance to show that the temperature at the contact patch of a tire sliding on ice can reach the melting point, resulting in a thin layer of water at the contact interface. Yavari et al., [40] investigated the bulk temperature distribution of the tire under steady state conditions. Using a finite element model, the authors coupled the mechanical rolling contact problem with a thermo-viscoelasticity problem to come up with a simplified solution to predict the temperature distribution of a tire.

A Tire-Ice Model (TIM) was also discussed in this section. This model was developed in-house [19] to capture the temperature rise due to the pressure distribution at the contact patch. Once the pressure distribution has been determined, the temperature rise can be determined based off of Jaeger's formulations.

A literature review of the temperature rise due to braking was also presented in this section. Under conditions of severe sliding, due to the slip angle α or the slip ratio s, the power consumed can be used to determine how much heat is produced.

Finally, the friction at the tire-ice interface was discussed. In order to properly model the friction at the interface, the ice surface and ambient conditions must be well characterized. Literature review of the effect of the thin water film was explained. At ice surface temperatures close to freezing, the viscous friction due to this thin water film must be considered. When the ice surface temperature is very low, typically under -10°C, the ice surface can be considered to be mostly dry.

2.7 Bicycle Model

The first to formally derive a fully general set of linearized equations for the basic bicycle model was Francis Whipple in 1899 [42]. There are numerous degrees of freedom associated with vehicle dynamics. The most simplified vehicle dynamic model is a two-degree-of-freedom bicycle model, representing the lateral and yaw motions. It is able to decouple the longitudinal direction, because it does not directly affect the lateral or yaw stability of the vehicle. A three-degree-of-freedom model adds longitudinal acceleration to the model, therefore enabling one to describe the full vehicle motion in the X-Y plane.

Whipple treats the front and rear sections of the bicycle symmetrically throughout the derivation. He first derived nonlinear governing equations of motions for a basic bicycle model with an active rigid rider, and then linearized about the vertical equilibrium configuration. It was not until 1910 that Physicist Felix Klein and Arnold Sommerfield [43] introduced the effects of gyroscopes into the derivation of the bicycle model. This was done by having all the mass and inertia of the front assembly in the front wheel. Somewhat similar to Whipple [42],

they used a Newtonian analysis of the front and rear sections of the bicycle, and treated the two parts as two trailers attached to the steering axis. The linearized equations of motions were derived using axis parallel to the steering axis.

Because of the simplicity of the bicycle model, it is commonly used in real-time applications and autonomous systems. The three degrees of freedom kinematic bicycle model is one of the models frequently used because of the belief that it is able to capture enough of the nonholonomic constraints of the actual vehicle dynamics. Many new vehicle features, such as Electronic Stability Programs (ESP), indirect Tire Pressure Monitoring Systems (TPMS), road-tire friction monitoring systems, etc. rely on models of the underlying vehicle dynamics. The so-called bicycle vehicle model is a rather simple model structure that is frequently being used in the vehicle dynamics literature.

Chapter 3

Indoor Experimental Analysis

An experimental investigation of pneumatic tires on smooth ice was conducted in this study. The purpose of the study is to enhance the understanding of the tire-ice contact interaction at the contact patch through experimental studies for a pneumatic tire traversing over solid ice and to determine how these results conform to the Advanced Tire-Ice Interface Model ($ATIIM$). A design of experiment has been formulated that gives insight into the effect of operational parameters, specifically: wheel slip, toe angle, camber angle, normal load, inflation pressure, ice surface temperature, and traction performance. The coordinate system used in this investigation is shown in Figure 2.5.

3.1 Test Setup and Procedures

For this experimental study, an indoor testing facility developed in the Terramechanics, Multibody, and Vehicle Systems (TMVS) Laboratory at Virginia Tech was used to investigate the performance of pneumatic tires on ice. Prior work in this area has been conducted at TMVS mainly for the longitudinal performance of the tire with respect to several

parameters, such as the slip ratio, inflation pressure, or normal load. The Terramechanics Rig has been shown to provide repeatable results under various operating conditions that can be defined by the user. By adjusting the camber angle and/or the toe angle of the tire, the tire performance under various handling configurations can be studied. The rig is a single-wheel tester that simulates normal quarter-car loads up to 10 kN [44].

3.1.1 Terminology

In this investigation several parameters were controlled in order to determine the traction performance of a pneumatic tire on ice. The camber angle of a tire is the angle of a tire from zero degrees relative to the z-axis when viewed from the front of the vehicle [4]. If the bottom of the tire is further out than the top of the tire, this is known as negative camber angle. And if the top of the tire is further out than the bottom, this is known as positive camber angle as seen in Figure 3.1.

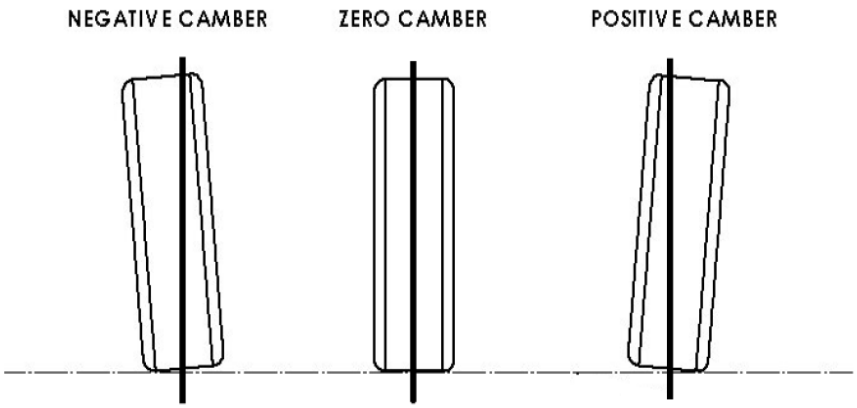

Figure 3.1: Camber angle of the tire relative to the z-axis when viewed from the front of the vehicle.

Zero camber angle is usually associated with solid rear axles, such as in the drag racing industry. To keep them simple there is no way of adjusting the camber angle and

they are locked at zero degrees of camber angle due to the design of the axles. For the purpose of launching a vehicle from a dead stop the driven tires should not have a positive or negative camber angle. A camber angle of zero degrees leads to the largest contact patch and therefore the greatest grip capacity for the tire is developed.

Negative camber is typically used for road racing and circle track racing vehicles. Because of the severe side loading of tire, the tire deforms and typically more heavily loads the outside edge of the tire than the inside edge [4]. However for production vehicles, high amounts of camber can cause uneven tire wear and other handling issues for which most drivers would not be comfortable with. During cornering, if the outside tire has negative camber, it will more evenly load the entire tire producing maximum cornering traction in the respective direction.

Positive camber angle will typically be used for the inside tire during cornering. It works the same way as negative camber angle does on the outside tire. While the tire is flexing, positive camber angle on the inside tire may be needed so the contact patch of the tire is at it's greatest for the purpose of producing the maximum amount of grip at the interface.

The slip angle of a tire is the angle which the tire makes relative to the x-axis. In general terms [4], the slip angle is the difference between the direction a wheel is traveling and the direction that the wheel is pointing as seen in Figure 3.2.

When a toe angle or cornering maneuver is introduced into the configuration of the tire, a slip angle is developed at the contact patch due to the lateral elastic properties and the dynamics of the tire. The presence of a slip angle produces a side force F_Y that is perpendicular to the wheel plane, and the wheel will move along a path at an angle α with the wheel plane as shown in Figure 2.5. This angle is caused by the deflection of the tire

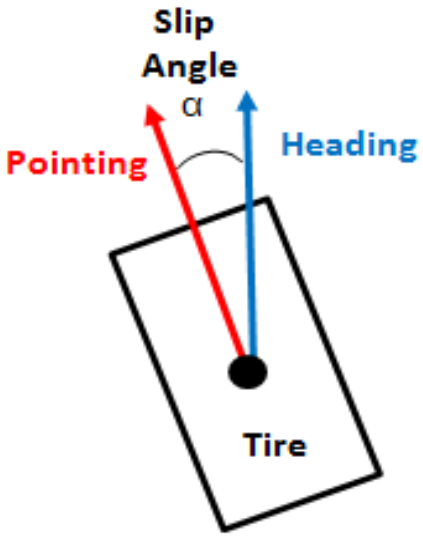

Figure 3.2: Slip angle of the tire relative to the x-axis when viewed from the front the vehicle.

plies and tread elements. As the slip angle increases with the normal load on the wheel, the cornering force increases until it reaches a maximum value where the tire begins sliding laterally. The tire does not necessarily point in the same direction as the direction of travel in most applications. Only at near-zero speeds and nearly straight driving does a slip angle not occur. As the slip angle grows, the lateral forces are increased, but it is only limited to the tread grip capacity and the normal load at the contact patch. In general, the friction capability of the tire and terrain interface is represented by a friction ellipse. The limiting factors of the generation of the forces is the normal load and the stress distribution.

Typically, slip angles are designed to be as part of the steering configuration to promote specific handling characteristics. If the ratio of front to rear slip angles is greater than 1:1, the vehicle will tend to understeer, while a ratio of less than 1:1 will produce oversteer [4]. When a vehicle is designed to understeer, it will have a tendency to turn less sharply than is intended. When a vehicle suspension is designed to produce oversteer, the vehicle will tend to turn more sharply than what was intended. A balance between the two results

in a vehicle that handles well in most conditions.

A vehicle applies a shear force to the terrain surface from the contact patch through the transmission of forces from the engine. The shear force that is developed produces a thrust and an associated slip. In order to accurately predict the tractive performance, it is required to have an in-depth knowledge base of the shear stress-shear displacement relationship under various loads.

Handling is defined by Harty [45] as a percentage of the available friction of the maximum achievable lateral acceleration utilized by the vehicle-driver combination. Therefore, Harty [45] views the task of the vehicle designer as having two main goals, namely: to raise the linearity limit and to increase the frictional limit available. The frictional limit available allows for control of the vehicle. At low percentages, the vehicle operates within the linearity limit e.g., a given steering input results in a certain vehicle response. At higher percentages than the frictional limit, control of the vehicle is unmanageable.

When a cornering maneuver is applied, a non-symmetrical shear stress distribution about the YZ plane is developed at the contact patch. For small slip angles, the cornering force at the contact patch is shifted towards the trailing edge of the tire with a distance labeled the pneumatic trail. The pneumatic trail generates a moment about the Z axis, which aligns the direction of the wheel with the direction of travel. The aligning moment is one of the primary resorting moments that helps the steered tire return to the original position [4]. When the maneuver applied results in a value higher than the frictional limit available, the contact patch developed from the stress distribution is mostly a region of pure sliding, and control of the vehicle is extremely difficult. Therefore, it is of importance to properly characterize the tire in order to provide a safe and reliable prediction of the performance of the tire to prevent unsafe driving conditions. By imposing various steering configurations onto the tire, the contact patch and the tire properties change. This study

aims to investigate the performance of the tire at various handling scenarios. In order to understand handling, the definition of ride comfort must be explained.

When a vehicle has adequate ride comfort, Karnopp [46] explains that the suspension of the vehicle is designed such that chassis of the vehicle is isolated from any irregularities present in the terrain that causes vibrations at high frequency and an unsafe human environment. In its broadest sense, the perceived ride is the cumulative product of many factors. The tactile vibrations transmitted to the feet, body and hands through the seat are the factors most commonly associated with ride.

Standards have been designed to keep passengers safe while operating a vehicle. In order to safely maintain allowable human responses to vibrations, the chassis of the vehicle and the wheel should closely follow the vertical input imposed on the tire by the deformable terrain. The closer they match, the better handling capabilities the vehicle will have and wheel hop and loss of wheel contact with ground can be eluded.

The traction performance of a tire is typically measured by the drawbar pull performance in the field of Terramechanics [47]. The longitudinal drawbar pull is defined as the difference between the longitudinal thrust developed at the tire-ice interface and the resistive force acting on the tire as seen in Equation (3.1). Resistive forces include, but are not limited to, frictional properties of the terrain and resistive forces present in the testing facility. The difference in the slip ratio where the maximum drawbar pull occurs could be helpful in assessing the impact of the adhesion and sliding portions of the contact patch on the tractive capability of the tire. It is hypothesized that, as the tread wears down, the maximum drawbar pull occurs at a lower slip ratio value due to the contact patch becoming mostly a slip region.

$$DrawbarPull(DP) = F_{Thrust} - F_{Resistive} \tag{3.1}$$

A general graphical representation of the tractive performance of a pneumatic tire is shown in Figure 3.3.

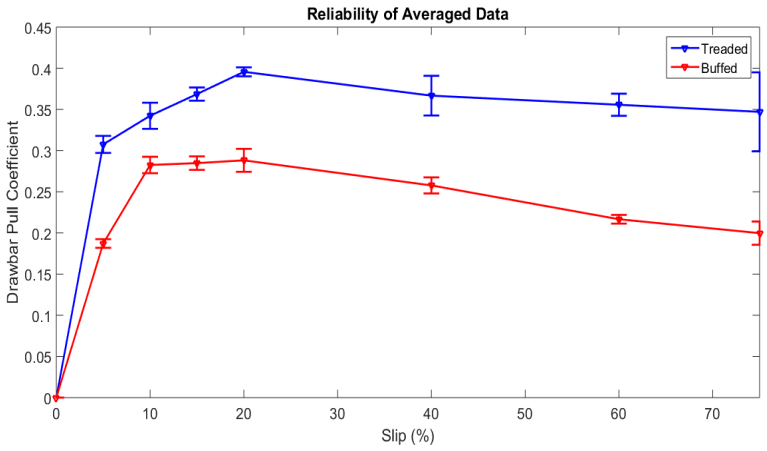

Figure 3.3: Traction performance of a pneumatic tire traversing over a sandy loam. Two tires of the same design with varying tread depth were used to investigate the drawbar pull performance of the tire at a camber and slip angle of 0°. The treaded tire has a tread depth of 7.97 mm. The buffed tire represents a tire shaved to a tread depth of 0.75 mm. The highest standard deviation occurred at 75% slip for the treaded tire and has a value of 0.09.

Notice that this curve has three distinct shapes. First there's an almost straight section at small slip angles where an increase in slip ratio gives a proportional increase in longitudinal force. The slope of this section of the curve provides the "stiffness" of the tire. At a 0% slip ratio, the drawbar pull coefficient will always be 0. In order to account for the true 0% slip value, the data has been offset. In low slip region of the curve, the tread is not sliding at any point in its contact patch. A tire designed to have more stiffness in the tread and sidewalls will have a steeper slope in this area of the curve. At higher slip ratios, portions of the tire patch are sliding, and less increase in drawbar pull is noticed with an increase of slip. This is called the transition region. As the curve tops out, more

of the contact patch is sliding and the tire produces less drawbar pull [4]. After the peak of the curve, longitudinal force can fall off about 20% within a few degrees of extra slip. At these high slip ratios, most of the contact patch is sliding and can therefore not produce any additional tractive forces.

3.1.2 Candidate Tires

For the purpose of the investigation of pneumatic tires on ice, two different pneumatic tires were chosen to be experimentally studied. These specific tires were also chosen to validate the Advanced Tire-Ice Interface Model and to test the model's limits regarding the size of the tire. The initial development of the model used the Standard Reference Test Tire ($SRTT$) [48].

The first tire tested was the Standard Reference Test Tire ($SRTT$). This tire was chosen to be tested again in order to compare previous results and to retest the tire with new instrumentation which will be discussed in Section 3.2. These new tests with the inclusion of the new instrumentation served the purpose of providing validation results for the Advanced Tire-Ice Interface Model. The $SRTT$ which can be seen in Figure 3.4 is a P225/60R16. The 16" pneumatic tire had a full tread depth of approximately 7.97 mm. The $SRTT$ used in this investigation was also the same tire which was tested in 2013. The reason the same tire was used was to help provide other comparisons such as to study the effect of aging and hardening.

The Pirelli tire which can be seen in Figure 3.5 was a P235/55R19. The Pirelli Scorpion Verde All Season Plus XL tire was chosen to be tested in order to test the limits of the original development of TIM. Using this 19" tire also helped to determine the effects for which an All-Season tire would have on ice as compared to the Standard Reference Test

Figure 3.4: Tread pattern of P225/60R16 Standard Reference Test Tire ($SRTT$)

Tire. This specific tread pattern design was composed of four deep grooves along the middle with sipes along the edges of the contact patch to help promote fluid flow in the direction away from the contact patch.

Figure 3.5: Tread pattern of P235/55R19 Pirelli Scorpion Verde All Season Plus XL

3.1.3 Test Facility and Equipment

The testing was conducted in the Terramechanics Rig at the Terramechanics, Multi-body, and Vehicle Systems (TMVS) Laboratory at Virginia Tech. Figure 3.6 and Figure 3.7 show the Terramechanics Rig with a thin layer of solid ice and water on top.

The single wheel tester was mainly designed and fabricated by Biggans [44], to simu-

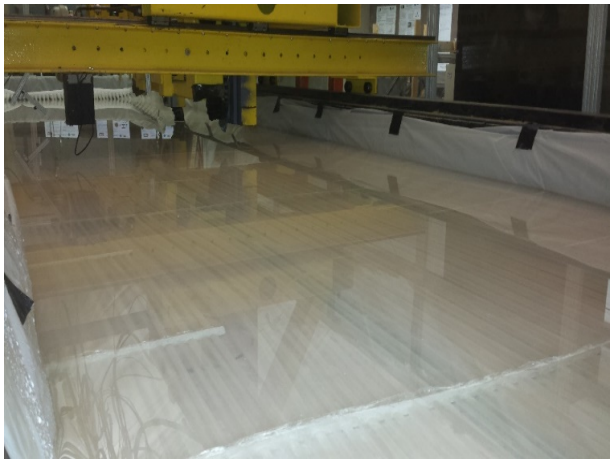

Figure 3.6: Terramechanics Rig at TMVS with water on top of solid ice.

Figure 3.7: Terramechanics Rig at TMVS with water on top of solid ice.

late a front left (driver) tire. With the opportunities to test on various terrains, the unique rig allows the tire performance to be measured under various operating conditions. The Rig uses two separate motors to control the wheel speed and the speed of the carriage assembly, thus allowing the user to impose a controlled slip at the contact patch. The speed of the carriage was set to 7 cm/s for this study. The carriage assembly contains two air springs and a flow control valve that helps maintain a constant normal load at the wheel center. The normal load on the tire was controlled using the Active Normal Load Control system developed by Naranjo [49] at the Terramechanics, Multibody, and Vehicle Systems (TMVS)

Laboratory. The system is a closed loop control system consisting of a pneumatic flow control valve. While the forces and moments at the contact patch are collected via a KISTLER P650 force hub, the pneumatic flow control valve regulates the amount of air flowing through the air springs based on the Z axis force feedback received from the KISTLER sensor at the wheel hub. This allows for the system to self-regulate and to maintain a constant normal load on the wheel. Interchangeable rods of various lengths allow the tire to be set at various toe and camber angles prior to beginning each run, thus simulating steering maneuvers.

In order to match real-world scenarios, the tire is cooled down to the same temperature as the ice surface or colder. This is done by placing the tire in a Thermotron Chamber, which is a temperature chamber that can be controlled to a constant temperature well below freezing. The tire is placed in the chamber and the bulk temperature is periodically measured using an infrared thermometer until the tire reaches the desired temperature before each test trial.

The ice layer on the Terramechanics Rig is formed using a set of plastic tubes under the layer itself. In these tubes, ethylene glycol is pumped through the tubes and is set at a specific temperature in order to allow water to freeze around the tubes. A thermocouple is placed on top of the ice surface in order to regulate the temperature. If at some point, the ice surface temperature increases higher than the set value, the system will begin to pump ethylene glycol through the tubes in order to bring the temperature back to the preset value. There are two sets of tubes in the system. One corresponds to the supply of the ethylene glycol and the other handles the return of the fluid. They are connected on both ends using copper metallic headers.

The TekScan Pressure Pad [50] has also been employed during this investigation. The Pressure Pad is the 3150 Model which serves to measure pressure distribution for pneumatic tire applications. In this instance, modifications have been made to the pressure pad in order

to allow dynamic conditions, such as slip at the contact patch to be measured. The set-up, which is shown in Figure 3.8, allows the tire to climb up to the ramp and onto the testing platform. The testing platform mimics the smooth ice by having the same static coefficient of friction of the ice used for testing. In this case, the static coefficient of friction of the pressure pad system is approximately 0.15 as seen in Figure 3.10.

A protective layer was placed on top of the TekScan pressure pad which had thickness of a 314 μm. This protective film is made up of tempered glass in order to protect the pad from the shear forces which are experienced under slip conditions at the contact patch. The complete system allows for the instrument to be attached to the U-Channels in the Terramechanics Rig vane, to prevent the system to move during measurements as shown in Figure 3.9.

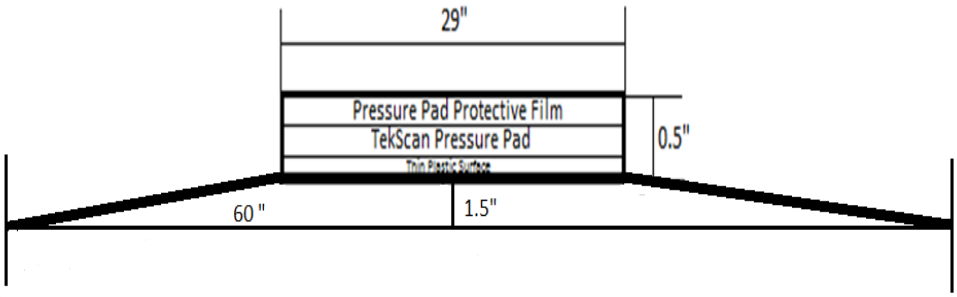

Figure 3.8: Test-Setup to allow dynamic conditions to be tested on the TekScan Pressure Pad which will allow the tire to climb onto a testing surface similar to that of smooth ice.

In order to clamp the protective film and pressure pad down to the rigid wooden platform, metal strips were used to keep the film and pad from moving during shearing applications. The metal strips were clamped to the wooden platform using a combination of washers, nuts and bolts as shown in Figure 3.11. Black protective tape was placed on top of the bolt heads to keep the pneumatic tire safe during operation as shown in Figure 3.9.

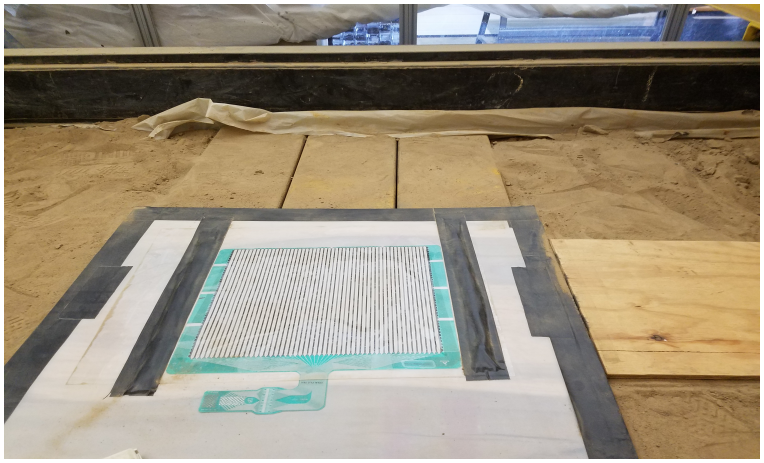

Figure 3.9: Final design for the test-setup to allow dynamic conditions to be tested on the TekScan Pressure Pad. System is composed of a wooden rigid platform covered with a plastic sheet on which the pressure pad and the protective film lays on.

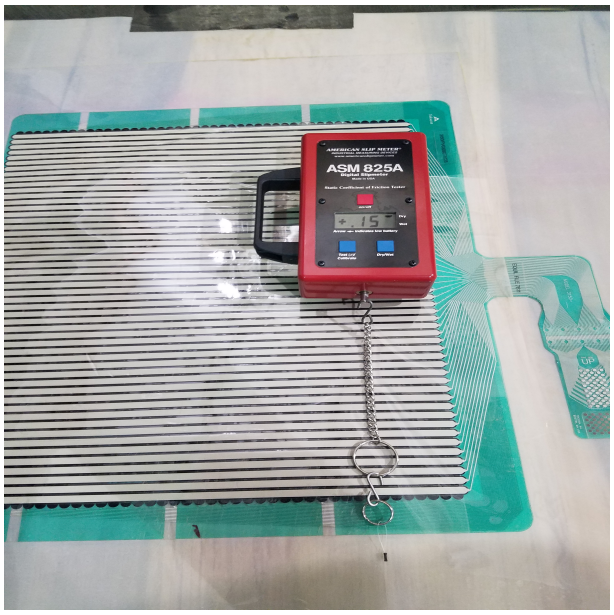

Figure 3.10: Static coefficient of friction of the pressure pad measuring system which mimics the smooth ice surface used for traction measurement.

3.1.4 Design of Experiment

In order to validate the Advanced Tire-Ice Interface Model that was originally developed at TMVS [19], a design of experiment was prepared to capture the tire performance

Figure 3.11: 3150 TekScan pressure pad with metal strips and bolts to attach the protective film to the wooden board to prevent the pressure pad from moving during testing.

under various controlled operating conditions. The two candidate tires for this investigation were the 225/60R16 97S Uniroyal (Michelin) Standard Reference Test Tire (*SRTT*, Tire A) and a 235/55R19 Plus XL Pirelli Scorpion All Season Tire (Tire B). The effects of camber and toe on solid ice were investigated using interchangeable toe and camber rods of various length on the Terramechanics Rig at the Terramechanics, Multibody, and Vehicle Systems (TMVS) Laboratory at Virginia Tech [44]. Three levels of camber angles were chosen to be investigated: nominal value 0°, as well as +2° and -2°. Three levels of toe angles were also chosen: nominal value 0°, +2°, and -2°. Three inflation pressures were investigated as 60%, 80% and 100% of the maximum inflation pressure. The normal load applied was 60%, 100%, and 120% Load Index (LI), using an Active Normal Load Control on the Terramechanics Rig developed by Naranjo [51].

The design of experiment matrix including all test conditions is presented in Table 3.1. The ice surface temperature was maintained at either -3°C or -10°C using a thermocouple to measure the ice surface temperature. The tests were conducted at eight different slip ratios, as indicated in Table 3.1. Three test runs were conducted for each test condition to ensure

repeatability; the data for the three runs were then averaged. The slip ratios were divided into two groups: low (0%, 5%, 10%, 15%) and high (20%, 25%, 30%, and 40%). Each test went incrementally through all the slip ratios in one group.

Table 3.1: Design of Experiment Matrix for the Indoor Experimental Investigation

Operational Parameters	Number of Levels	Level 1	Level 2	Level 3	Level 4
Tires	2	225/60R16 *SRTT*	235/55R19 Pirelli		
Ice Temperature	2	$-3\,^{\circ}$C	-10 °C		
Camber Angle	3	0°	2°	-2°	
Toe Angle	3	0°	2°	-2°	
Load on the Tire	3	60% Load Index	100% Load Index	120% Load Index	
Inflation Pressure	3	60% Inflation Pressure	100% Inflation Pressure	120% Inflation Pressure	
Slip Ratio	8	0% 20%	5% 25%	10% 30%	15% 40%

3.2 Experimental Methodology

This section will discuss several topics regarding the methods used during the experimental study. This includes the novel methods developed to measure the pressure distribution and the temperature distribution under all of the conditions investigated. Before the

temperature rise is measured, the ice surface must be prepared in order to allow consistent testing conditions. The preparation procedure is also presented in this section.

3.2.1 Ice Surface Preparation

The ice is formed on top of insulation boards which are placed in the Terramechanics Rig after the test bed is covered with a tarp. Custom tubing made out of LLDPE Material are laid out the entire length of the test bed. Using an external pump and a thermocouple to record the ice temperature, the system is preset to a constant temperature, and coolant is pumped through the tubes until the preset temperature is reached, at which the system is then turned off. Once the system is initiated and allowed sufficient time for the pump to warm up, water is sprayed at a low rate through a garden hose connected to a tap. Once water freezes, another layer of water is sprayed on top of the ice. This is repeated at regular intervals until the ice thickness reaches the desired length. To reduce the variation in tire performance and to maintain a consistent testing environment, a repeatable ice surfacing procedure must be followed before the beginning of each trial. The first step is to remove all the debris left behind on the ice surface using a metal scraper as shown in Figure 3.12.

The path of travel for the wheel was 16 ft. in length. Scraping was done in the lateral direction for the entire path of the wheel, which created a testing surface of 3 ft. x 16 ft. The second step consisted of using a squeegee, as shown in Figure 3.13, to completely remove all ice and tread particles off of the test track. This step also helps to remove water which may be present in the path.

After the ice surface was prepared, it was tested using an American Slip Meter to ensure the completed preparation was consistent as the others by measuring the static coefficient of friction of the surface. The ASM 825A American Slip Meter, shown in Figure 3.14,

Figure 3.12: Metal scraper used to smooth the ice and create a consistent ice surface to be used for testing and allow repeatable conditions.

Figure 3.13: Rubber squeegee used as the final part of the ice preparation. This steps removes all debris left behind from scraping.

was employed during this investigation to study the friction of the ice surface prior to each test run.

Table 3.2 shows one set of friction measurements prior to the start of a test run. Note the consistency of the static coefficient of friction between the presented test runs. The ASM 825A American Slip Meter, was equipped with standard pegs depending on whether the ice surface was dry or wet. A system of loops and strings are attached to the meter. Once the

Figure 3.14: ASM 825A American Slip Meter used to measure the static coefficient of friction of dry and wet surfaces.

system is ready to measure, it is placed on the surface and with the user applying a constant force by pulling the meter with the string, the static coefficient of friction is recorded at the point where the meter begins to slip relative to the ice surface. It is critical for the ice surface to be prepared in a very repeatable and controlled manner. Ice parameters affect the performance of the tire greatly, and it is important to keep these parameters consistent to allow data comparability. Once the ice surface has been prepared and the friction has been measured, the tire is instrumented with the temperature measuring system to collect temperature distribution data at the contact patch.

Table 3.2: Friction Measurements using the ASM 825A American Slip Meter

Trial Number	Number 1	Number 2	Number 3	Number 4	Number 5	Number 6
Coefficient of Friction	0.14	0.19	0.16	0.13	0.17	0.15
Average	0.157					

3.2.2 Pressure Distribution Measurement

In order to investigate the dynamic pressure distribution of the tire at the contact patch, several modifications were made to the existing TekScan system. Using the current TekScan system with a layer of Photodon 6 HS Tempered Glass allows shearing forces on the pressure pad film to occur. The Photodon 6HS Tempered glass is composed of several layers totaling up to a thickness of 315 μm, as shown in Figure 3.15.

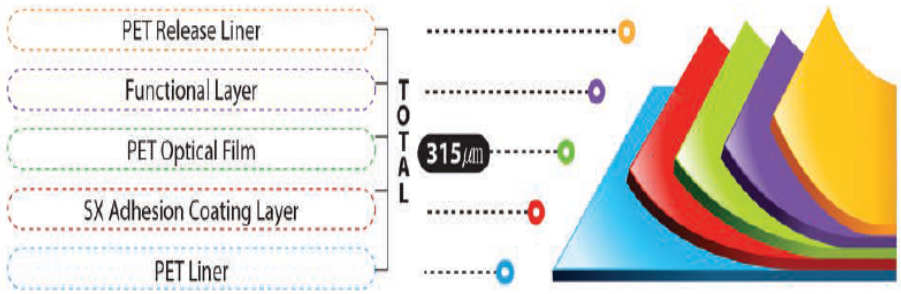

Figure 3.15: Layers composing the Tempered Glass used to protect the TekScan 3150 Pressure Pad from shearing forces during dynamics operating conditions

The protective layer to be placed on top of the TekScan pressure pad will allow the tire to climb onto a surface which will mimic smooth ice, supported by a rigid platform and then descend down a ramp back on to the original surface. In order to attach the pressure pad to a rigid surface, metal strips were used to clamp the pad and protective film to a wooden platform. This serve the purpose of further adhering the pad to the testing platform. The metal strips used are bolted through the protective film and a wooden platform as shown in Figure 3.16. The complete system will allow for the measurement device to be attached to the metal U-channels of the Terramechanics Rig. This will make sure that the pressure pad does not move during testing.

The Pressure Mapping Sensor 3150 was employed during this investigation. The pressure pad from TekScan has a testing length of 368.8 mm and a width of 435.9 mm. The

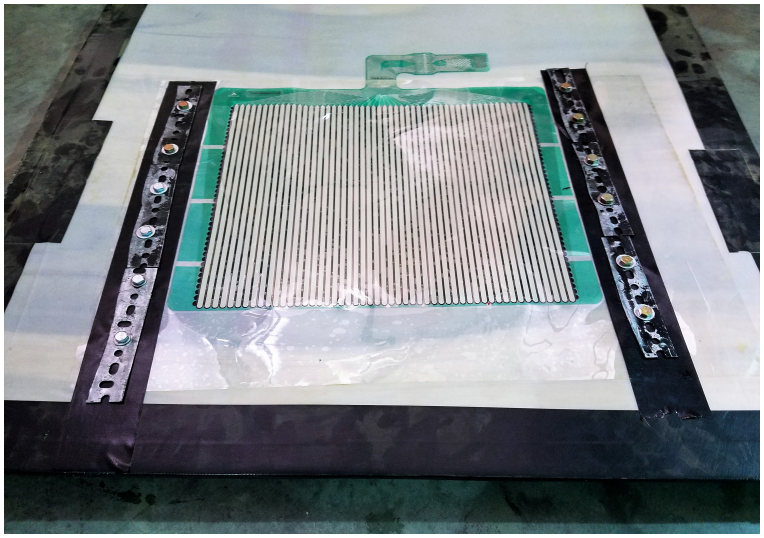

Figure 3.16: Metal strips have been used along with bolts to clamp the pressure pad to the wooden platform.

dimensions allows the pad to have 2,288 numbers of sensels which are capable of measuring data. This results in a spatial resolution of 1.4 sensels per sq-cm which is suitable for this study.

3.2.3 Thermocouples Measurement

In order to record the temperature distribution along the contact patch, thermocouples were instrumented into the tire tread surface. The thermocouples are calibrated by simply placing one of the metal junctions in a medium of a known temperature and the other metal junction on the object of interest. The voltage change can be measured and used in a calibration equation to precisely calculate the temperature of your object.

The thermocouples used were of K-Type with a resolution of 0.1°C where their individual dimensions are shown in Figure B.1.

The thermocouples were placed into the grooves of the tread blocks in the longitu-

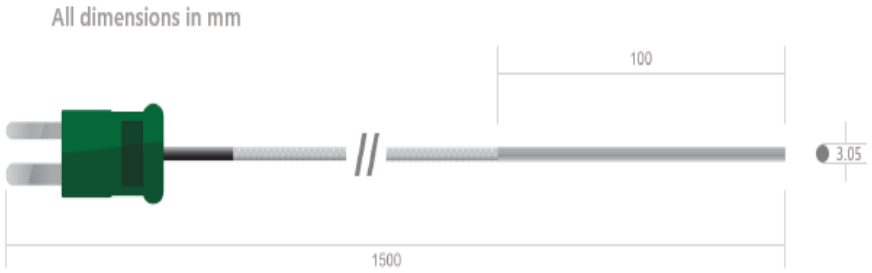

Figure 3.17: Dimensions of the K-type Thermocouples used for the investigation.

dinal direction of the contact patch. The wires were placed in between the tread blocks to make sure that they do not interfere with the normal operation of the tire. Placing these thermocouples at the contact patch proved to provide similar traction results as those measured without the instrumentation. Therefore it can be concluded that the installation of the thermocouples do not interfere with the normal operation of the tire. A base layer of white 100% silicone is placed into the groove prior to inserting the thermocouple. Once the thermocouple is fitted into the groove, clear 100% silicone is placed on top of the thermocouple to provide an additional layer of protection. The excess silicone is scraped off to prevent any additional asperities being formed at the contact patch. Once all of the thermocouples have been placed, the system is allowed 24 hours to dry and harden before testing.

In order to ensure that the thermocouples make direct contact with the ice surface, the tips of the thermocouples are exposed to the environment. The main challenge of the instrumentation of pneumatic tires is in the transmission of data between the measurement device and the logger during tire operation.

In order to account for the transmission of data, four wireless data loggers are attached to the sidewalls of the tire. The wires and data loggers are properly secured to the sidewalls using tape and 3M Heavy Duty Velcro as shown in Figure 3.19. In order to reduce any tire imbalances, the data loggers have been placed on both sides of the wheel at equidistant with

Figure 3.18: Instrumentation of the Standard Reference Test Tire ($SRTT$)

respect to each other.

Figure 3.19: Wireless Data Logger used to transmit data from the measurement device to the communication point.

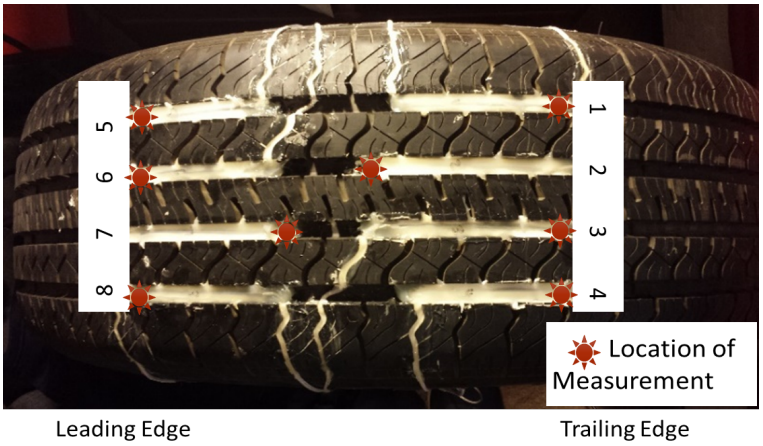

Figure 3.20: Location of temperature measurements taken from the thermocouples.

The temperature is measured at each point where the thermocouples are placed, as indicated. Figure 3.20 represents the exact locations of the measurements, and the locations where the tips of the thermocouples have been exposed. Note that thermocouples No. 2 and No. 7 have been inverted in order to capture the temperature at the middle of the contact patch.

3.3 Indoor Test Results

The following section will provide results which were measured during this experimental investigation along with a brief discussion highlighting the main contributions of the results collected.

3.3.1 Pressure Pad Measurements

The main input to the Advanced Tire-Ice Interface Model is the pressure distribution of the contact patch. Therefore, it is imperative to collect this data prior to taking any measurements. The original development of TIM was trained with data provided by Hankook Tires. Hankook Tires provided pressure distribution data for the Standard Reference Test Tire ($SRTT$). These measurements included the pressure distribution of the contact patch at various static and rolling conditions for various normal loads. The other portion of the data was composed of pressure distribution measurements of the $SRTT$ with an applied torque at the wheel center. In this case, it was evident the effects of applying a torque on the individual tread blocks.

The pressure distribution measured in-house were able to match the distribution of the pressure of those provided by Hankook. As the slip ratio increased from 0% to 30%,

the TekScan Pressure Pad was able to measure clear changes in the distribution as seen in Figure 3.21.

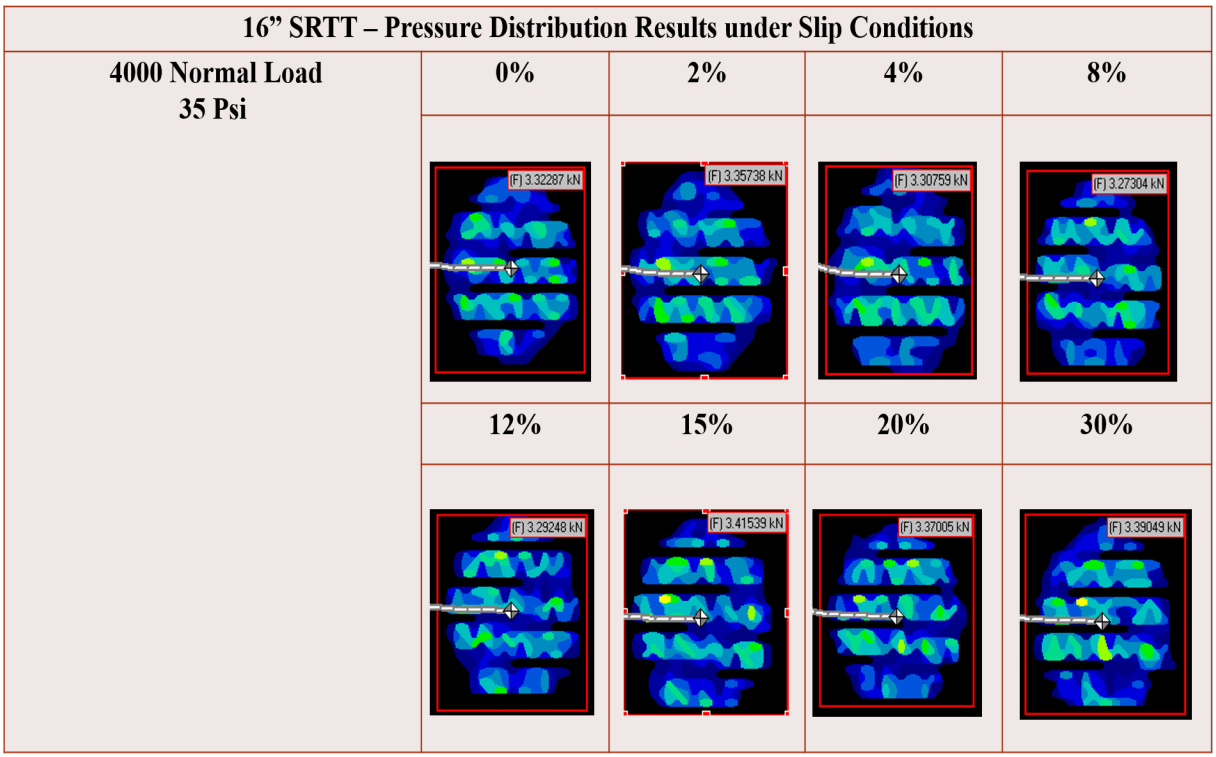

Figure 3.21: Raw data measured with the 3150 TekScan Pressure Pad at slip ratios up to 30%.

The raw measured pressure distribution had similar contact patch dimensions as those provided by Hankook Tire, but a lack of resolution for individual tread blocks provides difficulty in determining the effects of applying torque as opposed to an actual slip ratio.

As the slip ratio increased, it was also evident that the overall spread for higher pressure distribution increases, as is the case for the data provided by Hankook Tire. As shown in Figure 3.22, the higher the pressure distribution is, the more the distribution becomes uniform and moves towards the edges of the contact patch.

Regarding the temperature rise at the contact patch at various slip, the Advanced Tire-Ice Interface Model was capable of capturing the clear difference in temperature rise,

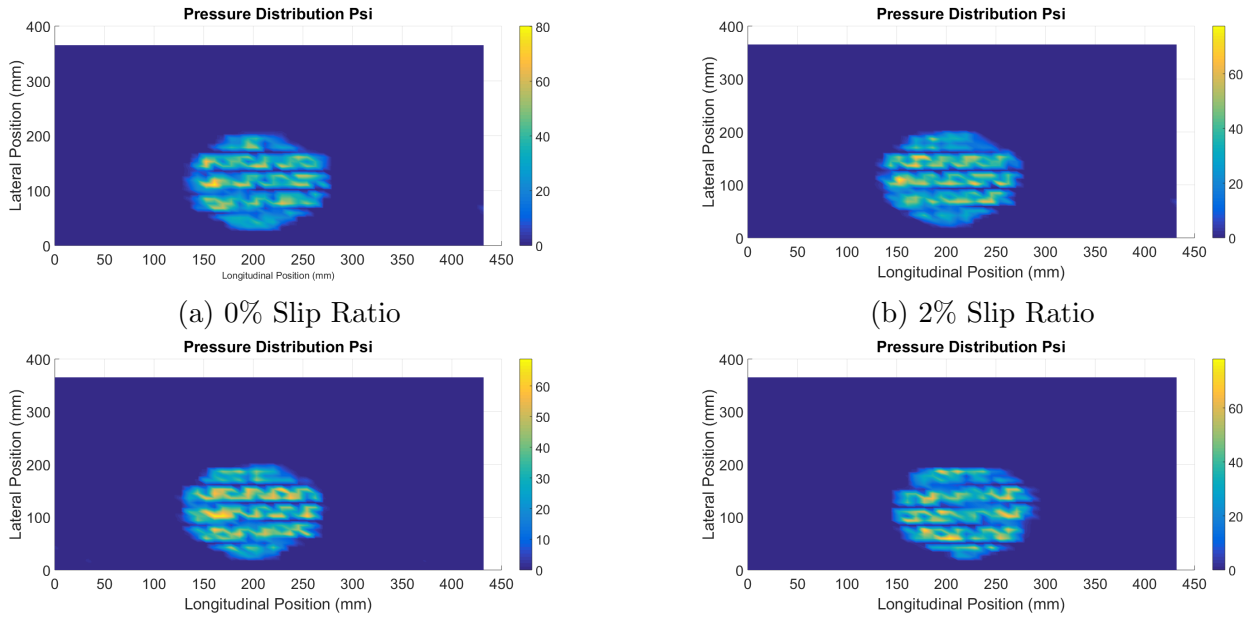

(a) 0% Slip Ratio

(b) 2% Slip Ratio

(c) 4% Slip Ratio

(d) 15% Slip Ratio

Figure 3.22: Pressure distribution data collected from the 3150 TekScan Pressure Pad. The results collected were used as an input to the Advanced Tire-Ice Interface Model to produce the results. The tire had an inflation pressure of 35 psi and a normal load of 4000N.

as shown in Figure 3.23. With the pressure distribution at various slip ratios measured, the Advanced Tire-Ice Interface Model can be used in conjunction with the data to predict the temperature rise at the contact patch. From the results, it is evident that the distribution of the temperature rise becomes more uniform with increasing slip. This tendency of the temperature rise to become more uniform can be attributed to the fact that as the slip ratio is increased at the contact patch, more of the contact interface is sliding as it loses traction. It is also true that the rise in temperature increases as the slip ratio increases. Comparing Figure 3.23a and Figure 3.23c shows this result. At the higher slip ratio, the edges of the contact patch are warmer as the slip ratio increases.

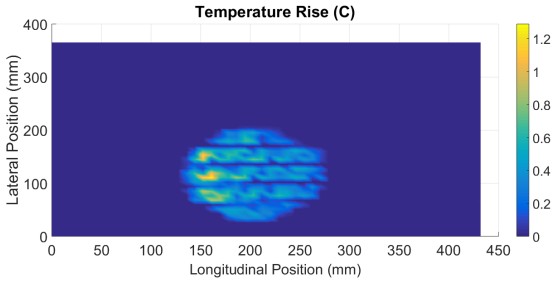

(a) 0% Slip Ratio

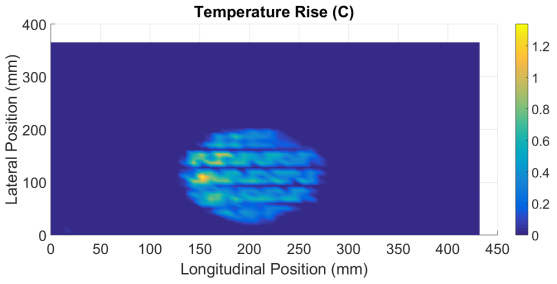

(b) 2% Slip Ratio

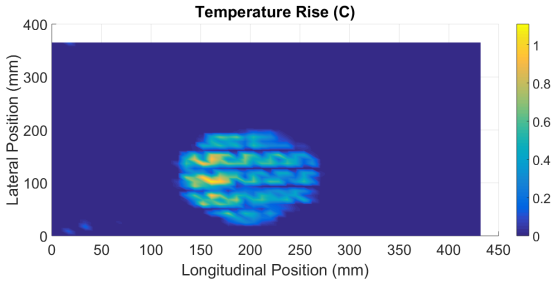

(c) 4% Slip Ratio

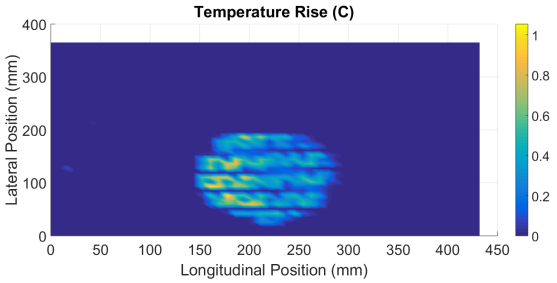

(d) 15% Slip Ratio

Figure 3.23: Temperature rise distribution collected from the 3150 TekScan Pressure Pad. The results collected were used as an input to the Advanced Tire-Ice Interface Model to produce the results shown. The tire had an inflation pressure of 35 psi and a normal load of 4000 N.

3.3.2 Temperature Rise Measurements

All of the conditions listed in Table 3.1 were investigated to determine the temperature rise at the contact patch using thermocouples. The channel number corresponds to those of Figure 3.20 for all of the scenarios presented. The results represent the temperature distribution of the tire during the time for which the contact patch is rolling on the ice surface.

First the effect of varying the inflation pressure on the temperature rise is studied. As shown for the 19" Pirelli All Season Tire in Figure 3.24 and Figure 3.25, as the inflation pressure is decreased, the temperature rise in the contact patch becomes more significant. Heat generation is proportional to the total surface area. Therefore as the inflation pressure decreases, the contact area increases which promotes heat generation. The case for 100% inflation pressure resulted in a higher fluctuation in the temperature.

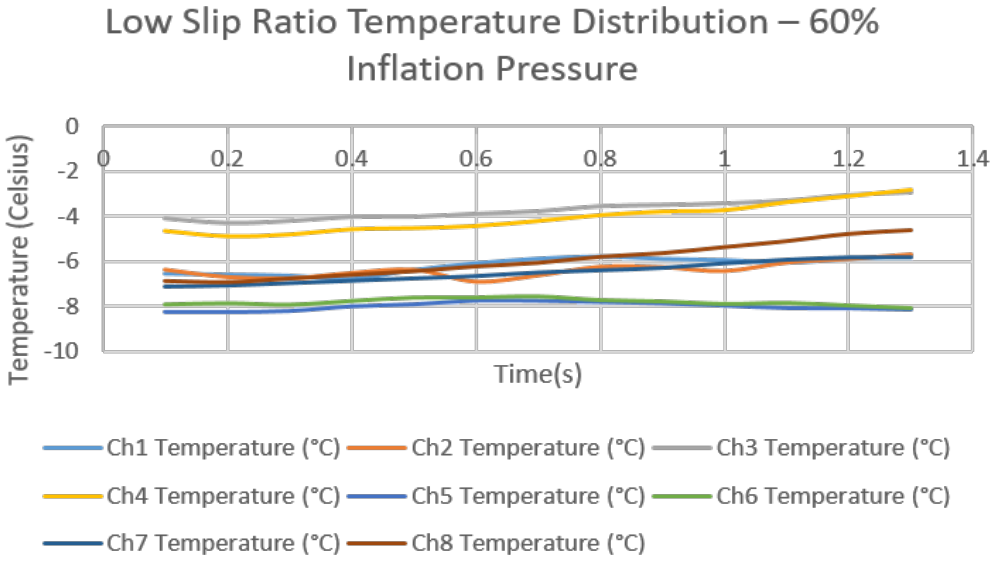

Figure 3.24: Temperature time history measurements which displays the effect of 60% inflation pressure for the 235/55R19 Pirelli Tire at low slip ratio. The testing conditions were set at 0° Toe Angle and 0° Camber Angle at 100% Load Index.

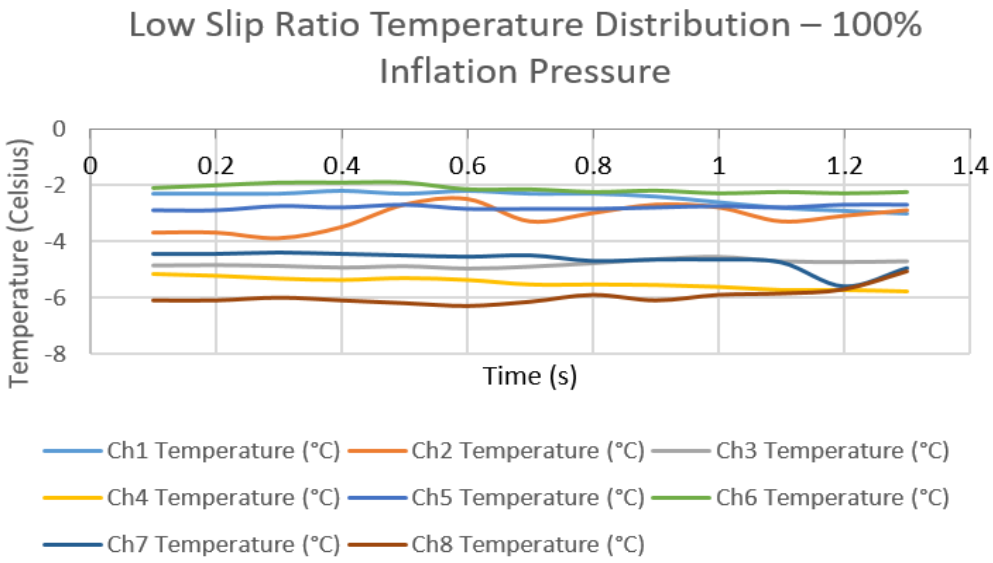

Figure 3.25: Temperature time history measurements which displays the effect of 100 % inflation pressure for the 235/55R19 Pirelli tire at low slip ratios. The testing conditions were set at 0° Toe Angle and 0° Camber Angle at 100% Load Index.

The effect of varying the normal load was also investigated as shown in Figure 3.26 and Figure 3.27. It is evident that there is higher variation in temperature with respect to the high slip ratio as the thermocouples try to reach an equilibrium. As the rate of friction generation increases, the tire tends to reach steady state slower than in the low slip ratio regions.

The temperature rise was more evident in experiments with a higher normal load on the tire especially in the case of high slip values. This is assumed to be the result of the increased area in the contact patch as well as the increased pressure distribution at higher normal loads.

When the toe angle of the tire was allowed to vary, it is observed that the temperature distribution being measured tries to become more consistent throughout the contact patch, as shown in Figure 3.29 compared to Figure 3.28.

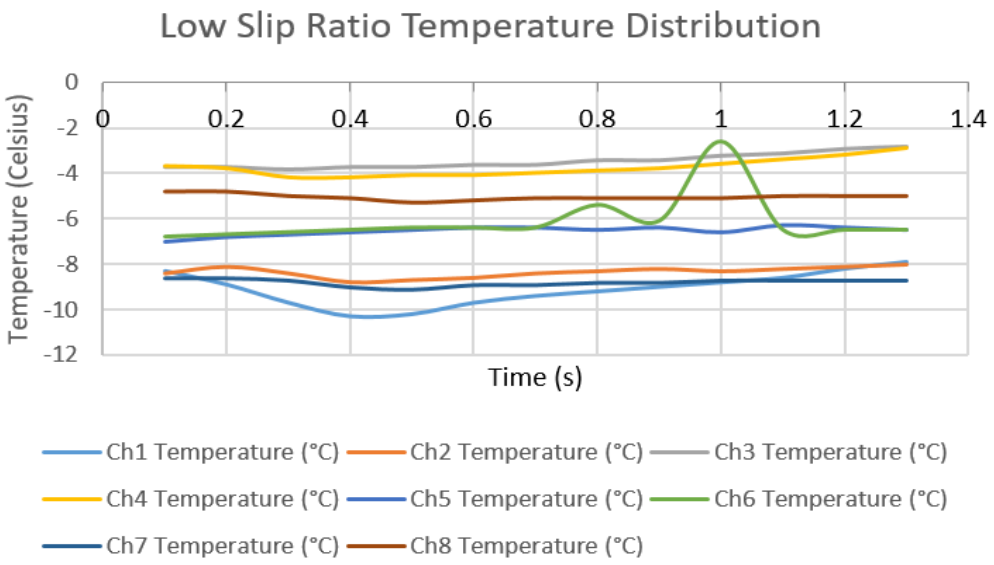

Figure 3.26: Temperature time history measurements which displays the effect of 100% normal load for the 235/55R19 Pirelli tire at low slip ratio. The testing conditions were set at 0° Toe Angle and 0° Camber Angle at 100% Load Index.

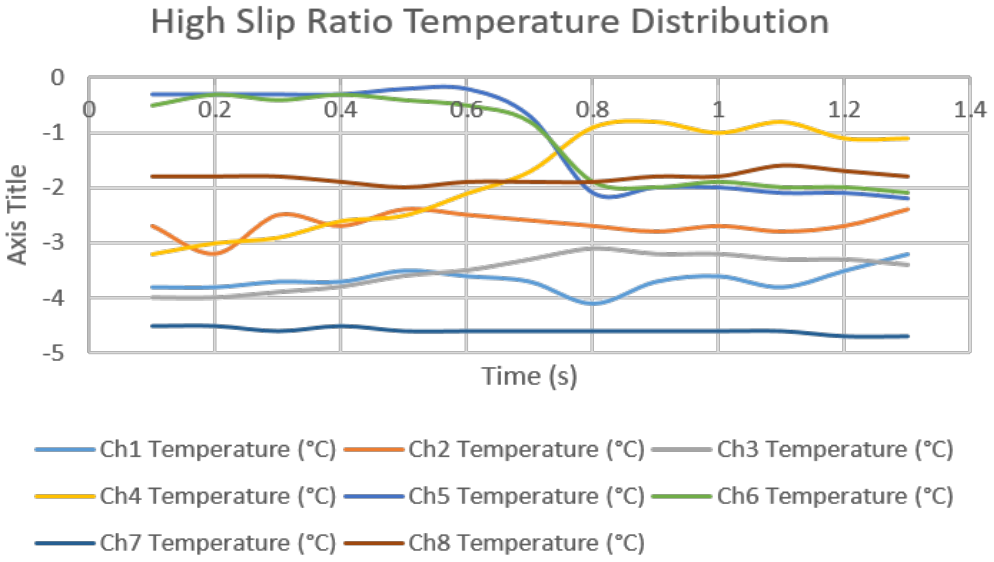

Figure 3.27: Temperature time history measurements which displays the effect of 100 % normal load for the 235/55R19 Pirelli tire at high slip ratios. The testing conditions were set at 0° Toe Angle and 0° Camber Angle at 100% Load Index.

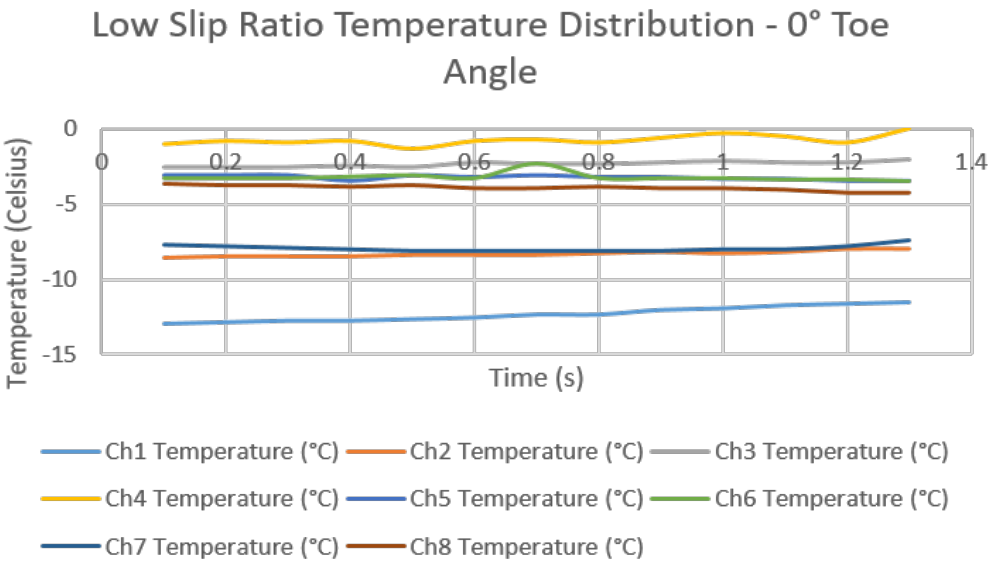

Figure 3.28: Temperature time history measurements which displays the effect of of varying the toe angle for the 235/55R19 Pirelli tire at low slip ratio. The testing conditions were set at 0° Toe Angle and 0° Camber Angle at 100% Load Index.

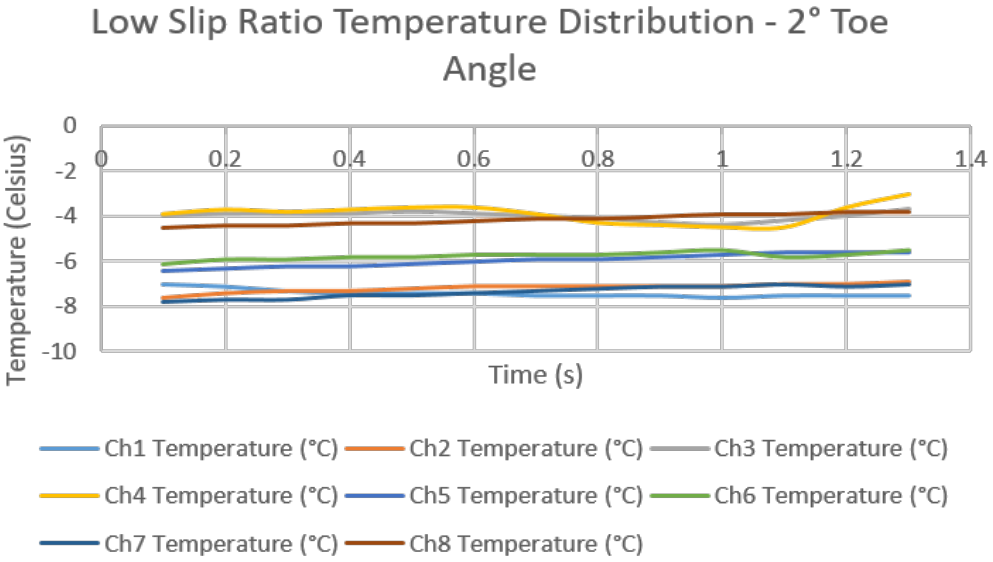

Figure 3.29: Temperature time history measurements which displays the effect of varying the toe angle for the 235/55R19 Pirelli tire at low slip ratios. The testing conditions were set at 2° Toe Angle and 0° Camber Angle at 100% Load Index.

This is hypothesized to be due to the change in shape of the contact patch. As the angle is increased, the temperature distribution seems to become more uniform due to the contact area decreasing. The difference in temperature between the middle of the contact patch and the sides was also found to be not as significant when the toe angle was allowed to vary.

Finally, the effect of applying a camber angle can be seen in Figure 3.30 and Figure 3.31 when the toe angle is kept at 0°.

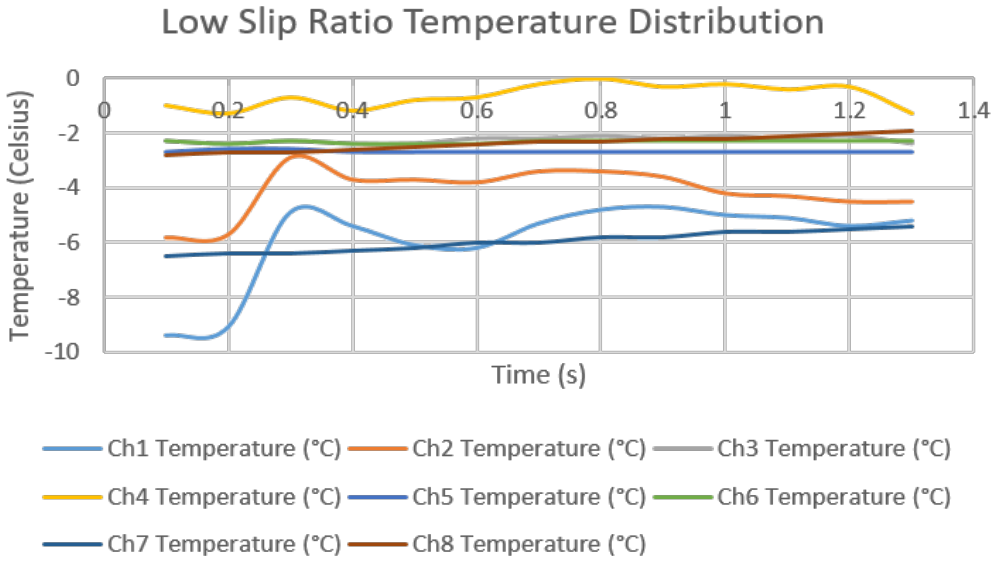

Figure 3.30: Temperature time history measurements which displays the effect of varying the camber angle for the 235/55R19 Pirelli tire at low slip ratio. The testing conditions were set at 0° Toe Angle and 0° Camber Angle at 100% Load Index.

With a 2° camber angle, it is evident that the overall bulk temperature of the tire increases where the pressure distribution increases due to the introduction of a camber angle. The side away from the wheel hub is higher in temperature with respect to the other side. When a positive camber angle is applied, the angle formed with respect to the neutral position points inwards, when viewed from the front.

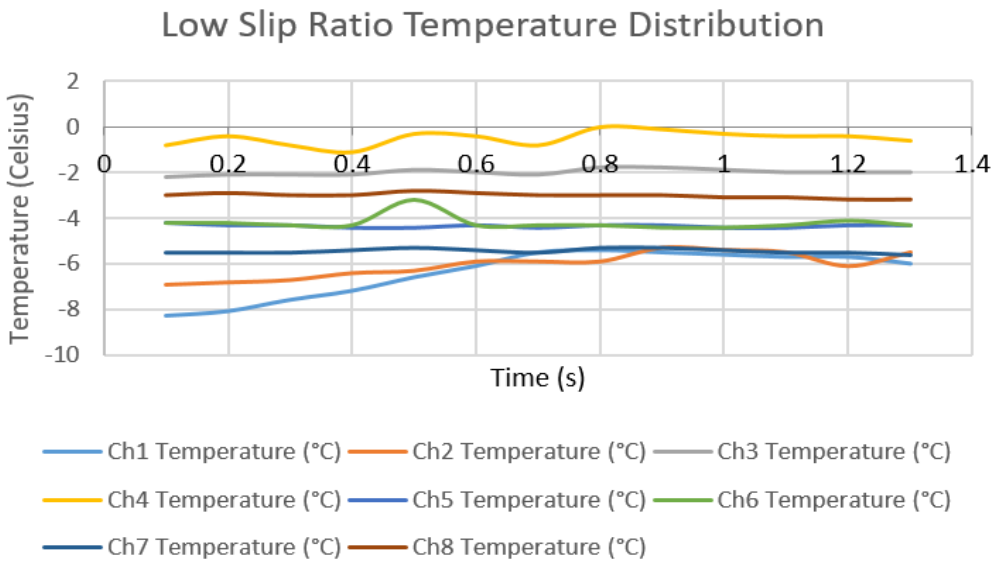

Figure 3.31: Temperature time history measurements which displays the effect of varying the camber angle for the 235/55R19 Pirelli tire at low slip ratios. The testing conditions were set at 2° Toe Angle and 2° Camber Angle when viewed from the front at 100% Load Index.

3.3.3 Slip Ratio Calculations

The longitudinal velocity of the carriage assemble of the Terramechanics Rig, as shown in Figure 3.32, is set to 7 cm/s. An additional electric step motor controls the angular velocity of the wheel separate from the carriage assembly. This setup allows the user to impose a direct slip ratio at the contact patch by managing the relative velocity between the carriage and the wheel. In order to control the slip, the effective rolling radius of the tire must be known, as shown in Equation (3.2). The rolling radius of the tire was measured using an in-house Wireless Internal Tire Sensor (WITS) [51]. The measurements were taken at different normal loads and inflation pressures and were used for the calculations of the slip ratio at the contact patch.

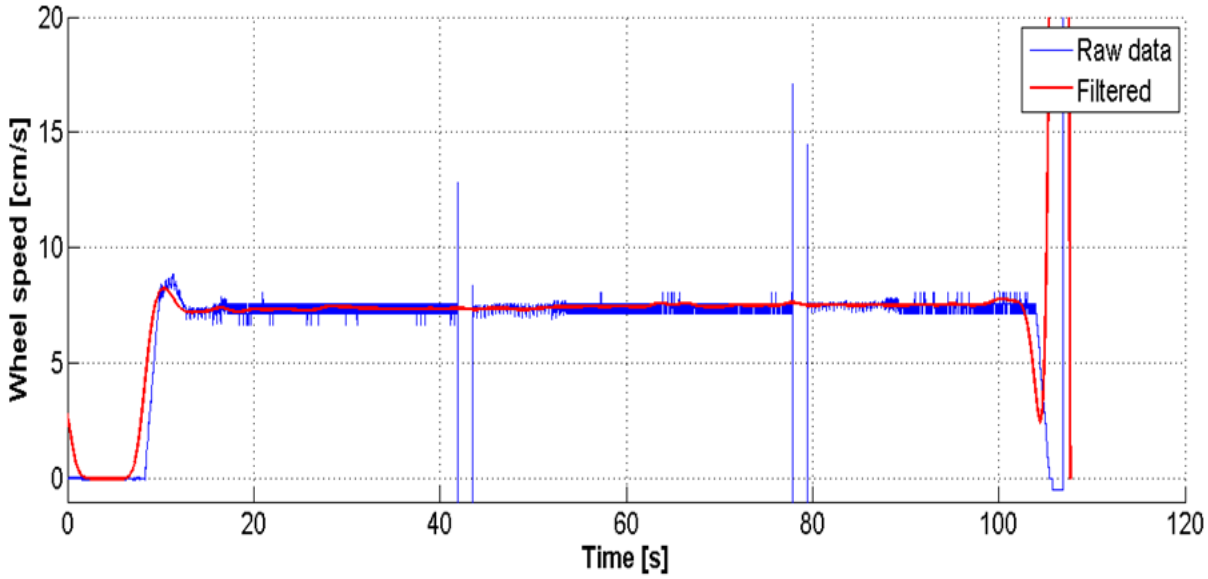

Figure 3.32: Calculated longitudinal velocity of the carriage assembly.

$$Calculated\ Slip\ Ratio = 1 - \frac{V_{Carriage}}{R_{effective} \cdot \omega} \tag{3.2}$$

3.3.4 Effect of Aging on the Tractive Performance of the Tire on Ice

Moving on to the tractive performance of the pneumatic tires on ice, we begin with the study of the aging effects. The *SRTT* shown in Figure 3.4 was the same tire tested for the original development of the Advanced Tire-Ice Interface Model. Exactly one year later, the *SRTT* was tested under the same conditions as before in order to determine the effects of which time has on the tractive performance of the tire on ice. As the tire ages, the rubber loses its flexibility and the tire hardens. The flexibility of the tire is one of the main contributions in the production of the tractive forces at the contact patch.

As seen in Figure 3.33, the averaged data between a test conducted in 2014 and

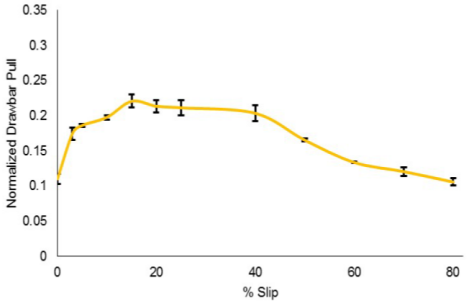

(a) Measured results taken in 2014. Adapted from [19] under fair use; Fair use determination attached.

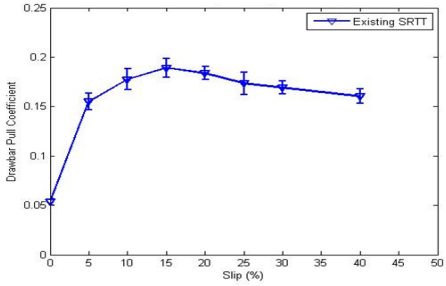

(b) Measured results taken in 2015

Figure 3.33: Variations of normalized drawbar pull from three test runs for the *SRTT*. Ice surface temperature at 10°C, Inflation pressure of 242 kPa and 100% load of 7000 N.

another experiment conducted in 2015 with the same testing conditions is presented. The inflation pressure was at 35 psi and normal load on the tire is 7000 N. From the two plots, it is evident that the two test results share the similar trend for the drawbar pull of the tire. The main difference to note is that there is approximately a 3% decrease in traction performance with the aged tire used in 2015. The peak drawbar pull also occurs earlier at about 10% to 15% where the data collected in 2014 had a peak at about 20% slip. This is important as it directly affects the handling of the vehicle. The tire is not able to generate as much friction as the tire ages since the contact patch begins to slide at a lower slip ratio.

3.3.5 Effect of Inflation Pressure

Over-inflated tires are not in as much contact with the road and may cause a bumpy ride. Under-inflated tires cause unnecessary wear on the tire treads, loss of steering control, increased friction and lower gas mileage. Inflation pressure controls the shape of the tire casing. Proper inflation pressure is critical to maintaining proper shape of the tire and proper stress distribution in the tire. This in turn reduces flexing and heat build-up and

ultimately prolongs the life of the tire.

The effect of the inflation pressure on the tire was taken into consideration during this study at various slip ratios. Figure 3.34a and Figure 3.34b represent the measured drawbar pull on the $SRTT$ for tire inflation pressures of 21 psi, 28 psi, and 35 psi, at 80% normal load, and respectively at 100% normal load.

The maximum drawbar pull coefficient for the scenarios investigated occurred between 0.21 and 0.16 and the saturated value occurred between 0.17 and 0.14. The experimental data shows that the drawbar pull has a higher peak at lower inflation pressures. Furthermore, as the inflation pressure increased, the maximum drawbar pull occurred at a lower slip ratio value. As the inflation pressure increases, the rolling resistance of the tire decreases. A tire with a lower inflation pressure will have a larger contact area and thus will produce more traction during operation on ice. Future active tire inflation system could provide a function for controlling the inflation pressure depending on how much resistance is required for the given driving conditions.

Tire pressure varies significantly with temperature because air takes up more volume at higher temperatures and less volume at lower temperatures. Tire pressure will change by one psi for approximately every 10°F of temperature change. Lower temperatures lead to lower tire pressure and higher temperatures to higher tire pressure. Therefore, it is critical to understand the effect on which the inflation pressure has on the traction performance of tire in winter conditions.

The rule of thumb is for every 10°F change in air temperature, tire pressures will change about 2% (up with higher temperatures and down with lower) [24]. This means that light-duty, standard-pressure tires (typically inflated to 30-50 psi) used in applications on cars, vans and light trucks will change by about 1 psi; where heavy-duty, high-pressure

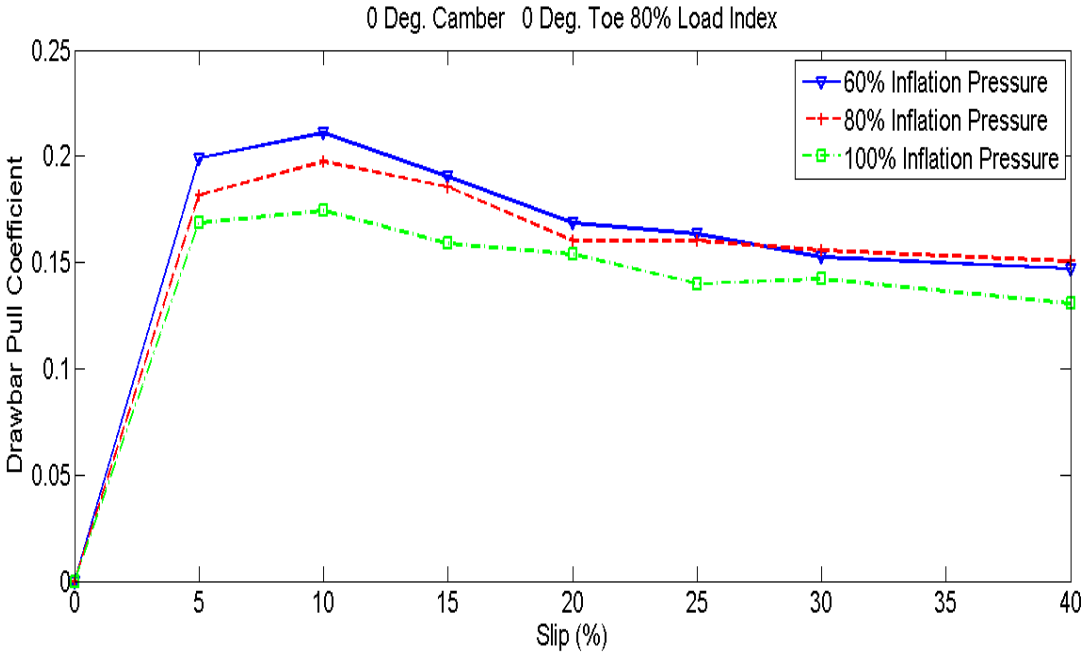

(a) 80% Normal Load (5600 N)

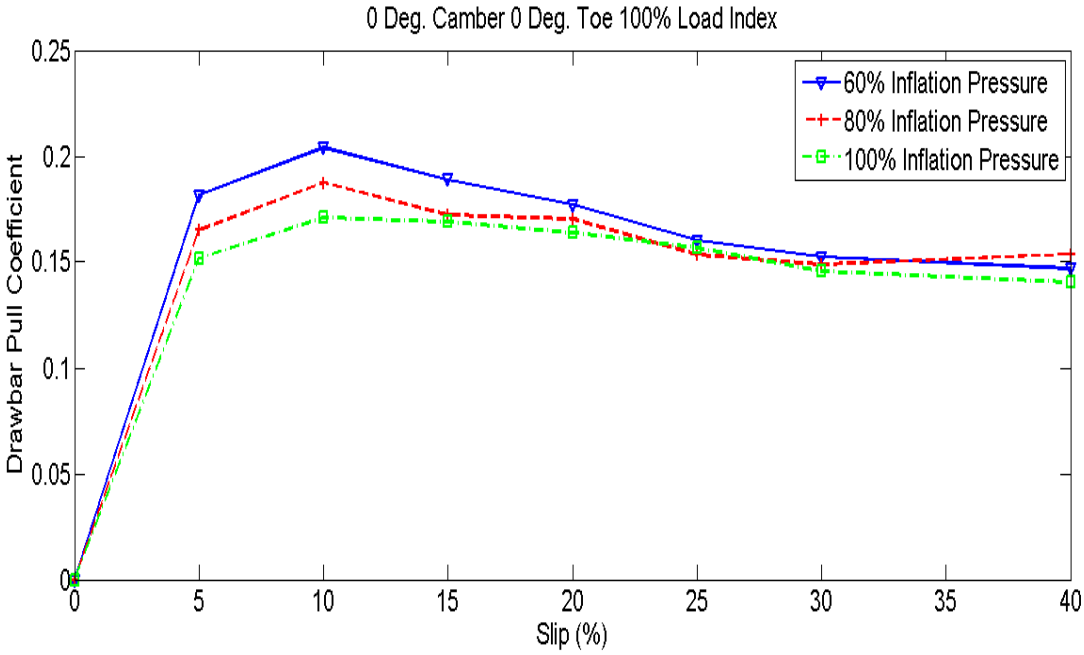

(b) 100% Normal Load (7000 N)

Figure 3.34: Drawbar pull coefficient of $SRTT$ at various inflation pressures with 0° Camber Angle and 0° Toe Angle.

tires (typically inflated to 80-100 psi) used in applications on recreational vehicles, buses and trucks will change by about 2 psi.

In most parts of North America, the difference between average summer and winter temperatures is about 50°F, which results in a potential loss of about 5 psi as winter's temperatures set in. And a 5 psi loss is enough to sacrifice handling, traction, and durability of pneumatic tires. Additionally, the difference between cold nighttime temperatures and hot daytime temperatures in most parts of the country is about 20°F [9]. This means that after setting tire pressures first thing in the morning, the vehicle's tire pressures will be almost 2 psi higher when measured in the afternoon. While that is expected, the problem is when the vehicle's tire pressures is set in the heat of the day, their cold pressures will probably be 2 psi low the following morning.

Since air is a gas, it expands when heated and contracts when cooled. In most parts of North America, this makes fall and early winter months the most critical times to check inflation pressures. During these seasonal changes, days are getting shorter, which results in the ambient temperatures getting colder and ultimately leads to the tires' inflation pressure going down.

3.3.6 Effect of Normal Load

The effects of varying the normal load was also studied. The normal load was kept constant throughout the run and was measured using the KISTLER P650 force hub. Per Table 3.1, three different normal loads were used to simulate a quarter car at various operating conditions. Figure 3.35 presents the effect of the normal load on the $SRTT$.

The steering configuration for this test was 0° for the toe and for the camber angle. From Figure 3.35 it is evident that the drawbar pull coefficient decreases with a reduction

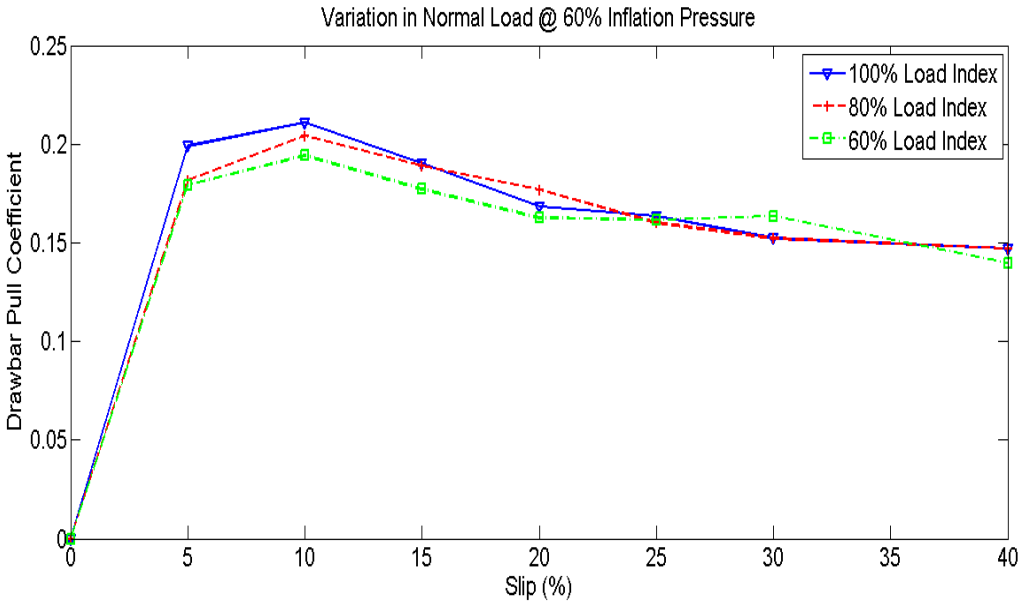

Figure 3.35: Drawbar pull coefficient of *SRTT* at various normal loads with 0° Camber Angle and 0° Toe Angle when the inflation pressure is at 60% of the maximum.

in normal load. It is hypothesized that this is due to the change in the contact area at various normal loads. When the normal load is increased, the tire is able to deform more. The increased amount of deformation leads to a larger contact area which in turns results in more area to generate friction from. It is also important to note the location of the maximum drawbar pull as this has a direct effect on the handling of the vehicle. The peak normalized drawbar pull occurred between a slip ratio of 5% and 10%. This is important since, by comparison, the maximum drawbar force occurred at 20% slip ratio during experiments on sandy loam [52].

3.3.7 Effect of Camber Angle

The effect of varying the camber angle was studied for 0°, 2°, and -2°. When a camber angle is imposed on the tire, the contact patch changes in area, providing a smaller footprint in which friction can be generated. Figure 3.36 represents the drawbar performance of the

SRTT. Other studies showed that on other types of terrain, the application of a camber angle led to a change in the traction performance of the tire. For example, on sandy loam it was found that as the camber angle was increased, the drawbar pull slightly decreased [52]. When the *SRTT* was tested on ice, a change in the camber angle while the toe angle was kept constant at 0° resulted in no significant difference in the traction performance, as shown in Figure 3.36.

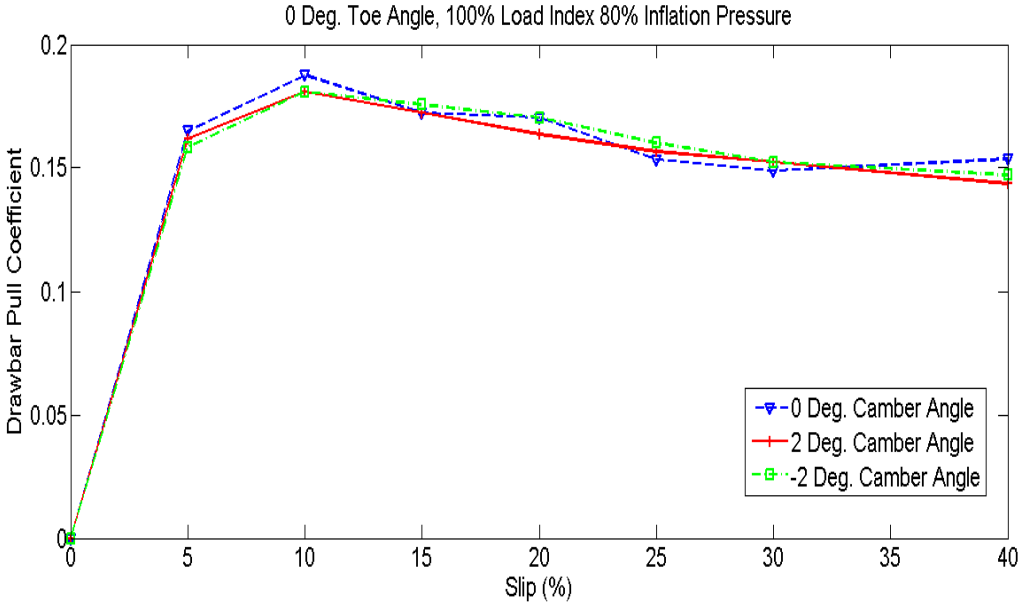

Figure 3.36: Drawbar pull coefficient of *SRTT* at various Camber Angles and 0° Toe Angle.

3.3.8 Effect of Toe Angle

The effect of the toe angle on the performance of the tire was investigated for 0°, +2°, and -2°. The toe angle was set at the beginning of each test and was held constant throughout the trial using interchangeable metallic rods. Figure 3.37 represents the drawbar pull coefficient for the *SRTT* obtained from testing for various toe angles. From the figure, it is evident that as the slip angle is increased, the maximum drawbar pull decreases when the camber angle is set at 0°.

Due to the assembly of the carriage, the Terramechanics Rig simulates the left front tire. A negative toe angle value represents a "toe-in" geometry that produces a drawbar force performance lower than the one produced by the positive toe angle configuration, or "toe-out" geometry.

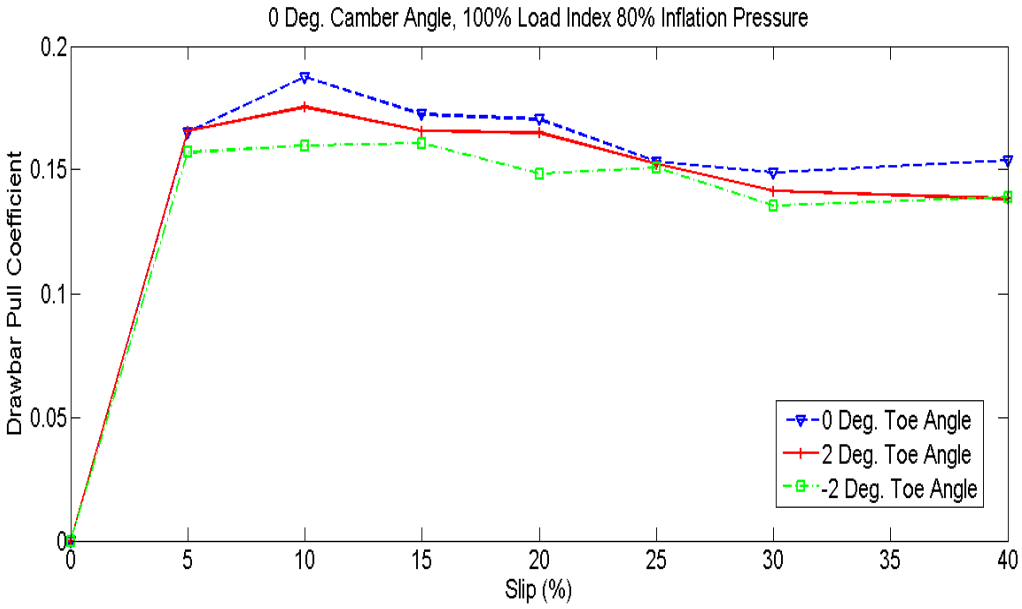

Figure 3.37: Drawbar pull coefficient of $SRTT$ tire at various slip angles and 0° Camber Angle.

3.3.9 Effect of Thin Water Film in Contact Patch

The influence of a thin water layer on top of the ice was also investigated experimentally. Tap water was sprayed from a hose directly on the ice surface prior to each test run in order the simulate wet conditions. A new design of experiment was created to investigate the influence of the water film on the ice layer as shown in Table 3.3.

When the contact patch remains dry, several outcomes may happen, depending on the ice surface temperature. For example, if the temperature of the ice is low enough, the tire tread adheres to the ice surface and, as the tire rotates, microscopic parts of the tread blocks

Table 3.3: Design of Experiment Matrix for Wet Film Experimental Investigation

Operational Parameters	Number of Levels	Level 1	Level 2	Level 3	Level 4
Tires	2	225/60R16 *SRTT*	235/55R19 Pirelli		
Ice Temperature	1	$-3\,^{\circ}$C			
Camber Angle	1	0°			
Toe Angle	1	0°			
Load on the Tire	1	100% Load Index (7000 N for *SRTT*) (8000 N for Pirelli)			
Inflation Pressure	1	80% Pressure (28 psi for *SRTT*) (40 psi for Pirelli)			
Slip Ratio	8	0% 20%	5% 25%	10% 30%	15% 40%

are left behind in the track. At low ice temperatures, this was observed as the tire skipped along its path during travel. The phenomenon occurred when the tread block deflected towards the trailing edge and snapped back to equilibrium causing increased wear and a peel-stick condition [31].

With the addition of the thin water layer, the friction was greatly reduced. With the water present, the tire tread displaces the water to the grooves and away from the tire through the sipes. The water is then quickly refrozen as it leaves the contact patch.

The traction which the tires were able to produce was greatly impacted by the addition of a water layer. As shown in Figure 3.38a, the 16" $SRTT$ had a significant decrease in the peak drawbar pull value by 11%. When the wet film was applied, the design of the tread pattern did not allow for the tread blocks to cut into the ice surface as well as the dry case.

When the 19" Pirelli tire was tested, the tire was able to approximately maintain the traction as a result of its tread pattern design. The 19" Pirelli tire is considered an All-Season Tire and the difference between the dry ice performance and wet film was not as significant. The introduction of sipes as shown in Figure 3.5 allowed for the water to be removed from the contact patch and to "dig-in" the ice surface to promote traction. When comparing the drawbar pull coefficient of the Pirelli Tire in Figure 3.38b, there is only a slight decrease in the absolute value. This decrease was only about 0.01-0.02.

3.3.10 Investigation of Small Slip Ratio Interval

Small slip ratio intervals were also investigated to more closely study the linear region of the drawbar pull curve. Figure 3.39 represents the individual longitudinal slip ratios which were measured. Recall that the slip ratio is held constant for a period of 20s as shown in the figure. Figure 3.40 represents the force using the indicated slip regions. The measurement indicates a quasi-static representation of the longitudinal force for the 235/55R19 Plus XL Pirelli Scorpion All Season Tire as shown in Figure 3.5. The data is averaged using a best fit line method which uses areas of high concentration to create the average line shown in Figure 3.40.

In Figure 3.40, it is shown that the maximum drawbar pull occurs at a slip ratio less than 4% for the 19" Pirelli Tire. Using a small step interval when measuring the longitudinal force allows for the exact location of where the maximum drawbar pull occurs with respect to

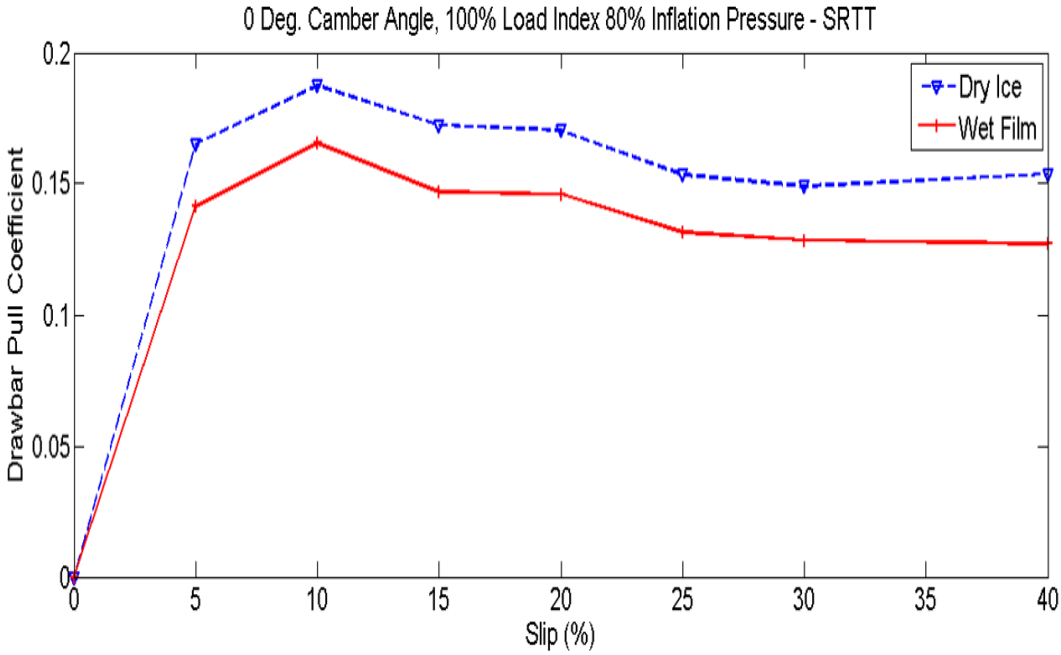

(a) Standard Reference Test Tire ($SRTT$)

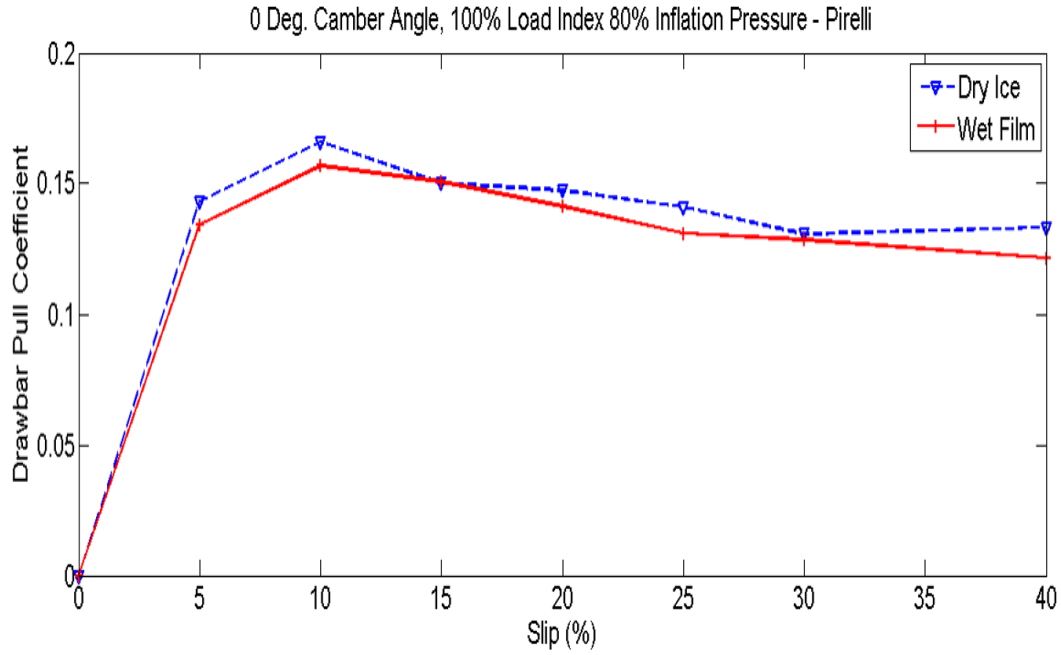

(b) Pirelli All-Season Tire

Figure 3.38: Drawbar pull coefficient of $SRTT$ and Pirelli All Season Tire at 80% inflation pressure, 100% Normal Load, with 0° Camber Angle and 0° Toe Angle.

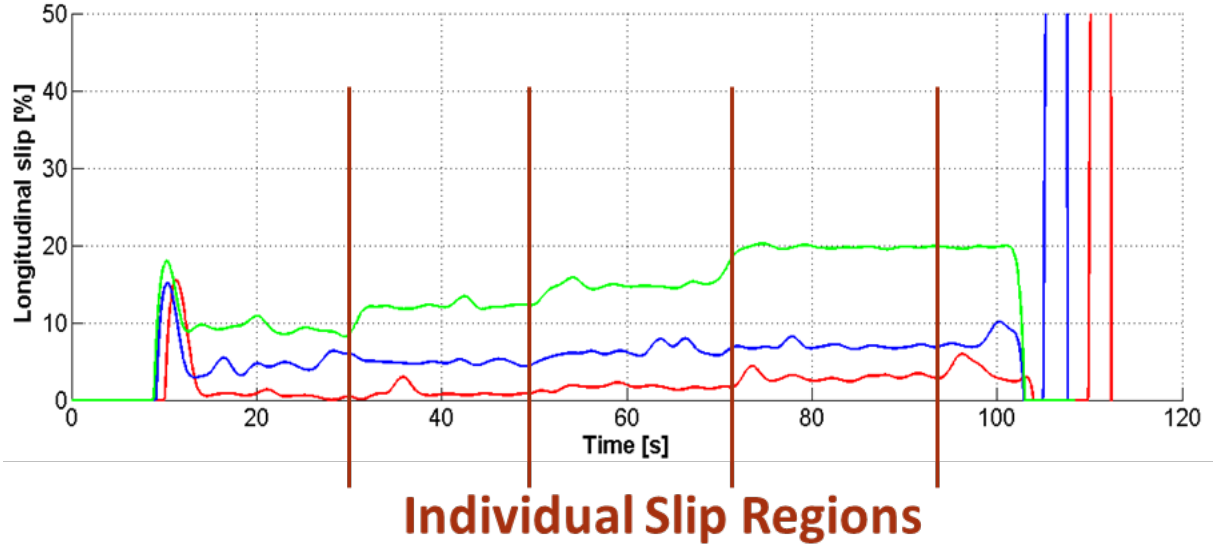

Figure 3.39: Measured longitudinal slip value used for the investigation of Tire B for the low slip ratio range.

the slip ratio. Figure 3.40 represents the raw data which was measured with a best fit line to highlight regions of high data concentration. It can be seen in the figure that the maximum longitudinal force measured was approximately 1,500 kN and then reached a residual value of approximately 1,300 kN after the tire began to slip and additional friction was not being generated.

3.4 Effect of Tread Patterns on the Performance of Tires on Ice

The following investigation consisted of a 225/60R16 97S Uniroyal (Michelin) Standard Reference Test Tire (SRTT, Tire A), a 235/55R19 asymmetrical tire (Tire B), a new SRTT (Tire C), a 215/60R16 asymmetrical winter tire (Tire D), and a 215/60R16 directional All-Season tire (Tire E). The tread designs are shown in Figure 3.41. The Load Index is a

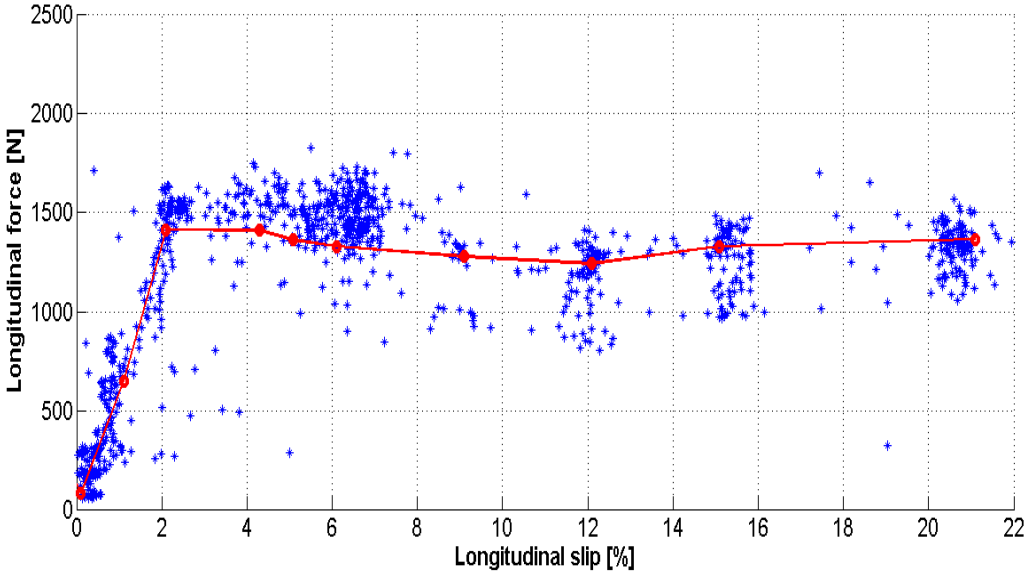

Figure 3.40: Quasi-static representation of the longitudinal force measurements of Tire B under nominal values (100% load, 80% inflation pressure, -10°C ice surface temperature, 0° Camber Angle and 0° Toe Angle).

number assigned to a tire to identify the tires ability to carry a load. The higher the load index is, the greater the load carrying capacity. Tire B was rated at 105 with a speed rating of V, Tire D was rated at 99 and H, and Tire E was rated at 94 and T respectively.

Figure 3.42 compares three distinct tread patterns. These tread patterns are composed of the most common types of tread pattern designs. The directional tire is labeled DT (Tire E) and the asymmetrical tire (Tire D) is labeled WT. On a dry ice surface with a temperature of $-10°C$, the SRTT and the winter tire (Tire D) shared the highest drawbar pull. This occurred at an inflation pressure of 100% of the rated maximum. The design of the asymmetrical winter tire led to an increase in traction compared to the directional tire. On dry ice, it was evident that the biting effect was present as the measured drawbar pull was higher than others in Figure 3.42. Even in the high slip ratio range, the design of the tire led to a higher tractive performance, while the results for the other tires diminished in this region. The winter tire was made of several sipes aligned in succession at the shoulder

Figure 3.41: Drawbar pull measurement of three tires at an ice surface temperature of -10°C.

of the tire. By introducing sipes into the tread design, more individual tread blocks are created which allows for a higher ratio of edges for the tire to use to produce traction [53]. Increasing the number of sipes will lead to a tire tread block which will deform less and act as a solid block of rubber. Decreasing the number of sipes and tread blocks will lead to a tire to act less stiff and the tread blocks will deform more as the tire progresses. Tire B is also composed of an asymmetrical tread pattern. When this tire was loaded with a camber angle, the angle will load selectively the wider or narrower ribs of the tire, depending on the orientation of the angle. Imposing a camber angle on the tire results in more or less contact on those ribs which will ultimately yield more or less traction. By increasing the area in contact, the tire is able to generate more tractive forces. In other tread pattern designs such as Tire A (Symmetrical), a change in camber angle resulted in no significant change in the tractive performance.

The hardness of the tires was measured at room temperature using a Shore A Durometer and presented in Table 3.4. The locations of the measurements are at the center of a

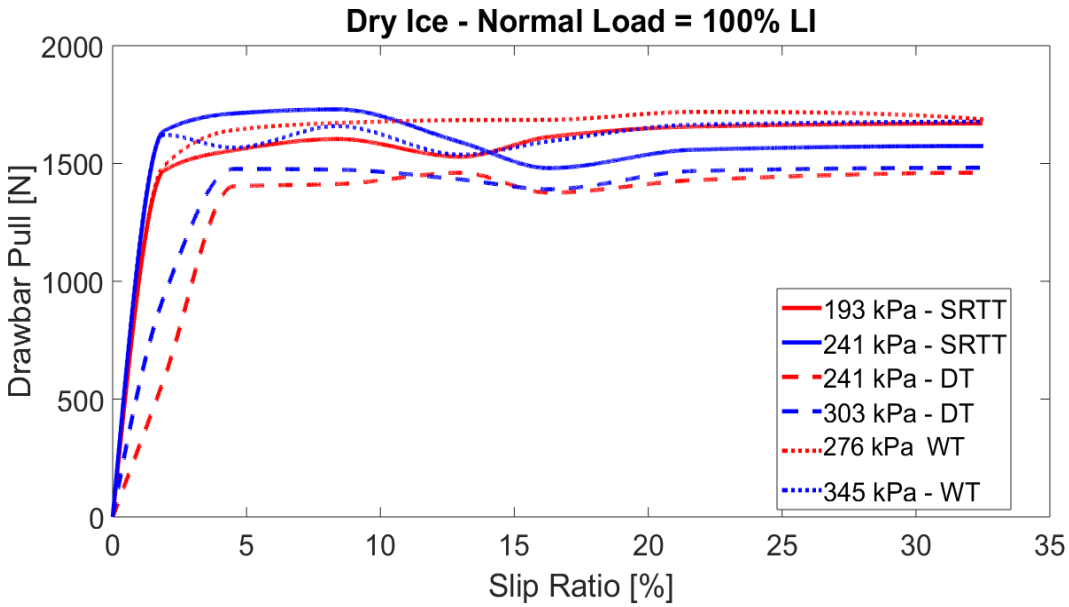

Figure 3.42: Drawbar pull measurement of three tires at an ice surface temperature of −10°C and 0° Camber and Toe Angle.

tread block, the shoulder of the tire, and at the sidewall. The sidewall was measured to capture a measurement that resembles the bulk property of the tire when averaged with the other measurement locations. The rubber of the winter tire is softer compared to that of all the tires tested, as shown in Table 3.4. Using a Shore A Durometer shows that the hardness of the directional tire (Tire E) was higher to that of the winter tire, as shown in Table 3.4. This shows that the hardness of the rubber is also significant in regards to the traction performance. The design of the tread pattern and the hardness of the rubber will be the dominating factor which dictates the traction performance of pneumatic tires on ice.

When the ice surface temperature is reduced to −3 °C and a water film is observed, the drawbar pull is reduced, as shown in Figure 3.43. In this scenario, the directional tire recorded the highest drawbar pull. The all-season directional tire (DT) had deep grooves running in an unidirectional pattern, as well as along the middle of the contact patch, as shown in Figure 3.41. This design of the tread pattern was effective in removing the water

Table 3.4: Shore A Hardness Measurement

Test Conditions	Tread Block	Side Wall	Shoulder	Average	Tire Temperature
Tire A	60.5	61	72.5	64.7	
Tire B	66	65.6	67.5	66.3	
Tire D	58.5	56.5	54.5	56.5	19.9 °C
Tire E	65.5	66.5	72.5	68.2	
Tire A	66.5	57.5	78	67.3	
Tire B	65	67	66.5	66.2	
Tire D	53.5	48	54.5	52	−3 °C
Tire E	65	66.5	74	68.5	
Tire A	69	62	77	69.3	
Tire B	69	67	68.5	68.2	
Tire D	55.5	50	51.5	52.3	−10 °C
Tire E	70	64	71	68.3	

from the contact patch and providing higher traction performance on ice, which explains why the drawbar pull increases again before falling to the saturated value in Figure 3.43. The winter tire measured the lowest drawbar pull. This shows that once a thin water film serves as the contact interface, an emphasis of water removal must be made during the design of the tread pattern. Therefore, comparing Figure 3.42 and Figure 3.43 shows that a design compromise must be made for a tire traversing on smooth ice. The design must be effective in removing the water away from the contact interface, as well as providing a biting effect on dry ice by using sipes.

3.5 Discussion on the Experimental Results

With the reduction of traction available at the surface in icy conditions, the dynamics of the vehicle becomes more unpredictable as the system can become unstable. In order to design an appropriate safety system, the tire-ice interaction must be closely investigated.

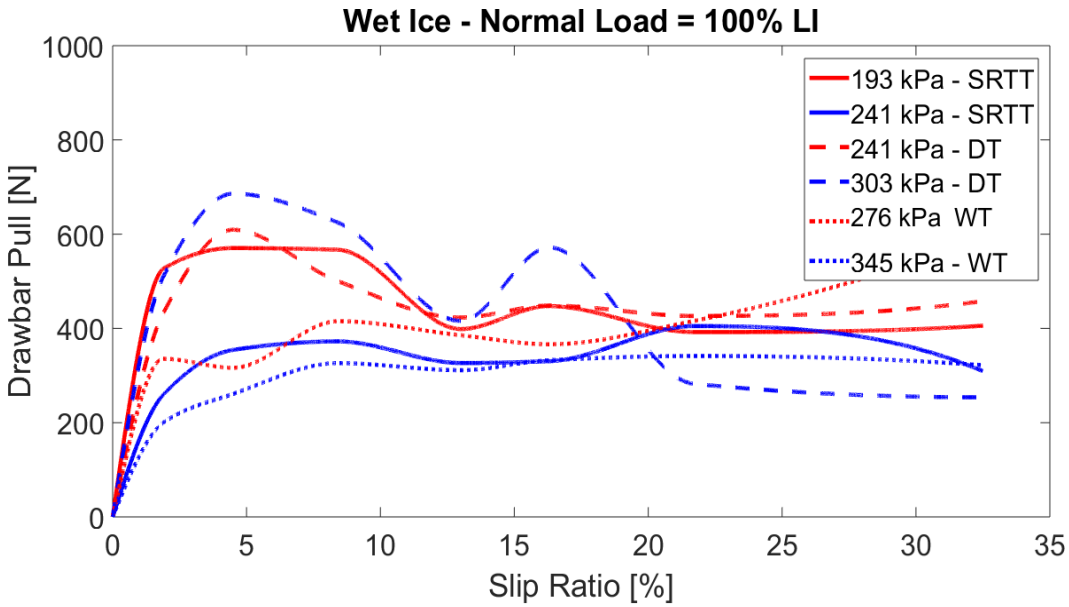

Figure 3.43: Drawbar pull measurement of three tires at an ice surface temperature of −3°C and 0° Camber and Toe Angle.

This study aims at enhancing the understanding of the tire-ice contact interaction at the contact patch through experimental studies for a pneumatic tire traversing over solid ice.

This study investigates the effects of various parameters at the tire-ice interface. Based on the findings from the literature review, a design of experiment was carried out to understand the effect of the normal load, inflation pressure, toe and camber angles during the operation of two candidate tires. A novel method to measure the temperature directly at the tire-ice interface was introduced, which is based on the instrumentation of the tire tread with thermocouples.

A reduction of drawbar performance was observed with a decrease in normal load for the entire slip ratio range investigated. A decrease in the slip ratio value at which the maximum normalized drawbar pull (i.e., drawbar pull coefficient) is achieved was detected when the inflation pressure was increased. When operating at lower inflation pressures, an increased contact area was observed that leads to increased friction levels at low slips. How-

ever, at high slips, with an increased contact area there is also an increased heat generation, which enhances frictional melting of the ice surface, thus the friction levels are lower at higher slips. With the addition of a thin water film, there is a significant decrease in the available traction at the contact patch found for the $SRTT$, as expected. The 19" Pirelli All-Season Tire performed better than the Standard Reference Test Tire with a thin liquid layer present at the interface. When a camber angle is applied, the contact area of the tire changes with respect to the applied angle. This reduction in area led to non-significant changes on the tractive performance of the car. However, an increase in toe angle led to a decrease in peak drawbar pull coefficient, but it also led to an increase in the lateral force at the tire-ice interface.

The experimental study accomplished its goal of collecting relevant force and moment test data for the tires studied on solid ice. Furthermore, the data is to be used for validation purposes for the Advanced Tire-Ice Interface Model ($ATIIM$).

Chapter 4

Advanced Tire-Ice Interface Model ($ATIIM$)

The material properties are vastly affected by the bulk temperature of the tire. As the tire operates on the ice surface, the tire's contact patch temperature will rise. Therefore, in order to quantify the performance of the pneumatic tire, the temperature distribution at the contact patch must be determined.

To study the temperature rise of the contact patch under normal operating conditions, a Tire-Ice Model was developed to identify the rise in temperature at the contact patch as well as to identify areas of dry and wet regions in the contact patch [19]. Once the temperature rise is determined, the dynamic friction coefficient is obtained at the tire-ice interface. Since the original development of TIM several additional modules have been implemented in order to improve and extend its original capabilities. Those improvements will be discussed in detail in the following section.

4.1 Model Overview

Numerical formulations can be used to estimate the temperature under various moving scenarios according to the formulations developed by Jaeger [20]. The Band Heat Source method is employed and expended to quantify the heat transfer at (x, y, z) due to a moving heat sink located at (X, Y, Z). Assuming friction work is the only heat source in the interface in conjunction with the pressure distribution at the contact patch, Jaegers formulation allows for temperature measurements of each tread block as they contact the ice surface. A thermal balance between the tire surface and the ice surface is then employed to determine the dynamic friction coefficient at the contact patch. This method is employed as opposed to others because it is shown in literature that the Band Heat Source method takes into account the most important aspects which are critical for the tire-ice contact interface.

The assumptions [27] taken into account for the Advanced Tire-Ice Interface Model are:

1. The contact between the tread block and the ice surface occurs in the plane $z_t = z_i = 0$.

2. The frictional work equals the heat generated in the interface.

3. Heat is generated only at the interfaces where the tread blocks contact the ice surface and flows into the tread or the ice surface.

4. Generation of heat is uniformly distributed at the contact between the individual tread block and the ice surface.

5. Thermal resistance at the interface is neglected, implying that the temperatures of the tread and of the ice surface are equal at the tire-ice interface.

6. Only the effects of two tread blocks (contact areas) are considered next to point of temperature computation in the contact patch.

7. The dimensions of the pixels of the contact patch are assumed to be uniform rectangles of length L along the x axis and of width B along the y axis.

8. The tread is a uniform semi-infinite solid with $z_T > 0$, neglecting the penetration of asperity into the tread.

9. Heat is generated only in the actual contact areas as a result of friction between the tread and the ice surface.

10. Heat generation is uniformly distributed over the actual contact areas.

11. Heat flows from the tread to the ice (or from the ice to the tread) only through the actual contact areas.

12. The effects of only two actual contact areas nearest to the point at which the temperature is computed are considered.

13. Asperities are thermally independent from each other.

As the temperature rise causes the temperature distribution to reach the melting point of the ice surface, wet regions in the contact patch begin to form. This thin water film results in low levels of friction. Therefore, in order to quantify the performance of the pneumatic tire, both dry and wet regions must be taken into account. ATIIM uses the relative ice surface temperature to determine if the temperature rise is sufficient enough to melt the ice.

The Advanced Tire-Ice Interface Model ($ATIIM$) is a modular-structured model having six main modules as seen in Figure 4.1. The first and second module captures the

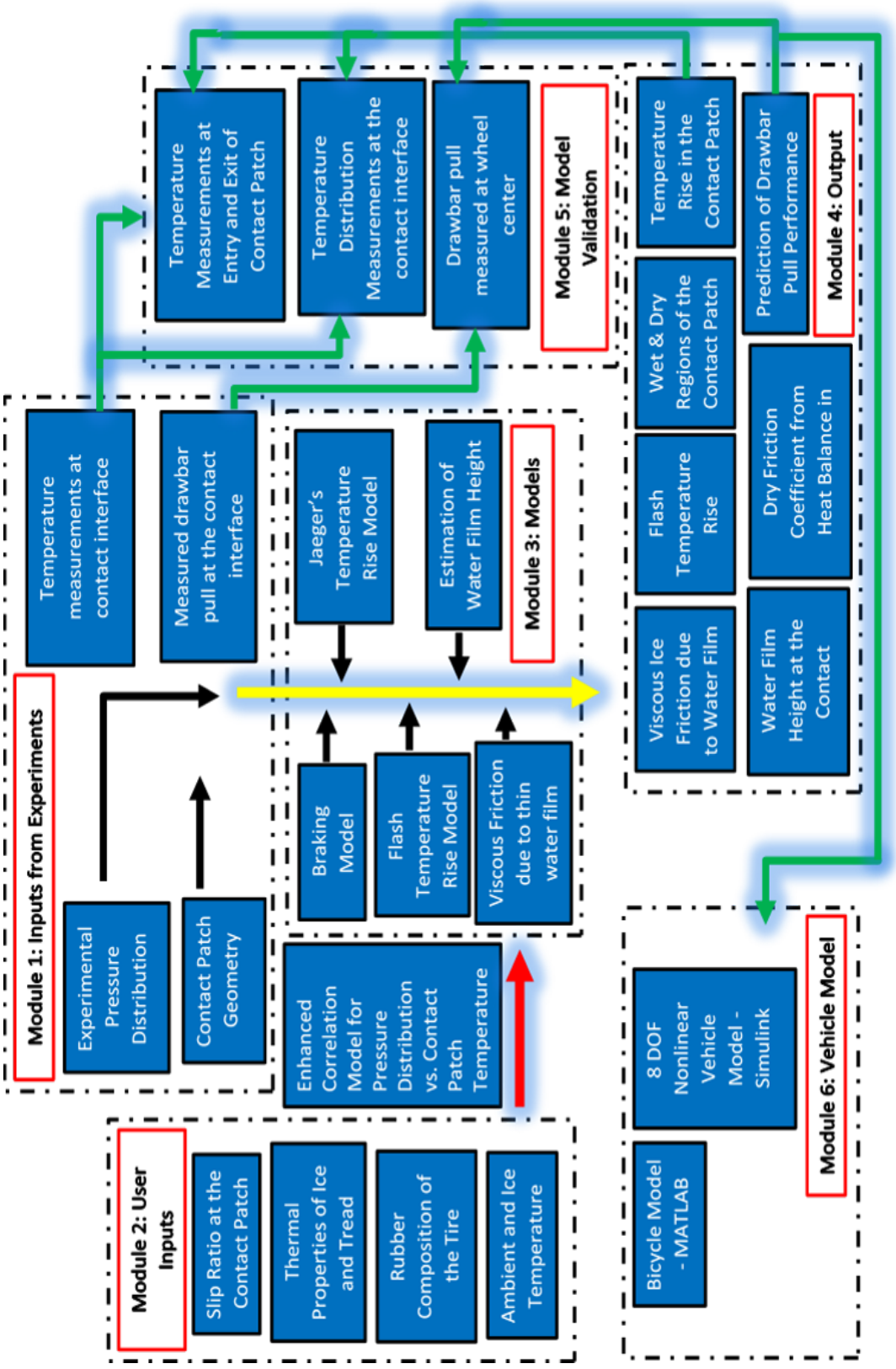

Figure 4.1: Modular structure of the Advanced Tire-Ice Interface Model. The blue color scheme corresponds to the extension of the model from its original development.

pressure distribution and geometry in the contact patch including the thermal properties of the ice surface and the tire. If the pressure distribution is in the form of an image, the model is capable of using the color-bar to numerically map the pressure distribution at each individual pixel. If the numerical values are already known, only thermal parameters are used as an input. The third module computes the temperature rise in the contact patch [20] and classifies the contact patch into wet and dry regions based on the temperature difference at the contact patch. The Band Heat Source method is employed to quantify the heat transfer at (x, y, z) due to a moving heat sink located else where at (X, Y, Z) as shown in Figure 4.2.

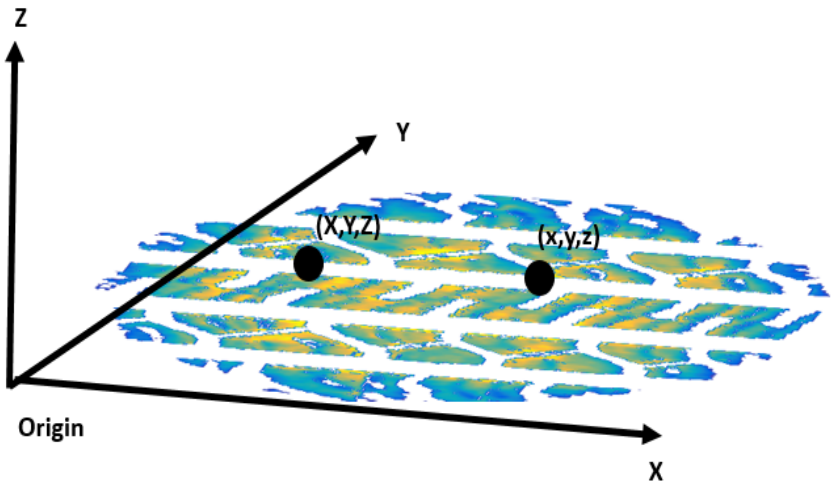

Figure 4.2: Basis of Jaegers' formulation for the Advanced Tire-Ice Interface Model. Used to quantify the heat transfer at (x, y, z) due to a moving heat sink located else where at (X, Y, Z).

With the heat sink known, Jaegers formulation allows for temperature measurements of each tread block as they contact the ice surface. This makes up the main base of the model. Once the temperature rise is determined, the model is capable of using ΔT to determine various outputs listed in the next module. The fourth module is made up of the model outputs. With the temperature rise computed, the height of the water film at the contact

patch can be determined. With the known height of the water film at the contact interface, the advanced model is also capable of determining the viscous friction due to the water film. The results prove that the friction is the greatest when the water film is at the minimum. Using the fluid height and the longitudinal force at the contact patch, the average friction values based on the principle of heat balance can be calculated as an additional output to the advanced model. Finally, the fifth module accounts for the validation of the results. Indoor experimental results are used in conjunction with temperature measurements at the contact patch to determine the accuracy of the Advanced Tire-Ice Interface Model.

4.1.1 Governing Equation of Advanced Tire-Ice Interface Model

The Band Heat Source method is employed and expended to quantify the heat transfer at (x, y, z) due to a moving heat sink located at (X, Y, Z), as shown in Equation (4.1).

$$\Delta T = \frac{Q\alpha}{8k\pi\alpha t^{\frac{3}{2}}} \times \exp - \frac{(X-x)^2 + (Y-y)^2 + (Z-z)^2}{4\alpha t} \tag{4.1}$$

In Equation (4.1), The temperature rise at the point (X, Y, Z) at time t in an infinite solid due to a quantity of heat Q instantaneously released at (x, y, z) with no internal heat generation is presented. k is the thermal conductivity and α is the heat transfer coefficient ($\alpha = \gamma/(\rho C)$). This solution solves the problem which is referred to as the moving-heat source problem [54]. With ΔT known, it can be used to calculate the temperature rise at a nearby point. Since the original development of the Advanced Tire-Ice Interface Model, several state of the art formulations have been implemented which further extends the 3-D capabilities of the advanced model.

4.1.2 Effect of Thin Water Film

All contacting asperities behave in an elastic-plastic-viscous manner and the resulting hysteretic loss is dissipated in the contact area as heat. If the heat flow is sufficiently high and the contact time is long, it can cause the ice surface to soften or even to melt. Hence, as opposed to other friction surfaces like dry and wet roads the friction process on ice is strongly related to thermodynamics and especially the phase transition of ice to water [33]. Therefore, it is critical to establish the height of the fluid layer at the interface due to the temperature rise of the contact patch during operation.

This phase transition can be taken into account by using the first law of thermodynamics. More precisely, the thermodynamic conservation law consists of, on one hand, the energy generated by the friction process and, on the other hand, the heat flows into the ice and rubber as well as the heat needed for the melting process [13]. Since the heat transfer to rubber is much smaller than the heat transfer to ice, the conservation law can be simplified. Therefore, the model is based on the crucial assumption that the required frictional energy for the melting process is only caused by viscous shearing in the liquid layer which allows the water film height to be determined [33].

The height of the liquid layer is driven by an equilibrium between the heat built up by viscous friction, energy consumption for phase transition between ice and water, and heat flow into the cold underlying ice. In addition, the microscopic squeeze-out phenomena of melted water resulting from rubber asperities are also taken into consideration. The size and microscopic real contact area of these asperities are derived from roughness parameters of the free rubber surface using Greenwood-Williamson contact theory and compared with the measured real contact area [13].

From known fluid mechanics, for a given sliding velocity v the viscous shear strain τ

can be described simply by Newton's law as shown in Equation (4.2). In Equation (4.2), η is the viscosity of the water and h is the height of the fluid layer, which is the only unknown parameter.

$$\tau = \frac{\eta v}{h} \tag{4.2}$$

To solve for h, the one dimensional simplified heat equation, as shown in Equation (4.3) is used.

$$\frac{\partial T(z,t)}{\partial t} - \alpha \frac{\partial^2 T(z,t)}{\partial^2 z} = 0 \tag{4.3}$$

The solution of Equation (4.3) in terms of a time-dependent heat flux [13] $q_{ice}(t)$ is determined to be:

$$q_{ice}(t) = -\gamma \frac{\partial T(0,t)}{\partial z} = \gamma \frac{T_m - T_{ice}}{(\pi \alpha t)^{1/2}} \tag{4.4}$$

In Equation (4.4) the initial condition used is $T(z,0) = T_{ice}$ where T_{ice} is the ice temperature. The boundary conditions used is $T(0,t) = T_m$, where T_m is the melting temperature or the contact temperature at the interface [33]. Finally, it is possible to formulate a balance between the phase transition from ice to water and viscous shearing due to the thin fluid layer determined by h. Using Equation (4.2) and Equation (4.3) it is possible to formulate a equation to estimate the height of the fluid layer where the first terms on the right hand side makes up for the phase transition with ρ for density and L for the specific latent heat of ice as shown in Equation (4.5).

$$\frac{\eta v^2}{h(t)} = \rho L \frac{dh(t)}{dt} + \gamma \frac{T_m - T_{ice}}{(\pi \alpha t)^{1/2}} \tag{4.5}$$

Next, in order to include the squeeze-out effect, it is required to take into account surface roughness using the well known Navier- Stokes equation. This equation along with the contact theory of Greenwood-Williamson are used simultaneously to generalizes the classical Hertzian elastic contact approach of one single spherical rubber asperity to a large number of asperities [55]. With notations of [55], the squeeze-out phenomenon for an average asperity of diameter D is:

$$\frac{dh(t)}{dt} = -\frac{8}{3\eta} \frac{p}{\langle D \rangle^2} h(t)^3 \tag{4.6}$$

Combining Equation (4.5) and Equation (4.6), it is now possible to formulate an equation to estimate the height of the fluid layer h as shown in Figure 4.3.

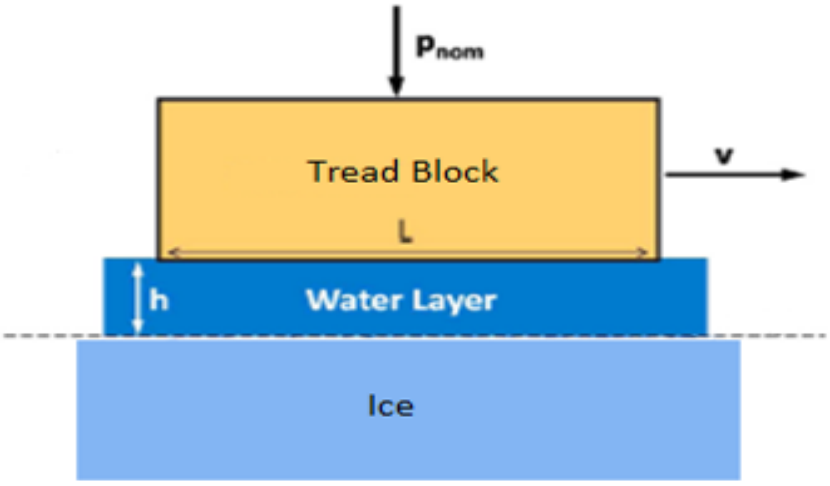

Figure 4.3: Schematic representing the notation regarding the thin fluid layer at the contact interface. Adapted from [13] under fair use; Fair use determination attached.

$$\frac{dh(t)}{dt} = \frac{1}{\rho L}\left(\frac{\eta v^2}{h(t)} - \gamma\frac{T_m - T_0}{\sqrt{(\pi\alpha t)}}\right) - \frac{8}{3\eta}\frac{p}{\langle D\rangle^2}h(t)^3 \tag{4.7}$$

In Equation (4.7), the left hand side represents the change of height as a function of time. The first factor on the right hand side accounts for the melting energy which is dependent on the latent heat L and the density ρ. The first term in the parenthesis is the heat source term. This term represents the viscous friction depending on the viscosity η, sliding velocity v and the height of the liquid layer h. The following term accounts for the heat sink. In this term, the heat transfer to the cold ice depending on the temperature difference $T_m - T_0$ and the heat transfer coefficient α is shown. Finally, the final term takes into account the squeeze-out below the asperities into the equation. This term is dependent on the height of the liquid layer h, the pressure p and the contact diameter D of the asperities on the ice surface as per Navier- Stokes equations.

4.1.3 Effect of Viscous Ice Friction

In general, the friction coefficient of a rubber block on an ice surface is mainly determined by the viscous friction in the thin film of melted water under the microscopic contact patches [33]. The resulting friction coefficient between rubber and ice is therefore given by the shear forces influenced by the predicted water height.

The thermodynamic friction model is based on the assumption that a balance between frictional energy from viscous shearing, and the melting energy for the phase transition from ice to water as well as the heat flow into the ice, exist. If the velocity of the liquid layer is assumed to be the same as the sliding velocity v of the rubber block, then the viscous shear strain can be described by Newton's Law [13] as shown in Equation (4.2). Using the heat conservation law between the frictional energy and the melting energy, it is possible to

formulate Equation (4.8).

$$\frac{\eta v^2}{h(t)} = \rho_{ice} L_{ice} \frac{dh(t)}{dt} \cdot \chi_{T_{ice}(0,t)=T_m} - \gamma_{ice} \cdot \partial_z T_{ice}(z,t)|_{z=0} \tag{4.8}$$

As previously mentioned, the first term on the right hand side accounts for the phase transition from ice to water as a result of laws of thermodynamics. However, this term only occurs if the ice temperature at the contact interface has reached the melting temperature of ice [13]. The characteristic function $\chi_{T_{ice}(0,t)=T_m}$ takes this into account by being equal to one if $T_{ice}(0,t) = T_m$ and zero if $T_{ice}(0,t) < T_m$. The second term on the right hand side describes the heat flux into the ice block [54].

To compute the average height of the fluid layer at the contact interface Equation (4.9) is used.

$$h(t) = \frac{1}{A_{Nom}} \int_{A_{Nom}} h(x,t) dx \tag{4.9}$$

Equation (4.9) represents the liquid layer averaged over the whole rubber block area. This average can be interpreted as the water height observed from a fixed position on the ice while the rubber block is sliding over this point [13].

Finally, using Equation (4.6), Equation (4.8) and Equation (4.9) it is possible to formulate an advanced model which accounts for the fluid height at the contact interface and allows for the viscous friction to be estimated. The final differential equation is presented in Equation (4.10):

$$\frac{dh(t)}{dt} = \frac{1}{\rho_{ice} L_{ice}} \left(\frac{\eta \kappa v^2}{h(t)} - \gamma_{ice} \cdot \partial_z T_{ice}(z,t)|_{z=0} \right) \cdot \chi_{T_{ice}(0,t)<T_m} - \frac{8}{3\eta} \frac{p}{\langle D \rangle^2} h(t)^3 \tag{4.10}$$

In Equation (4.10) the following initial condition $h(0) = h_0$ is used in integration. This equation is similar in relation to the water film height presented in the previous section. The difference is that in Equation (4.10), the boundary conditions are applied such that the friction can be evaluated at the ice surface. With Equation (4.10), it is now possible to determine the viscous friction coefficient as:

$$\mu(t) = \frac{F_{Shear}(t)}{F_z} = \frac{\tau_{Shear}(t) A_{nom}}{F_z} = \frac{\tau_{Shear}(t)}{p_{nom}} \tag{4.11}$$

When the shear forces alone are investigated using Newton's Law as previously mentioned:

$$\tau_{Shear}(t) = \frac{\kappa \eta_{water} v}{h(t)} \tag{4.12}$$

κ accounts for the relative contact area due to the fact that the friction forces only act in the region A_{Real} of active contact area. Therefore the friction coefficient is shown in Equation (4.13):

$$\mu(t) = \frac{\kappa \eta_{water} v}{p_{nom}} \frac{1}{h(t)} \tag{4.13}$$

4.1.4 Effect of Temperature Rise under Locked Wheel Conditions

In winter conditions, the natural instinct a driver has during emergency conditions is to push the brake pedal to its full position in hopes of stopping before the accident. ABS brake systems are designed to prevent the wheel from locking up, but in winter conditions, the system may fail and cause the tires to lock up and skid to an uncontrollable position.

Under these locked wheel conditions it is important to understand the temperature rise at the contact patch in hopes to prevent ice melting and further debilitate the traction capabilities of the pneumatic tire.

Slip between the tread surface and the road causes frictional heat generation during the locked wheel conditions and severe braking of a tire. The frictional force under these conditions have a component due to hysteresis and a component due to the adhesive force at the contact patch. The hysteresis component affects not only the external tread surface, but also the bulk rubber material, to a certain depth.

Because a point on the tire continually enters and exits the contact patch, an average heat generation and heat transfer over the circumference of the tire is calculated. The frictional energy generated during sliding is consumed by the rubber abrasion process, heat transfer into the surface of the road, and heat transfer into the surface of the tread rubber [56]. From literature [57][58][59][56], it is assumed that the frictional heat generated obeys the following relationship under severe braking:

$$Q_1(x) = q_1 e^{\epsilon(a-x)} \tag{4.14}$$

In Equation (4.14), ϵ (1/m) is the penetration depth (tread block depth) constant for friction. Based on the assumptions, Equation (4.14) states that the frictional heating is greatest on the surface and reduces exponentially with depth [59]. Using the slip ratio defined in Equation (3.2), and under conditions of severe sliding, the power consumed by the tire during these conditions can be formulated as [58]:

$$W_2 = (\sin^2 \alpha + s^2)^{1/2} \mu_d V F_z \tag{4.15}$$

In Equation (4.15) μ_d is the coefficient of sliding friction, F_z is the normal load on the tire and V is the translational velocity. If Equation (4.14) is integrated, it is then possible to obtain the total heat generated in the tire tread as [58]:

$$\int_0^a Q_1(x)sdx = \frac{q_1 S}{\epsilon}(1 - e^{-\epsilon a}) \tag{4.16}$$

In Equation (4.16), S is the slip ratio defined in Equation (3.2). q_1 can be determined to be [58]:

$$q_1 = \frac{\epsilon(\sin^2\alpha + s^2)^{1/2}\delta\mu_d V F_z}{1 - e^{-\epsilon a}} \tag{4.17}$$

Where α is the slip angle of the tire. Equation (4.17) is possible because the heat flow into the rubber and total energy of heat generated can be equivalent to each other. In Equation (4.17), ϵ is now the ratio of heat energy that flows into the tread rubber compared to the overall rate of heat generation. Equation (4.17) represents the heat generated during severe braking.

4.1.5 Estimation of Tractive Performance

Using the known temperature rise, it is possible to determine the drawbar pull at the contact patch during operations on an ice surface. Taking into account the heat transfer to the tread, the heat transfer into the ice, and the heat transfer due to the thin liquid layer at the interface, it is possible to calculate the generated heat in the dry and wet regions of the contact patch.

The law of heat conduction, also known as Fourier's law, states that the time rate of

heat transfer through a material is proportional to the negative gradient in the temperature and to the area, at 90° angles to that gradient, through which the heat flows [54]. Fourier developed his theory of heat conduction at the beginning of the nineteenth century. It states (in actual notation) that the temperature profile of an isolated system will evolve following the conservation equation:

$$c_v(T)\frac{\partial}{\partial t}T(\bar{r},t) = \bar{\nabla}\cdot[\kappa\bar{\nabla}T] \tag{4.18}$$

In Equation (4.18), $T(\bar{r},t)$ t is the temperature measured at position $\bar{r}$ at time t, $c_v(T)$ is the specific heat per unit volume, and κ is the thermal conductivity. Fourier's law may be applied, in particular, to a system in contact with two heat reservoirs at different temperatures [54]. For this study, the stationary state has the form of:

$$J = -\kappa(T)\frac{dT}{dx} = Const \tag{4.19}$$

In Equation (4.19), J is the stationary heat flux through the system. This law has been extensively tested in experiments in fluids and crystals. However, we do not understand yet many of its fundamental aspects [54]. Using the conservation law previously mentioned above and following Fourier's Law of Conduction, a heat balance can be performed at the tire-ice interface such that:

$$q_{generated} = q_{tread} + q_{ice} + q_{waterfilm} \tag{4.20}$$

Using the Fourier's Law of Conduction, the Advanced Tire-Ice Interface Model is able to estimate drawbar pull performance of a pneumatic tire on ice. At 80% Load Index

the simulation results matched the experimental data the best as shown in Figure 4.18. In the lower slip ratio range it is harder to obtain accurate predictions due to the fact that the pressure distribution used for the original model was measured under a certain applied torque as opposed to being subjected to a specific slip ratio.

$$q_{generated}A_{total} - q_{dry}A_{dry}(= q_{tread} + q_{ice} + q_{waterfilm}) \times A_{wet} \tag{4.21}$$

After determining the total heat generated, the average coefficient of friction is calculated based off of the pressure distribution at each image pixel, and is averaged for each slip ratio:

$$q_{generated} = \mu_{average}\rho_{average}V_{tire}S \times A_{total} \tag{4.22}$$

4.1.6 Modeling the effect of Rubber Compound on the Performance of Tire on Ice

To account for the rubber composition of the pneumatic tire, the Shore A hardness measurement of the rubber can be used to characterize the thermal properties, specifically the thermal diffusivity, as shown in Figure 4.4. The stiffness of rubber under small tensile or comprehensive strains can be determined taking into respect the dimensions of the rubber sample and a value for the Young's Modulus of the rubber. Therefore, there should be a method to determine the Young's Modulus for vulcanized rubbers by others means, such as indentation [60].

The original hardness test consist of the measurement of the increase in depth of penetration of a rigid cylindrical indenter having a truncated conical end into a flat pad of

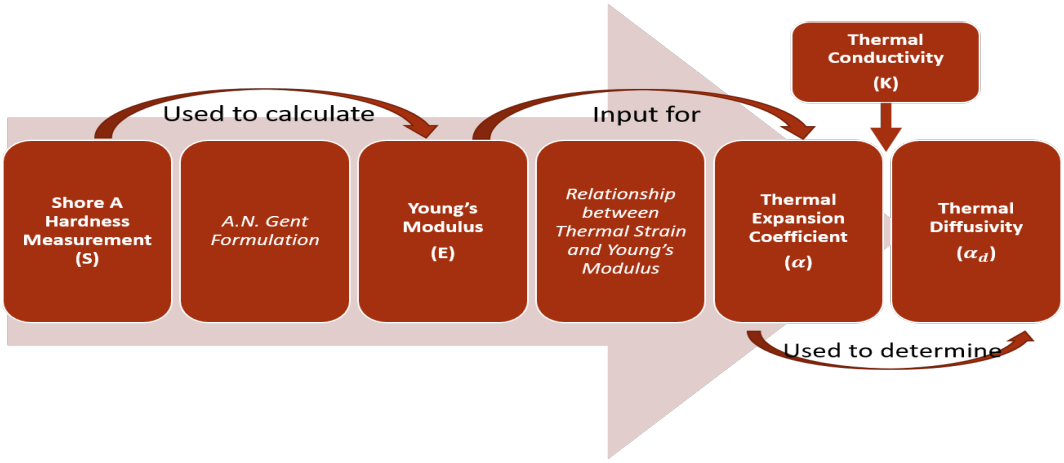

Figure 4.4: Flow chart representing the processing of identifying the thermal diffusivity from a Shore A Hardness measurement.

rubber. If the indentation is small enough, compared to the rubber pad, and the rubber is isotropic, the relation between the total amount of indentation d and the value of Young's Modulus E can be determined by classical elasticity theory [60] as:

$$d = F/2.67Er \tag{4.23}$$

where F is the load applied by the indenter and r is the radius of the spherical end of the indenter. Taking into account the function mechanism of the indenter and its geometry, it is possible to formulate the relationship between Young's Modulus and Shore Hardness [60] as:

$$E = \frac{0.0981(56 + 7.62336S)}{0.137505(254 - 2.54S)} \tag{4.24}$$

In Equation (4.24), S is the Shore A Hardness measured from a durometer.

Now that the Young's Modulus is calculated from the Shore A Hardness measurement, it is now possible to determine the Thermal Expansion Coefficient α, using the relationship

between thermal strain and Young's Modulus. Material's thermal expansion coefficient and the elastic modulus are related [14] through the mathematical formula:

$$\alpha = \frac{\gamma_G \rho c_v}{3E} \tag{4.25}$$

where the Grüneisen variable, γ_G is a dynamic constant which varies within one order of magnitude between the ranges of $0.4 < \gamma_G < 4$ [14]. In Equation (4.25), ρ is the density and c_v is the specific heat of the rubber.

A qualitative approach to the thermal strain concept can be identified using Figure 4.5.

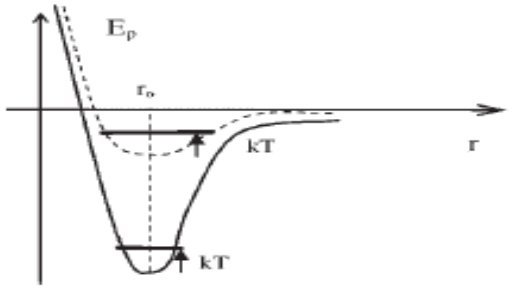

Figure 4.5: Potential energy as a function of distance for weak (dashed line) and strong (continuous line) bond. Adapted from [14] under fair use; Fair use determination attached

The potential energy is not symmetric. The average distance between atoms shifts towards the right hand side of Figure 4.5 as the materials are expected to expand when they are heated [14]. Materials showing a deeper potential, such as stiffer materials, show less potential asymmetry. Therefore, these materials present a lower thermal expansion coefficient than materials having a shallow potential (soft materials).

Once the thermal expansion coefficient (α) has been calculated, it can be used in conjunction with the thermal conductivity (K) to determine the thermal diffusivity (α_d). The thermal diffusivity measures the rate of heat transfer of a material as it transfers from hot to cold. In the original development of the Advanced Tire-Ice Interface Model, the

thermal diffusivity served as a static input for the characterization of the thermal properties of the rubber. Being able to determine the thermal diffusivity directly from a measurement, such as the Shore A Hardness, allows the user of the model to quickly characterize the thermal properties of a tire for a rapid simulation.

The thermal diffusivity can be calculated with the well known formulation as:

$$\alpha_d = \frac{K}{\rho c_p} \tag{4.26}$$

where K is the thermal conductivity, ρ is the density of the rubber, and c_v is the specific heat of the rubber. The thermal conductivity identifies the rate at which heat is transferred through a material. It can be expressed as:

$$\frac{dQ}{dt} = -KA\frac{dT}{dx} \tag{4.27}$$

where $\frac{dQ}{dt}$ represents the change of heat with respect to time and $\frac{dT}{dx}$ represents the change in temperature with respect to a one dimensional length.

Equation (4.25) can also be represented by the common formulation of thermal expansion as:

$$\alpha = \frac{\Delta L}{L(\Delta T)} \tag{4.28}$$

With this representation, it is possible to take into account the thermal expansion caused in the rubber of a tire during loading [61]. For the case of a rubber tire, Δx represents the height of a tread block. ΔL represents the difference between the unloaded radius of the tire and the effective rolling radius ($\Delta L = R_{Unload} - R_{Eff}$). L is the effective rolling radius

(R_{Eff}).

4.2 Numerical Results

Once the governing equations have been implemented into the Advanced Tire-Ice Interface Model ($ATIIM$), the model becomes capable of simulating various scenarios which can also be studied experimentally. For the following numerical simulations the classical physical parameters are taken from Table 4.1.

Table 4.1: Physical Parameters for simulations

Physical Parameters	Value
Density of ice, ρ_{ice}	917 g/m^3
Latent Heat of ice, L_{ice}	330,000 J/kg
Heat Transfer coefficient of ice, λ_{ice}	2.25 $W/(mK)$
Viscosity of Water, η_{water}	0.00182 Pas

4.2.1 Simulation Results for Estimating the Temperature Rise

The original development was capable of simulating the temperature rise of the Standard Reference Test Tire. This study was capable of also estimating the temperature rise at the contact patch of the 19" Pirelli All-Season Tire. First the results for the Standard References Test Tire are presented in Figure 4.6. $ATIIM$ is capable of simulating the temperature rise under different conditions based off of the pressure distribution data. As the torque at the wheel center is increased, the temperature rise tends to be greatest at the rear of the individual tread blocks compared to Figure 4.6b and Figure 4.6c. In general, when the tread blocks are observed as a whole unit, the temperature rise is highest at the rear at the contact patch and tends to be even greater towards the middle of the trailing edge.

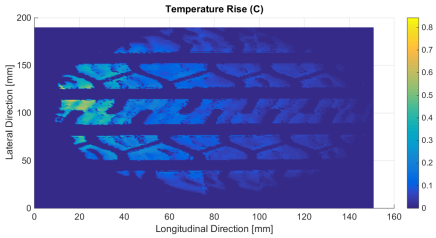

(a) Static Condition

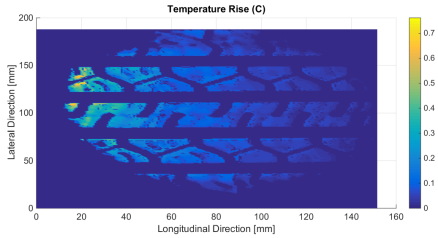

(b) Free-Rolling Condition

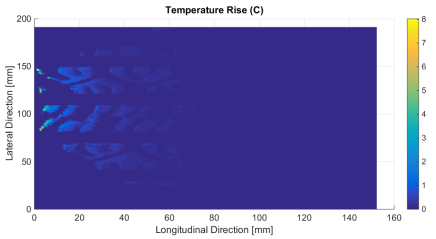

(c) 4,000 N-m Torque Applied at Wheel Center

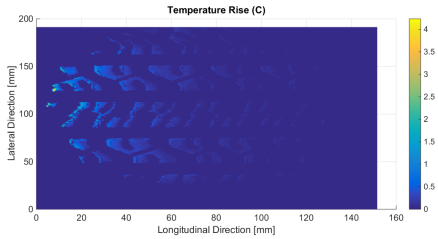

(d) 8,000 N-m Torque Applied as Wheel Center

Figure 4.6: Four temperature rise simulations from the Advanced Tire-Ice Interface Model for the Standard Reference Test Tire. The normal load was 4,000 N and the inflation pressure was 35 psi, with an ice surface temperature of -10°C.

This is evident when Figure 4.6c is compared to Figure 4.6d. It is also shown that the edges of the contact patch tend to have a higher temperature rise, especially towards the leading edge of the contact patch.

When the pressure distribution for the 19" Pirelli All-Season tire is used as an input of the advanced model, the temperature difference can also be estimated, as shown in Figure 4.7. In Figure 4.7, it is clearly evident the effects on which the normal load has on the shape of the contact patch. As the normal load on the tire is increased, the shape of the contact patch becomes more like a rectangle. When the normal load was 4000 N, the shape of the contact patch resembled an oval. Meaning that as the normal load increases, the pressure distribution is highest towards the edges of the contact patch. Also, when a camber angle is applied, the change in shape of the contact patch changes to a more trapezoid-like shape. As this is a +4° camber angle, the shorter side of the contact patch is at the outer edge of the contact patch.

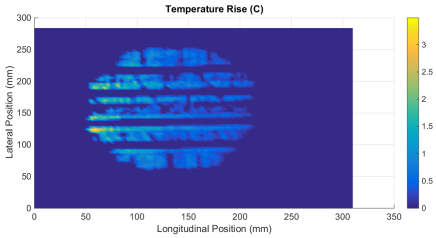

(a) Normal Load: 4000 N

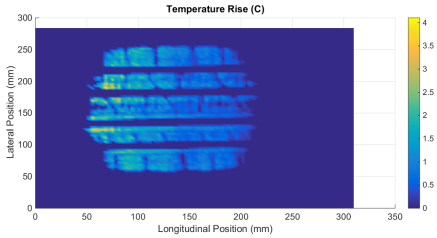

(b) Normal Load: 7000 N

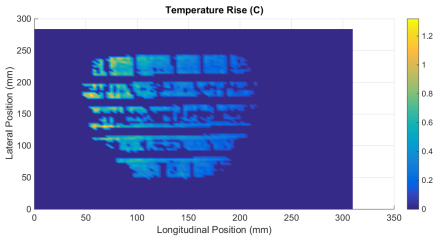

(c) Normal Load: 7000 N Camber Angle" +4°

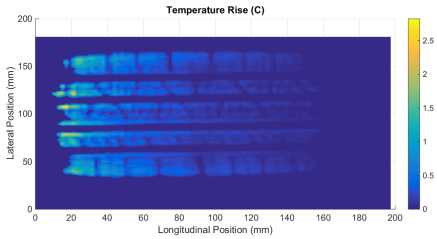

(d) Normal Load: 10,500 N

Figure 4.7: Four temperature rise simulations from the Advanced Tire-Ice Interface Model for the 19" Pirelli All-Season Tire. The inflation pressure varied between 15 psi for Figure 4.7a and all others at 35 psi, and an ice surface temperature of -10°C.

In regards to the temperature rise for the 19" Pirelli tire, the results proved that the advanced model was capable of predicting the temperature rise for tire of different sizes. The heat generated causes the largest temperature rise at the rear of the contact patch. As the normal load increases, the rise in temperature is even more significant. In Figure 4.7c, the direct effect of pressure distribution is evident when it is compared to that of Figure 4.7b. When a camber angle is applied, the pressure distribution will be greater on the side which the axle will push against. The increase in pressure distribution at the top part of contact patch results in a higher temperature rise.

In general, the visual pattern of the temperature rise in the contact patch shows to be similar to that of the $SRTT$. Figure 4.7 and Figure 4.6 both show that temperature rise is highest in areas of increased pressure distribution. Whether it occurs at the edges or the rear of the contact patch, it is hypothesized that the pressure distribution has a more direct affect on the rise in temperature compared to that of the geometry of the contact patch. It

is also realized that closer to the leading edge, the temperature rise is highest near the edges of the contact patch but as you progress towards the rear, the rise in temperature is greatest towards the middle of the trailing edge. This could provide visual insight into how the heat is transferred throughout the contact patch.

4.2.2 Simulation Results for Predicting the Influence of a Thin Water Film

The current study includes the investigation of the effects of the water fluid height on an ice surface of -3°C. From simulations, Figure 4.8, Figure 4.9, and Figure 4.11 show that the area of wet compared to dry will increase as the normal load increases. When the normal load increases, the area of the contact patch increases, and therefore produces more heat generation from friction at the interface.

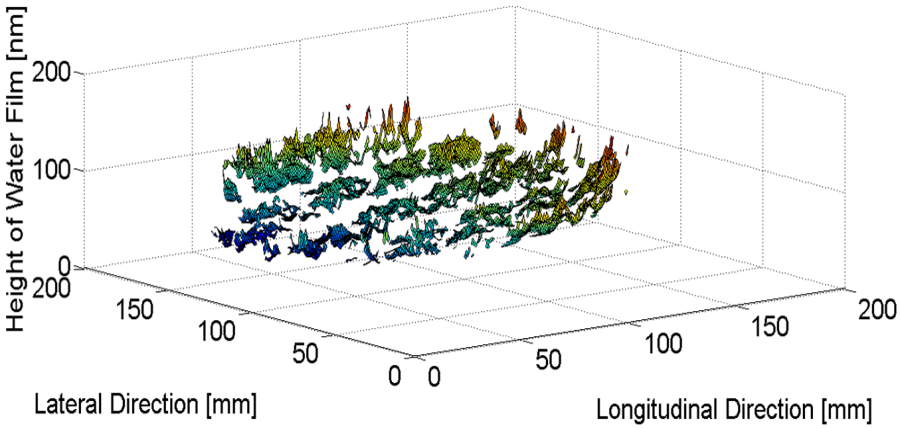

Figure 4.8: Simulation results of thin liquid layer under the contact patch due to temperature rise, an inflation pressure of 35 psi, a normal load of 4 kN and an applied torque of 4000 N-m at the wheel center for the Standard Reference Test Tire.

At 4,000 N, as shown in Figure 4.8, the tire has a contact patch which causes the pressure distribution to be highest at the perimeter of the contact patch. This is shown as

the edges and the rear of the contact patch has a higher fluid height, due to an increase in temperature rise.

As the tire rolls on ice, the temperature rise has been shown to be the greatest at the rear. As the temperature rise increases, it will eventually lead to melted ice and a fluid layer will form. This is shown in Figure 4.8, Figure 4.9, and Figure 4.11. In areas which the temperature rise is the largest, the thin fluid layer is simulated to be the highest, as expected

At various normal loads, different fluid heights will occur. In Figure 4.8, the maximum fluid height occurs at the edge of the contact patch and has a magnitude of about 110 nm. In Figure 4.9, the normal load is increased by 75% and results in a water film profile which has its greatest magnitude at the trailing edge. The greatest value simulated was about 130 nm. Finally, in Figure 4.11, the normal load was increased to 8.5 kN and produced a water film profile which had its peak at the edges closer to the rear, and the trailing edge itself. At these peak values, the maximum magnitude was about 155 nm. Therefore, as the normal load was increased by 4.5 kN, the water film increased by 45 nm.

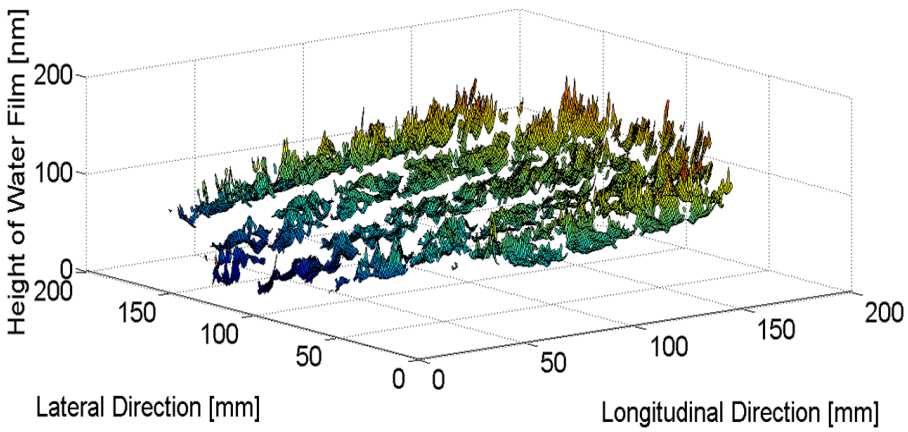

Figure 4.9: Simulation results of thin liquid layer under the contact patch due to temperature rise, an inflation pressure of 35 psi, a normal load of 7 kN and an applied torque of 4000 N-m at the wheel center for the Standard Reference Test Tire.

When the torque was allowed to vary, the fluid height was higher at the rear edges

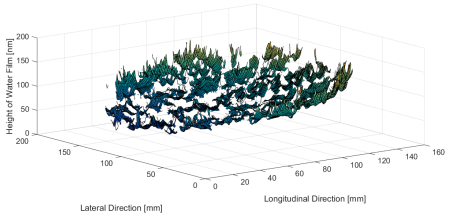

(a) Static Condition

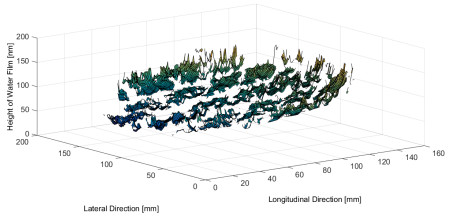

(b) Free-Rolling Condition

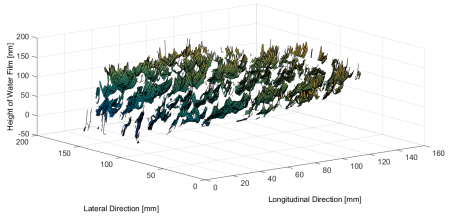

(c) 4,000 N-m Torque Applied at Wheel Center

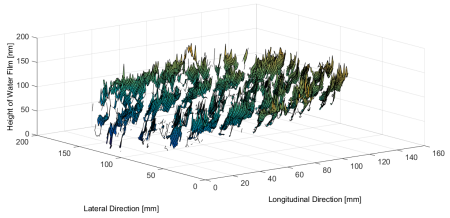

(d) 8,000 N-m Torque Applied as Wheel Center

Figure 4.10: Four simulations from the Advanced Tire-Ice Interface Model for the Standard Reference Test Tire. The results show the fluid height at the contact patch at various torques applied at the wheel center. The normal load was 4,000 N and the inflation pressure was 35 psi.

of the tread blocks, as shown in Figure 4.10. This can be seen by the repetition of the sharp peaks along the longitudinal direction of the contact patch. These sharp peaks can be visualized as waves which are slanted in the direction which the torque is applied. In Figure 4.10, it is evident that the fluid height will be the largest at the rear edges of the tread blocks, as the torque is increased.

The Tire-Ice Model has shown to be able to estimate the thin fluid layer of melted ice, when the ice surface was -3°, due to a rise in temperature. At low normal loads, the fluid height was more uniform throughout the contract patch. When the normal load was increased to 100% and 120%, the trend quickly developed which showed to have the highest fluid height at the trailing edge of the contact patch. From the leading edge of the contact patch to the trailing edge, the rise in the thin liquid layer is up to approximately 150 nm when the normal load is at 120% load index. Once the height of the fluid layer is known, the friction at the contact patch can be determined.

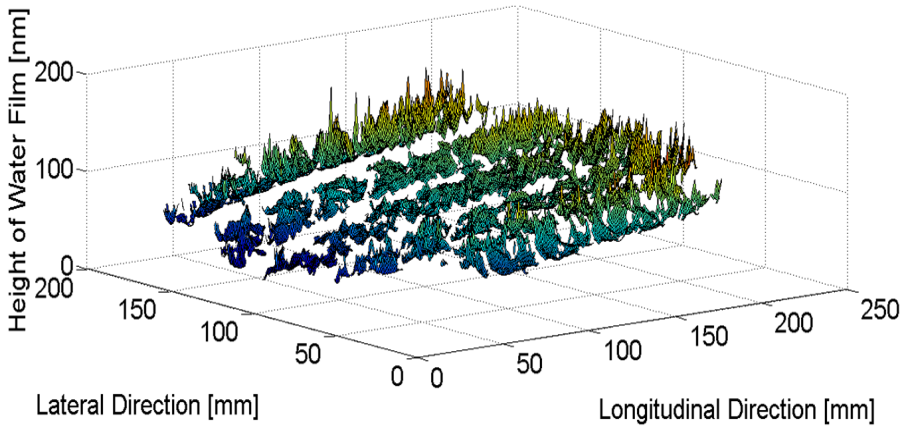

Figure 4.11: Simulation results of thin liquid layer under the contact patch due to temperature rise, an inflation pressure of 35 psi, a normal load of 8.5 kN and an applied torque of 4000 N-m at the wheel center for the Standard Reference Test Tire.

4.2.3 Simulation Results for Prediction of the Viscous Ice Friction of Tractive Performance

Once the height of the thin fluid layer due to melted ice is determined, the viscous shear friction due to the water can be calculated. Implementing Newton's Law Equation (4.12) into the Advanced Tire-Ice Interface Model leads to the determination of the friction at the contact patch under a thin fluid at the tire-ice interface.

Employing the Advanced Tire-Ice Interface Model leads to the results shown in Figure 4.12, Figure 4.13, and Figure 4.14. In the last section, the height of the water film is described. This thin layer is in the order of nanometer and it increases in height at the trailing edge of the contact patch. Under these conditions, the resulting friction can be determined.

As mentioned, the height of the film is largest at the trailing edge of the contact patch. This means that there will be less friction at the trailing edge of the contact patch, as shown for example in Figure 4.14. At the leading edge, the height of the fluid is the smallest,

and we have a friction level of about 0.3. At the trailing edge, we only see a friction level of about 0.1. It is important to note here that these results are for an ice surface temperature of -3°C, which is why we see a predominately wet contact patch.

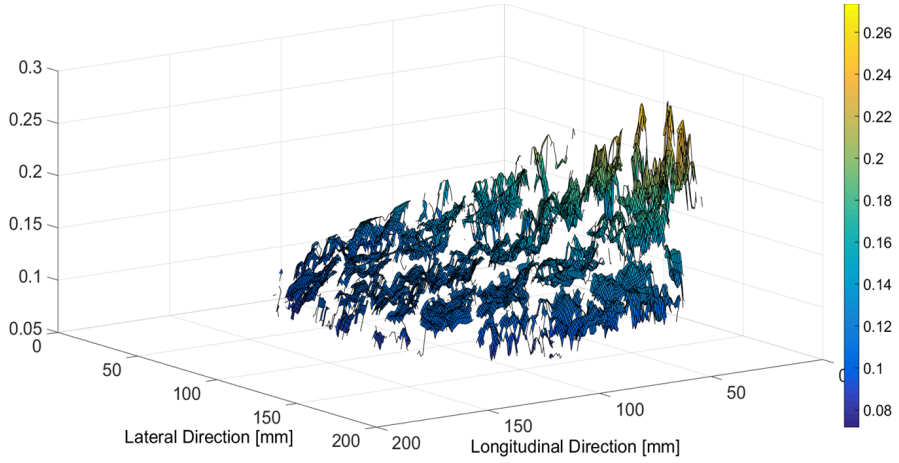

Figure 4.12: Simulation results of viscous friction due to the thin liquid layer under the contact patch from the rise in temperature, an inflation pressure of 35 psi, a normal load of 4 kN and an applied torque of 0 N-m at the wheel center for the Standard Reference Test Tire.

There is also a clear increase in friction as the normal load is increased. As this is expected, the increase occurs mainly in the area leading up to the leading edge of the contact patch. There is a lower coefficient of friction between the 0 mm to 50 mm positions in the longitudinal direction in Figure 4.13 than in Figure 4.14.

Regardless of the normal load on the tire, the viscous friction is the highest at the middle of the leading edge of the contact patch. This is true in all of the simulations for an inflation pressure of 35 psi. As the contact patch enters the contact zone with the ice, it is dry and rapidly becomes wet as the contact patch begins to slide at lower coefficient of frictions.

When the torque was allowed to vary, the maximum friction became more concentrated at the middle of the leading edge. When the tread blocks began to deform from the

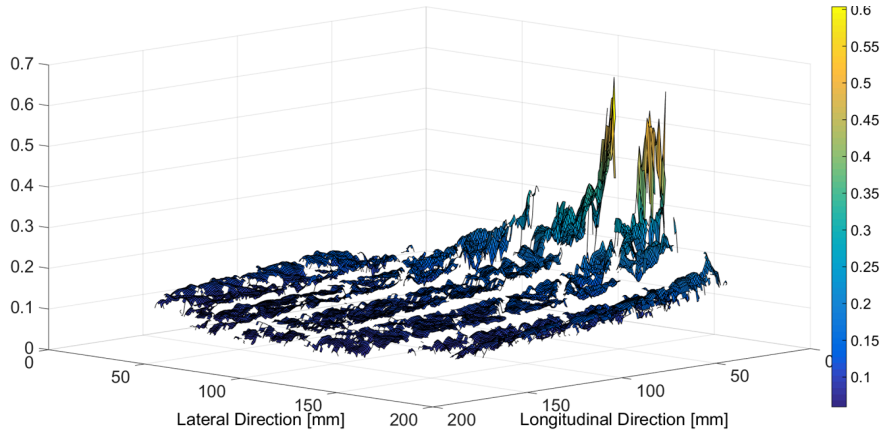

Figure 4.13: Simulation results of viscous friction due to the thin liquid layer under the contact patch from the rise in temperature, an inflation pressure of 35 psi, a normal load of 7 kN and an applied torque of 0 N-m at the wheel center for the Standard Reference Test Tire.

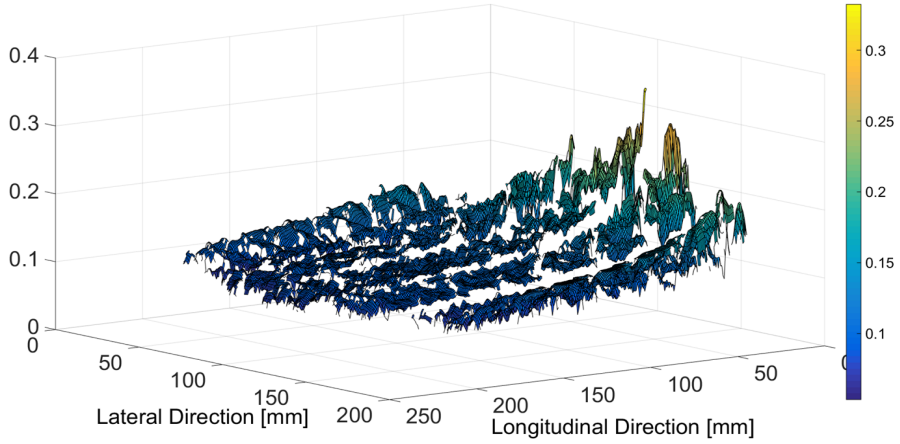

Figure 4.14: Simulation results of viscous friction due to the thin liquid layer under the contact patch from the rise in temperature, an inflation pressure of 35 psi, a normal load of 8.5 kN and an applied torque of 0 N-m at the wheel center for the Standard Reference Test Tire.

applied torque, the trend of the coefficient of friction becomes more like that of Figure 4.13. In this figure, only a small portion has a coefficient of friction greater than 0.1. The rest of the contact patch is at a relatively low friction level. Therefore, as the leading edge enters the contact patch, the contact area is completely dry and has the friction capabilities provided

by the ice surface.

In general, the friction coefficient is decreasing with increasing temperatures both in simulation and in experiment. This observation can easily be explained by the more dominant melting of ice for higher temperatures which results in a higher water layer and a lower friction coefficient.

4.2.4 Simulation Results of the Temperature Rise under Locked Wheel Conditions and Braking Conditions

When an emergency situation occurs, and the wheels become locked and begin to slide, the tire will undergo a rapid increase in temperature. This rise in temperature will occur specifically in the contact patch at the tire-ice interface. When the phenomena of the flash temperature [39] is implemented into the Advanced Tire-Ice Interface Model, the following result are obtained.

In Figure 4.15, the figures on the left-hand side include the contact patch under driving conditions and the figures on the right-hand side show the tire under braking conditions. After implementing the governing equations to include the braking model, a higher temperature rise at the contact patch can be observed. The rise in temperature is more dominant at the middle of the trailing edge and at the edges of the contact patch.

As the torque is applied at the wheel center, the difference in temperature rise is evident. In Figure 4.15c and Figure 4.15d, the difference between braking and driving conditions can be observed. Specifically in the middle of the trailing edge at the contact patch, the slight increase in the distribution of the rise in temperature is evident. As the torque is increased, the rise in temperature is even distributed further into the middle of the contact patch and to the edges.

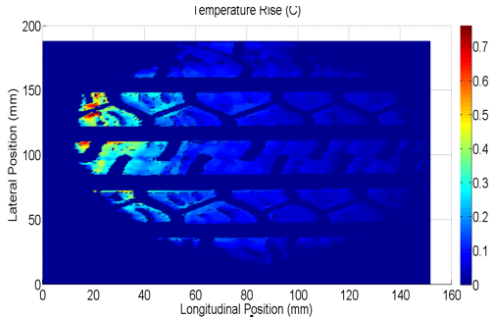

(a) Free-Rolling Condition

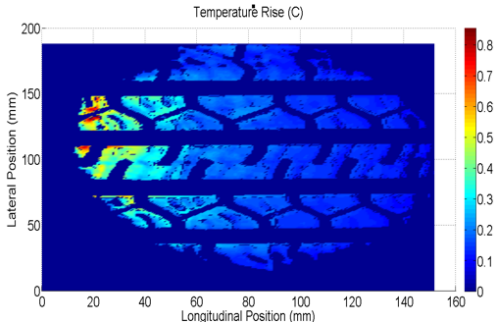

(b) Free-Rolling Condition (Braking)

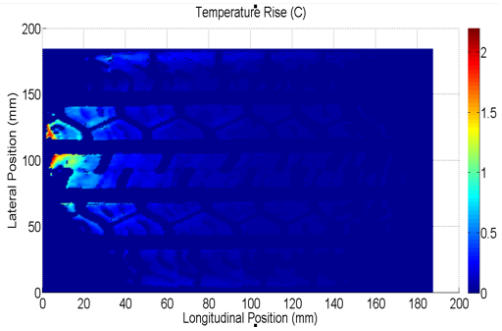

(c) 4,000 N-m Torque Applied at Wheel Center

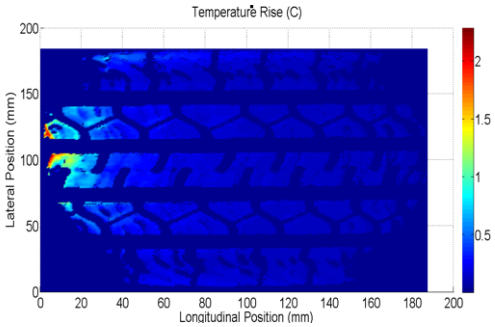

(d) 4,000 N-m Torque Applied as Wheel Center (Braking)

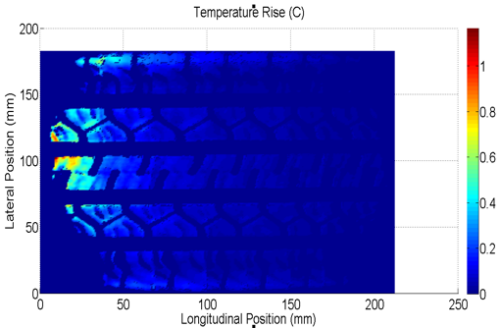

(e) 8,000 N-m Torque Applied as Wheel Center

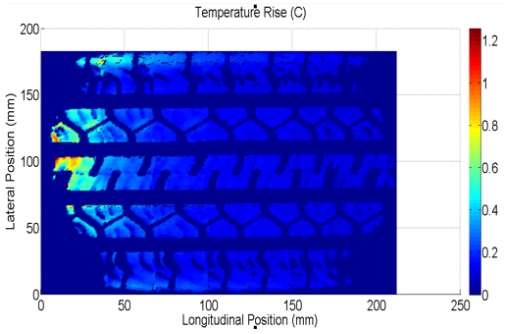

(f) 8,000 N-m Torque Applied as Wheel Center (Braking)

Figure 4.15: Simulations from the Advanced Tire-Ice Interface Model for the Standard Reference Test Tire. The results show the implementation of the braking model to estimate the temperature rise during braking maneuvers The normal load was 4,000 N, ice surface temperature of -10°C, and the inflation pressure was 35 psi.

Figure 4.16 represents the simulation for the Standard Reference Test Tire under a locked wheel condition. The normal load on the tire is 7 kN and the inflation pressure remained at 35 psi. When the tire is in the current configuration, the Advanced Tire-Ice Interface Model estimates that the contact patch will increase by approximately 5°C, when the ice surface temperature is -3°C.

In Figure 4.17 a sudden increase in temperature for a locked 16 SRTT under a 2° slip angle, is observed. Here the contact patch is 100% wet as well, as the rapid increase in temperature led to the melting of ice. Something to note is that even though the temperature rise was sudden, there is still a slight difference in temperature in the contact patch specifically in areas of higher pressure distribution, developed by the introduction of a slip angle at the contact patch. It should also be mentioned that as the normal load decreases and the slip angle becomes 0°, we see that the temperature rise is still rapid, but the absolute increase is not as significant as shown in Figure 4.16.

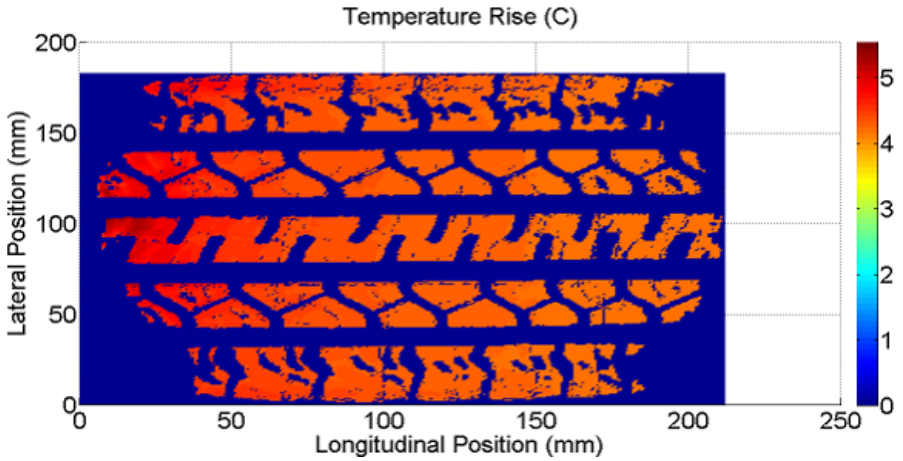

Figure 4.16: Simulation results of flash temperature due to the locked wheel condition. The operating conditions include an ice surface temperature of -10°C, inflation pressure of 35 psi, a normal load of 7 kN and an applied torque of 0 N-m at the wheel center for the Standard Reference Test Tire.

In general, these results could be used to develop rubber material which have a slower rate of internal heat generation during sliding. Under locked wheel conditions, it could be

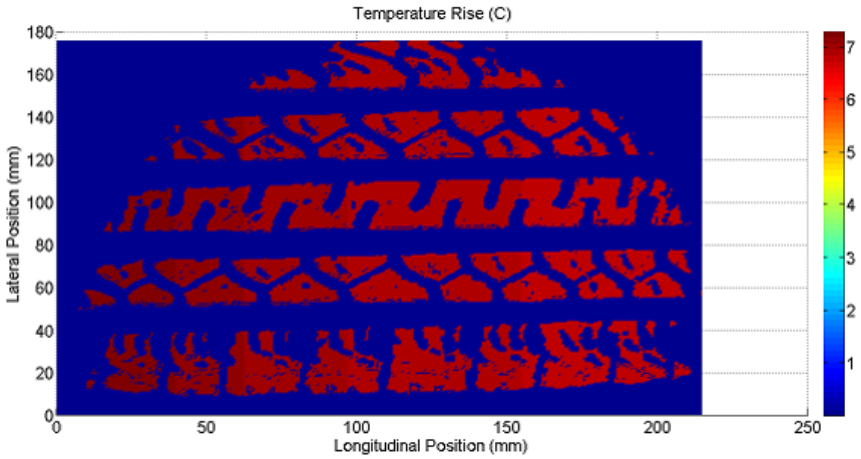

Figure 4.17: Simulation results of flash temperature due to the locked wheel condition. The operating conditions include a 2° slip angle, ice surface temperature of -10°C, an inflation pressure of 35 psi, a normal load of 8.5 kN and an applied torque of 0 N-m at the wheel center for the Standard Reference Test Tire.

beneficial if the temperature of the tire remains close to that of the ice surface in order to prevent the ice from melting. This in turn can lead to an increased coefficient of friction. The brake model itself could also provide useful information in racing conditions. For example, when racers approach a sharp corner and have to quickly decelerate, it is of importance to estimate and measure the temperature distribution during these maneuvers to further improve existing technologies.

4.2.5 Simulation Results for Prediction of Tractive Performance

Knowing the fluid height and the resulting friction is important for driving in wintry conditions. The drawbar pull for which a tire is capable of producing is also a critical parameter to determine the traction at the tire-ice interface. In Figure 4.18 and Figure 4.19, the drawbar pull is presented for the *SRTT* at two different normal loads. The slip ratio investigated were 0%, 5%, 10%, 15%, 20%, 25%, 30%, and 40%.

The Advanced Tire-Ice Interface Model was capable of predicting drawbar pull per-

formance of a pneumatic tire similar to that of the measured results. Even though this is true, the accuracy degraded at higher normal loads. This is hypothesized to be a result of the input data used as the pressure distribution. The pressure distribution data used was measured under an applied torque at the wheel center as opposed to a slip at the contact patch. Therefore, this causes a discrepancy in the low slip range for higher normal loads. Even though there were differences in the data, the trend was still shown using the Advanced Tire-Ice Interface Model.

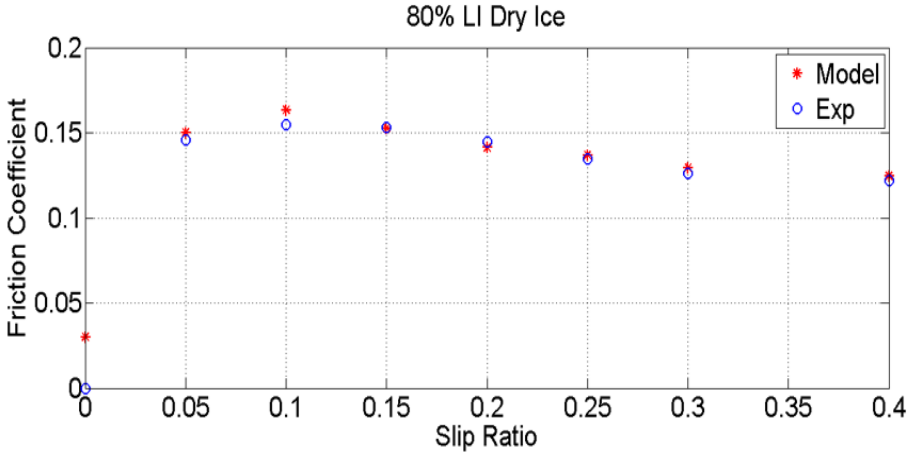

Figure 4.18: Simulation results for prediction of tractive performance due to temperature rise, an inflation pressure of 35 psi, a normal load of 7 kN and an applied torque of 0 N-m at the wheel center for the Standard Reference Test Tire.

Regardless of the input data used, the advanced model showed agreement to the experimental results in the high slip ratio range. After 20%, the model was capable of simulating the measured results of the drawbar pull. Therefore, it can be concluded that the model is capable of determining the slip ratio at which the contact patch is mostly sliding. In this scenario, the tractive performance have saturated, and the tire is not able to produce any more friction.

The *ATIIM* also had difficulty in determining the maximum absolute value of the drawbar pull. In Figure 4.18, the Advanced Tire-Ice Interface Model overestimated the trac-

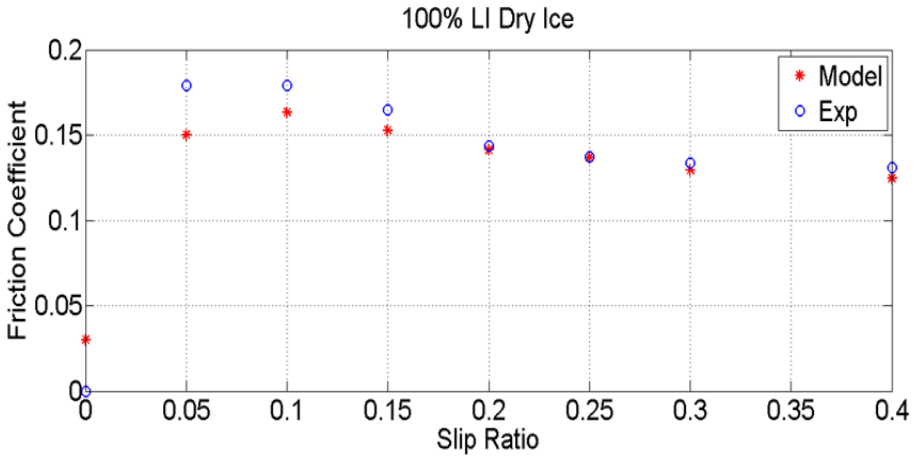

Figure 4.19: Simulation results for prediction of tractive performance due to temperature rise, an inflation pressure of 35 psi, a normal load of 8.5 kN and an applied torque of 0 N-m at the wheel center for the Standard Reference Test Tire.

tion performance of the pneumatic tire, but in Figure 4.19 the traction was underestimated. This instability occurs mainly in the lower slip ratio range as the contact patch area is mainly in the adhesion region. These results are critical for ABS-braking algorithm and are needed to improve such systems for operation in wintry conditions.

4.3 Validation

The experimental results obtained provide appropriate validation data required for the Advanced Tire-Ice Interface Model ($ATIIM$). $ATIIM$ is validated for two parameters, namely temperature rise in the contact patch and the friction level generated at the tire-ice interface.

Temperature rise from simulations are validated against temperature distribution measurements at the contact patch under various operating conditions using K-Type thermocouples. The drawbar pull was measured at different conditions of normal load, inflation pressure, and ice temperatures as well as various steering configurations (Table 3.1).

As shown by both, the simulations from *ATIIM* and the test data, a rise in temperature was observed from the leading edge to the trailing edge of the contact patch. The rise in temperature can be quantified with respect to the load on the tire. As the wheel load increases, the difference in temperature rise increases, as also reflected in the experimental study.

Previous methods to validate the Advanced Tire-Ice Interface Model include using an infrared camera facing the sidewall to capture the temperature at the leading and trailing edges of the contact patch [19]. Although this provided a base understanding of the temperature, the distribution inside the contact patch was of the most interest. The first suggestion, which later proved to be unfeasible, was to instrument the tire by puncturing thermocouples through the inside of the carcass, just until they went all the way through the tread block on the other side. Eventually, the original method of instrumentation lead to the destruction of the tire, so the novel method used in this study was proposed.

Figure 4.20 shows the average temperature measurement superimposed on the tire's contact patch for simulation with a 60% load index and a 2° camber angle. The measured temperature while rolling are averaged during the duration of contact and are presented on the simulations of the same testing conditions. The maximum temperature rise measured was 1°C.

Figure 4.7c can be used to compare Figure 4.20. Under these conditions, the model was capable of simulating the temperature rise with an error of 0.17%. As for the simulation, the model predicted a slightly higher temperature rise for the Pirelli Tire. Also from Figure 4.7c and Figure 4.20, the effect of applying a camber angle was observed. Here, the side where the angle is being applied produces a slightly higher temperature than the opposing side, as observed. Figure 4.21 also had a camber angle applied on the wheel. In this case, the maximum temperature rise measured was 2.2°C. Figure 4.7b predicted a rise in temperature

of approximately 4°C, slightly higher than what was measured.

Figure 4.21 and Figure 4.22 present the temperature distribution measured directly at the contact patch, similar to that of Figure 4.20. In Figure 4.22, the camber angle is 0°, and a more uniform rise in temperature was measured at the contact patch. In this scenario, the maximum rise in temperature under the maximum normal load tested, was 5.4°C. As shown in Figure 4.7d, the maximum temperature rise simulated was 2.5°C, for the same conditions tested. For this load on the tire, the model simulated a lower temperature rise than what was measured using the thermocouples.

From Figure 4.20, Figure 4.21, and Figure 4.22 it can be seen that the model was capable of estimating the measured results the bests at lower normal loads, when compared to Figure 4.7. If the tire thermal parameters were closer to their actual value, the model could have provided more accurate results. This was the case for the Standard Reference Test Tire.

Figure 4.20: Temperature distribution measurements of contact patch for the P235/55R19 All-Season Pirelli Tire. The operating conditions were an ice surface temperature of -10°C, inflation pressure of 35 psi, a normal load of 60% load index, +2° camber angle, and an applied torque of 0 N-m at the wheel center.

In Figure 4.23, Figure 4.24, and Figure 4.25 the measured temperature distribution

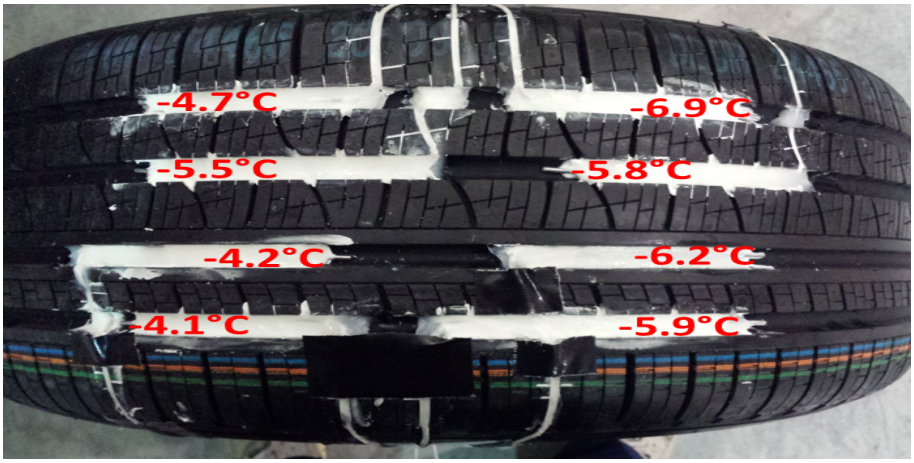

Figure 4.21: Temperature distribution measurements of contact patch for the P235/55R19 All-Season Pirelli Tire. The operating conditions were an ice surface temperature of -10°C, inflation pressure of 35 psi, a normal load of 80% load index, +2° camber angle, and an applied torque of 0 N-m at the wheel center.

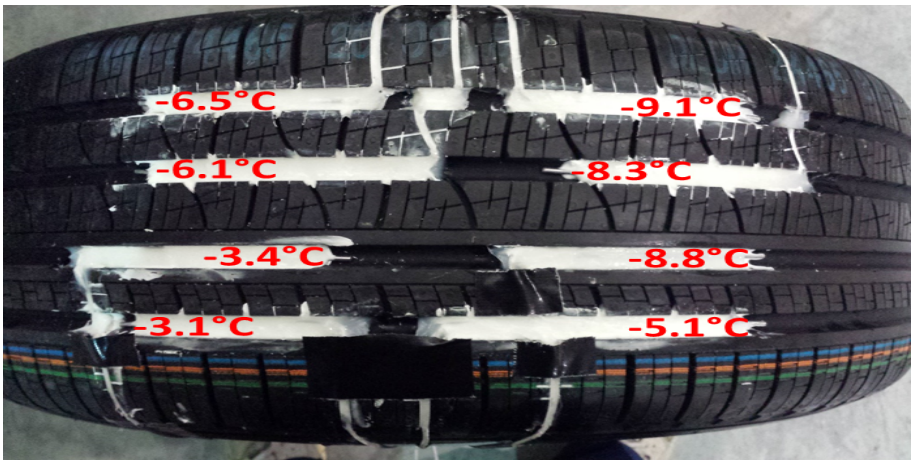

Figure 4.22: Temperature distribution measurements of contact patch for the P235/55R19 All-Season Pirelli Tire. The operating conditions were an ice surface temperature of -10°C, inflation pressure of 35 psi, a normal load of 120% load index, and an applied torque of 0 N-m at the wheel center.

of the contact patch is averaged and directly presented on top of the simulation provided by the Advanced Tire-Ice Interface Model, for the Standard Reference Test Tire ($SRTT$). In Figure 4.23, the normal load was the lowest at 60% load index. For this scenario, the Advanced Tire-Ice Interface Model predicted a rise in temperature of only 0.25°C. As for

the measured results, the maximum difference in temperature occurred at the middle of the trailing edge as simulated. The measured results provided a maximum temperature rise of 1.5°C. There is a clear difference between the measured and predicted values for this specific testing scenario, but as the normal load is increased, the model is capable of providing more accurate results.

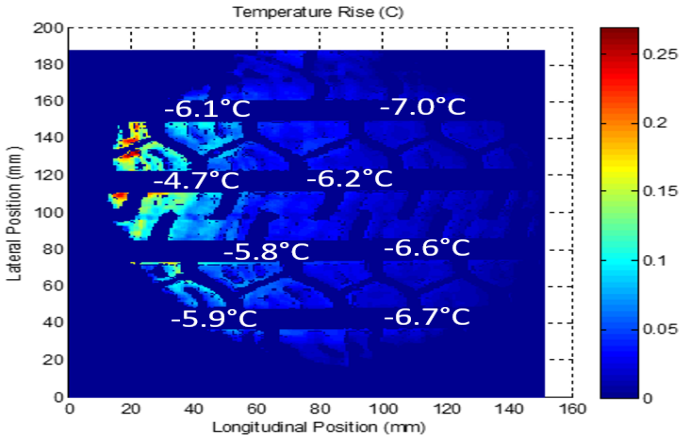

Figure 4.23: Temperature distribution measurements of contact patch for the P225/60R16 *SRTT* directly on simulation provided by *ATIIM*. The operating conditions were an ice surface temperature of -10°C, inflation pressure of 35 psi, a normal load of 60% load index, and an applied torque of 0 N-m at the wheel center.

Figure 4.24, the results for the Standard Reference Test Tire at a normal load of 100% load index is presented. In this figure, it is evident that the advanced model is becoming more accurate as the normal load increases. In this specific scenario, the highest measured temperature rise was about 1.4°C. The simulation provided a maximum rise in temperature of 1.4°C at the middle of the contact patch. The simulation was equivalent to the results of the measured data. Although the advanced model matched in the middle, the model was not able to simultaneously match the results at the edges of the contact patch.

It should be mentioned that, as shown in Figure 3.20, the two middle thermocouples have been inverted in order to capture the temperature distribution closer to the middle of the contact patch.

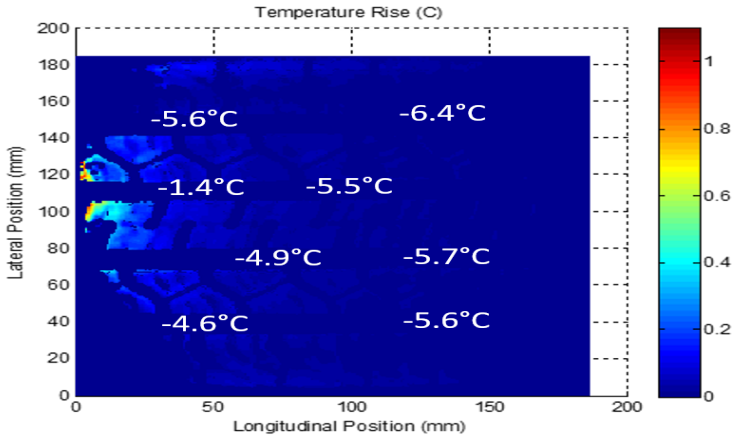

Figure 4.24: Temperature distribution measurements of contact patch for the P225/60R16 *SRTT* directly on simulation provided by *ATIIM*. The operating conditions were an ice surface temperature of -10°C, inflation pressure of 35 psi, a normal load of 100% load index, and an applied torque of 0 N-m at the wheel center.

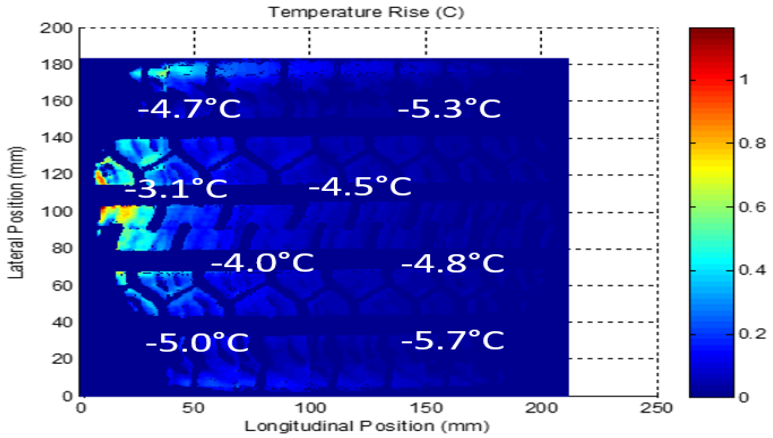

Figure 4.25: Temperature distribution measurements of contact patch for the P225/60R16 *SRTT* directly on simulation provided by *ATIIM*. The operating conditions were an ice surface temperature of -10°C, inflation pressure of 35 psi, a normal load of 120% load index, and an applied torque of 0 N-m at the wheel center.

In Figure 4.25 the advanced model was capable of predicting the temperature rise more accurately at the edges of the contact patch as opposed to results in Figure 4.24. In Figure 4.25, the maximum measured difference in temperature between the leading and trailing edges of the contact patch, was approximately 1.4°C. The simulation though provided

only a maximum rise of temperature of 1°C, which occurred mainly at the center of the trailing edge.

The variation of normal load can be examined to determine how the model behaves, as the normal load is increased. When the measured and predicted results are compared, it can be observed that the model tends to estimate the rise in temperature at the edges of the contact patch more accurately, as the normal load is increased. In Figure 4.24, the model was able to estimate the rise in temperature closer to the middle as opposed to Figure 4.23. When the normal load is further increased to 120% load index, the model is able to predict the rise in temperature rise more accurately, at the edges of the contact patch, when compared to the measured results. This is observed in when it is compared to Figure 4.23 and Figure 4.24.

The validation plots of Figure 4.26, Figure 4.27, and Figure 4.28 all represent the results for predicted traction of the 235/55R19 All-Season Pirelli Tire. The results for the Standard Reference Test Tire are presented in [19]. Figure 4.26 shows the 19" Pirelli Tire at nominal operating conditions which includes a camber angle of 0°, and an inflation pressure of 80% of the maximum value. The normal load is varied from 80% load index in Figure 4.26 up to 120% load index in Figure 4.28.

When the variation of normal load is taken into account, the model is able to more accurately predict the friction results at higher normal loads. In Figure 4.26, the 60% load index is shown. This case has the worse match between the measured and predicted results. As the normal load increases to 100% load index, the model is able to more accurately predict the measured results, as shown in Figure 4.27. Finally, Figure 4.28 represents the comparison between the measured and predicted values, at 120% load index. In this figure, it can be observed that the model most accurately estimated the friction levels under dry winter conditions.

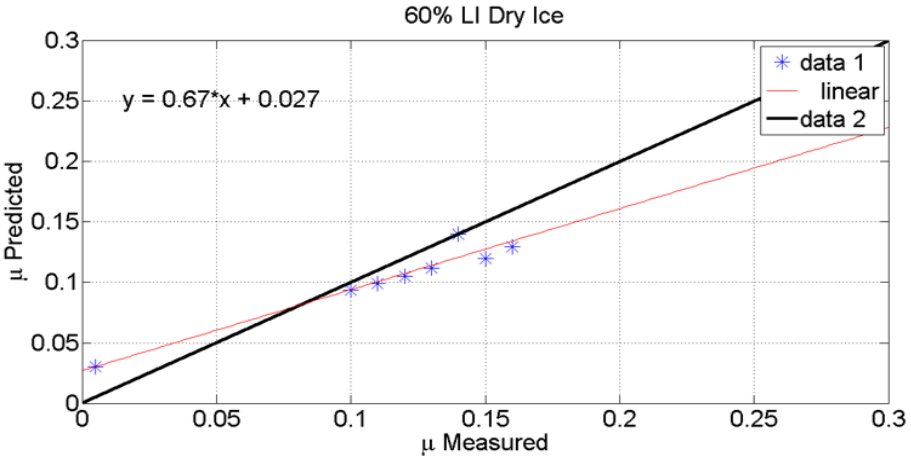

Figure 4.26: Comparison of the measured and friction values predicted by *ATIIM* for a normal load of 60% load index (LI), an inflation pressure of 80% of maximum, camber angle of 0°, and dry friction conditions for the 19" All-Season Pirelli Tire.

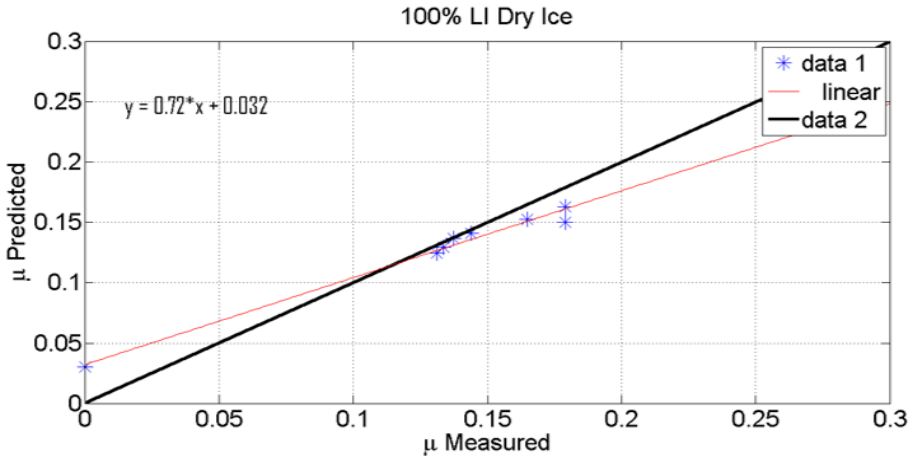

Figure 4.27: Comparison of the measured and predicted friction values simulated by *ATIIM* for a normal load of 100% load index (LI), an inflation pressure of 80% of maximum, camber angle of 0°, and dry friction conditions for the 19" All-Season Pirelli Tire.

Also from the validation figures, it can be observed the range of which the traction levels were measured on an ice surface with a temperature of -10°C. Between Figure 4.26, Figure 4.27, and Figure 4.28 the friction level laid between the range of 0.1 and 0.2. As the normal load is increased to 120% load index, the data became more concentrated around the 0.15 friction level.

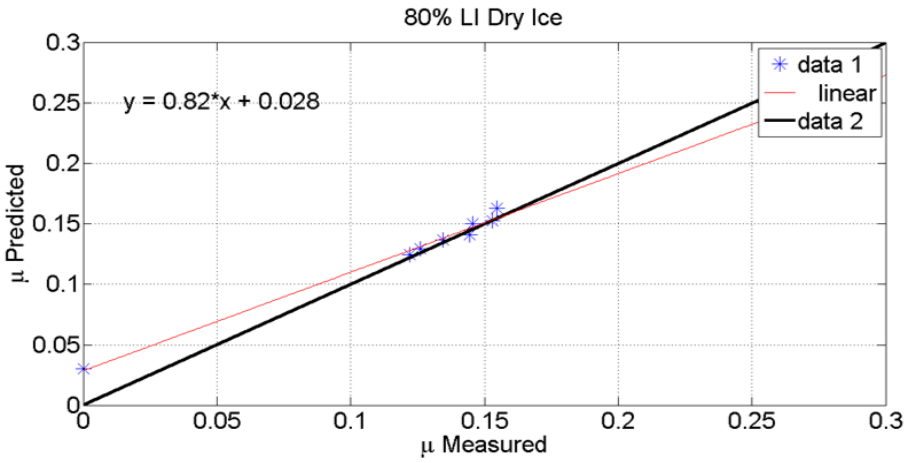

Figure 4.28: Comparison of the measured and friction values predicted by $ATIIM$ for a normal load of 120% load index (LI), an inflation pressure of 80% of maximum, camber angle of 0°, and dry friction conditions for the 19" All-Season Pirelli Tire.

4.4 Discussion of the Advanced Tire-Ice Interface Model

To study the temperature rise of the contact patch under normal operating conditions, an Advanced Tire-Ice Interface Model was developed to identify the rise in temperature at the contact patch as well as to identify areas of dry and wet regions in the contact patch [19]. Once the temperature rise is determined, the dynamic friction coefficient is obtained at the tire-ice interface. Since the original development of TIM several additional modules have been implemented in order to improve and extend its original capabilities.

The numerical solution of the theoretical model allows for a full dynamical analysis of the friction coefficient of rough rubber on ice. This includes the ability to estimate the height of the fluid layer at the contact interface and how the water dictates the viscous friction at the contact patch.

Comparing the simulation results with experimental results, a good qualitative agreement has been shown with respect to the pressure, normal load, and ice temperature dependency of the model. This includes especially the confirmation of the well-known effect that

the friction coefficient of rubber on ice is lower under warm conditions, or when more ice is able to melt into water.

Although the Advanced Tire-Ice Interface Model is capable of predicting the dynamics conditions at the interface, there are still multiple areas of improvements which can implemented in the future. First thing is to provide a more enhanced correlation mode to more accurately compare the effects of pressure distribution on the rise in temperature. This could help the accuracy of the model improve as normal load is varied between 80% and 120% load index. Secondly, if the effects of rubber composition is implemented, the model could be capable of determining the effect of different wheel types (Summer, All-Season, and Winter Tires).

The results presented can be used to further develop upon an existing tire model. This tire model would have an additional parameter, temperature rise, and would help to estimate the traction result in real-time. Eventually, these results could be used as a control implementation to allow SMART programs to control the torques on the wheel under different driving conditions such as ice. Once the Advanced Tire-Ice Interface Model is used as part of a more general tire model, a complete package can be used as an additional module to a more comprehensive vehicle model.

Chapter 5

Implementation of Advanced Tire-Ice Interface Model into Tire Models

Four fundamental factors play a role in developing simple theoretical tire models that can be used to study the tire force and moment generation capability:

- Frictional properties in the tire-road interface
- Distribution of the normal contact pressure
- Compliance of the tread rubber
- Compliance of the belt/carcass

5.1 Dugoff Tire Model

The Dugoff Tire Model is mainly used to characterize handling, but it is also widely used to provide fast and reliable traction results. It is an empirical tire model providing

analytical relations for the longitudinal and lateral forces as functions of the slip angle and slip ratio. The model also accounts for the coupling between lateral and longitudinal forces.

As shown in Figure 5.1, Point P of the tire tread centerline represents the sliding boundary at contact patch due to the shear at the interface. Points on the tread forward of point P adhere to the ground surface without sliding, as this is considered the adhesion region of the contact patch. At point P, the elastic stresses due to tread deformation reach a value corresponding to the tire-road shear stress limit and the rubber begins to slide relative to the ground. This corresponds to the points after point P.

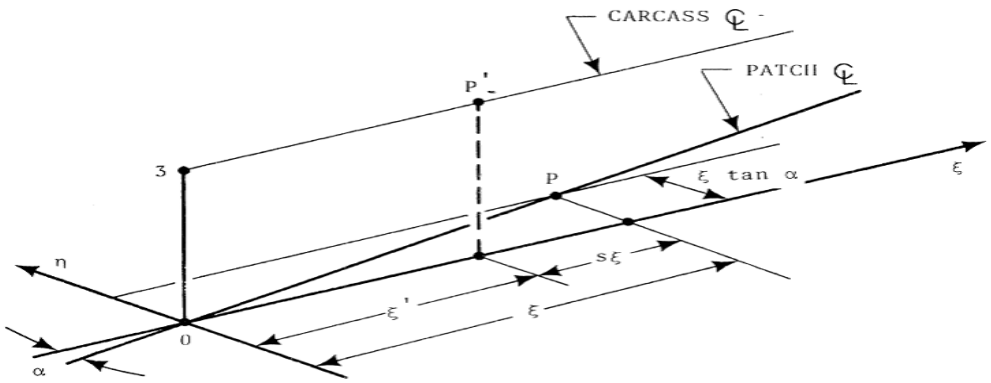

Figure 5.1: Schematic representing the Dugoff tire model. Adapted from [15] under fair use; Fair use determination attached.

If ζ is the longitudinal coordinate of point P, then $\frac{\zeta}{\Delta t}$ is equivalent to the tire's longitudinal velocity [15]. Therefore, the main formula to the model, which represents the longitudinal deformation of point P relative to point P' is given by:

$$\zeta - \zeta^{'} = u_w \Delta t = u_w \Delta t (1 - \frac{R\Omega}{u_w}) = u_w \Delta t s = s\zeta \tag{5.1}$$

The Dugoff tire model has been shown to be valid for pure longitudinal and lateral forces. The advantage of the Dugoff tire model though, is that it introduces a simplified rep-

resentation of tire characteristics [15]. With only a few parameters, the model can be simply fitted to experimental data. Therefore, in order to train the model, only the longitudinal stiffness C_λ and the lateral stiffness C_α should be determined.

If the slip ratio is defined as λ, the longitudinal and lateral force can be respectively written as:

$$F_x = \frac{C_\lambda \lambda f(z)}{1-\lambda} \tag{5.2}$$

$$F_y = \frac{C_\lambda \tan\alpha f(z)}{1-\lambda} \tag{5.3}$$

Where,

$$f(z) = \begin{cases} z(2-z) \ for \ z < 1 \\ 1 \ for \ z >= 1 \end{cases}$$

The variable z accounts for the longitudinal and lateral stiffnesses, as well as the normal load and the peak coefficient of friction. z is given by:

$$z = \frac{\mu F_z (1-\lambda)}{2\sqrt{(C_\lambda \lambda)^2 + (C_\alpha \tan\alpha)^2}} \tag{5.4}$$

5.2 Compatible Dugoff Model with the Advanced Tire-Ice Interface Model

In order to account for the temperature rise at the contact patch, the parameters which make up the Dugoff Tire Model must be trained to include the influence of temperature change. The original Dugoff Tire model is capable of matching the measured results in the linear region as shown in Figure 5.10. In the nonlinear region, the model fails to capture the dynamics. The reason being that with large slip ratio the Dugoff model does not show that the tire friction coefficient μ decreases when the slip ratio is enough large.

In order to account for the nonlinear range, an improvement can be made to the model which captures the tire surface temperature, which appropriately scales the original Dugoff Tire Model. In order capture the peak of the drawbar pull a magnifying factor is used, which accounts for the temperature difference at the contact patch. The longitudinal force is scaled with the factor H as follows:

$$F_x = \frac{C_\lambda \lambda f(z)}{1-\lambda} \cdot H \tag{5.5}$$

$$H = (\Delta T - 0.75\mu_{max}) \cdot S^2 - (\Delta T - 0.75\mu_{max}) \cdot S + 1.27 \tag{5.6}$$

Equation (5.6) comes from a modification of a similar attempt in literature [62]. Here the authors used the scale factor to capture the peak. By modifying the terms, it is shown that the inclusion of temperature can be used to further improve the scaling factor. Using the maximum temperature rise simulated from the Advanced Tire-Ice Interface Model, the Dugoff Tire model can be modified to further improve its accuracy in the nonlinear range.

5.3 Magic Formula

A tire model must be fast, accurate, and reliable. Empirical models such as the Magic Formula are also used to provide quick tire model dependent on experimental data. These types of model though, are limited to the scope of which the experimental data was collected. Therefore, the data must be used sparingly. Regardless, the Magic Formula [63] is well understood and openly used in both the academic and industrial settings. Therefore, the implementation of the Advanced Tire-Ice Interface Model into the Magic Formula will serve as the basis for this study.

Due to the input of a tire model, which is continuously varying, the formula is subjected to two possible representations [63]:

- Formulas containing series. (i.e. Fourier series, polynomials, splines)
- Formulas containing special functions.

Each method has its own advantages and disadvantages. For example, if a series is to be used, a large number of coefficients will be needed to get a close curve fit [5]. Therefore, this will lead to extrapolation for which in most cases, it is difficult to interpolate beyond the fitted range. The Magic Formula, developed by Pacejka [63], has been shown to be able to match real test results. It is capable of characterizing steady state data using tire parameters to account for the formula's coefficients. The Magic Formula for the longitudinal force of a pneumatic tire is shown:

$$F_x = D_x \sin C_x \arctan[B_x\kappa_x - E_x[B_x\kappa_x - \arctan(B_x\kappa_x)]] + S_{vx} \tag{5.7}$$

5.3.1 Compatible Magic Formula with the Advanced Tire-Ice Interface Model

In order to account for the temperature rise at the contact patch, the parameters which make up the Magic Formula must be trained to include the influence of temperature change. In order to do this, it is required to make two assumptions [64] regarding the influence of tire surface temperature on the force, namely:

1. The force changes in proportion to the tire surface temperature.
2. The coefficient of dependency of the tire surface temperature on the maximum force has a differential proportional value from that of the stiffness.

Considering the two points, the magic formula can be rewritten to include the influence of tire surface temperature as:

$$F_x(\kappa, T) = D_x(T) \sin C_x \arctan[B_x(T)\kappa_x - E_x[B_x(T)\kappa_x - \arctan(B_x(T)\kappa_x)]] + S_{vx} \quad (5.8)$$

Where,

$$D_x(T) = D_{x0} \cdot \{1 + \frac{\partial \mu}{\partial T}(T - T_m)\} \quad (5.9)$$

$$K_x(T) = K_{x0} \cdot \{1 + \frac{\partial C_p}{\partial T}(T - T_m)\} \quad (5.10)$$

$$B_x(T) = \frac{K_x(T)}{C_x \cdot D_x(T)} \tag{5.11}$$

In Equation (5.9), $D_x(T)$ is the peak value of tire force including the influence of the tire surface temperature and D_{x0} is the peak steady state value. In Equation (5.10), $K_x(T)$ represents the respective stiffness dependent on the force. This value will include the influence of the tire surface temperature. It is almost equivalent to $\frac{\partial F_x(\kappa,T)}{\partial \kappa}$ at $\kappa = 0$. K_{x0} is the maximum stiffness at steady state. T_m is the average tire surface temperature used for the steady state conditions. In Equation (5.9), $\frac{\partial \mu}{\partial T}$ is the change of tire force with temperature. In Equation (5.10), $\frac{\partial C_p}{\partial T}$ is the change in stiffness with respect to the tire surface temperature. The last two parameters identified are to be determined experimentally.

When the influence of tire surface temperature is included in the Magic Formula, overall peak longitudinal force is decreased as the temperature difference is increased, as shown in Figure 5.2. For this simulation, the ice surface temperature has been set to $-3°$C. This observation of a decrease in longitudinal force with an increase in temperature is appropriate. Eventually, the temperature rise will lead to the ice surface melting and will greatly impact the longitudinal force. Also, as the temperature difference increases, the maximum drawbar pull occurs at a lower slip ratio value which was also found to be true for the experiments presented in Chapter 3.

The lateral force can also be calculated using the effects of tire surface temperature using the same procedure. In Figure 5.3, it can be observed that the effects of including tire surface temperature are not as significant as in the case for the longitudinal force. For the lateral force, it is evident that the force hardly changed. As the temperature rise increased, the lateral force slightly decreased. The main observation of the figure though is found at the low slip angles. In this range, the stiffness is greatly affected by the inclusion of the

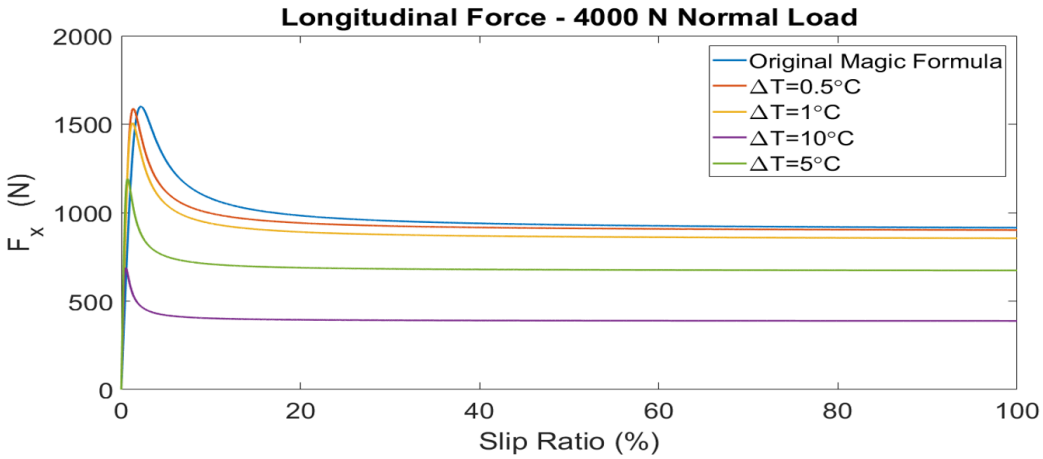

Figure 5.2: Magic Formula with the inclusion of tire surface temperature. Peak longitudinal force decrease with an increase in temperature change. Inflation pressure is 35 psi. Normal load is 4 kN.

tire surface temperature. It is shown that the lateral stiffness increases with an increase in temperature change.

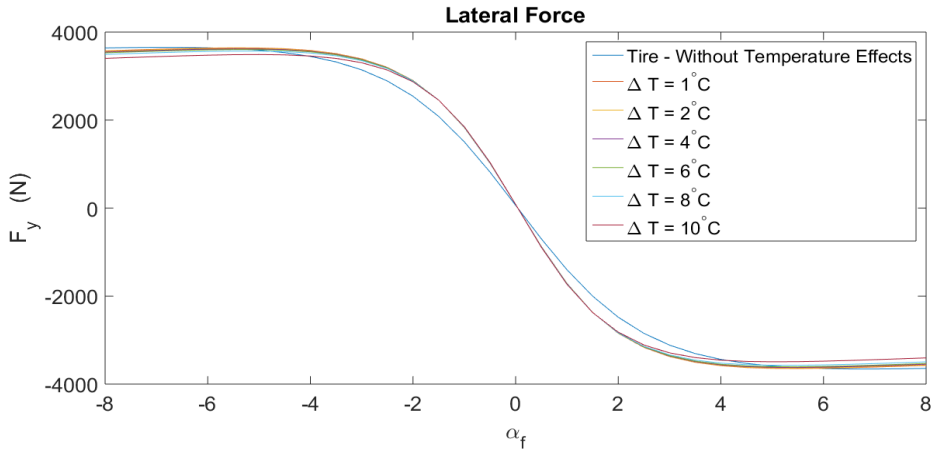

Figure 5.3: Magic Formula with the inclusion of tire surface temperature. Lateral stiffness increases with an increase in temperature change. Inflation pressure is 35 psi. Normal load is 4 kN.

5.3.2 Revisions of the Modified Magic Formula for the Advanced Tire-Ice Interface Model

When the influence of tire surface temperature is included in the Magic Formula, the overall peak longitudinal force is decreased as the temperature difference is increased, as shown in Figure 5.4. For this simulation, the ice surface temperature has been set to -3°C. This observation of a decrease in longitudinal force with an increase in temperature is appropriate. Eventually, the temperature rise will lead to the ice surface melting and will significantly impact the longitudinal force.

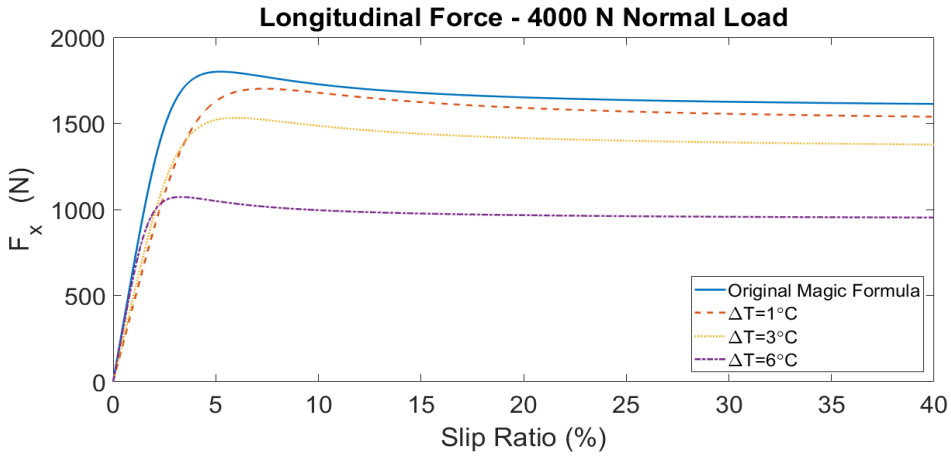

Figure 5.4: Predicted longitudinal force with the inclusion of tire surface temperature. As the temperature rise increases, the longitudinal force decreases.

In the literature [64] there is a limitation that does not account for the effects due to the viscous friction at the contact interface. Therefore, previous formulations accounted for the dry and wet conditions independently. Fitting longitudinal force measurements at different ice surface temperature led to the development of a shift factor, as shown in Figure 5.5.

The shift factor will place emphasis on specific terms depending on the amount of water in the contact patch, as seen in Equation (5.12) and Equation (5.13).

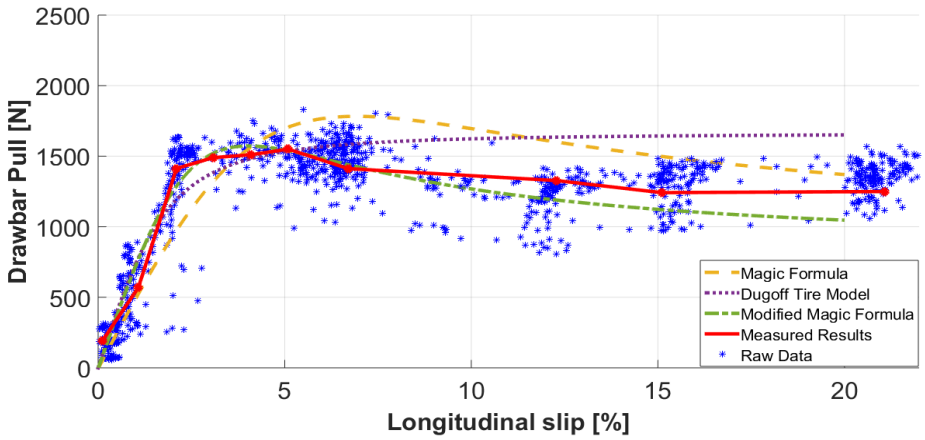

Figure 5.5: Raw data measured with the Kistler System on the Terramechanics Rig. Simulation results from the Dugoff Tire Model [15], the Magic Formula (Pacejka Tire Model), and the Modified Magic Formula (Modified Pacejka Tire Model) are shown for comparison. The load index was at 100% Load Index and the inflation pressure of the P225/60R16 SRTT was at 241 kPa. The ice surface temperature was -3°C.

$$D_x(T) = D_{x0} \cdot \{1 + \frac{\partial \mu}{\partial T} \cdot k_{shift}(T - T_m)\} \tag{5.12}$$

$$K_x(T) = K_{x0} \cdot \{1 + \frac{\partial C_p}{\partial T} \cdot k_{shift}(T - T_m)\} \tag{5.13}$$

The shift factor, as shown in Equation (5.14), Equation (5.15), and Equation (5.16), will vary how the friction and stiffness of the tire changes as the temperature difference between the tire surface and the ice varies. The shift factor also allows for the peak drawbar pull to occur at a lower slip ratio value as one should expect to occur on an ice surface. This factor is an experimental formulation that must be determined for the different tires under investigation. Equation (5.14) represents the results for the Standard Reference Test Tire (SRTT).

$$k^1_{shift} = \frac{25}{3}\Delta T^2 + \frac{5}{3} \tag{5.14}$$

$$k^2_{shift} = \frac{7}{3}\Delta T^2 + \frac{1}{3} \tag{5.15}$$

$$k^3_{shift} = \frac{64}{5}\Delta T^2 + \frac{1}{8} \tag{5.16}$$

Equation (5.15) represents the measured results for the 19" All-Season Pirelli Tire. Equation (5.16) represents the results for the 16" Directional Tire, as shown in Figure 3.41. In order to generalize the shift factor to account for all of the tires tested, the average of the equations obtained experimentally can be used. This will allow for an average shift factor to be calculated which can be used for all of the tires and conditions tested. The average shift factor used in Equation (5.12) and Equation (5.13) is determined to be:

$$k^3_{shift} = \frac{352}{45}\Delta T^2 + \frac{17}{24} \tag{5.17}$$

Figure 5.5 represents the longitudinal force at one ice surface temperature. Using the temperature rise estimated from the Advanced Tire-Ice Interface Model, the maximum temperature difference can be used to simulate the longitudinal force using the generalized shift factor, shown in Equation (5.17). Figure 5.5 represents the original and modified Magic Formula used in this investigation along with experimental results. Figure 5.5 shows that using the Modified Magic Formula leads to a longitudinal force estimation much closer to that of the averaged measured results. The simulation using the Dugoff Tire Model provided better results compared to the original Magic Formula in the low slip ratio region. The Dugoff

Tire Model was able to match the experimental results in the linear region, but the Modified Magic Formula continued to approach the measured results even in the nonlinear range.

The estimation of the longitudinal force obtained based on the Advanced Tire-Ice Interface Model (ATIIM) can be applied to a real-time simulation. A full vehicle model could be coupled with a real-time tire model augmented with ATIIM for real-time simulations. Furthermore, driving simulations with interactive human-in-the-loop systems for trucks and passenger cars will also be possible using the implementation of ATIIM into a real-time simulation model.

5.3.3 Estimation of Drawbar Pull

With the viscous friction determined, it is now possible to estimate the drawbar pull with the Modified Pacejka Tire Model (Modified Magic Formula). As shown in Figure 5.6, the ATIIM was able to capture the measured drawbar pull of the SRTT. Two inflation pressures, namely 193 kPa and 241 kPa were used for this comparison. The temperature rise was recorded to be larger at lower inflation pressure. The measured peak temperature difference, shown in the legend, was used as a direct input into ATIIM. The normal load for this specific case was 4 kN. As shown, the Modified Magic Formula was able to predict the measured results with minimum differences. However, unlike the Modified Magic Formula, the original Magic Formula overestimated the measured results in most cases. Only in the near-zero slip ratio range did the original Magic Formula match the measured results.

When the normal load on the tire is increased to 100% LI, the model was not as accurate as it was for the lower normal loads, as shown in Figure 5.7. The Modified Magic Formula predicted the drawbar pull to be slightly higher than the measured results. This can be explained by the complex phenomenon which occurs when the contact patch has

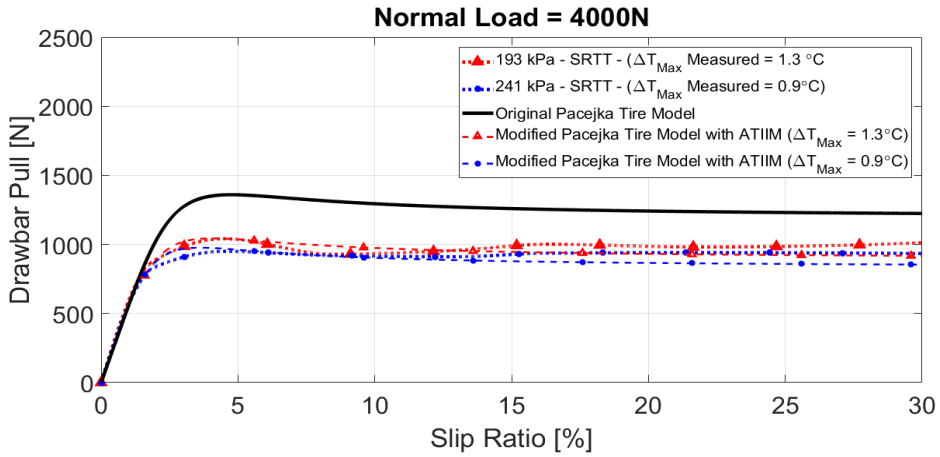

Figure 5.6: Comparison between measured and predicted results using the ATIIM. The ice surface temperature was set to -10°C.

a combination of wet and dry regions. Even with the Modified Magic Formula predicting a higher drawbar pull, the estimation is still within an acceptable range. The maximum difference between the predicted and measured value, shown in Figure 5.7, occurred at 15% slip ratio. At this point, the contact patch is completely sliding as there is no more traction generation due to the lack of an adhesion regions [15]. At 15%, the difference between the predicted and the measured results was <10%, while the original Magic Formula was approximately 30% higher than the measured results.

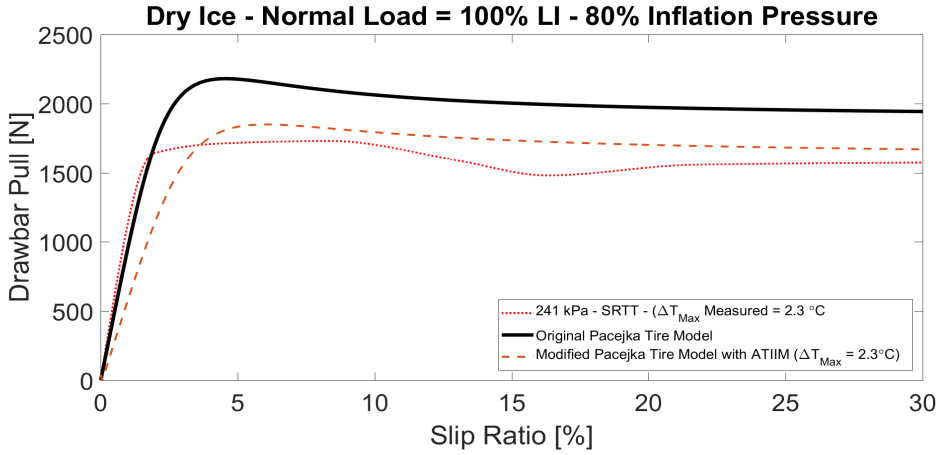

Figure 5.7: Comparison between measured and predicted results using the ATIIM. The ice surface temperature was set to -10°C.

When the ice surface temperature was increased to -3°C from -10°C, the predicted and the measured results decreased significantly even though the normal load is the same, as shown in Figure 5.8. The decrease in tractive performance is due to the water film formed at the contact patch. This occurs as the ice surface temperature gets closer to that of the melting point. Figure 5.8 shows that the Modified Magic Formula was able to predict the drawbar pull at the increased inflation pressure with more accuracy compared with the lower inflation pressure. As the inflation pressure is reduced, the area increases. Since the area is proportional to the heat generated at the contact patch, the increased area may result in more water at the contact interface. This would provide an explanation for the decrease in model performance at the lower inflation pressure of Figure 5.8. However, in both cases studied, the model overestimated the drawbar pull. Also, the location of the peak drawbar pull occurred at a different slip ratio for the two predicted simulations compared to that of the original formula. It has been shown that, as the temperature rise increases, the peak drawbar pull occurs at a lower slip ratio. This is due to the tires contact patch transitioning from an adhesion region to a full sliding region [15]. As the temperature rise increases, more water is present in the contact patch and the tires contact patch transitions to a region that is completely sliding much sooner.

5.4 Comparison of Models

Using the temperature rise estimated from the Advanced Tire-Ice Interface Model, the maximum temperature difference can be used to simulate the longitudinal force. Figure 5.9 represents the original and compatible Magic Formula (Modified Pacejka Tire Model with ATIIM) used in this investigation along with experimental results. Figure 5.9 shows that using the Modified Magic Formula (Modified Pacejka Tire Model with ATIIM) leads to a

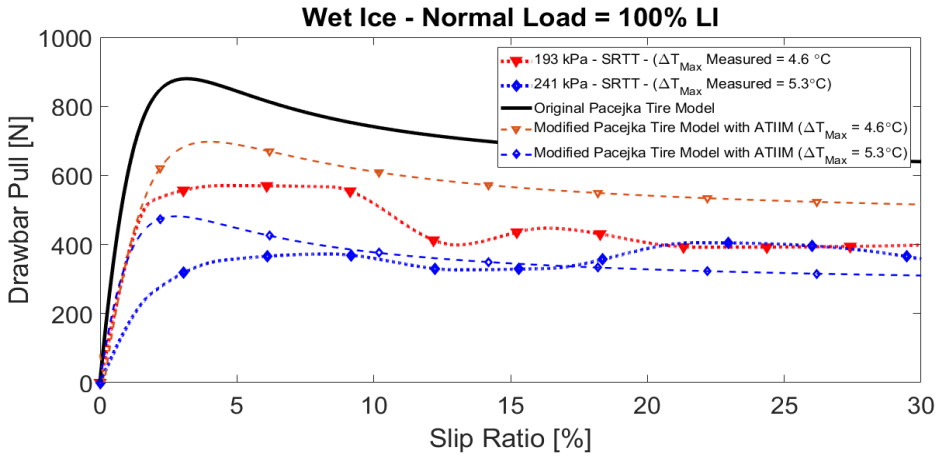

Figure 5.8: Comparison between measured and predicted results using the ATIIM. The ice surface temperature was set to -3°C.

longitudinal force estimation much closer to that of the averaged measured results.

The simulation using the Dugoff Tire Model provided better results compared to the original Magic Formula, in regards to the measured results when Figure 5.9 and Figure 5.10 are compared. The Dugoff Tire Model was able to match the experimental results in the linear region, but the Modified Magic Formula (Modified Pacejka Tire Model with ATIIM) continued to approach the measured results even in the nonlinear range. In Figure 5.10, it is evident that the longitudinal tire forces calculated from the original Dugoff model are consistently higher than the values calculated by the original Magic Formula (Pacejka Tire Model) model when the drawbar pull is in the linear region.

As shown in Figure 5.9, it is evident that the Modified Magic Formula (Modified Pacejka Tire Model with ATIIM) is simulating the lower end of the measured raw data. The original Magic Formula overestimated the raw data throughout the whole slip ratio range. In Figure 5.10 the Dugoff Tire Model is closest to the raw data in the linear range and into the transition point to the nonlinear region. Only the modified Dugoff Tire Model (Modified Dugoff Tire Model with ATIIM) was capable of simulating the nonlinear dynamics as shown

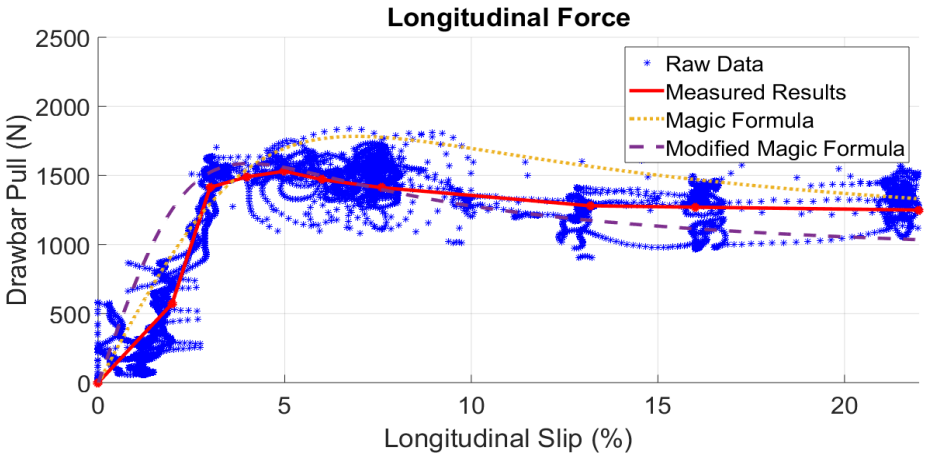

Figure 5.9: Comparison of Tire models for a P225/60R16 Tire at 35 psi and a normal load of 4 kN without the inclusion of the raw data.

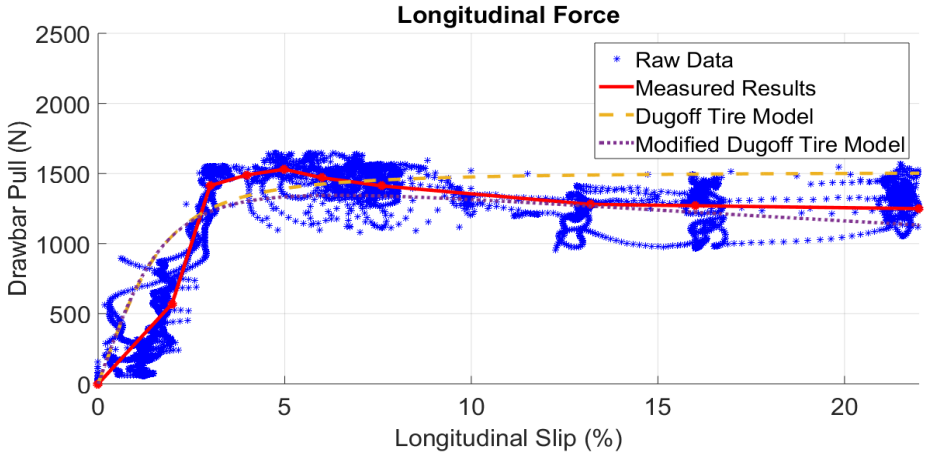

Figure 5.10: Comparison of Tire models for a P225/60R16 Tire at 35 psi and a normal load of 4 kN without the inclusion of the raw data.

in Figure 5.10.

Comparing the tire models leads to the conclusion that including the temperature dependency can be used to further improve tire models. From the models investigated, the Modified Magic Formula provides the closest representation to that of the measured results. The Dugoff Tire Model struggled to capture the response in the nonlinear range which is of critical importance in wintry conditions. This model though was capable of representing

the linear range of the longitudinal force. When modified, the model was also capable of capturing the nonlinear dynamics of the tire.

5.5 Further Validation

Once the pressure distribution and the temperature rise has been recorded and simulated, as per Chapter 3 the measured and predicted peak temperature rise can be compared at low slip ratios. The peak temperature rise is considered to be the largest difference between the leading edge and the trailing edge of the contact patch. A linear regression has been used to compare the measured and predicted temperatures, as shown in Figure 5.11. At low normal loads, the Advanced Tire-Ice Interface Model has been shown to predict temperature rise with the highest correlation value to a 1:1 regression.

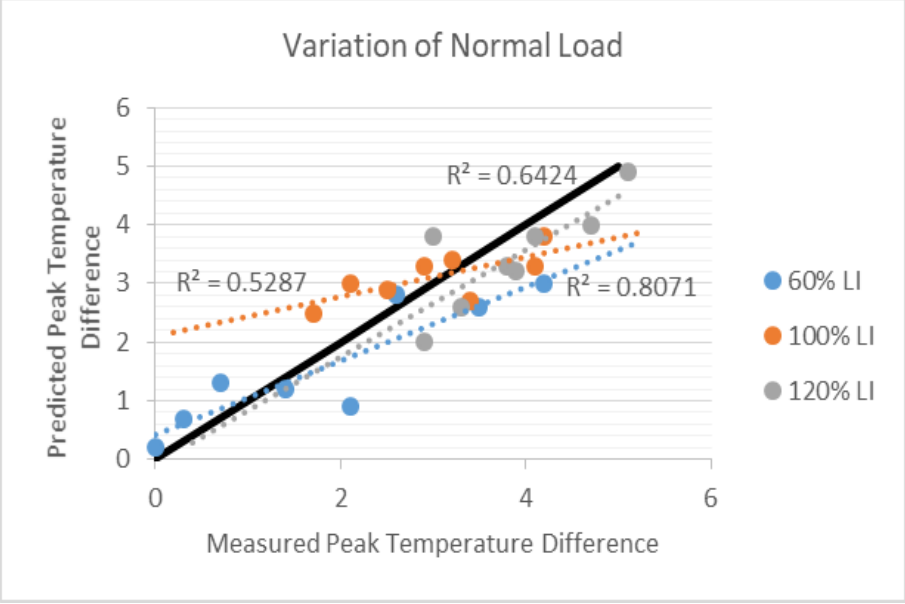

Figure 5.11: Validation of the peak temperature difference between leading edge and trailing edge. The normal load was allowed to vary as shown for the SRTT. The inflation pressure was 80% of the rated maximum and the ice surface temperature was -10°C.

Figure 5.11 also represents how the Advanced Tire-Ice Interface Model performs in relation to the wet/dry regions due to the temperature of the contact patch and the ice. At a low load index, it was observed that the contact region was mainly dry. With lower friction levels, the temperature rise is not as significant. Therefore, water is not expected to be formed in the contact patch. However, when the normal load is at the highest level recorded, water can be expected on the contact patch due to the increase in friction. At 100% of the load index, some type of combination between wet and dry will exist in the contact patch. As shown in Figure 5.11, the ATIIM showed difficulties in capturing the complex combination of the two.

Figure 5.12 represents the validation of the measured and predicted drawbar pull. The correlation between the predicted and the measured friction coefficient values for the low slip ratio range (0 - 10%), and for different normal loads is shown.

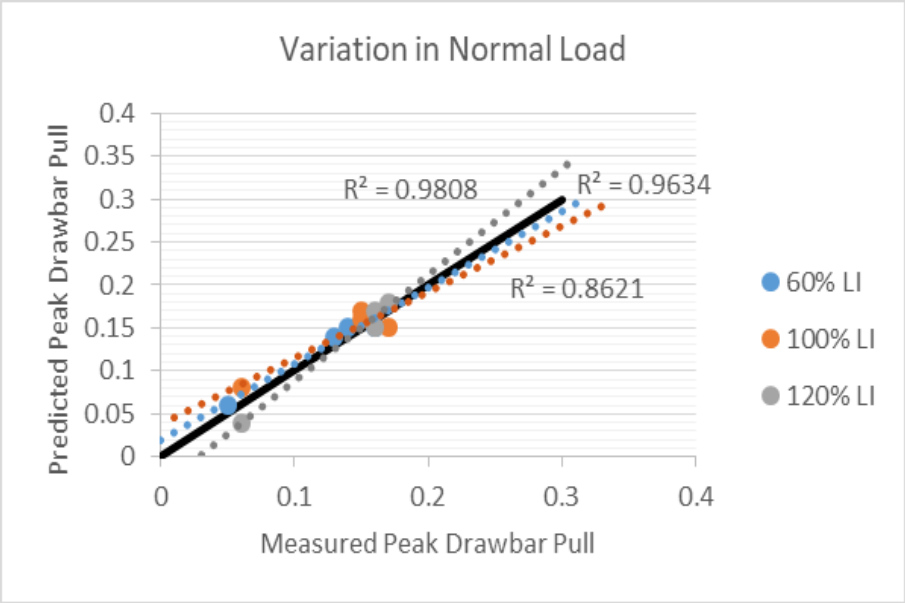

Figure 5.12: Validation of the peak drawbar pull. The normal load was allowed to vary as shown for the SRTT. The inflation pressure was 80% of the rated maximum and the ice surface temperature was -10°C.

The peak drawbar pull is considered to be the highest value of the tractive force on

the tire, as shown in Figure 5.6, Figure 5.7, and Figure 5.8. The specific values of Figure 5.12 have been normalized against the normal load. Both of the extremes of the normal loads used for testing, recorded high correlations. Again, as the complex nature of both the wet and dry conditions occur, the correlation dropped at 100% LI. However, the determinant coefficient R^2 is in the range of 0.8-0.98, indicating an acceptable scatter around the 1:1 line.

5.5.1 Validation of k_{shift}

As the temperature of the ice surface gets closer to the melting point, the longitudinal force drastically decreases due to the formation of a thin water film at the contact interface. The height of the fluid layer will be relative to the temperature difference between the contact patch and the ice surface. Therefore, the characterization of the contact patch should take into account a combination of a wet and dry region. As the majority of the contact patch becomes wet, the viscous friction becomes the dominant means of traction generation. By including a factor, namely k_{shift}, a nonlinearity is set in the modification of the Magic Formula to place emphasis on the respective terms due to the effect of having a combination of a dry and wet contact patch.

Figure 5.13 represents the measured difference of the longitudinal force based on the variation of the temperature for the Standard Reference Test Tire. For this investigation, a sweep of both the ice surface temperature and the tire temperature allows for the determination of how the drawbar pull changes with respect to the temperatures of the ice and tire. In Figure 5.13 it is shown that, as the relative difference between the contact patch and the ice surface temperature becomes larger, the change in the longitudinal force increases. This is to be expected due to the formation of a thin water film and its effect on the drawbar pull.

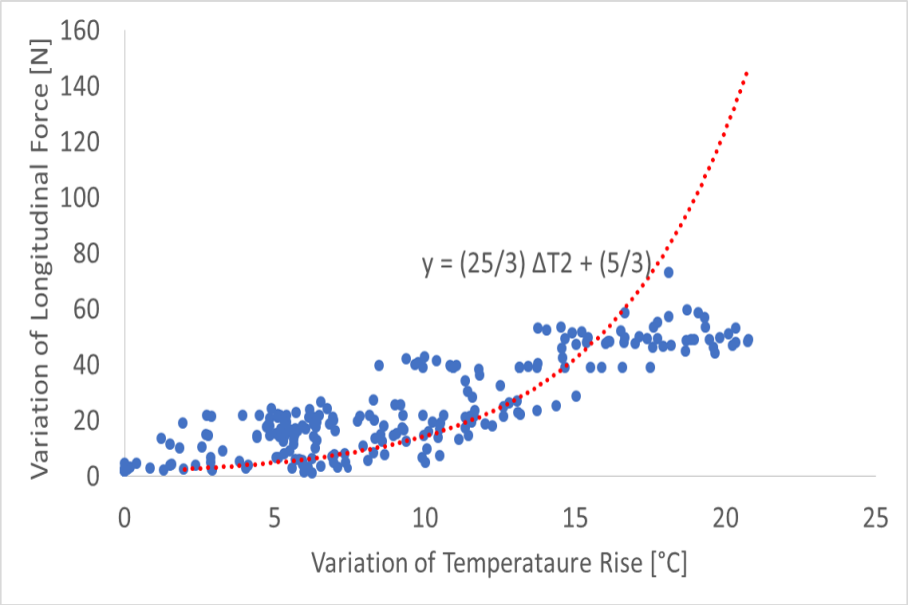

Figure 5.13: Experimental validation of k_{shift} for the Standard Reference Test Tire. Represents the variation of the temperature rise relative to the ice surface temperature and its effect on the tractive performance of the SRTT on ice.

Figure 5.14 represents the measured difference of the longitudinal force based on the variation of the temperature for the 19" All-Season Pirelli tire, as shown in Figure 3.41. Notice again, as referenced in 3, there is a smaller variation in the drawbar pull with respect to the rise in temperature. This can be attributed to the tread pattern design. The 19" All-Season Pirelli Tire has deep grooves along the middle which helps to filter water away from the contact patch once the temperature rise becomes large enough to promote melting.

A further improvement to the shift factor may be found using a probabilistic distribution rather than a quadratic correlation. The reason a quadratic correlation was used to represent the shift factor as opposed to a linear relationship is because the effect of the viscous friction becomes substantially significant as the temperature rise increases to the melting point. By using the quadratic relationship, an emphasis is placed on the dominant effect of the viscous friction compared to the dry friction.

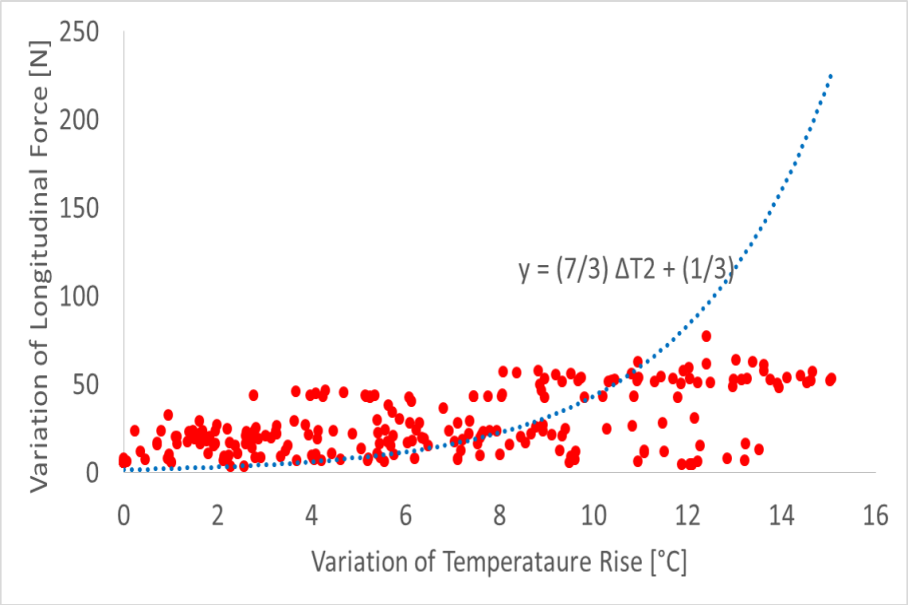

Figure 5.14: Experimental validation of k_{shift} for the 19" All-Season Pirelli Tire. Represents the variation of the temperature rise relative to the ice surface temperature and its effect on the tractive performance on ice.

5.6 Discussion

A tire model must be fast, accurate, and reliable. Empirical models such as the Magic Formula are used to provide quick tire model dependent on experimental data. These types of model though are limited to the scope of which the experimental data was collected, and the data must be used sparingly. Four fundamental factors play a role in developing simple theoretical tire models that can be used to study the tire force and moment generation capability. Models such as the Magic Formula and the Dugoff Tire Model use frictional properties in the tire-terrain interface and the compliance of the tread rubber, belt, and carcass to properly characterize the tractive performance of a pneumatic tire.

In this chapter, the Magic Formula was modified to include the effects of which temperature rise had on the longitudinal and lateral forces of a tire on smooth ice. This was done by altering the parameters which the Magic Formula uses. The Dugoff Tire Model was

then used to compare the measured and simulated results. Although the Dugoff Tire Model failed to capture the nonlinear dynamics of the tire, the model was capable of matching the measured results in the linear range. Regardless, the Dugoff Tire Model did perform better than the original Magic Formula in all aspects. This shows that by including the influence of tire surface temperature, the tire models can be improved upon.

Chapter 6

Vehicle Models

6.1 Implementation of ATIIM into Bicycle Model

By using the predicted temperature rise from the Advanced Tire-Ice Interface Model (ATIIM), it is possible to determine the longitudinal force using a Modified Pacejka Tire Model, which includes the contact temperature. As shown in Figure 6.1, there are main differences between the models which should be noticed. First, as the temperature is included for a tire traversing over ice, the longitudinal force is reduced when compared to the original Pacejka Tire Model. This is to be expected as the coefficient of friction of the ice surface is 0.15. An additional characteristics of the Modified Pacejka Tire Model is the change of the location of the maximum drawbar pull simulated. On ice, the maximum drawbar pull occurs at a much lower slip than other terrains, which signifies that there is less friction available from the terrain. This is also shown in Figure 6.1. Compared to the original Pacejka Tire Model, Figure 6.1 shows that the peak drawbar pull from the Modified Pacejka Tire Model occurs at a slip ratio 50% lower than the original Model.

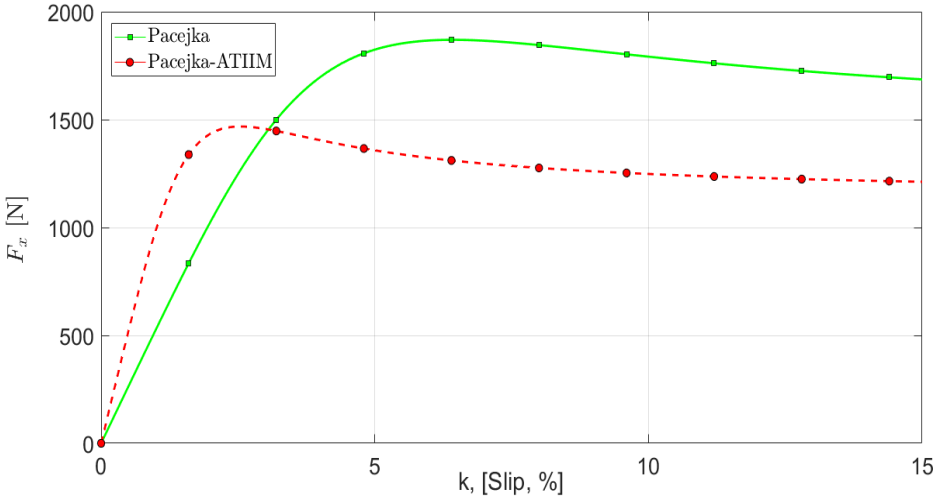

Figure 6.1: Comparison between Pacejka Tire Model and the Modified Pacejka Tire Model which includes ATIIM.

Now that the longitudinal force can be predicted with the inclusion of the tire temperature, a vehicle model [42] can be developed in order to further study the implementation of the Advanced Tire-Ice Interface Model.

6.1.1 Development of Bicycle Model

The physical vehicle model is represented in Figure 6.2. The base O $\mathbf{\{ijk\}}$ is used as the reference point for the inertial frame. The base T $\mathbf{\{t}_x\mathbf{, t}_y\mathbf{, t}_z\mathbf{\}}$ is attached to the vehicle. The base F $\mathbf{\{e}_x\mathbf{, e}_y\mathbf{, e}_z\mathbf{\}}$ is part of the front axle. The point T identifies the center of mass of the vehicle. F and R locate the front and rear of the vehicle respectively. It is also the point where the wheels are attached. The distance a separates the points F and T and the distance b separates the points T and R.

The generalized coordinates of the system are:

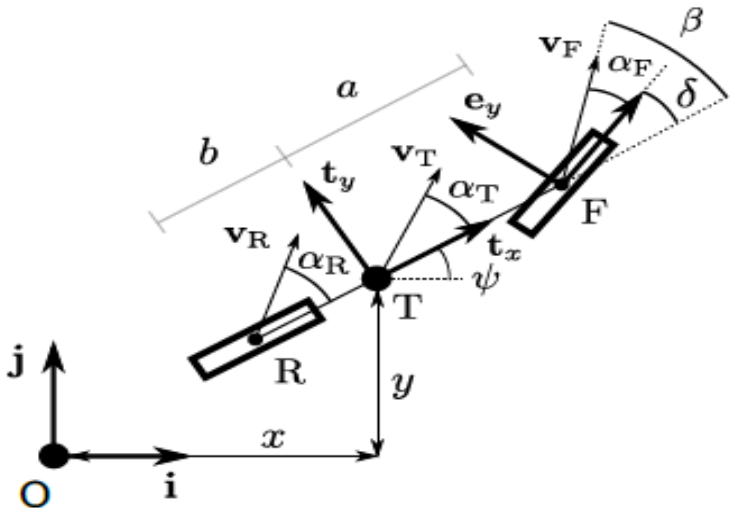

Figure 6.2: Physical Model of Bicycle Model.

$$q_1 = x \tag{6.1}$$

$$q_2 = y \tag{6.2}$$

$$q_3 = \psi \tag{6.3}$$

Where x and y are the longitudinal coordinates of the center of mass in the horizontal and vertical directions. ϕ is the absolute steering angle (yaw rate) of the vehicle. The position vector of the center of mass in relation to the point O is:

$$\mathbf{r_O^T} = x\mathbf{i} + y\mathbf{j} \tag{6.4}$$

Taking the derivative of the position vector with the respect to time leads to the velocity vector as:

$$\mathbf{r_O^T} = \dot{x}\mathbf{i} + \dot{y}\mathbf{j} \tag{6.5}$$

Using the LaGrange method for the formulation of the bicycle model, the kinetic energy of the model can be determined by:

$$T = \frac{1}{2} m_T \mathbf{v_O^T} \cdot \mathbf{v_O^T} + \frac{1}{2} I_T \psi^2 \tag{6.6}$$

The velocity of the front axle is given by:

$$\mathbf{v_O^F} = \mathbf{v_O^T} + \mathbf{r} \wedge \mathbf{r_T^F} \tag{6.7}$$

Where $\mathbf{r_T^F}$ is the position vector of point F in relation to point T. Therefore,

$$\mathbf{v_O^F} = (\dot{x} - a\dot{\psi}\sin\psi)\mathbf{i} + (\dot{y} + a\dot{\psi}\cos\psi)\mathbf{j} \tag{6.8}$$

The speed on the rear axle is:

$$\mathbf{v_O^R} = \mathbf{v_O^T} + \mathbf{r} \wedge \mathbf{r_T^R} \tag{6.9}$$

Where $\mathbf{r_T^R}$ is the position vector of point R in relation to point T. Continuing,

$$\mathbf{v_O^R} = (\dot{x} + b\dot{\psi}\sin\psi)\mathbf{i} + (\dot{y} - b\dot{\psi}\cos\psi)\mathbf{j} \tag{6.10}$$

Using Equation (6.8) and Equation (6.10), the slip angles of the front and rear respectively can be written as:

$$\alpha_f = \arctan \frac{(\dot{y} + a\dot{\psi}\cos\psi)}{(\dot{x} - a\dot{\psi}\sin\psi)} - (\delta + \psi) \tag{6.11}$$

$$\alpha_r = \arctan \frac{(\dot{y} - b\dot{\psi}\cos\psi)}{(\dot{x} + b\dot{\psi}\sin\psi)} - \psi \tag{6.12}$$

The force at the front axle is given as:

$$\mathbf{F_F} = F_{x,F}\mathbf{e_x} + F_{y,F}\mathbf{e_y} \tag{6.13}$$

Which can be rewritten as:

$$\mathbf{F_F} = [F_{x,F}\cos(\delta + \psi) - F_{y,F}\sin(\delta + \psi)]\mathbf{i} + [F_{x,F}\sin(\delta + \psi) + F_{y,F}\cos(\delta + \psi)]\mathbf{j} \tag{6.14}$$

The force at the rear axle is given as:

$$\mathbf{F_R} = F_{x,R}\mathbf{t_x} + F_{y,F}\mathbf{t_y} \tag{6.15}$$

Which again can be rewritten as:

$$\mathbf{F_R} = [F_{x,R}\cos(\psi) - F_{y,R}\sin(\psi)]\mathbf{i} + [F_{x,R}\sin(\psi) + F_{y,R}\sin(\psi)]\mathbf{j} \tag{6.16}$$

Summing all of the generalized forces:

$$Q_k = \sum_{j=1}^{p} \mathbf{F_j} \cdot \frac{\partial \mathbf{p_j}}{\partial q_k} \tag{6.17}$$

Which can be rewritten as for each coordinate:

$$Q_1 = \mathbf{F_F} \cdot \frac{\partial \mathbf{P_O^F}}{\partial q_1} + \mathbf{F_R} \cdot \frac{\partial \mathbf{P_O^R}}{\partial q_1} \tag{6.18}$$

$$Q_2 = \mathbf{F_F} \cdot \frac{\partial \mathbf{P_O^F}}{\partial q_2} + \mathbf{F_R} \cdot \frac{\partial \mathbf{P_O^R}}{\partial q_2} \tag{6.19}$$

$$Q_3 = \mathbf{F_F} \cdot \frac{\partial \mathbf{P_O^F}}{\partial q_3} + \mathbf{F_R} \cdot \frac{\partial \mathbf{P_O^R}}{\partial q_3} \tag{6.20}$$

Where:

$$\frac{\partial \mathbf{P_O^F}}{\partial q_1} = \frac{\partial \mathbf{P_O^F}}{\partial x} = \mathbf{i} \tag{6.21}$$

$$\frac{\partial \mathbf{P_O^F}}{\partial q_2} = \frac{\partial \mathbf{P_O^F}}{\partial y} = \mathbf{j} \tag{6.22}$$

$$\frac{\partial \mathbf{P_O^F}}{\partial q_3} = \frac{\partial \mathbf{P_O^F}}{\partial \psi} = -a \sin\psi \mathbf{i} + a \cos\psi \mathbf{j} \tag{6.23}$$

And,

$$\frac{\partial \mathbf{P_O^R}}{\partial q_1} = \frac{\partial \mathbf{P_O^R}}{\partial x} = \mathbf{i} \tag{6.24}$$

$$\frac{\partial \mathbf{P_O^R}}{\partial q_2} = \frac{\partial \mathbf{P_O^R}}{\partial y} = \mathbf{j} \tag{6.25}$$

$$\frac{\partial \mathbf{P_O^R}}{\partial q_3} = \frac{\partial \mathbf{P_O^R}}{\partial \psi} = b \sin\psi \mathbf{i} - b \cos\psi \mathbf{j} \tag{6.26}$$

Substituting Equation (6.14), Equation (6.16), Equation (6.21), Equation (6.22), Equation (6.23), Equation (6.24), Equation (6.25), Equation (6.26) into Equation (6.18), Equation (6.19), and into Equation (6.20):

$$Q_1 = F_{x,F}\cos(\psi+\delta) + F_{x,R}\cos(\psi) - F_{y,F}\sin(\psi+\delta) - F_{y,R}\sin(\psi) \tag{6.27}$$

$$Q_2 = F_{x,F}\sin(\psi+\delta) + F_{x,R}\sin(\psi) + F_{y,F}\cos(\psi+\delta) + F_{y,R}\cos(\psi) \tag{6.28}$$

$$Q_3 = F_{x,F}a\sin(\delta) + F_{y,F}a\cos(\delta) - F_{y,R}b \tag{6.29}$$

Following Lagrangian's Formulation as:

$$\frac{d}{dt}\left(\frac{\partial T}{\partial \dot{q}_k}\right) - \frac{\partial T}{\partial q_k} = Q_k \tag{6.30}$$

For the three generalized coordinates of the system:

$$\frac{\partial T}{\partial q_1} = \frac{\partial T}{\partial x} = 0 \tag{6.31}$$

$$\frac{\partial T}{\partial q_2} = \frac{\partial T}{\partial y} = 0 \tag{6.32}$$

$$\frac{\partial T}{\partial q_3} = \frac{\partial T}{\partial \psi} = 0 \tag{6.33}$$

$$\frac{\partial T}{\partial \dot{q}_1} = \frac{\partial T}{\partial \dot{x}} = m_T\dot{x} \tag{6.34}$$

$$\frac{\partial T}{\partial \dot{q}_2} = \frac{\partial T}{\partial \dot{y}} = m_T\dot{y} \tag{6.35}$$

$$\frac{\partial T}{\partial \dot{q}_3} = \frac{\partial T}{\partial \dot{\psi}} = m_T \dot{\psi} \tag{6.36}$$

$$\frac{d}{dt}(\frac{\partial T}{\partial \dot{q}_1}) = \frac{d}{dt}(\frac{\partial T}{\partial \dot{x}}) = m_T \ddot{x} \tag{6.37}$$

$$\frac{d}{dt}(\frac{\partial T}{\partial \dot{q}_2}) = \frac{d}{dt}(\frac{\partial T}{\partial \dot{y}}) = m_T \ddot{y} \tag{6.38}$$

$$\frac{d}{dt}(\frac{\partial T}{\partial \dot{q}_3}) = \frac{d}{dt}(\frac{\partial T}{\partial \dot{\psi}}) = I_T \ddot{\psi} \tag{6.39}$$

Substituting Equation (6.31), Equation (6.32), Equation (6.33), and Equation (6.37), Equation (6.38), Equation (6.39), into Equation (6.30) yields the equations of motion as:

$$m_T \ddot{x} = F_{x,F} \cos(\psi + \delta) + F_{x,R} \cos(\psi) - F_{y,F} \sin(\psi + \delta) - F_{y,R} \sin(\psi) \tag{6.40}$$

$$m_T \ddot{y} = F_{x,F} \sin(\psi + \delta) + F_{x,R} \sin(\psi) + F_{y,F} \cos(\psi + \delta) + F_{y,R} \cos(\psi) \tag{6.41}$$

$$I_T \ddot{\psi} = F_{x,F} a \sin(\delta) + F_{y,F} a \cos(\delta) - F_{y,R} b \tag{6.42}$$

Representing the system into a linear state space, the state vectors can be chosen as:

$$z_1 = x \tag{6.43}$$

$$z_2 = y \tag{6.44}$$

$$z_3 = \psi \tag{6.45}$$

$$z_4 = \dot{x} \tag{6.46}$$

$$z_5 = \dot{y} \tag{6.47}$$

$$z_6 = \dot{\psi} \tag{6.48}$$

Therefore, the state equations become:

$$\dot{z_1} = z_4 \tag{6.49}$$

$$\dot{z_2} = z_5 \tag{6.50}$$

$$\dot{z_3} = z_6 \tag{6.51}$$

$$\dot{z_4} = \frac{F_{x,F}\cos(z_3+\delta) + F_{x,R}\cos(z_3) - F_{y,F}\sin(z_3+\delta) - F_{y,R}\sin(z_3)}{m_T} \tag{6.52}$$

$$\dot{z_5} = \frac{F_{x,F}\sin(z_3+\delta) + F_{x,R}\sin(z_3) + F_{y,F}\cos(z_3+\delta) + F_{y,R}\cos(z_3)}{m_T} \tag{6.53}$$

$$\dot{z_6} = \frac{F_{x,F}a\sin(\delta) + F_{y,F}a\cos(\delta) - F_{y,R}b}{I_T} \tag{6.54}$$

The nonlinear state space equations can be written as:

$$\dot{\mathbf{x}} = \mathbf{f}\left(\mathbf{x}, \mathbf{u}\right) \tag{6.55}$$

The state vector used for linearization is as follows:

$$\mathbf{x} = \begin{bmatrix} \mathrm{x}_1 \\ \mathrm{x}_2 \\ \mathrm{x}_3 \\ \mathrm{x}_4 \\ \mathrm{x}_5 \\ \mathrm{x}_6 \end{bmatrix} \tag{6.56}$$

And the input vector is:

$$\mathbf{u} = \begin{bmatrix} \delta \\ F_{x,\mathrm{F}} \\ F_{x,\mathrm{R}} \\ F_{y,\mathrm{F}} \\ F_{y,\mathrm{R}} \end{bmatrix} \tag{6.57}$$

The vector $\mathbf{f}$ in Equation (6.55) can be represented as:

$$\mathbf{f} = \begin{bmatrix} \mathrm{f}_1 \\ \mathrm{f}_2 \\ \mathrm{f}_3 \\ \mathrm{f}_4 \\ \mathrm{f}_5 \\ \mathrm{f}_6 \end{bmatrix} = \begin{bmatrix} \dot{\mathrm{x}}_1 \\ \dot{\mathrm{x}}_2 \\ \dot{\mathrm{x}}_3 \\ \dot{\mathrm{x}}_4 \\ \dot{\mathrm{x}}_5 \\ \dot{\mathrm{x}}_6 \end{bmatrix} \tag{6.58}$$

To linearize the system, the vehcile must be driving in a straight line with a set reference velocity. Therefore, the states at the point of operation is given by:

$$\mathrm{x}_{1,op} = x_{op} = ? \tag{6.59}$$

$$\mathrm{x}_{2,op} = y_{op} = ? \tag{6.60}$$

$$\mathrm{x}_{3,op} = \psi_{op} = 0 \tag{6.61}$$

$$\mathrm{x}_{4,op} = v_{\mathrm{T},op} = v_{\mathrm{T},0} \tag{6.62}$$

$$\mathrm{x}_{5,op} = \alpha_{\mathrm{T},op} = 0 \tag{6.63}$$

$$\mathrm{x}_{6,op} = \dot{\psi}_{op} = 0 \tag{6.64}$$

where $V_{T,op}$ is the initial velocity at the operating point for linearization. The operating point of the inputs is:

$$\delta_{op} = 0 \tag{6.65}$$

$$F_{x,\mathrm{F},op} = 0 \tag{6.66}$$

$$F_{x,\mathrm{R},op} = 0 \tag{6.67}$$

$$F_{y,\mathrm{F},op} = 0 \tag{6.68}$$

$$F_{y,\mathrm{R},op} = 0 \tag{6.69}$$

To linearize, a Taylor Expansion Series is used about the operating points. The series is truncated at the first order term as:

$$\mathbf{f}_{lin}\left(\mathbf{x},\mathbf{u}\right) = \mathbf{f}\left(\mathbf{x}_{op},\mathbf{u}_{op}\right) + \nabla\mathbf{f}\left(\mathbf{x}_{op},\mathbf{u}_{op}\right)\begin{bmatrix} \mathbf{x}-\mathbf{x}_{op} \\ \mathbf{u}-\mathbf{u}_{op} \end{bmatrix} \tag{6.70}$$

where:

$$\mathbf{x}_{op} = \begin{bmatrix} \mathrm{x}_{1,op} \\ \mathrm{x}_{2,op} \\ \mathrm{x}_{3,op} \\ \mathrm{x}_{4,op} \\ \mathrm{x}_{5,op} \\ \mathrm{x}_{6,op} \end{bmatrix}. \tag{6.71}$$

$$\mathbf{u}_{op} = \begin{bmatrix} \delta_{op} \\ F_{x,\mathrm{F},op} \\ F_{x,\mathrm{R},op} \\ F_{y,\mathrm{F},op} \\ F_{y,\mathrm{R},op} \end{bmatrix}. \tag{6.72}$$

and,

$$\mathbf{f}\left(\mathbf{x}_{op}, \mathbf{u}_{op}\right) = \begin{bmatrix} v_{\mathrm{T},0} \\ 0 \\ 0 \\ 0 \\ 0 \\ 0 \end{bmatrix}, \tag{6.73}$$

The Jacobian $\nabla\mathbf{f}$ can be calculated numerically as part of the MATLAB software. It is equivalent to:

$$\nabla \mathbf{f} = \begin{bmatrix} \frac{\partial f_1}{\partial x} & \frac{\partial f_1}{\partial y} & \frac{\partial f_1}{\partial \psi} & \frac{\partial f_1}{\partial v} & \frac{\partial f_1}{\partial \alpha_{\mathrm{T}}} & \frac{\partial f_1}{\partial \dot{\psi}} & \frac{\partial f_1}{\partial \delta} & \frac{\partial f_1}{\partial F_{x,\mathrm{F}}} & \frac{\partial f_1}{\partial F_{x,\mathrm{R}}} & \frac{\partial f_1}{F_{y,\mathrm{F}}} & \frac{\partial f_1}{\partial F_{y,\mathrm{R}}} \\ \frac{\partial f_2}{\partial x} & \frac{\partial f_2}{\partial y} & \frac{\partial f_2}{\partial \psi} & \frac{\partial f_2}{\partial v} & \frac{\partial f_2}{\partial \alpha_{\mathrm{T}}} & \frac{\partial f_2}{\partial \dot{\psi}} & \frac{\partial f_2}{\partial \delta} & \frac{\partial f_2}{\partial F_{x,\mathrm{F}}} & \frac{\partial f_2}{\partial F_{x,\mathrm{R}}} & \frac{\partial f_2}{F_{y,\mathrm{F}}} & \frac{\partial f_2}{\partial F_{y,\mathrm{R}}} \\ \frac{\partial f_3}{\partial x} & \frac{\partial f_3}{\partial y} & \frac{\partial f_3}{\partial \psi} & \frac{\partial f_3}{\partial v} & \frac{\partial f_3}{\partial \alpha_{\mathrm{T}}} & \frac{\partial f_3}{\partial \dot{\psi}} & \frac{\partial f_3}{\partial \delta} & \frac{\partial f_3}{\partial F_{x,\mathrm{F}}} & \frac{\partial f_3}{\partial F_{x,\mathrm{R}}} & \frac{\partial f_3}{F_{y,\mathrm{F}}} & \frac{\partial f_3}{\partial F_{y,\mathrm{R}}} \\ \frac{\partial f_4}{\partial x} & \frac{\partial f_4}{\partial y} & \frac{\partial f_4}{\partial \psi} & \frac{\partial f_4}{\partial v} & \frac{\partial f_4}{\partial \alpha_{\mathrm{T}}} & \frac{\partial f_4}{\partial \dot{\psi}} & \frac{\partial f_4}{\partial \delta} & \frac{\partial f_4}{\partial F_{x,\mathrm{F}}} & \frac{\partial f_4}{\partial F_{x,\mathrm{R}}} & \frac{\partial f_4}{F_{y,\mathrm{F}}} & \frac{\partial f_4}{\partial F_{y,\mathrm{R}}} \\ \frac{\partial f_5}{\partial x} & \frac{\partial f_5}{\partial y} & \frac{\partial f_5}{\partial \psi} & \frac{\partial f_5}{\partial v} & \frac{\partial f_5}{\partial \alpha_{\mathrm{T}}} & \frac{\partial f_5}{\partial \dot{\psi}} & \frac{\partial f_5}{\partial \delta} & \frac{\partial f_5}{\partial F_{x,\mathrm{F}}} & \frac{\partial f_5}{\partial F_{x,\mathrm{R}}} & \frac{\partial f_5}{F_{y,\mathrm{F}}} & \frac{\partial f_5}{\partial F_{y,\mathrm{R}}} \\ \frac{\partial f_6}{\partial x} & \frac{\partial f_6}{\partial y} & \frac{\partial f_6}{\partial \psi} & \frac{\partial f_6}{\partial v} & \frac{\partial f_6}{\partial \alpha_{\mathrm{T}}} & \frac{\partial f_6}{\partial \dot{\psi}} & \frac{\partial f_6}{\partial \delta} & \frac{\partial f_6}{\partial F_{x,\mathrm{F}}} & \frac{\partial f_6}{\partial F_{x,\mathrm{R}}} & \frac{\partial f_6}{F_{y,\mathrm{F}}} & \frac{\partial f_6}{\partial F_{y,\mathrm{R}}} \end{bmatrix}. \tag{6.74}$$

Using $\mathbf{u}_{op}$ and $\mathbf{x}_{op}$ as the operating points for the Jacobian $\nabla \mathbf{f}$, the matrix becomes:

$$\nabla \mathbf{f}\left(\mathbf{x}_{op}, \mathbf{u}_{op}\right) = \begin{bmatrix} 0 & 0 & 0 & 1 & 0 & 0 & 0 & 0 & 0 & 0 & 0 \\ 0 & 0 & v_{\mathrm{T},0} & 0 & v_{\mathrm{T},0} & 0 & 0 & 0 & 0 & 0 & 0 \\ 0 & 0 & 0 & 0 & 0 & 1 & 0 & 0 & 0 & 0 & 0 \\ 0 & 0 & 0 & 0 & 0 & 0 & 0 & \frac{1}{m_T} & \frac{1}{m_T} & 0 & 0 \\ 0 & 0 & 0 & 0 & 0 & -1 & 0 & 0 & 0 & \frac{1}{m_T v_{\mathrm{T},0}} & \frac{1}{m_T v_{\mathrm{T},0}} \\ 0 & 0 & 0 & 0 & 0 & 0 & 0 & 0 & 0 & \frac{a}{I_{\mathrm{T}}} & -\frac{b}{I_{\mathrm{T}}} \end{bmatrix} \tag{6.75}$$

Therefore, the linearized system becomes:

$$f_{1,lin} = \dot{x} = v_{\mathrm{T}} \tag{6.76}$$

$$f_{2,lin} = \dot{y} = v_{\mathrm{T},0}\left(\psi + \alpha_{\mathrm{T}}\right) \tag{6.77}$$

$$f_{3,lin} = \dot{\psi} = \dot{\psi} \tag{6.78}$$

$$f_{4,lin} = \dot{v}_{\mathrm{T}} = \frac{F_{x,\mathrm{F}} + F_{x,\mathrm{R}}}{m_T} \tag{6.79}$$

$$f_{5,lin} = \dot{\alpha}_{\mathrm{T}} = \frac{F_{y,\mathrm{F}} + F_{y,\mathrm{R}}}{m_T v_{\mathrm{T},0}} - \dot{\psi} \tag{6.80}$$

$$f_{6,lin} = \ddot{\psi} = \frac{aF_{y,\mathrm{F}} - bF_{y,\mathrm{R}}}{I_T} \tag{6.81}$$

Which can be represented as the common state space equations as:

$$\dot{\mathbf{x}} = \mathbf{A}\mathbf{x} + \mathbf{B}\hat{\mathbf{u}} \tag{6.82}$$

$$\begin{bmatrix} \dot{x} \\ \dot{y} \\ \dot{\psi} \\ \dot{v}_{\mathrm{T}} \\ \dot{\alpha}_{\mathrm{T}} \\ \ddot{\psi} \end{bmatrix} = \begin{bmatrix} 0 & 0 & 0 & 1 & 0 & 0 \\ 0 & 0 & v_{\mathrm{T},0} & 0 & v_{\mathrm{T},0} & 0 \\ 0 & 0 & 0 & 0 & 0 & 1 \\ 0 & 0 & 0 & 0 & 0 & 0 \\ 0 & 0 & 0 & 0 & -\frac{K_{\mathrm{F}}+K_{\mathrm{R}}}{m_T v_{\mathrm{T},0}} & -\frac{m_T v_{\mathrm{T},0} + \frac{aK_{\mathrm{F}} - bK_{\mathrm{R}}}{v_{\mathrm{T},0}}}{m_T v_{\mathrm{T},0}} \\ 0 & 0 & 0 & 0 & -\frac{aK_{\mathrm{F}} - bK_{\mathrm{R}}}{I_T} & -\frac{a^2 K_{\mathrm{F}} + b^2 K_{\mathrm{R}}}{I_T v_{\mathrm{T},0}} \end{bmatrix} \begin{bmatrix} x \\ y \\ \psi \\ v_{\mathrm{T}} \\ \alpha_{\mathrm{T}} \\ \dot{\psi} \end{bmatrix} \ldots$$

$$+ \begin{bmatrix} 0 & 0 & 0 \\ 0 & 0 & 0 \\ 0 & 0 & 0 \\ 0 & \frac{1}{m_T} & \frac{1}{m_T} \\ \frac{K_{\mathrm{F}}}{m_T v_{\mathrm{T},0}} & 0 & 0 \\ \frac{aK_{\mathrm{F}}}{I_T} & 0 & 0 \end{bmatrix} \begin{bmatrix} \delta \\ F_{x,\mathrm{F}} \\ F_{x,\mathrm{R}} \end{bmatrix} \tag{6.83}$$

6.1.2 Simulation Results

In order to further compare the differences between the original Pacejka Tire Model, and the Modified Pacejka Tire Model, a double lane change was simulated in MATLAB and

the results were used to compare the two model. The steering input for the vehicle model is shown in Figure 6.3. The front wheel of the bicycle model was steered in a sinusoidal pattern with a maximum amplitude of 10° over a period of a ten second simulation. This steering maneuver will ensure that the trajectory of the vehicle follows a double lane change, and leads to the yaw angle result as shown in Figure 6.4. The trajectory is shown in Figure 6.5. This represents the double lane change maneuver which the vehicle model is able to perform if the Modified Pacejka Tire Model is used when the terrain which the vehicle operates on has a coefficient of friction of 0.15.

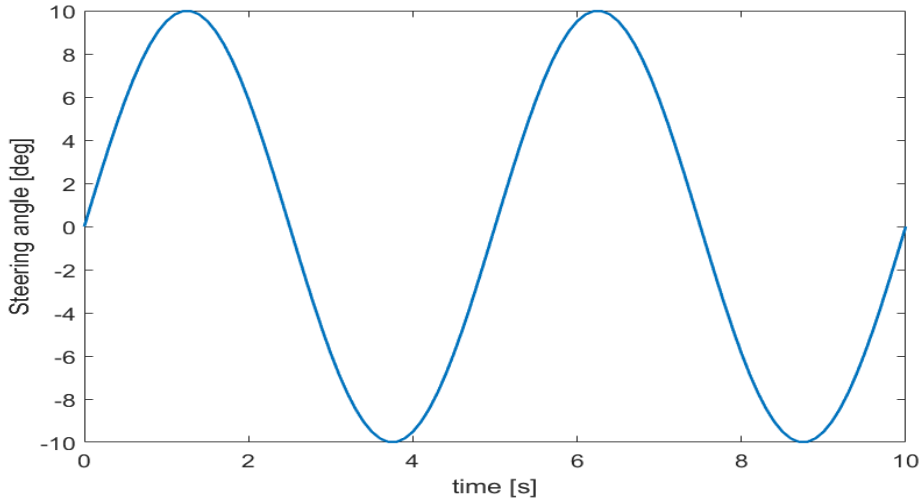

Figure 6.3: Steering input used for the ten second double lane change maneuver.

The double lane change maneuver, originally known as the moose test, is used to evaluate the handling performance of a vehicle, and is used in the vehicle design procedures and assessment (ISO 3888-2:2011). Using three cone lanes with a total length of 61 m, a double lane change is defined. This test must be completed at maximum speed. If no cone are overturned at the end of the test, the vehicle passes the test. The velocity for the simulations performed was kept constant at 10 m/s. A PID Control algorithm was used to maintain the desired speed during the double lane change maneuver. Equation (6.84)

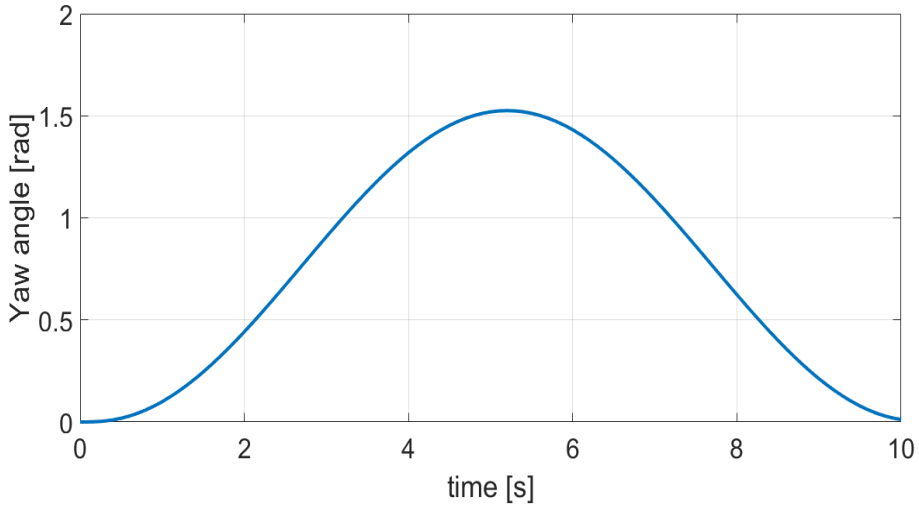

Figure 6.4: The resulting yaw angle during the simulation from the double lane change maneuver

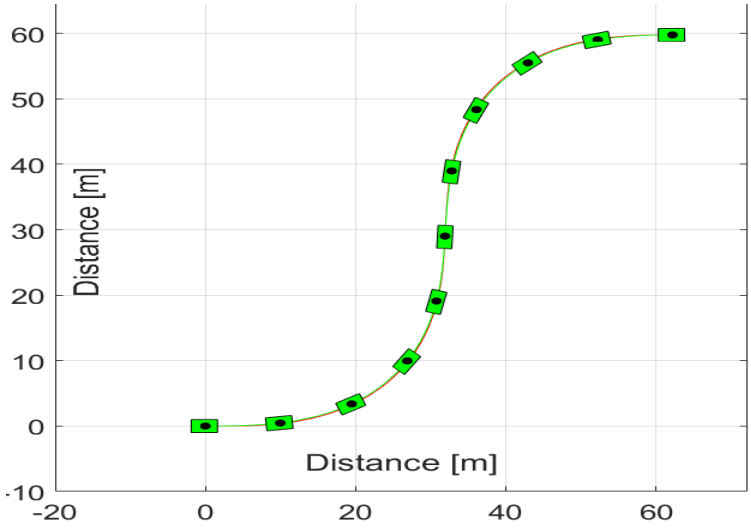

Figure 6.5: Trajectory of vehicle model during a double lane change maneuver

represents the velocity equation, where v_{ref} represents the initial velocity set by the user.

$$Output = K \cdot (v_{ref} - v) \tag{6.84}$$

Figure 6.6 represents the velocity of the vehicle during the simulation. As shown, the

control algorithm was capable of maintaining the desired velocity within a 1% margin of error. With the velocity set, the double lane change maneuver was performed in MATLAB, and the vehicle yaw rate was recorded, as shown Figure 6.7.

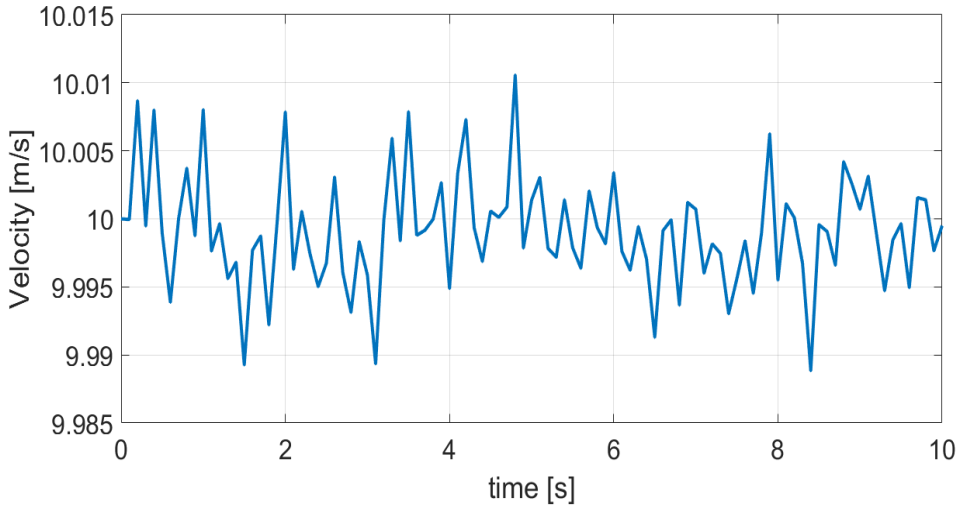

Figure 6.6: Velocity of the bicycle model during simulation.

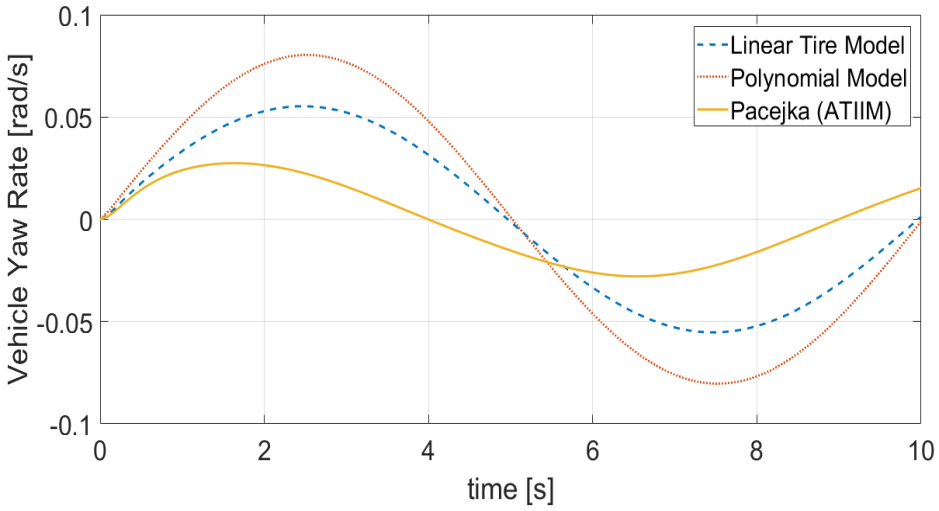

Figure 6.7: Vehicle Yaw rate from the simulation of the Bicycle Model during a double lane change maneuver on a surface of low coefficient of friction. Three tire models are used for comparison.

In Figure 6.7, three tire models are used to compare the yaw rate of the bicycle model

during a double lane change maneuver. A linear and polynomial tire model were chosen due to their simplicity. A linear tire model is commonly used in control applications because of its ability to be computationally efficient. However, there are certain limitations to a linear tire model such as the fact that the model is not able to account for the combined slip [43]. It is too simple to represent the coupled behavior. The polynomial tire model can also be accurate, simple, and computationally efficient. The polynomial tire model allows for fast convergence during the optimization process and also allows the use of a reduced set of data points to calculate the longitudinal forces [43]. In comparison, as shown in Figure 6.7, by including the Advanced Tire-Ice Interface Model into the tire model the vehicle is able to follow the desired driving path with less yaw when compared to the other models, due to the improvement in the estimation of the tire forces.

The front and rear slip angles of the wheels can also be determined from the double lane change simulation. Figure 6.8, it is shown that the front wheel will experience a lower slip angle during the double lane change maneuver when the Modified Pacejka Model is used. When compared, the decrease in the front slip angle for the front wheel between Pacejka-ATIIM and the original Pacejka model can be attributed to the improvement in the estimation of the longitudinal tire force. This signifies that as the front wheel is steered to turn the vehicle into the desired heading, the tire will experience less lateral force and will have a greater possibility of staying in the linear range of the friction eclipse during operation.

Figure 6.9 represents the slip angle of the rear wheel during a double lane change maneuver. For the rear wheel, there is a significant reduction in the slip angle when the Modified Pacejka Tire Model is used. With the inclusion of the temperature in the contact patch from ATIIM, the rear tire is able to follow the desired trajectory with minimal slip.

With the Modified Pacejka Tire Model, it has been shown through simulation that

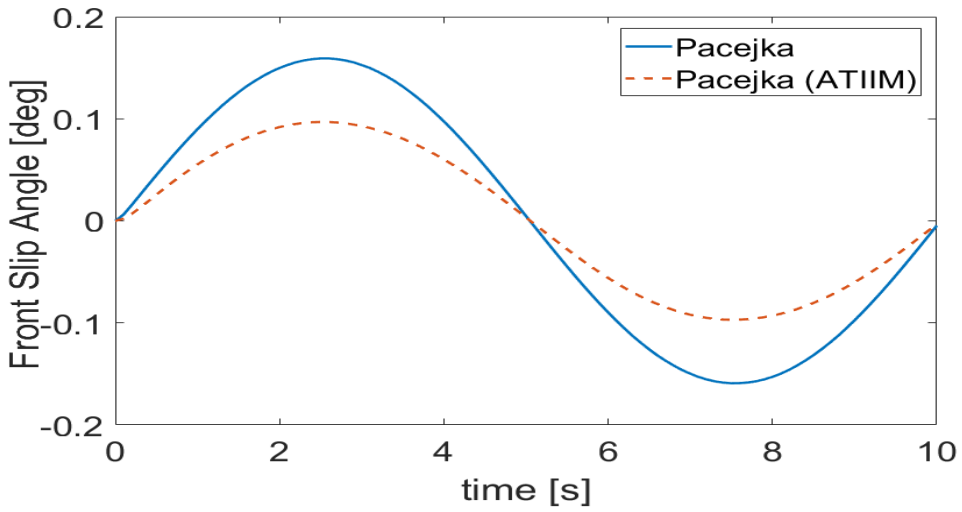

Figure 6.8: Front slip angle from the simulation of the double lane change maneuver using the bicycle model.

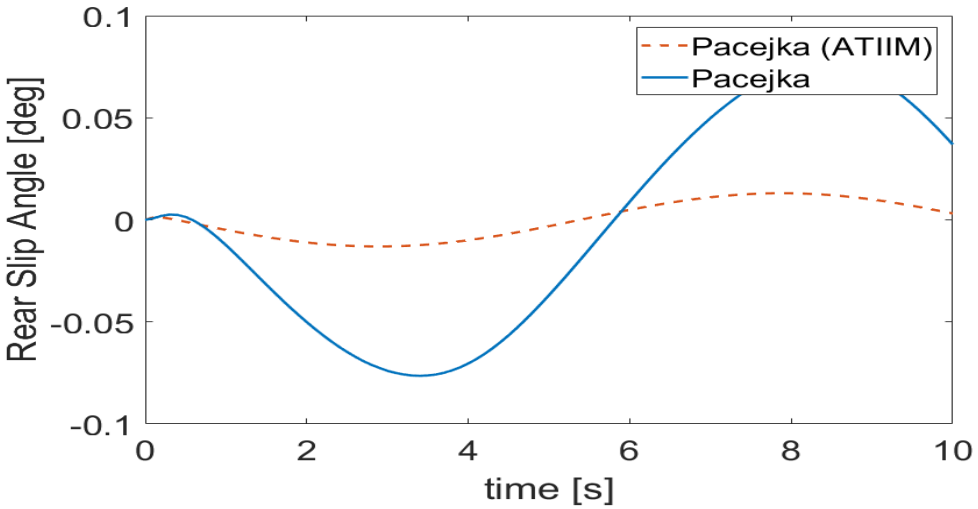

Figure 6.9: Rear slip angle from the simulation of the double lane change maneuver using the bicycle model.

the overall dynamics of the vehicle improves with the inclusion of the contact temperature, for a vehicle traversing over ice. This improvement can lead to a vehicle which handles much better on ice. Specifically, electronic control systems can use these results to improve the stability of the car on surfaces with a low coefficient of friction. A traction control system,

which uses wheel speed sensors to determine if a wheel is slipping can benefit from such models by keeping the tractive efforts of the wheel in the linear range of Figure 6.1. If a slip is detected between the road and the wheel, the Traction Control system ensures that only the minimum amount of torque is supplied to the slipping wheel to generate the required amount of friction for the vehicle to move. This is done by reducing the wheel speed to force the tire to operate in the linear range. In this range, the tire will experience an increase in traction and will not begin to slip on the surface. Therefore, using the Modified Pacejka Tire Model in conjunction with the Advanced Tire-Ice Interface Model, the control systems are able to more accurately to predict the forces at the contact patch and help to maintain the vehicle in the correct heading.

6.2 Implementation of ATIIM into 4DOF Vehicle Model

The maximum predicted temperature rise from the Advanced Tire-Ice Interface Model ($ATIIM$) can again be used to estimate the longitudinal forces, as in Figure 6.1, for terrains of low coefficient of friction such as ice. The forces can be used as an input for a 4 degree-of-freedom vehicle. Unlike the the two-wheeled bicycle model, the 4 DOF vehicle model [65] is made up of four wheels and is able to more accurately represents the vehicle body under real-world scenarios.

6.2.1 Development of 4DOF Nonlinear Vehicle Model

The physical vehicle model is represented in Figure 6.10. The base P $\{\mathbf{n}_x, \mathbf{n}_y, \mathbf{n}_z\}$ is attached to the non-suspended body of the vehicle. The system has four degrees-of-freedom (DOF): two coordinates positioning the point P namely x and y, the orientation of the

vehicle in the horizontal plane Ψ, and the angle of inclination Φ. The front view of the vehicle is shown in Figure 6.11.

The base for O is $\Omega = \mathbf{t_x}, \mathbf{t_y}, \mathbf{t_z}$. The base for P is $\Psi = \mathbf{n_x}, \mathbf{n_y}, \mathbf{n_z}$. Also, for P, $\Phi = \mathbf{s_x}, \mathbf{s_y}, \mathbf{s_z}$. The base O for $\mathbf{t_x}, \mathbf{t_y}, \mathbf{t_z}$ is used as the reference point for the inertial frame. The vectors $\mathbf{t_x}, \mathbf{t_y}, \mathbf{t_z}$ point to the longitudinal, transverse, and vertical directions respectively. The origin coincides with the point P which holds in the plane formed by the vectors $\mathbf{t_x}$ and $\mathbf{t_y}$. The vector $\mathbf{n_x}$ forms an angle with the vector $\mathbf{t_x}$ and the vector $\mathbf{t_z}$ is parallel to the vector $\mathbf{n_z}$.The point P identifies the center of mass of the vehicle. The distance a separates the points between the front axle and the center of mass and the distance b separates the points between the rear axle and the center of mass.

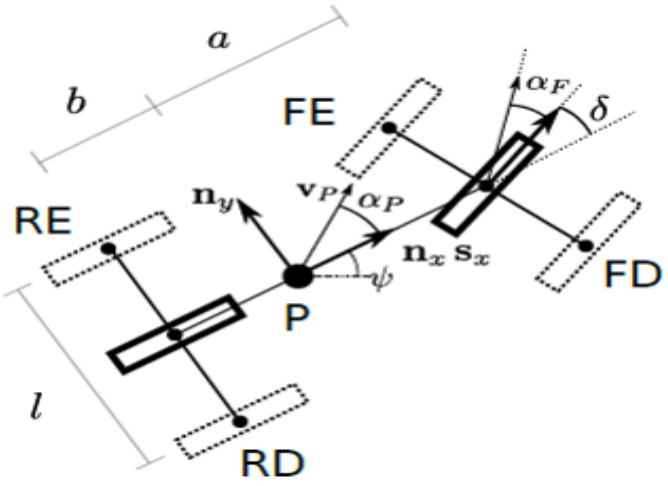

Figure 6.10: Physical Model of 4 Degree-of-Freedom Vehicle Model - Aerial View.

The development of the vehicle model begins by identifying the center of the contact patch for all four wheels. These position vectors are given as:

$$\mathbf{r_P^{FD}} = a\mathbf{n_x} - \frac{l}{2}\mathbf{n_y} \tag{6.85}$$

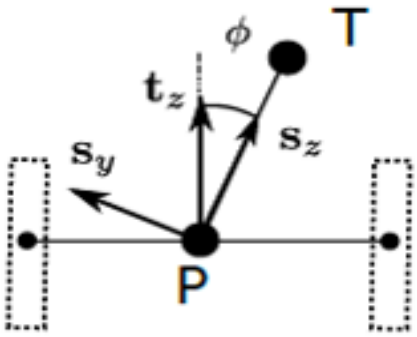

Figure 6.11: Physical Model of 4 Degree-of-Freedom Vehicle Model - Front View.

$$\mathbf{r_P^{FE}} = a\mathbf{n_x} - \frac{l}{2}\mathbf{n_y} \tag{6.86}$$

$$\mathbf{r_P^{RE}} = -b\mathbf{n_x} - \frac{l}{2}\mathbf{n_y} \tag{6.87}$$

$$\mathbf{r_P^{RD}} = -b\mathbf{n_x} + \frac{l}{2}\mathbf{n_y} \tag{6.88}$$

The velocity of point P is given by:

$$\mathbf{v_p} = v_p \cos\alpha_p \mathbf{n_x} + v_p \sin\alpha_p \mathbf{n_y} \tag{6.89}$$

Taking the derivatives of the position vectors, the velocity of each wheel becomes:

$$\mathbf{v_P^{FD}} = (v_p \cos\alpha_p + \frac{l}{2}\dot{\psi})\mathbf{n_x} + (v_p \sin\alpha_p + a\dot{\psi})\mathbf{n_y} \tag{6.90}$$

$$\mathbf{v_P^{FE}} = (v_p \cos\alpha_p - \frac{l}{2}\dot{\psi})\mathbf{n_x} + (v_p \sin\alpha_p + a\dot{\psi})\mathbf{n_y} \tag{6.91}$$

$$\mathbf{v_P^{RD}} = (v_p \cos\alpha_p + \frac{l}{2}\dot{\psi})\mathbf{n_x} + (v_p \sin\alpha_p - b\dot{\psi})\mathbf{n_y} \tag{6.92}$$

$$\mathbf{v_P^{RE}} = (v_p \cos\alpha_p - \frac{l}{2}\dot{\psi})\mathbf{n_x} + (v_p \sin\alpha_p - b\dot{\psi})\mathbf{n_y} \tag{6.93}$$

With the velocity vectors known, the slip angles can be determined as the arctan of each vector:

$$\alpha_{FD} = \arctan(\frac{v_p \sin\alpha_p + a\dot{\psi}}{v_p \cos\alpha_p + \frac{l}{2}\dot{\psi}}) - \delta \tag{6.94}$$

$$\alpha_{FE} = \arctan(\frac{v_p \sin\alpha_p + a\dot{\psi}}{v_p \cos\alpha_p - \frac{l}{2}\dot{\psi}}) - \delta \tag{6.95}$$

$$\alpha_{RD} = \arctan(\frac{v_p \sin\alpha_p - b\dot{\psi}}{v_p \cos\alpha_p + \frac{l}{2}\dot{\psi}}) \tag{6.96}$$

$$\alpha_{RE} = \arctan(\frac{v_p \sin\alpha_p - b\dot{\psi}}{v_p \cos\alpha_p - \frac{l}{2}\dot{\psi}}) \tag{6.97}$$

The velocity of point T with respect to the inertial frame is:

$$\mathbf{v_T} = (v_p \cos\alpha_P + \dot{\psi} h \sin\phi)\mathbf{n_x} + (v_p \sin\alpha_P - \dot{\phi} h \cos\phi)\mathbf{n_y} + (-\dot{\phi} h \sin\phi)\mathbf{n_z} \tag{6.98}$$

Taking the derivative of Equation (6.98)

$$\begin{aligned}\mathbf{a_T} = (\dot{v_p}\cos\alpha_P - v_p(\dot{\psi}+\dot{\alpha_p})\sin\alpha_p + \ddot{\psi}h\sin\phi + 2h\dot{\phi}\dot{\psi}\cos\phi)\mathbf{n_x}... \\ +(\dot{v_p}\sin\alpha_P + v_p(\dot{\psi}+\dot{\alpha_p})\sin\alpha_p - \ddot{\phi}h\cos\phi + h(\dot{\phi}^2+\dot{\psi}^2)\sin\phi)\mathbf{n_y}... \\ +(-h\ddot{\phi}\sin\phi - h\dot{\phi}^2\cos\phi)\mathbf{n_z}\end{aligned} \tag{6.99}$$

Now that the acceleration of point T has been formulated, the forces at the center of each wheel can be given by:

$$\mathbf{F_{FD}} = (F_{FD,x}\cos\delta - F_{FD,y}\sin\delta)\mathbf{n_x} + (F_{FD,x}\sin\delta + F_{FD,y}\cos\delta)\mathbf{n_y} \tag{6.100}$$

$$\mathbf{F_{FE}} = (F_{FE,x}\cos\delta - F_{FE,y}\sin\delta)\mathbf{n_x} + (F_{FE,x}\sin\delta + F_{FE,y}\cos\delta)\mathbf{n_y} \tag{6.101}$$

$$\mathbf{F_{RD}} = F_{RD,x}\mathbf{n_x} + F_{RD,y}\mathbf{n_y} \tag{6.102}$$

$$\mathbf{F_{RE}} = F_{RE,x}\mathbf{n_x} + F_{RE,y}\mathbf{n_y} \tag{6.103}$$

Using Newton's Third Law of Motion,

$$m\mathbf{a} = \sum \mathbf{F_{ext}} \tag{6.104}$$

Using the acceleration equation of point T and the tire forces, Equation (6.104) becomes:

$$\begin{aligned} &m(\dot{v_p}\cos\alpha_P - v_p(\dot{\psi}+\dot{\alpha_p})\sin\alpha_p + \ddot{\psi}h\sin\phi + 2h\dot{\phi}\dot{\psi}\cos\phi)... \\ &= (F_{FD,x}+F_{FE,x})\cos\delta - (F_{FD,y}+F_{FE,y})\sin\delta + (F_{RD,x}+F_{RE,x}) \end{aligned} \tag{6.105}$$

in the $\mathbf{n_x}$ direction, and:

$$\begin{aligned} &m(\dot{v_p}\sin\alpha_P + v_p(\dot{\psi}+\dot{\alpha_p})\sin\alpha_p - \ddot{\phi}h\cos\phi + h(\dot{\phi}^2+\dot{\psi}^2)\sin\phi)... \\ &= (F_{FD,x}+F_{FE,x})\sin\delta - (F_{FD,y}+F_{FE,y})\cos\delta + (F_{RD,y}+F_{RE,y}) \end{aligned} \tag{6.106}$$

in the $\mathbf{n_y}$ direction. To relate point T with respect to P:

$$\mathbf{r_P^T} = \mathbf{h s_z} \tag{6.107}$$

Therefore, the acceleration of the center of mass at point P:

$$\begin{aligned}\mathbf{a_p} = (\dot{v_p}\cos\alpha_p - v(\dot{\alpha_p} + \dot{\psi})\sin\alpha_p)\mathbf{s_x}... \\ +(\dot{v_p}\sin\alpha_p\cos\phi + (\dot{\alpha_p} + \dot{\psi})\cos\alpha_p\cos\phi)\mathbf{s_y}... \\ -(\dot{v_p}\sin\alpha_p\cos\phi + v(\dot{\alpha_p} + \dot{\psi})\cos\alpha_p\sin\phi)\mathbf{s_z}\end{aligned} \tag{6.108}$$

The moments must also be formulated. Using the forces at each individual wheel, and its respective distance with respect to the center of mass:

$$\mathbf{M_{FD}} = \mathbf{r_P^{FD}} \wedge \mathbf{F_{FD}} \tag{6.109}$$

$$\mathbf{M_{FE}} = \mathbf{r_P^{FE}} \wedge \mathbf{F_{FE}} \tag{6.110}$$

$$\mathbf{M_{RD}} = \mathbf{r_P^{RD}} \wedge \mathbf{F_{RD}} \tag{6.111}$$

$$\mathbf{M_{RE}} = \mathbf{r_P^{RE}} \wedge \mathbf{F_{RE}} \tag{6.112}$$

Substituting the respective equations into Equation (6.109), Equation (6.110), Equation (6.111), Equation (6.112):

$$\mathbf{M_{FD}} = \sin\phi(aF_{FD,x}\sin\delta + aF_{FD,y}\cos\delta + \frac{l}{2}F_{FD,x}\cos\delta - \frac{l}{2}F_{FD,y}\sin\delta)\mathbf{s_y} \tag{6.113}$$

$$\begin{aligned}
&... + \cos\phi(aF_{FD,x}\sin\delta + aF_{FD,y}\cos\delta + \frac{l}{2}F_{FD,x}\cos\delta - \frac{l}{2}F_{FD,y}\sin\delta)\mathbf{s_z} \\
\mathbf{M_{FE}} &= \sin\phi(aF_{FE,x}\sin\delta + aF_{FE,y}\cos\delta - \frac{l}{2}F_{FE,x}\cos\delta + \frac{l}{2}F_{FE,y}\sin\delta)\mathbf{s_y} \qquad (6.114) \\
&... + \cos\phi(aF_{FE,x}\sin\delta + aF_{FE,y}\cos\delta - \frac{l}{2}F_{FE,x}\cos\delta + \frac{l}{2}F_{FE,y}\sin\delta)\mathbf{s_z} \\
\mathbf{M_{RD}} &= \sin\phi(\frac{l}{2}F_{RD,x} - bF_{RD,y})\mathbf{s_y} + \cos\phi(\frac{l}{2}F_{RD,x} - bF_{RD,y})\mathbf{s_z} \qquad (6.115) \\
\mathbf{M_{RE}} &= \sin\phi(-\frac{l}{2}F_{RE,x} - bF_{RE,y})\mathbf{s_y} + \cos\phi(-\frac{l}{2}F_{RE,x-bF_{RE,y}})\mathbf{s_z} \qquad (6.116)
\end{aligned}$$

The moment generated about the center of mass, due to the weight of the vehicle is:

$$\mathbf{M_P} = \mathbf{r_P^T} \wedge \mathbf{P} = mgh\sin\phi\mathbf{s_x} \qquad (6.117)$$

and the moment generated by the torsional spring which connects the two axles can be calculated as:

$$\mathbf{M_K} = -K\phi\mathbf{s_x} \qquad (6.118)$$

and the damping is:

$$\mathbf{M_K} = -C\dot{\phi}\mathbf{s_x} \qquad (6.119)$$

In order to represent the motion of the vehicle, the angular motion must be taken into account. This can be represented in matrix form as:

$$m\mathbf{r_P^T a_p} + \mathbf{w_\Phi I_p w_\Phi} + \mathbf{I_P \dot{w}_\Phi} = \sum \mathbf{M_{ext,P}} \qquad (6.120)$$

in relation to point P. $\mathbf{I_P}$ is the inertia tensor with respect to point P, and is equivalent to:

$$\begin{bmatrix} I_{xx} & -I_{xy} & -I_{xz} \\ -I_{xy} & I_{yy} & -I_{yz} \\ -I_{xz} & -I_{yz} & I_{zz} \end{bmatrix} \tag{6.121}$$

Expanding equation Equation (6.120):

$$\begin{aligned} I_{xx}\ddot{\phi} - I_{yz}\dot{\psi}^2 - I_{xz}\ddot{\psi}\cos\phi - I_{xy}\ddot{\psi}\sin\phi + \frac{(I_{zz} - I_{yy})\dot{\psi}^2\sin(2\phi)}{2} + 2I_{yz}\dot{\psi}^2\cos^2\phi... \\ -\dot{v_p}hm\cos\phi\sin\alpha_p - (\dot{\alpha_p} + \dot{\psi})hmv_p\cos\alpha_p\cos\phi... \\ = mgh\sin\phi - K\phi - C\dot{\phi} \end{aligned} \tag{6.122}$$

in the $\mathbf{s_x}$ direction. In the $\mathbf{x_z}$ direction:

$$\begin{aligned} I_{zz}(\ddot{\psi}\cos\phi - \dot{\phi}\dot{\psi}\sin\phi) - \dot{\phi}(I_{xy}\dot{\phi} + I_{xx}\dot{\psi}\sin\phi) + \dot{\psi}\sin\phi(I_{yy}\dot{\phi} + I_{xy}\dot{\psi}\sin\phi)... \\ -\dot{\psi}\cos\phi(I_{yz}\dot{\phi} - I_{xz}\dot{\psi}\sin\phi) - I_{yz}(\ddot{\psi}\sin\phi + \dot{\phi}\dot{\psi}\cos\phi) - I_{xz}\ddot{\phi}... \\ = \cos\phi a(F_{FD,x} + F_{FE,x})\sin\delta + a(F_{FD,y} + F_{FE,y})\cos\delta... \\ +\frac{l}{2}(F_{FD,x} - F_{FE,x})\cos\delta + \frac{l}{2}(-F_{FD,y} + F_{FE,y})\sin\delta... \\ +\cos\phi\frac{l}{2}(F_{RD,x} + F_{RE,x}) - b(F_{RD,y} + F_{RE,y}) \end{aligned} \tag{6.123}$$

Therefore, the equations of motion for 4 DOF vehicle model is given by Equation (6.106), Equation (6.107), Equation (6.123), Equation (6.124).

6.2.2 Simulation Results

In order to further compare the differences between the original Pacejka Tire Model, and the Modified Pacejka Tire Model, a constant radius turn at constant velocity was simulated in MATLAB and the results were used to compare the two tire models. Only the rear wheels were driven for this simulation.

The constant radius turn is used to characterize a vehicle under steady state conditions. This test is performed at a constant forward speed. A PID controller such as Equation (6.84) is again employed to control the constant velocity. In Figure 6.12, the velocity is shown to be constant at the initial value of $8m/s$ within a 1% margin of error.

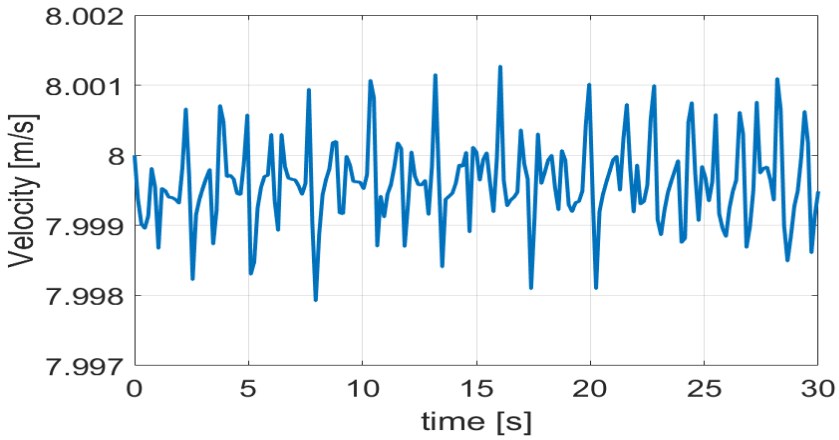

Figure 6.12: Velocity of the vehicle during a constant radius turn using the Modified Pacejka Tire Model.

The trajectory is shown in Figure 6.13. This trajectory represents the vehicle model with the original Pacejka Tire Model. With the inclusion of the Advanced Tire-Ice Interface Model, the tire surface temperature can be used to modify the original Pacejka Tire Model. The results are shown in Figure 6.14. When the Modified Pacejka Tire Model is used, the vehcile is able to follow the desired path from the start on a surface with a low coefficient of friction. In Figure 6.13, the vehicle had to take a larger turn angle at the beginning in order

to follow the desired path. The trajectory also represents that the vehicle using the original Pacejka Tire Model will exhibit an understeer characteristics as the driver needs to increase the steer angle in order to maintain the constant radius. The Modified Pacejka Tire Model exhibits a neutral steer. In other words, while the vehicle is traveling at a constant speed, the driver maintains the constant steering angle to keep the vehicle turning at the constant radius.

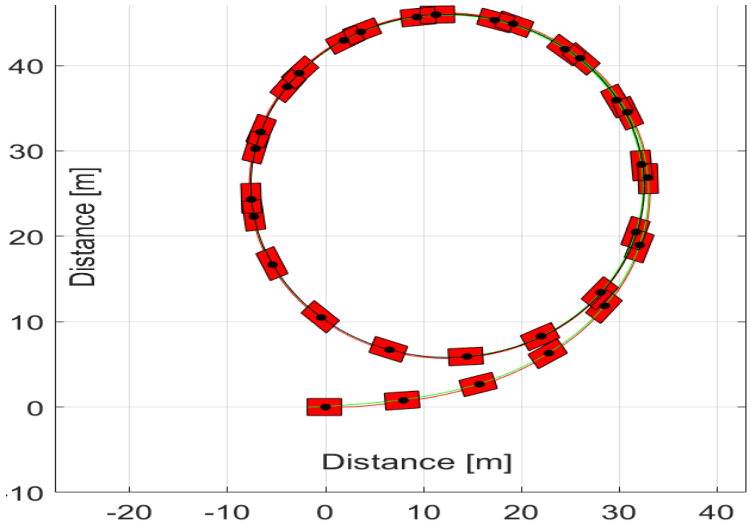

Figure 6.13: Trajectory of 4DOF Vehicle Model from the simulation of the constant radius turn using the original Pacejka Model.

As the vehicle travels about a constant radius, the vertical forces on the tire will offset such that wheels which are on the outside of the turn will experience a higher vertical load. This is shown in Figure 6.15. The combined vertical loads on the axles are shown in Figure 6.16. The difference between the forces experienced by the axles can be attributed to the location of the center of mass for the vehicle.

When examining the handling characteristics of a vehicle, the roll angle is of importance because it dictates the performance of the vehicle in terms of roll-over. Using the Modified Pacejka Tire Model, allows the vehicle to remain in a neutral steer configuration and results in a much lower roll angle at the beginning of the simulation, as shown in Fig-

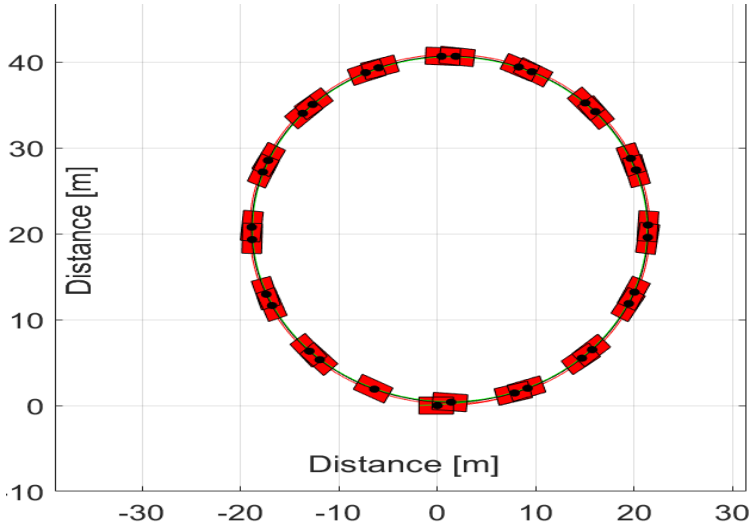

Figure 6.14: Trajectory of 4DOF Vehicle Model from the simulation of the constant radius turn using the Modified Pacejka Model.

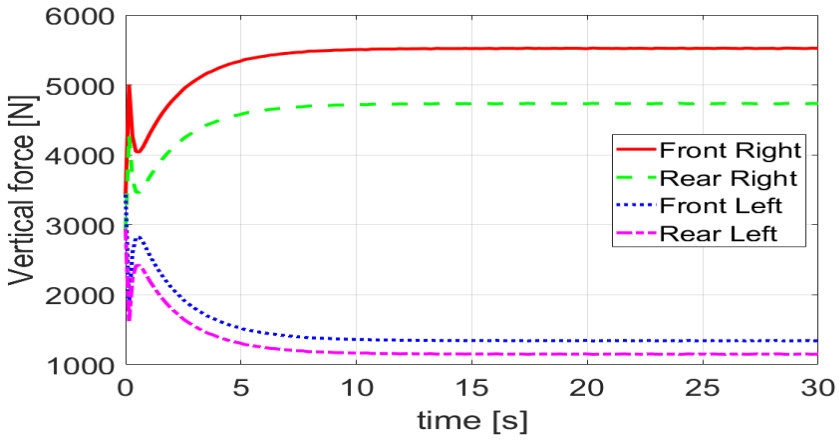

Figure 6.15: Vertical loads on tire showing offset of tire forces during a constant radius turn.

ure 6.17. Although the roll angles are different at the beginning of the simulation, the angles converge as the vehicle progresses through the constant radius turn. This is to be expected, as the vehicle body will experience a constant roll angle as the vehicle turns.

The yaw rate represents the rate at which the heading of the vehicle body will turn as the vehicle progresses through the constant radius turn simulation. As shown in Figure 6.18, the vehicle with the Modified Pacejka Tire Model will experience a lower yaw rate. Due to

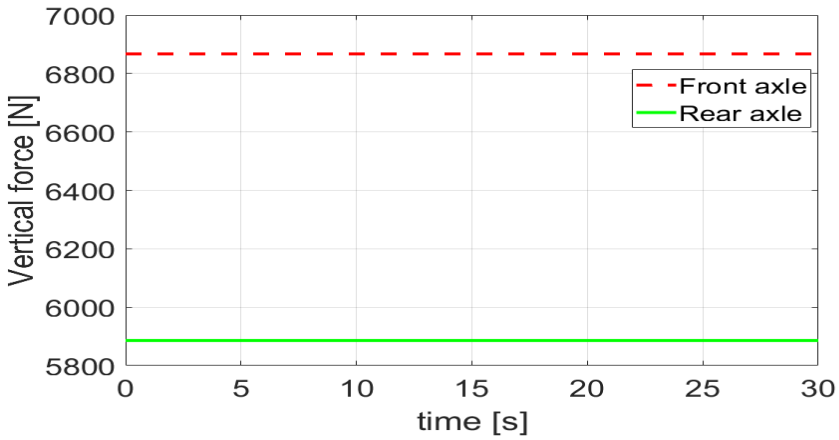

Figure 6.16: Combined axle loads on vehicle showing offset of forces due to the location of the center of mass.

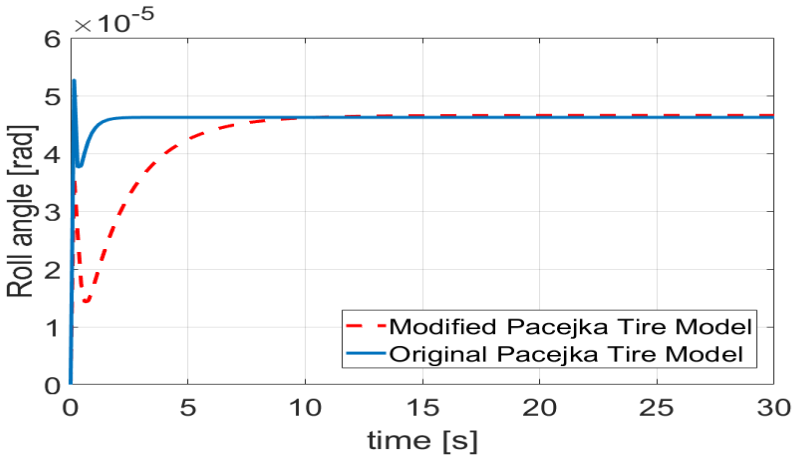

Figure 6.17: Comparison of the roll angle of the vehicle body using the original Pacejka Tire Model and the Modified Pacejka Tire Model.

the improvement in the estimation of the tire forces using ATIIM, the heading of the vehicle will be able to follow the desired path without a sudden change in yaw at the beginning of the simulation.

Again, the difference between the two tire models can be represented by the difference in the yaw for which vehicle body will experience. Examining the yaw angle in Figure 6.19, it is shown that the vehicle using the Modified Pacejka Tire Model will again experience a

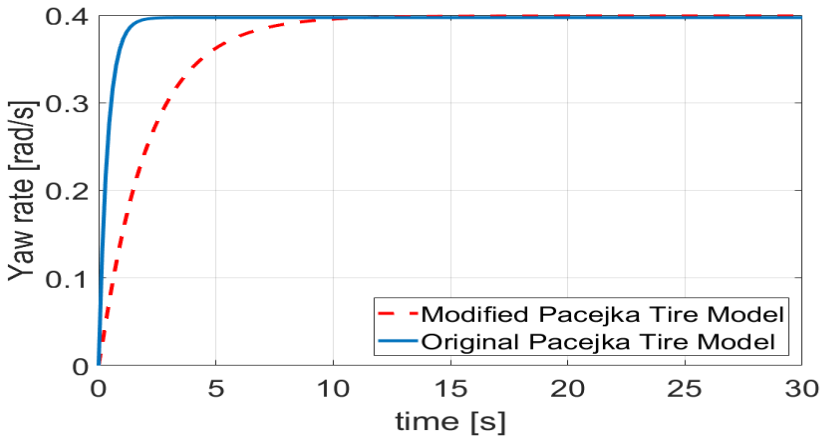

Figure 6.18: Comparison of the yaw rate of the vehicle body using the original Pacejka Tire Model and the Modified Pacejka Tire Model.

lower yaw angle meaning that the vehicle will show better handling characteristics This is only true when the temperature is included for a tire traversing over a smooth ice, as done with the Modified Pacejka Tire Model.

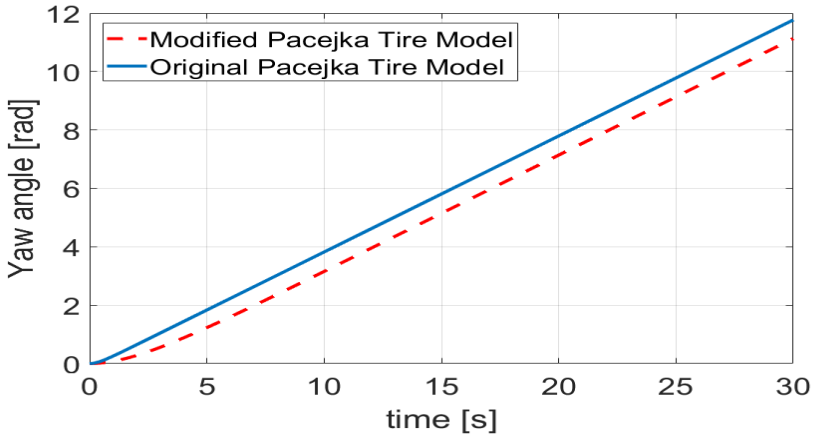

Figure 6.19: Comparison of the yaw angle of the vehicle body using the original Pacejka Tire Model and the Modified Pacejka Tire Model.

6.3 Full Vehicle Implementation in CarSim

To validate the developed vehicle models, a full vehicle model was implemented in CarSim and was simulated to show the effects of the Modified Pacejka Tire Model and the original Pacejka Tire Model. CarSim is a commercially available software package which is composed of validated data collected by automotive engineers.

The two drawbar pull for the Modified Pacejka Tire Model and the original Pacejka Tire Model were used as an input into the CarSim models to define the tire behavior for various surfaces of low coefficient of friction. The vehicle were then simulated to perform a double lane change to investigate the performance of the vehicle. Using the longitudinal forces obtained at different slip ratios from the Terramechanics Rig and the CarSim vehicle model, the handling performance of the vehicle can be investigated.

6.3.1 Vehicle Model Description

The vehicle models used during the investigation consisted of Class A - Class E vehicles. The model is composed of a four-wheeled motor vehicle without any rear attachments, such as a trailer. Both the front and rear axles were set to be solid-axle suspension to keep the simplicity of the model. For the tire used, a P225/60R16 Standard Reference Test Tire was used in order to compare tire forces results with those collected in the Terramechancis Rig. The five classes of vehicle used are shown in Figure 6.20.

6.3.2 Simulation Results

Simulating a double lane change maneuverer in CarSim is an appropriate method to validate the bicycle model. The initial velocity for the simulations ranged between 60 km/h

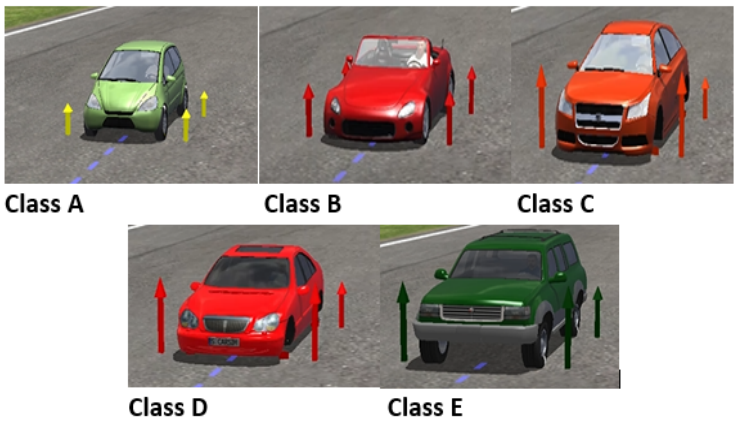

Figure 6.20: Comparison of the different classes of vehicles used for the simulations in CarSim.

up to 120 km/h. The coefficient of friction for the surface which the vehicle traveled on was simulated to have a low coefficient of friction of 0.15, such as smooth ice. As the velocity increased from 60 km/h to 120 km/h, the effects between the tire models became more evident. Due to the low coefficient of friction, it is expected that the vehicle will yaw more than if the coefficient of friction was higher.

At 60 km/h, the two vehicle maintained similar paths of travel up until the second steering maneuver during the double lane change simulation. At this point, the tire forces predicted from the original Pacejka Tire Model (black vehicle), caused the body of the vehicle to yaw more than the other vehicle (blue vehicle). This is shown in Figure 6.21. As the velocity increased to 80 km/h, as shown in Figure 6.22, the separation between the vehicle heading and the desired path of travel increased even more for the vehicle simulating the original Pacejka Tire Model (black vehicle).

When the velocity is increased to 120 km/h, the separation between the vehicle is even greater, as one should expect. This is shown in Figure 6.23. Even after the double lane change maneuver, the vehicle with the original Pacejka Tire Model is not able to maintain

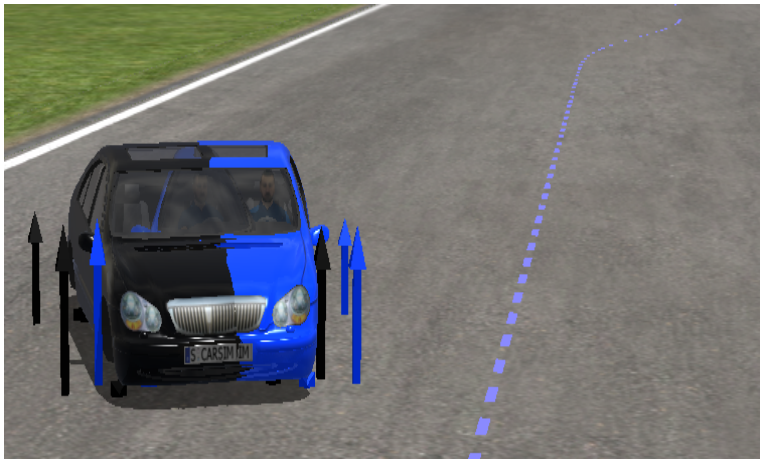

Figure 6.21: Comparison of the Modified Pacejka Tire Model (Blue) and Original Pacejka Tire Model (Black) at 60 km/h in CarSim.

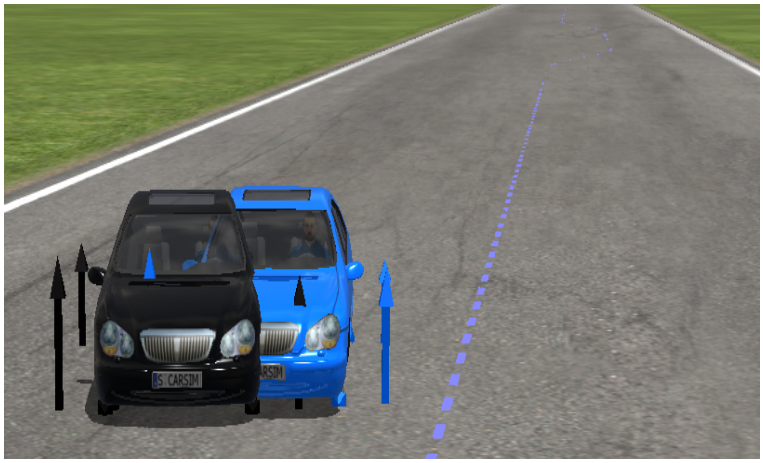

Figure 6.22: Comparison of the Modified Pacejka Tire Model (Blue) and Original Pacejka Tire Model (Black) at 80 km/h in CarSim.

the desired path. At this point, the yaw rate is the highest, which is shown in Figure 6.24 and can be confirmed using the bicycle model in Figure 6.7. Using the Modified Pacejka Tire Model decreased the yaw rate which the body of the vehicle experiences.

As shown from the CarSim simulations, by more accurately predicting the longitudinal forces using the Modified Magic Formula, the simulations are able to more accurately represent the real-world scenarios of a vehicle driving on a terrain of a low coefficient of

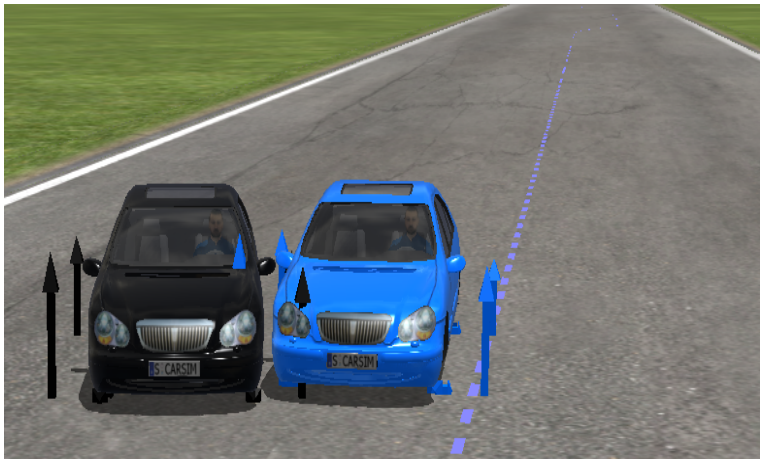

Figure 6.23: Comparison of the Modified Pacejka Tire Model (Blue) and Original Pacejka Tire Model (Black) at 120 km/h in CarSim.

friction. When the friction is low, a vehicle may certainly become unstable, but the extent of how much additional yaw the vehicle may experience is what is important. By using the Modified Pacejka Tire Model, the vehicle will indeed become unstable at some extreme point, but it is able to more accurately predict when this threshold may occur. Unlike the Modified Pacejka Tire Model, the original Pacejka Tire Model predicts this threshold to occur much sooner than it would in real-world scenario.

6.4 Discussion

A tire model must be fast, accurate, and reliable. Empirical models such as the Magic Formula are used to provide quick tire model dependent on experimental data. These types of model though are limited to the scope of which the experimental data was collected, and the data must be used sparingly. Four fundamental factors play a role in developing simple theoretical tire models that can be used to study the tire force and moment generation capability. Models such as the Magic Formula and the Dugoff Tire Model use frictional properties in the tire-terrain interface and the compliance of the tread rubber, belt, and

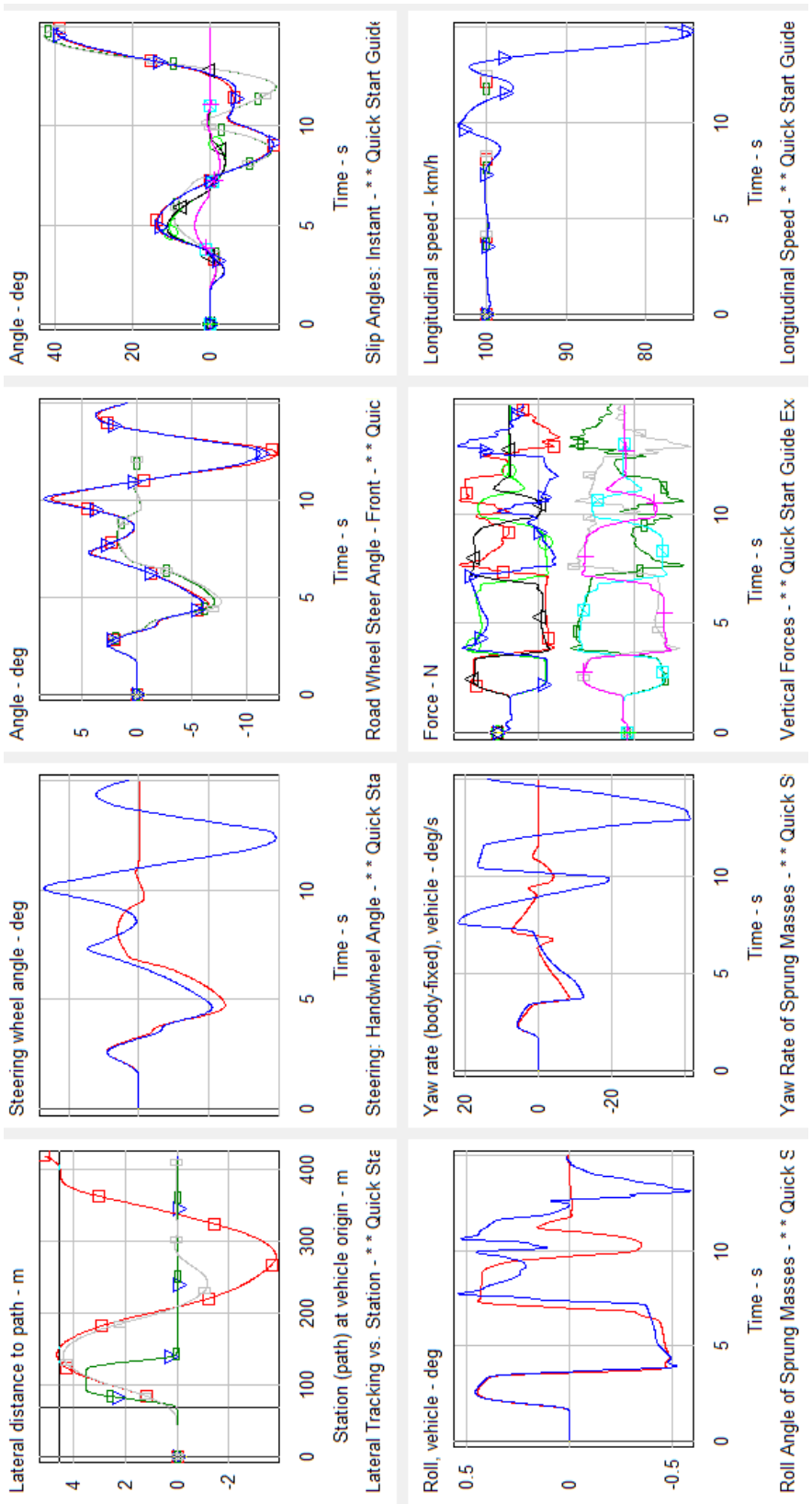

Figure 6.24: Plot window from CarSim comparing the Modified Pacejka Tire Model (Red) and Original Pacejka Tire Model (Blue) at 120 km/h in CarSim.

carcass to properly characterize the tractive performance of a pneumatic tire.

In this chapter, the Magic Formula was modified to include the effects of which temperature rise had on the longitudinal and lateral forces of a tire on smooth ice. This was done by altering the parameters which the Magic Formula uses. The results showed that by including the influence of tire surface temperature into the model, the tire models can be improved to more accurately represent the tire forces.

Chapter 7

Conclusions of Current Study

This chapter presents a summary of the research, highlighting the important results that were obtained. Main contributions along with a list of publications and research papers written are also presented in this chapter. Finally, the chapter ends with the directions for future research to be pursued.

7.1 Summary of Research Outcomes

The research conducted in this study was intended to extend the original tire-ice model and to investigate the tractive performance of tires on ice with various operational parameters. The parameters included the effect of toe and camber angles, the effect of varying the inflation pressure, the effect of the normal load, the effect of ice surface temperature, and the effect of the slip ratio at the contact patch. This experimental study was conducted at the Terramechanics, Multibody, and Vehicle Systems (TMVS) Laboratory at Virginia Tech using the Terramechanics Rig.

The research goals of this project were to:

1. Enhance the understanding of the tire-ice contact interaction at the contact patch through experimental studies and a semi-empirical Advanced Tire-Ice Interface Model (*ATIIM*).

2. Perform an experimental analysis between Winter Tires and All−Season Tires in order to further expand our knowledge base of tire traction on ice. This includes investigating the effects of tire composed of difference rubber composition.

3. Validate and extend the Tire-Ice Model for the various simulations investigated by developing modules to account for new scenarios.

4. Develop the Advanced Tire-Ice Interface Model and implement it into a tire model in order for vehicle dynamics simulations.

The research study began with an extensive literature review regarding various aspects regarding to the characterization of ice and a pneumatic tire. This includes studying the previous work on this topic, studying the parameters which characterizes the ice surface conditions. The literature review continues with an explanation of tire parameters and mechanics. Finally, the literature review is concluded with a brief presentation of exiting tire-ice models used for tractive investigations.

The experimental portion of this research has led to a quantification of the effects of different operational parameters during operation of tires on ice. In the Terramechanics, Multibody, and Vehicle Systems (TMVS) Laboratory, the pressure pad was employed to measure pressure distribution at the contact patch under dynamics conditions. It was found that the raw measured pressure distribution had similar contact patch dimensions as those provided by Hankook Tire, but a lack of resolution for individual tread blocks provides

difficulty in determining the effects of applying torque as opposed to an actual slip ratio. It was evident that as the slip ratio increased, the overall spread for higher pressure distribution increases.

When the effect of tire age was investigated, it was shown that the rubber loses its flexibility and the tire hardens with aging. The flexibility of the tire is one of the main contributions in the production of the tractive forces at the contact patch. From the two plots, shown in Figure 3.33, it is evident that the two test results share the similar trend for the drawbar pull of the tire. The main difference to note is that there was approximately a 3% decrease in traction performance with the aged tire used in 2015.

Allowing the inflation pressure to vary showed that the drawbar pull has a higher peak at lower inflation pressures. Furthermore, as the inflation pressure increased, the maximum drawbar pull occurred at a lower slip ratio value. As the inflation pressure increases, the rolling resistance of the tire decreases. A tire with a lower inflation pressure will have a larger contact area and thus will produce more traction during operation on ice.

The effects of varying the normal load was also studied. The normal load was kept constant throughout the run and was measured using the KISTLER P650 force hub. It was shown that the drawbar pull coefficient decreases with a reduction in normal load. It is hypothesized that this is due to the change in the contact area at various normal loads. When the normal load is increased, the tire is able to deform more. The increased amount of deformation leads to a larger contact area which in turns results in more area to generate friction from.

The effect of varying the camber angle was studied for 0°, 2°, and -2°. When a camber angle is imposed on the tire, the contact patch changes in area, providing a smaller footprint in which friction can be generated. When the SRTT was tested on ice, a change in the

camber angle while the toe angle was kept constant at 0° resulted in no significant difference in the traction performance. Unlike the camber angle, the effect of varying the toe angle led to the conclusion that as the slip angle is increased, the maximum drawbar pull decreases when the camber angle is set at 0°.

The influence of a thin water layer on top of the ice was also investigated experimentally. Tap water was sprayed from a hose directly on the ice surface prior to each test run in order the simulate wet conditions. With the addition of the thin water layer, the friction was greatly reduced. With the water present, the tire tread displaces the water to the grooves and away from the tire through the sipes. The water is then quickly refrozen as it leaves the contact patch.

To study the temperature rise of the contact patch under normal operating conditions, an Advanced Tire-Ice Interface Model was developed to identify the rise in temperature at the contact patch as well as to identify areas of dry and wet regions in the contact patch [19]. Once the temperature rise is determined, the dynamic friction coefficient is obtained at the tire-ice interface. Since the original development of TIM several additional modules have been implemented in order to improve and extend its original capabilities. The model is now capable of estimating the water fluid height, and its resultant viscous friction levels. Using a comprehensive analysis of what occurs at the contact interface, such as the water film height and the viscous friction allows for a more thorough investigation of the tire performance on ice with respect to traction.

To validate the Advanced Tire-Ice Interface model:

1. Maximum temperature differences simulated from the model were compared against the maximum differences which were measured using K-Type thermocouples.

2. The measured maximum temperature rise was used as an input into the Advanced

Tire-Ice Interface Model to predict the longitudinal force for the tire models, and were compared against measured results of similar temperature rise.

7.2 Main Contributions of this Research

The main contributions of this research are:

7.2.1 Novel Contributions Regarding the Advanced Tire-Ice Interface Model

- Validated the Tire-Ice Model for the various simulations investigated and temperatures measured.
- Extended the Tire-Ice Model by developing modules to account for new scenarios investigated. The improved tire model is now identified as the Advanced Tire-Ice Interface Model.
- Implementation of the Advanced Tire-Ice Interface Model into an existing tire model to further its capabilities.
- Started to investigate the effect of tires composed of different rubber composition. This will provide insight into the traction performance of tires manufactured with certain rubber compounds.
- Developed vehicle models to investigate dynamic vehicle simulations using the estimated tire forces from the Advanced Tire-Ice Interface Model.

7.2.2 Novel Contributions Regarding the Experimental Study

- Developed a method to obtain bulk temperature measurements at the contact interface during operation.
- Developed a method to obtain dynamic pressure distribution measurements.
- Conducted a comparative analysis between Winter Tires and All−Season Tires based on a design of experiment.

7.3 Future Research Directions

In order to include the tire surface temperature in the Dugoff Tire model, further improvements can be made. The difference in this model would be in the number of parameters which vary with temperature. With the influence of temperature, the model's accuracy could improve in the nonlinear range. Other tire models can also be used to determined the respective differences between the models.

Before the end of the complete investigation, the modified tire model should be used to further characterize the tire by implementing the model into a more comprehensive tire and vehicle model. This could allow a further comparison between the effects of including tire surface temperature into the model.

Also, in order to improve the performance of the model, the inclusion of rubber compounds in the Advanced Tire-Ice Interface Model should be validated. To do this, a design of experiment should be developed that examines the performance of the rubber compounds of tires with a similar tread pattern design. Hardness and yields strength measurements should also be conducted via a Dynamic Mechanical Analysis (DMA) to have accurate representations of the rubber compounds.

Appendix A

Terramechanics Rig Brief Operations Manual

A.1 Initialization

1. Switch on the two main breakers (Breaker 15 & 27) to power on the Terramechanics Rig.

2. Power on the computer and laptop containing all of the measurement softwares. This also includes powering on all of the data acquisition equipment.

3. Under the KISTLER Start up Screen, select the COMM 1 as the input channel and then turn on the final hardware, initiating the KISTLER software.

4. Begin the calibration process of the KISTLER sensor following the Terramechanics Rig Operations Manual:

   (a) Before beginning the calibration process, allow the system to run for 15-minutes

as a warm-up

(b) Begin the Wheel Angle Calibration under the Offset menu

(c) After calibrating the wheel angle, set the input code as 3-5-7 as shown in the operations manual.

(d) Under the diagnostics menu, ensure that the system has reach a stable operating temperature.

(e) Perform a signal offset to account for data loss as the final step in the calibration process.

5. Power ON the voltage controller of the normal load controller after opening the LAB-VIEW VI on the computer. The flow controllers requires 24 V as the input voltage. Air will be released from the system.

6. Once the pneumatic flow valve has settled, the Rig is ready for operation and can be turned off until it is ready for use.

7. Lower the wheel for a test and remove the hook from the eye to disengage.

8. Before testing, ensure the light on the NI DAQ pad is ON. If not, reload the driver under: Control Panel >Administrative Tools >Services >NI Device Loader >Restart

A.2 Operation

1. To operate the Rig, begin by inputting the desired slip ratio in ladder units. This will be under Network 7 in the code through PicPRO.

2. After applying the slip ratio, compile and download the file to the controller. If at any point during operation the Rig suddenly stops, the file must be re-downloaded to the

controller.

3. In the LABVIEW software, set the input voltage to 1.60 before running the file VI.

4. Increase the voltage in increments less than 0.1 V to allow the controller to properly track the response. Set the normal load to the desired value.

5. Under the LMS Advanced Testing Software, scroll to the measure tab to begin an experiment.

   (a) Name the file as $TireType\_Slip1\_Slip2\_Slip3\_Slip4\_InfPressure\_NorLoad\_RunNumber$.

   (b) Arm the system and press the play button to begin measuring.

   (c) Review data after measuring to ensure desired slip ratio values are true.

A.3 Setting up Ice System

1. Lay the metal U-channels on the top level of the test chamber of the Terramechanics Rig. Start at the home position. The final channel will lay upside down in the chamber.

2. After the channels are laid, place two layers of 10 ft. wide 4 mm thick plastic sheeting on top of the U-channels. Ensure enough tarp slacks on the edges of the test chamber.

3. Next place a layer of pink foam insulation over the plastic tarp. Using gorilla tape, adhere the insulation to each other and the plastic sheeting at the edges.

4. Afterwards, lay two additional layers of plastic sheeting of the pink insulation foam.

5. The ice system can now be rolled out on top of the tarp. Make sure not to rip the tarp. The connecting end of the ice mat should be at the home position of the rig.

6. Now tape all the plastic tarp hanging out from the test chamber to the edges of test chamber using gorilla tape.

7. Connect the pipes to the ice mat. Make sure a click is heard to ensure a complete connection.

A.4 Ice Chiller Preparation

1. Switch ON the breaker switch 27 in the breaker box followed by the main breaker which can be found directly on the outdoor chiller unit.

2. Make sure the set point on the controller is set to a high value around 99 °F. The controller can be found directly on the chiller unit.

3. Allow the system to warm up for a period of 24 hours before turning on the compressor.

4. Fill the reservoir tank with ethylene glycol and turn black switch to the ON(HAND) position. This will initiate the compressor.

   (a) As the glycol flows through the ice mat, fluid will be drawn from the reservoir tank to fill the mat. Keep filling the tank up until the fluid level remains constant at the desired level.

5. Once the pressure has reached a constant value on the readout in the chiller unit (25-30 psi), the air in the system has been released.

6. Place the temperature sensor on the ice mat and set the temperature to around a temperature of about 22 °F and set the compressor to the AUTO position.

7. After letting the system cool, the mat is ready for the formation of ice.

Figure A.1: Pressure readout in the chiller unit. Can be found by removing the diamond shaped panel on the outdoor chiller unit.

8. Begin by spraying a thin layer of water in the test chamber. Continue the process until the desired ice thickness has been reached.

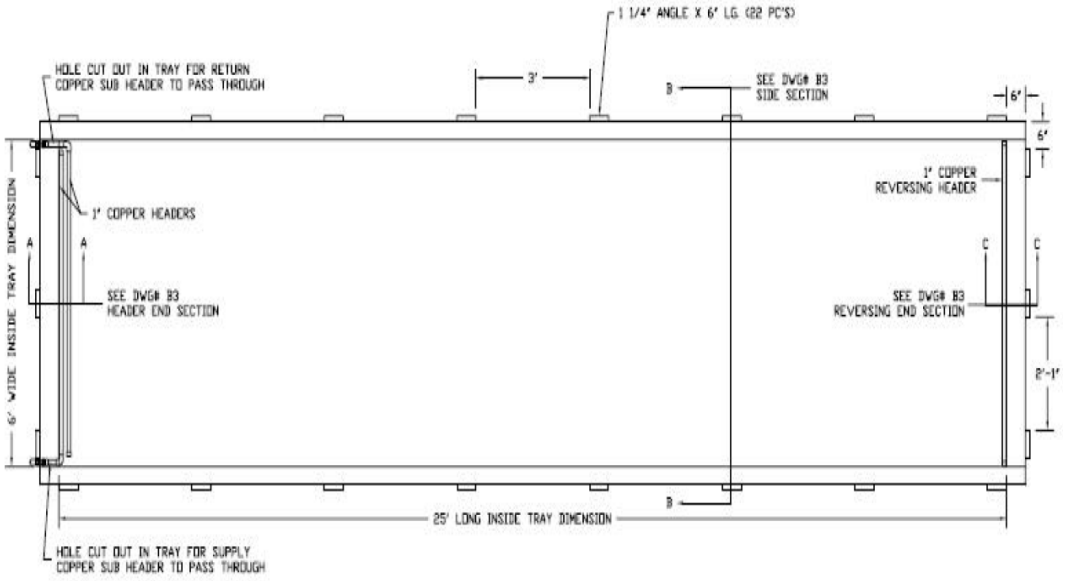

Figure A.2: Dimensions of the Custom Ice Rink System provided by Custom Ice Rink Build.

A.5 Melting the Ice

1. Switch OFF the chiller unit which leads to formation of a melt layer. Use the shop vacuum to remove the water periodically.

2. Use the water pump to empty the filled shop vacuum into the sink by connecting the outlet of pump to the sink.

3. When the ice layer becomes small enough, it can be broken using a chisel and hammer. Be careful with the ice pipes during this process.

Appendix B

Thermocouple Installation

B.1 Thermocouple Specifications

The thermocouples are of the following dimensions:

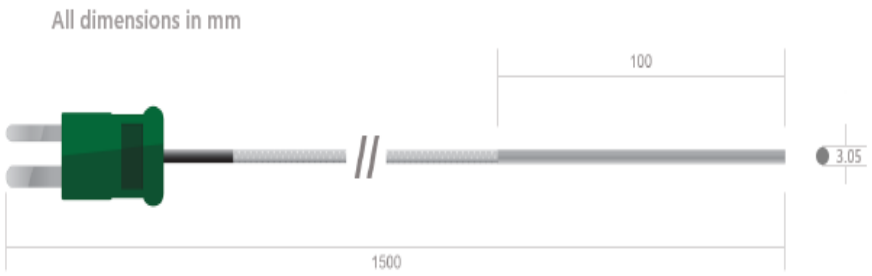

Figure B.1: Dimensions of the K-type Thermocouples used for the investigation.

The Wireless Data Loggers are a Model EL-WiFi-DTC. It is a WiFi-based, dual-channel wireless data logger for time and date-stamped temperature measurements using a Thermocouple probe (J, K, N, and T types supported). It adheres to the 802.11b standard and can integrate with any existing WiFi network. The data logger is powered by a built-in, re-chargeable battery to allow purely stand-alone performance, and is packaged in a small,

IP55-rated enclosure to tolerate dusty and sprayed water environments.

Features:

- Supports J, K, N, and T type thermocouple probes
- -270 to +1300°C(-454 to +2372°F) temperature measurements (probe dependent)
- Ingress Protection Rating of 55 resists dust and water spray
- Built-in display shows current, min/max readings, alarm states
- Wireless communication to any PC using WiFi
- 802.11b-compliant for universal compatibility
- Built-in, rechargeable battery for independent deployment
- Seamlessly uploads memory to host PC at programmable intervals
- Huge buffer memory of over 1,000,000 readings tolerates disconnects
- Programmable high/low alarm limits
- Built-in USB interface for battery charging and initial configuration

B.2 Thermocouple Installation

To install the thermocouples:

1. Begin by fitting the thermocouples and wire into the grooves and sipes of the tread. Once the thermocouples are out of way and do not interfere with the normal operation

Table B.1: EL-WiFi-DTC Specifications

Specification	Minimum	Typical	Maximum	Unit
Battery Life		<6		Month
USB Supply Voltage	4.5		5.5	VDC
Operating Temperature Range	-20 (-4)		+60 (+140)	°C (°F)
Temperature Measurement Range	-270 (-454)		+1300 (+2372)	°C (°F)
Temperature Measurement Resolution		0.1		°C
Temperature Display Resolution		0.1		°C
Temperature Accuracy		±1.5		°C
Number of Loggers per PC		253		Loggers

of the tire, apply 100% White Silicone at the wiring first. This will make sure that the thermocouples do not move during installation.

2. Apply 100% white Silicone to the entire length of the thermocouple, as shown in the figure below. Only leave the tips of the measuring equipment exposed.

Figure B.2: After fitting the wires and thermocouples into the tire tread, apply silicone to the wires and thermocouples to adhere the measuring system to the tire.

3. Push the thermocouples into the silicone so that the thermocouples are laying against the subtread. Wipe off any excess that might have reached the contact patch. Allow

the 100% White Silicone to dry for at least 4 hours.

4. After the silicone is dry, apply a layer of 100% Clear Silicone over the entire length of thermocouple again. This layer will serve as a protective layer for the thermocouple. This is shown in the figure below. Wipe off any excess that might have reached the contact patch.

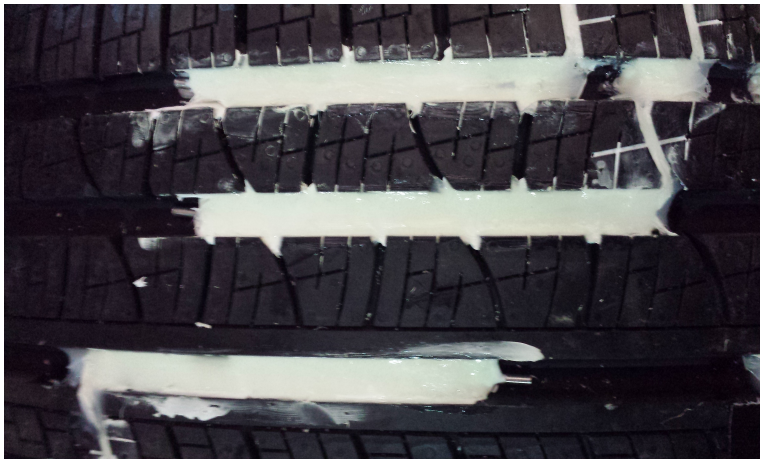

Figure B.3: Use an additional layer of 100% Clear Silicone to protect the thermocouple.

5. Allow the silicone to completely dry for 24 hours. After drying, the tire is ready to be tested.

6. Make sure that the thermocouples and wires do not interfere with the normal operation of the tire.

7. Next gather the wires together and use a zip-tie to keep them together.

8. Apply 3M Heavy Duty Velcro to the tire sidewall and the backside of the data loggers. Attach the data loggers to the wheel sidewall such that they are equal distance from each other and do not cause any wheel imbalances. This is shown in the figure below:

Figure B.4: Data loggers attached to the sidewall of the tire using 3M Heavy Duty Velcro.

Figure B.5: Data loggers are attached at an equal distance from each other to prevent wheel imbalances.

B.3 Thermocouple Removal

To remove the thermocouples:

1. Begin by using a hairdryer to heat up the silicone and release the bond to the tire tread.

2. Using a caulk remover, shown in the figure below, remove caulk from around the thermocouple. Be careful to not damage the measurement device.

Figure B.6: 3-in-1 Combo Caulk Removal Tool used to remove and apply caulk.

Figure B.7: After removing the thermocouples from the contact patch, the excess silicone can be peeled and scraped off.

3. Once the thermocouple can be removed from the contact patch, clean off the thermocouple by peeling and scraping the excess silicone off of the measuring device. Be careful not to damage the thermocouples.

4. Store the thermocouples with the data loggers in a dry and cool place when not in use.

Appendix C

Tire-Ice Model Documentation

C.1 Inputs to the tire−ice model

C.2 Pressure Distribution

1. Code begins with M-File: $pres_hankook_v2.m$

   (a) This code uses the pressure distribution bitmap files provided by Hankook Tires

   (b) Line 9 in the code which contains the MatLab function uigetfile must contain the path to the provided footprint distributions

   (c)

2. Next, the footprint of the tire is cropped out of the provided image by Hankook Tires by trial and error in order to extract the color bar for different pressure levels.

   (a) The model first reads the RGB value of the pressure map at each pixel and then compares this to the value of the color bar provided with the figure.

   (b) The color bar is then broken down into RGB values.

3. Afterwards, once the color bar and footprint are cropped for each operating condition, the RGB values of the color bar are compared to that of the footprint, and a footprint is created with numerical pressure values corresponding to the each pixel of the footprint.

   (a) The pressure distribution are saved as .mat files by the user in order to load them into the next MatLab file.

4. This module also outputs the geometry of the contact patch and its shape.

C.3 Tire Temperature Rise Simulations

1. The next file is M-File: $tempdv5.m$. This code reads the tire tread temperature in the actual contact area.

2. Based on Jaegers Temperature Rise Model as each tread block contacts the ice surface. This was employed by Fujikawa

   (a) J.C. Jaeger. Moving sources of heat and the temperature at sliding contacts. Journal and Proceedings of the Royal Society of New South Wales, 76:203 224, 1943

   (b) T. Fujikawa, A. Funazaki, and S. Yamazaki. Tire tread temperatures in actual contact areas. Tire Science and Technology, 22(1):19 - 41, 1994

3. The code is able to predict the temperature rise in the contact patch.

   (a) Inputs: Thermal Properties, Contact Patch Parameters

4. Based off of the predicted temperature at the contact patch and the temperature of the ice, the model then identifies the wet and dry regions of the contact patch

C.4 Output: Heat Balance and Wet Film Calculations

1. The final file is M-File: *heatv.m*. Each different file number corresponds to specific loading conditions applied to the tire and whether the surface is wet or dry.

2. The code calculates the average friction coefficient based on the principal of a heat balance

3. The heat balance is conducted using Fourier's Law of Thermal Conductivity

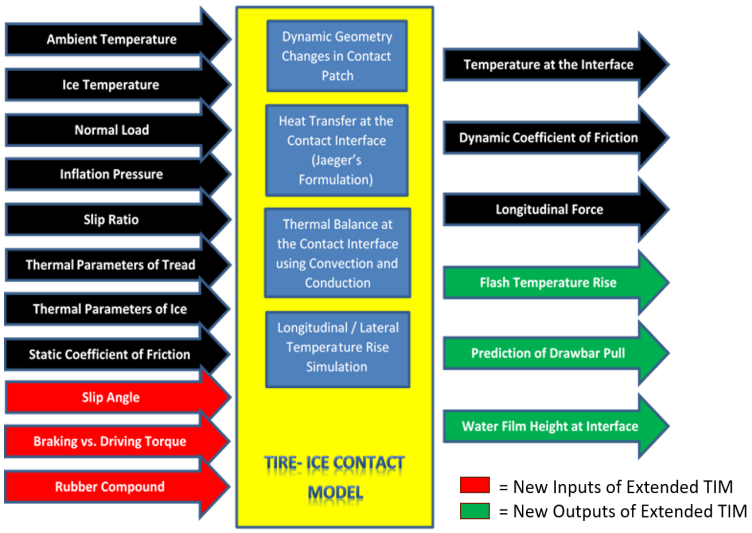

Figure C.1: Inputs and outputs representing the structure of the Advanced Tire-Ice Model. Items in red and green represent the extension of the model since its initial development.

Appendix D

Pressure Pad Measurement System

D.1 Pressure Pad Measurement System Calibration

1. Begin by conducting the equilibration process using the equilibrator shown below in Figure D.1. Clamps can be used to apply necessary pressure to the handle to ensure full connectivity.

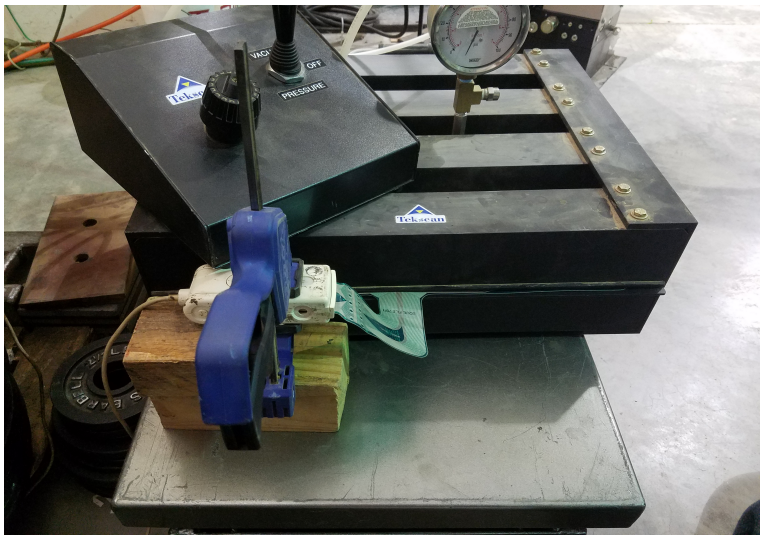

Figure D.1: Clamps are used to apply proper pressure to the handle

2. After equilibration, the pressure pad can be calibrated by applying a known load in the range of which the measurements will be collected.

3. Once the system has been calibrated, the pressure pad is ready to be installed.

D.2 Pressure Pad Protective Cover

1. Begin by cleaning the pressure pad surface from any debris and imperfections.

2. Follow the directions provided with the protective film.

   (a) The pressure pad should be sprayed with the included bottle and should be dried using the lint-free towel.

   (b) Place a 4 mm plastic sheeting under the pressure pad to serve as the platform which the pad will adhere to.

   (c) Remove the first layer of the film for application.

   (d) Begin by adhering one edge of the film to the pressure pad. Using your free hand, continue to press down on the film in the direction of the pressure pad.

   (e) Once the film has been applied, use a credit card to squeeze out the air bubbles from under the film.

   (f) Finally once you are satisfied with the application, remove the second layer of the protective film. This will leave behind a thin layer of tempered glass on top of the pressure pad.

3. Once the film has been applied, the pad is ready to clamped to the wooden platform.

D.3 Support Platform for Pressure Pad

1. Begin by placing three U-channels adjacent to each other as shown below.

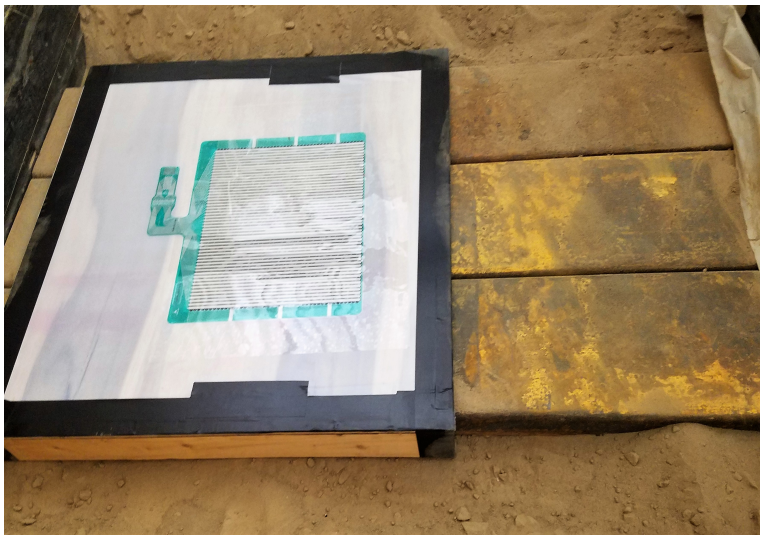

Figure D.2: Pressure Pad has been attached to a wooden platform and placed on top of three adjacent U-channels to secure the pad in place.

2. Using Gorilla Tape, tape the 4 mm plastic sheeting to the wooden platform. Make that there is no slack left behind in the plastic sheeting.

3. As shown in the picture 2"X4" have been attached to the wooden platform using nails. This will allow the platform to "wrap" around the U-channels, and make sure that the pressure pad stays secure in place during testing.

4. To allow the pressure distribution to be measured under dynamic conditions, the plastic sheeting must further be adhered to the wooden platform.

   (a) Using metal strips along the edges of the protective film, bolt the strips through the plastic sheeting and the wooden platform. This is shown in the figure below.

   (b) On the other side of the wooden platform, use a nut to tighten the bolt. This will prevent the metal strips from moving.

Figure D.3: 2" X 4" have been used as a peg to secure the wooden platform in place.

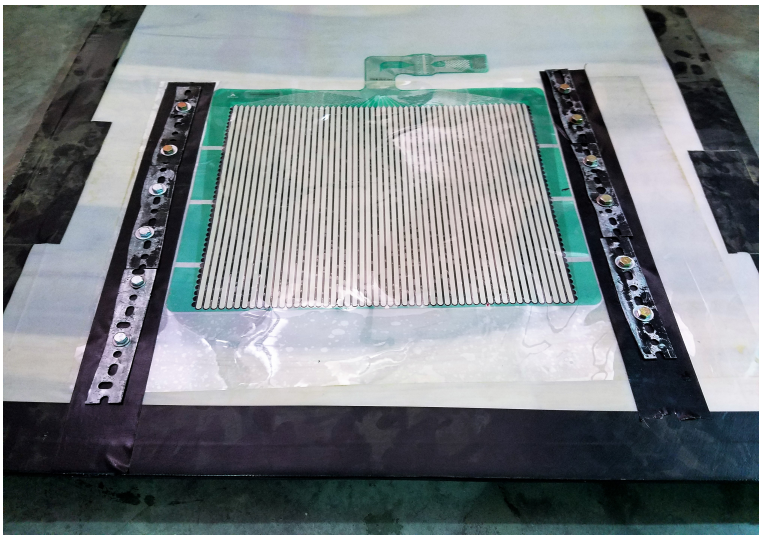

Figure D.4: Metal strips have been used along with bolts to clamp the pressure pad to the wooden platform.

(c) Once all of the metal strips have been bolted down, the pressure pad has now been fully attached to the wooden platform, and it is ready for dynamic testing.

5. Before beginning a test, use Gorilla Tape to cover the bolt head to prevent and damage being done to the tire. This is shown in the figure below.

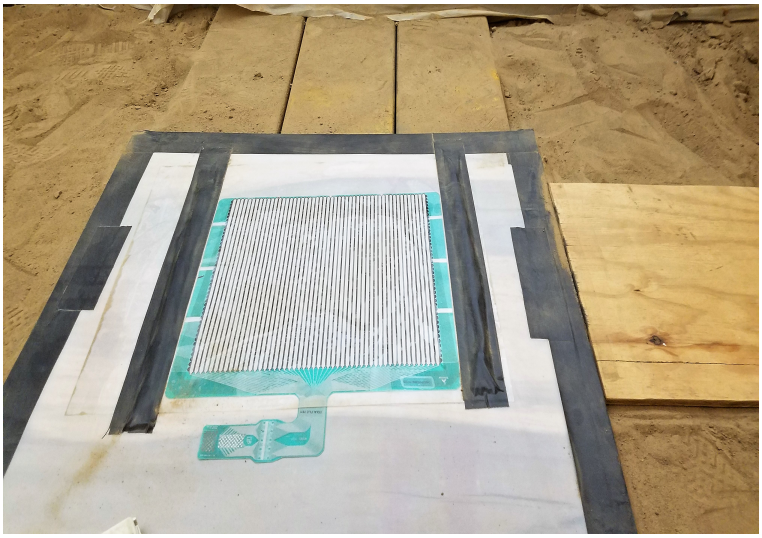

Figure D.5: Gorilla Tape has been used to cover the bolt heads.

6. Also shown in the figure is a wooden ramp leading up to the pressure pad. This ramp is used to prevent the tire from touching the soil which could eventually end up on the pressure pad itself.

Appendix E

Additional Results

E.1 Temperature Rise Results

E.1.1 Effect of Inflation Pressure

First the effect of varying the inflation pressure on the temperature rise is studied. As shown for the 19" Pirelli All Season Tire, as the inflation pressure is decreased, the temperature rise in the contact patch becomes more significant. Heat generation is proportional to the total surface area. Therefore as the inflation pressure decreases, the contact area increases which promotes heat generation. The case for 100% inflation pressure resulted in a higher fluctuation in the temperature.

E.1.2 Effect of Normal Load

The effect of varying the normal load was also investigated. It is evident that there is higher variation in temperature with respect to the high slip ratio as the thermocouples try

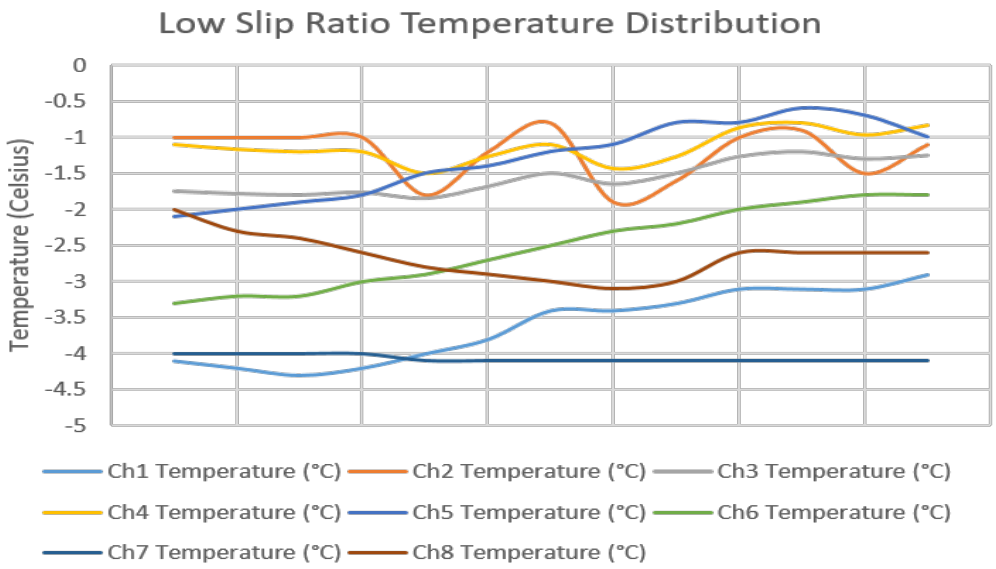

Figure E.1: Temperature time history measurements which displays the effect of 60% inflation pressure for the SRTT at low slip ratio. The testing conditions were set at 0° Toe Angle and 0° Camber Angle at 100% Load Index.

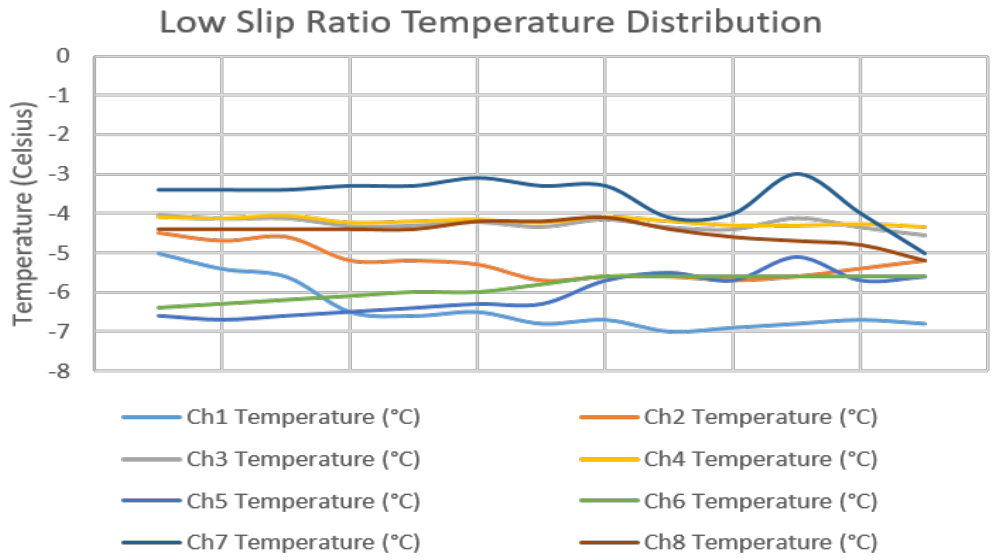

Figure E.2: Temperature time history measurements which displays the effect of 100 % inflation pressure for the SRTT at low slip ratios. The testing conditions were set at 0° Toe Angle and 0° Camber Angle at 100% Load Index.

to reach an equilibrium. As the rate of friction generation increases, the tire tends to reach steady state slower than in the low slip ratio regions.

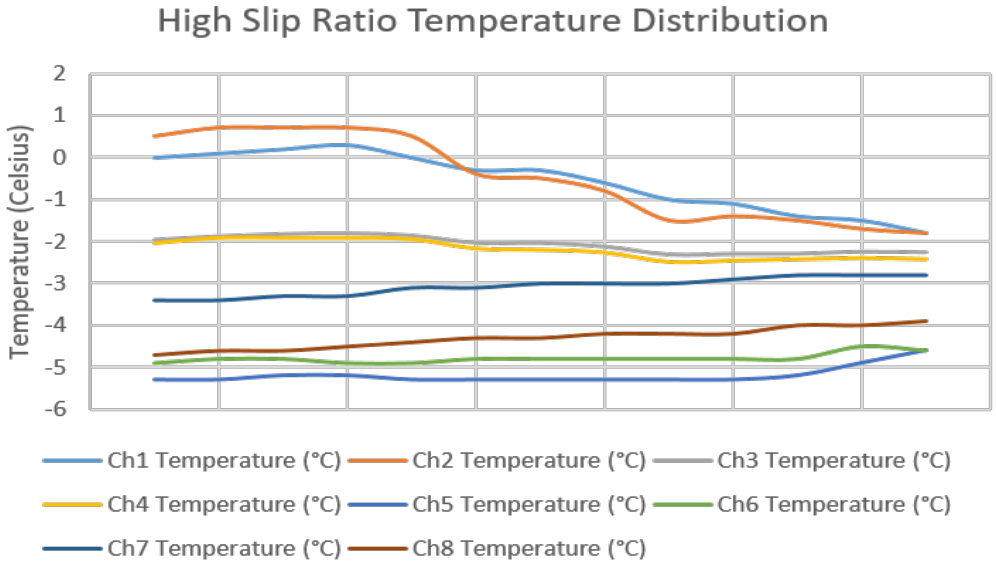

Figure E.3: Temperature time history measurements which displays the effect of 100% normal load for the SRTT at high slip ratio. The testing conditions were set at 0° Toe Angle and 0° Camber Angle.

E.2 Traction Results

E.2.1 Effect of Inflation Pressure

The increase in inflation pressure led to a decrease in peak normalized drawbar pull at lower slip ratios. As the inflation pressure increased the maximum drawbar pull occurred at a lower slip ratio value. Therefore, the reduction of inflation pressure causes the tire to slip at a higher slip ratio thus improving traction. As the inflation pressure is reduced, the rolling resistance of the tire is increased as the envelope effect becomes more dominant. This in turn causes heat generation.

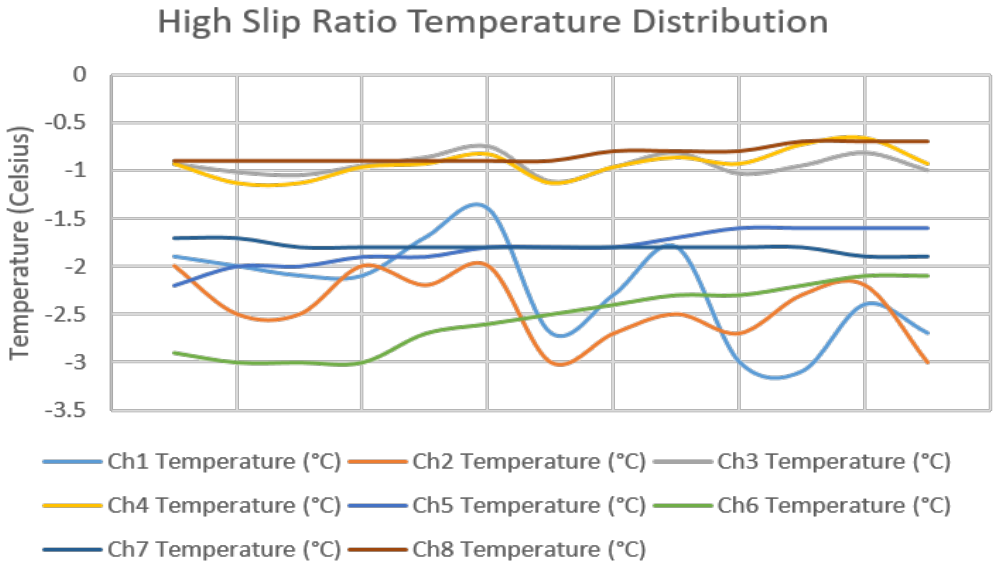

Figure E.4: Temperature time history measurements which displays the effect of 120 % normal load for the SRTT at high slip ratios. The testing conditions were set at 0° Toe Angle and 0° Camber Angle

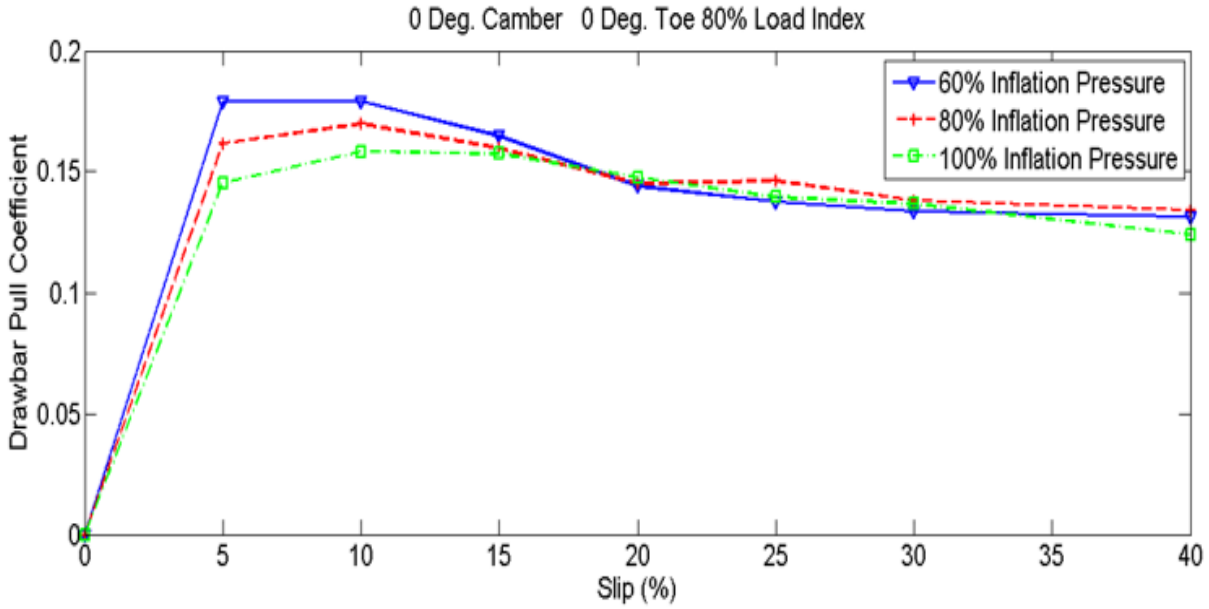

Figure E.5: Drawbar pull coefficient of Pirelli at various normal loads with 0° camber angle and 0° toe angle when the inflation pressure is at 80% of the maximum.

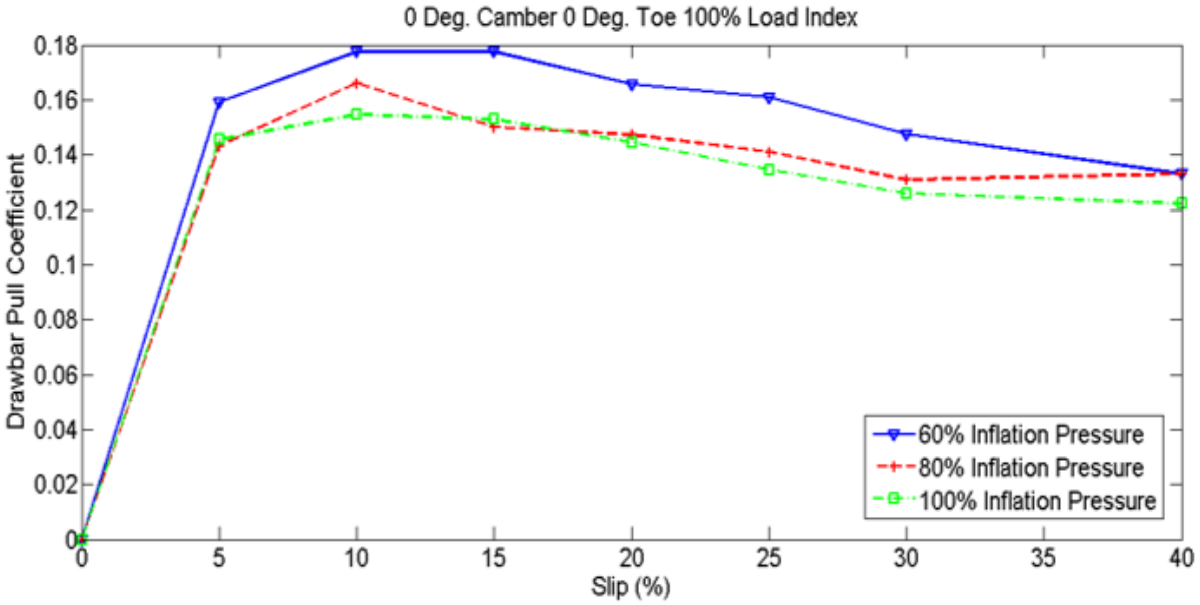

Figure E.6: Drawbar pull coefficient of Pirelli at various normal loads with 0° camber angle and 0° toe angle when the inflation pressure is at 100% of the maximum.

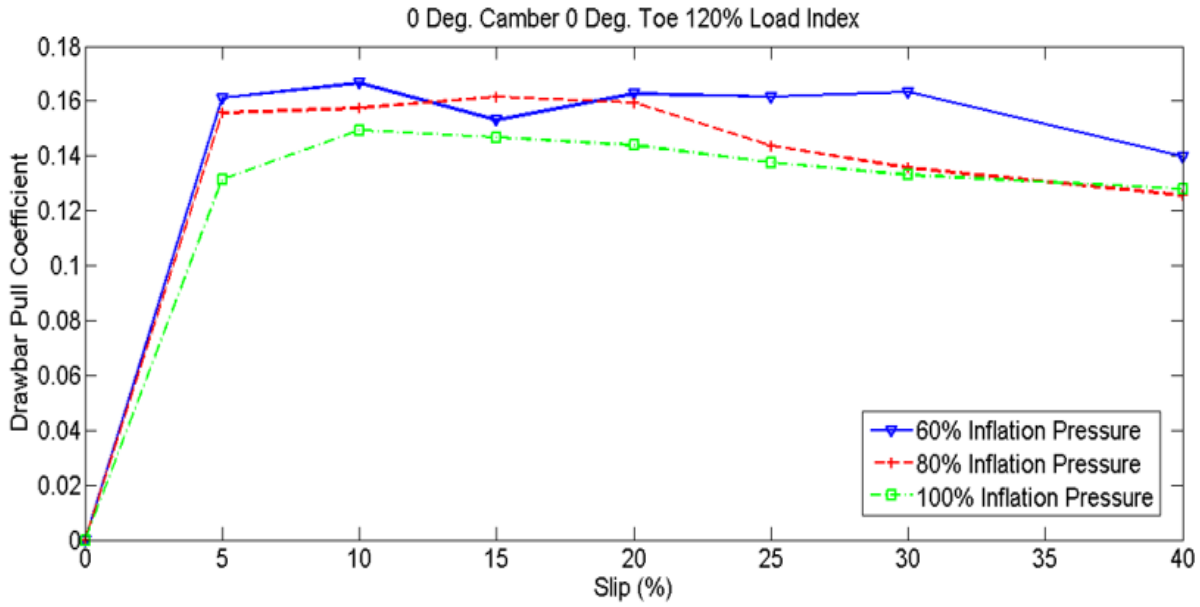

Figure E.7: Drawbar pull coefficient of Pirelli at various normal loads with 0° camber angle and 0° toe angle when the inflation pressure is at 120% of the maximum.

E.2.2 Effect of Normal Load

It is evident that the drawbar pull decreases with a reduction in normal load. It is hypothesized that this is due to the change in the contact area at various normal loads. Once the maximum drawbar pull has been reached, the drawbar pull will saturate to a residual value. At lower normal loads, the difference between the maximum peak drawbar pull and the residual value is not as high as the case of higher normal loads. The overall maximum drawbar pull of the Pirelli Tires were slightly lower than the traction performance investigated for the existing SRTT.

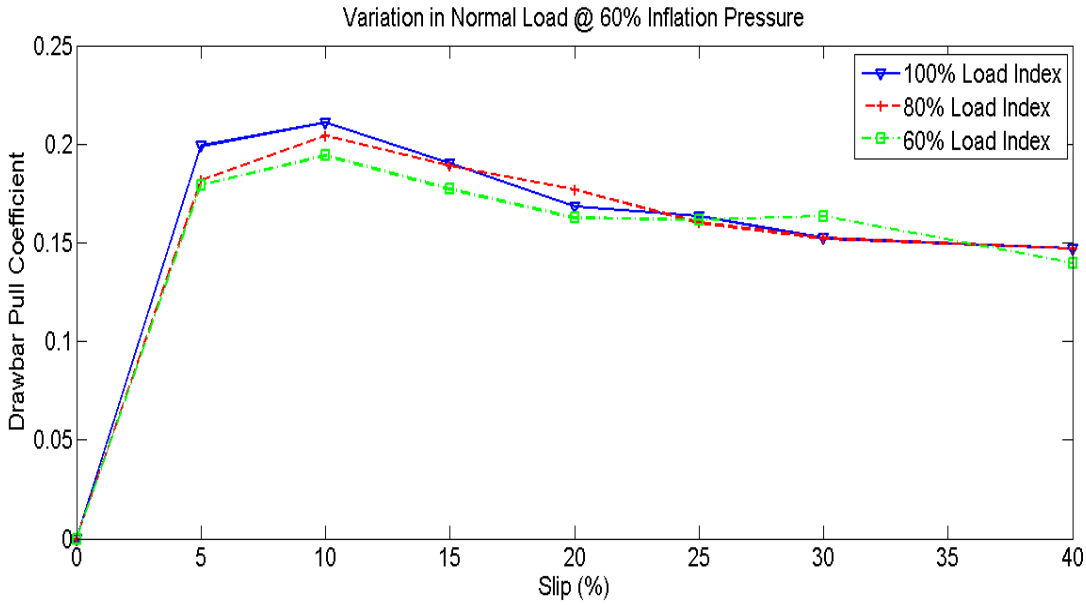

Figure E.8: Drawbar pull coefficient of Pirelli at various normal loads with 0° camber angle and 0° toe angle when the inflation pressure is at 60% of the maximum.

E.2.3 Effect of Camber Angle

No significant difference when the camber angle was varied. When a camber angle was applied, significant differences between the sides of the contact patch temperature differences were observed. More heat is generated as the shape of the pressure distribution changes.

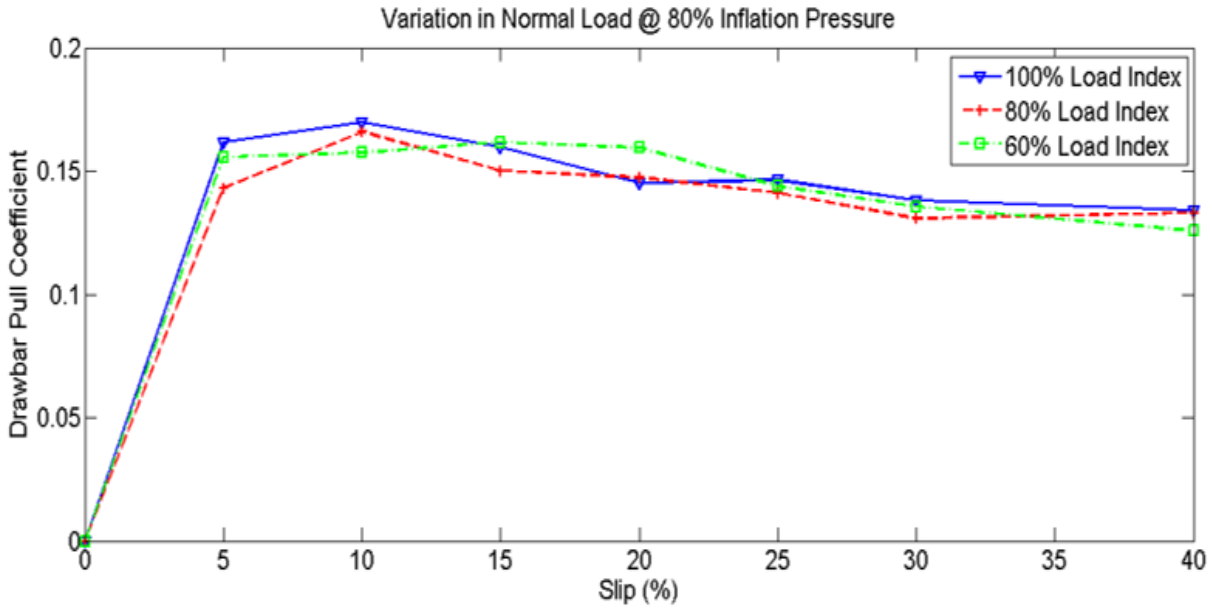

Figure E.9: Drawbar pull coefficient of Pirelli at various normal loads with 0° camber angle and 0° toe angle when the inflation pressure is at 80% of the maximum.

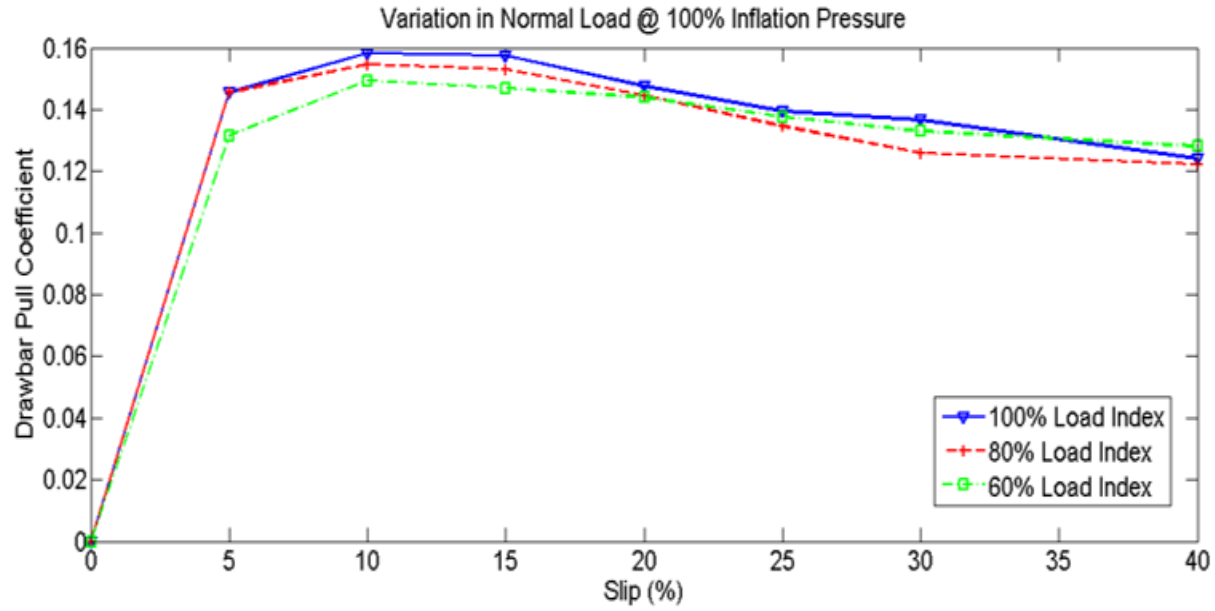

Figure E.10: Drawbar pull coefficient of Pirelli at various normal loads with 0° camber angle and 0° toe angle when the inflation pressure is at 100% of the maximum.

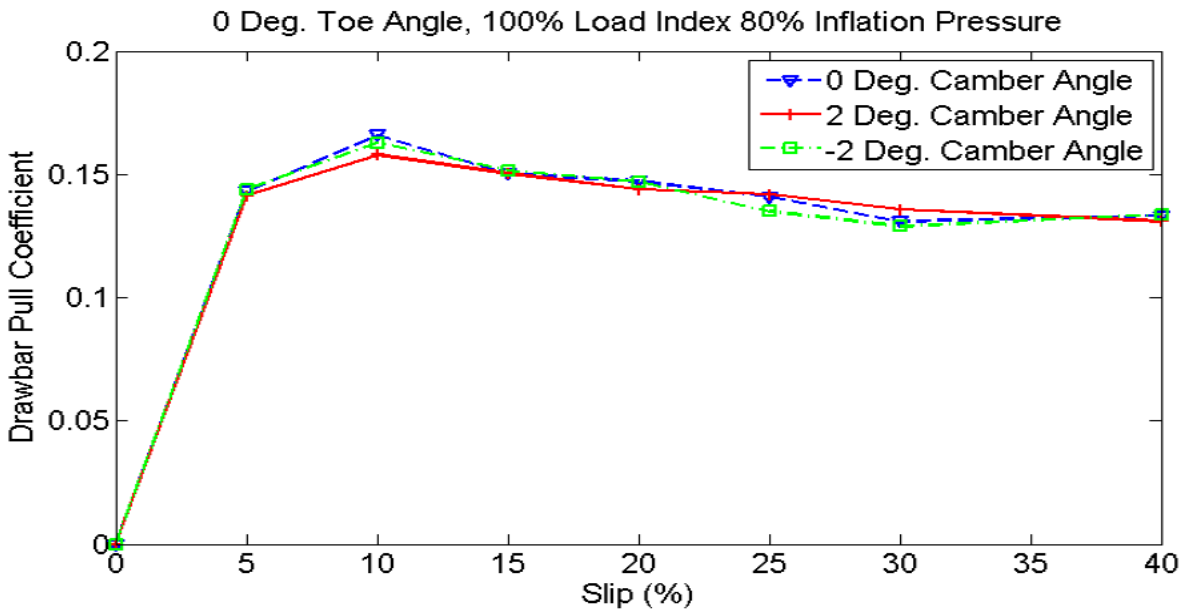

Figure E.11: Drawbar pull coefficient of Pirelli at various camber angles and 0° toe angle.

E.2.4 Effect of Toe Angle

As the toe angle is increased, the drawbar pull is reduced. The change of toe angle produced a different contact area which results in a reduction in traction performance. Even in the case of the existing SRTT, the positive (Toe out) toe has a higher drawbar pull than the negative (Toe in). For front vehicle suspensions, adding more toe-out will make the car smoother and increase low-speed steering by decreasing the cars turning radius. However, decreasing toe-out, will give the car more initial steering response.

E.3 Temperature Rise Simulations

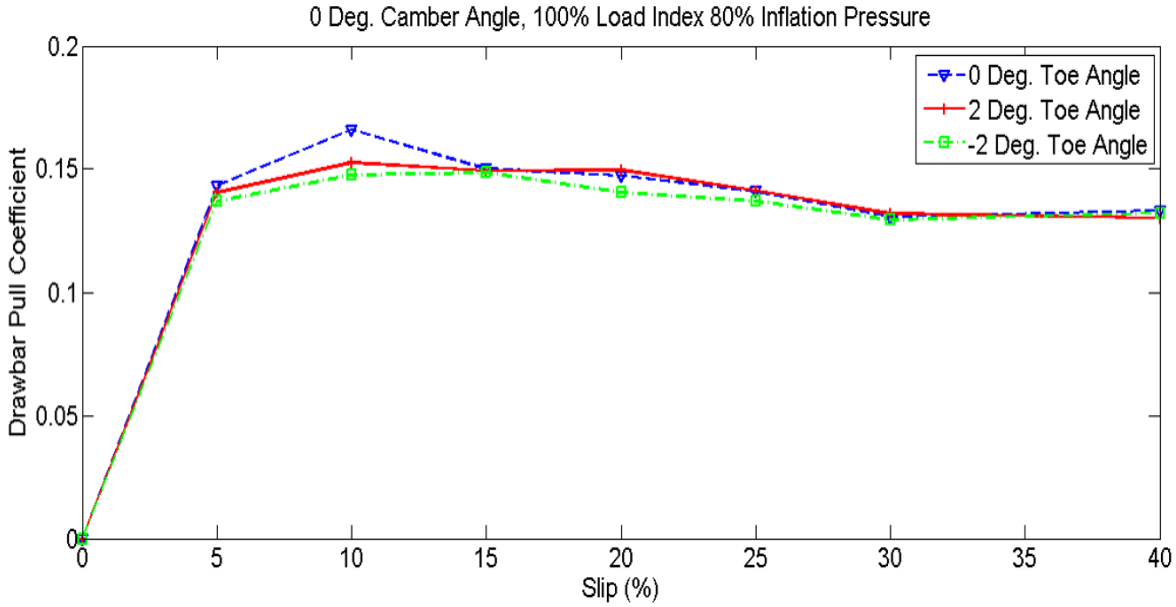

Figure E.12: Drawbar pull coefficient of Pirelli tire at various slip angles and 0° camber angle.

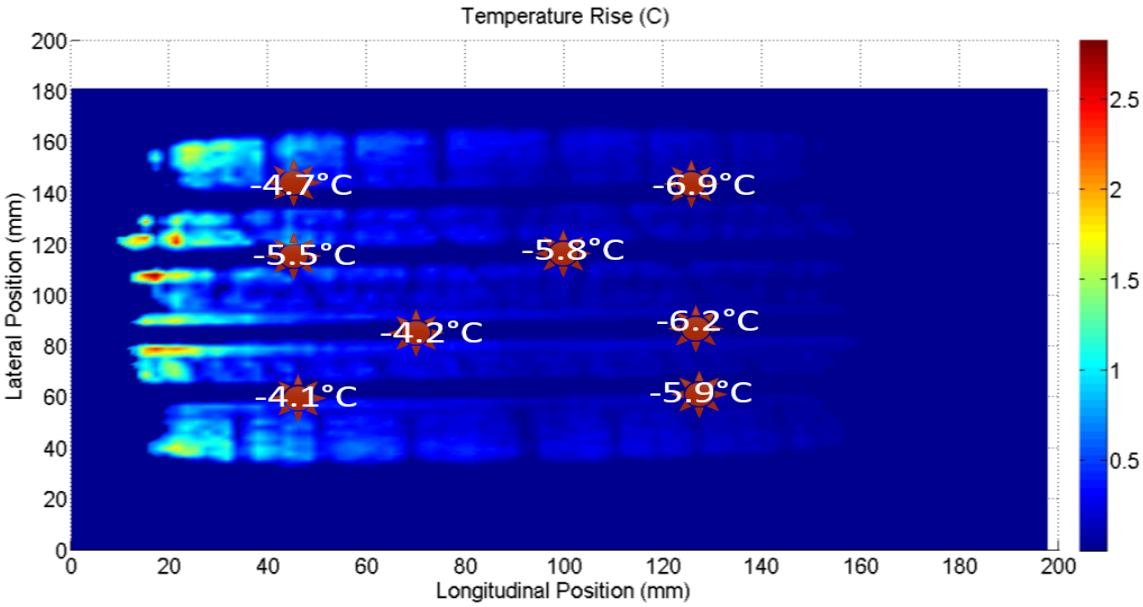

Figure E.13: Drawbar pull coefficient of Pirelli tire at various slip angles and 0° camber angle.

Bibliography

[1] Virginia Department of Emergency Management. *Icy Road Fatality Statistics.*, 2010 (accessed April 8, 2015). http://icyroadsafety.com/fatalitystats.shtml.

[2] Martin Giessler, Frank Gauterin, K Wiese, and B Wies. Influence of friction heat on tire traction on ice and snow. *Tire Science and Technology*, 38(1):4–23, 2010.

[3] Ken-ichi Shimizu, Mitsuya Nihei, and François Dorémieux. Effect of texture of iced road surface on characteristics of ice and snow tires. Technical report, SAE Technical Paper 920018, 1992.

[4] J.Y. Wong. *Theory of Ground Vehicle*. Wiley & Sons, 2008.

[5] Hans B. Pacejka. *Tire and Vehicle Dynamics*. Elsevier, third edition, 2012.

[6] Pep Boys. *What are the differences in tire tread design and what do they mean?*, 2009 (accessed August 20, 2016). https://www.pepboys.com/tires/treadsmart/tread_type/.

[7] North America Michelin. *How is a tire made?*, 2007 (accessed September 6, 2016). http://www.michelinman.com/US/en/help/how-is-a-tire-made.html.

[8] Michelin Publications. Tire grip capacity and how it is tested. *Society of Michelin Technology*, pages 1–96, 2001.

[9] Tire Rack. *Tire Rack's Tire Testing Program*, 2010 (accessed April 26, 2016). http://www.tirerack.com/tires/tiretech/techpage.jsp?techid=274.

[10] B.T. Kulakowski and D.W. Harwood. Effect of water-film thickness on tire pavement friction in: Surface characteristics of roadways. *International Research and Technologies, ASTM STP 1031*, pages 50–60, 1990.

[11] Guo K. Peng X, Xie Y. A new method for determining tire traction on ice. Technical report, SAE Technical Paper 2000-01-1640, 2000.

[12] GF Hayhoe and CG Shapley. Tire force generation on ice. Technical report, SAE Technical Paper 890028, 2013.

[13] Wiese K. Klapproth C., Kessel T. M. and Wies B. An advanced viscous model for rubber-ice friction. *Journal of Tribology International*, 99(2):169–181, 2016.

[14] Eric Le Bourhis. *Thermal Expansion and Elasticity*. Wiley-VCH Verlag GmbH Co. KGaA, 2007.

[15] Fancher P. Dugoff, H. and L. Segel. An analysis of tire traction properties and their influence on vehicle dynamic performance. SAE Technical Paper 700377. doi:10.4271/700377.

[16] US-Department of Transportation. *Federal Highway Administration, Road and Weather Management Program.*, 2005 (accessed April 8, 2015). http://www.ops.fhwa.dot.gov/weather/q1_roadimpact.htm.

[17] Sandu C. Bhoopalam A. K. and Taheri S. A tire-ice model (tim) for traction estimation. *Journal of Terramechanics*, 66:1 – 12, 2016.

[18] T. Fujikawa, A. Funazaki, and S. Yamazaki. Estimation of tire tread temperature in contact patch. *JSAE Review*, 12(1):44 – 49, 1991.

[19] Sandu C. Bhoopalam A. K. and Taheri S. A tire-ice model (tim) for traction estimation. *Journal of Terramechanics*, 66(12):1–12, 2016.

[20] J.C. Jaeger. Moving sources of heat and the temperature at sliding contacts. *Journal and Proceedings of the Royal Society of New South Wales*, 76:203 – 224, 1943.

[21] AD Roberts. Rubber-ice adhesion and friction. *The Journal of Adhesion*, 13(1):77–86, 1981.

[22] Gerasimos Skouvaklis, Jane R Blackford, and Vasileios Koutsos. Friction of rubber on ice: A new machine, influence of rubber properties and sliding parameters. *Tribology International*, 49:44–52, 2012.

[23] U.S. Department of Transportation. *The Pneumatic Tire*. National Highway Traffic Safety Administration, 2006.

[24] Tire Rack. *All- vs. Rear-Wheel Drive on Ice*, 2008 (accessed April 3, 2015). http://www.tirerack.com/tires/tests/TireTestServlet?perfType=LTPW_1.

[25] What-When-How. *Tire Construction*, 2012 (accessed September 6, 2016). http://whatwhenhow.com/automobile/tyreconstructionautomobile/.

[26] Alan Sidorov. The spin on winter tires vs. all-seasons. *Winnipeg Free Press*, Auto Articles:F2, 2011.

[27] T. Fujikawa, A. Funazaki, and S. Yamazaki. Tire tread temperatures in actual contact areas. *Tire Science and Technology*, 22(1):19 – 41, 1994.

[28] Mac DeMere. Z-rated tire test: Traditional summer vs. new all-season performance. *Motor Trend*, 47(12), 1996.

[29] Langer W. J. and Potts G. R. Development of a flat surface tire testing machine. *Society of Automotive Engineers*, SAE 800245, 1980.

[30] F*ülö*p T. and Tuononen A. Evolution of ice surface under a sliding rubber block. *Wear*, 307(1):52–59, 2013.

[31] A Schallamach. How does rubber slide? *Wear*, 17(4):301–312, 1971.

[32] D. F. Moore. *The Friction and Lubrication of Elastomers*. Oxford, 1972.

[33] Mundl R. Wiese K., Kessel T. M. and Wies B. An analytical thermodynamic approach to friction of rubber on ice. *Tire Science and Technology*, 40(2):124–150, 2012.

[34] Wangenheim M. and Ripka S. Temperature investigations in road/tire contact. *In Proceedings of the ASME 2009 International Mechanical Engineering Congress and Exposition*, 2009. "Paper No. IMECE2009-11165".

[35] Staples R. J. Lackey J. Clark S. K. Nybakken G. H., Collart D. and Dodge R. N. Preliminary measurements on heat balance in pneumatic tires. *National Aeronautical Space Administration Lewis Research Center*, 1971. "Grant NO. NGR 23-005-417".

[36] Hughes T. P. Bowden F.P. The mechanism of sliding on ice and snow. *Proceeding Royal Society of London*, 172:280–298, 1939.

[37] B.N.J. Persson and A.I. Volokitin. *Phys. Rev. B65*, 2002. 134106.

[38] Funazaki A. Fujikawa T. and Yamazaki S. Estimation of tire tread temperature in contact patch. *Society of Automotive Engineering*, 12(1):44–49, 1991.

[39] B.N.J. Persson. Rubber friction role of the flash temperature. *Journal of Physics: Condensed Matter*, 18(32), 2006.

[40] Tworzydlo W. W. Yavari B. and Bass J. M. A thermomechanical model to predict the temperature distribution of steady state rolling tires. *Tire Science and Technology*, 21(3):163–178, 1993.

[41] H. Sakai and K. Araki. Thermal engineering analysis of rubber vulcanization and tread temperatures during severe sliding of a tire. *Tire Science and Technology*, 27(1):22–47, 1999.

[42] F.J.W. Whipple. The stability of the motion of a bicycle. Master's thesis, Trinity College Cambridge, Cambridge, 1899.

[43] A. Klein, and F. Sommerfeld. ber die theorie des kreisels. *Stabilitt des Fahrrads*, Ch. IX, Section 8:863–884, 1910.

[44] Biggans J. S. Sandu C., Taylor B. and Ahmadian M. Building an infrastructure for indoor terramechanics studies: The development of a terramechanics rig at virginia tech. *In Proceedings, 16th ISTVS International Conference*, 30(1):177–185, 2008.

[45] Harty D. A review of dynamic intervention technologies and a method to choose between them. *International Vehicle Dynamics Expo*, 2005.

[46] D. Karnopp and D. Margolis. Adaptive suspension concepts for road vehicles. *Vehicle System Dynamics*, 13(1):145–160, 1984.

[47] International society for terrain-vehicle systems standards. *Journal of Terramechanics*, 14(3):153 – 182, 1977.

[48] ASTM F2493-14. Standard specification for p225/60r16 97s radial standard reference test tire. *ASTM International*, 2014. www.astm.org.

[49] S Naranjo. Experimental investigation of the tractive performance of an instrumented off road tire on a soft soil terrain. Master's thesis, Virginia Tech, Blacksburg, 2013.

[50] Tekscan. *Sensor Model/ Map 3150*, Accessed September 2, 2014. http://www.tekscan.com/3150-pressure-sensor.

[51] Taheri S. Naranjo S., Sandu C. and Taheri Sh. Experimental investigation of the tractive performance of an instrumented off road tire on a soft soil terrain. *Journal of Terramechanics*, 56(19):119–137, 2014.

[52] E. Jimenez and C. Sandu. Handling performance of pneumatic tire on sandy loam. *In Proceedings, 13th ISTVS European Conference*, pages 22–35, 2015.

[53] Yamaguchi M. Hiroki E. Yamazaki, S. and T. Suzuki. Effects of the number of siping edges in a tread block on the friction property and contact with an icy road. *Tire Science and Technology*, TSTCA, Vol. 28(1):55–69, 2000.

[54] Carslaw H.S. and Jaeger J.C. *Conduction of Heat in Solids*. Oxford Press, 1959.

[55] J. A. Greenwood and J. B. P. Williamson. Contact of nominally flat surfaces. *In Proceedings of the Royal Society of London*, 295(Series A):300–319, 1966.

[56] H. Sakai. The tire mechanics. *Grandprix Co.*, 1991.

[57] H. Sakai. Theoretical study of the effect of traction and braking forces on the cornering characteristics of a tire. *Bulletin of Society of Automotive Engineering*, 1971.

[58] H. Sakai. Theoretical and experimental studies on the dynamic properties of tires. *International Journal of Vehicle Design*, 2(1–3), 1981.

[59] H. Sakai. Friction and wear of tire tread rubber. *Tire Science and Technology, TSTCA*, 24(3):252–275, July-September 1996.

[60] A.N. Gent. On the relation between indentation hardness and young's modulus. *Rubber Chemistry and Technology*, Vol. 31(4):896–906, 1958.

[61] E. Sideridis and G. C. Papanicolaou. A theoretical model for the prediction of thermal expansion behaviour of particulate composites. *Rheologica Acta*, Vol. 27:608–616, 1988.

[62] Chen L. Luo Y. Bian, M. and K. Li. A dynamic model for tire/road friction estimation under combined longitudinal/lateral slip situation. SAE Technical Paper 2014-01-0123, 2014. doi:10.4271/2014-01-0123.

[63] Nyborg L. Bakker, E. and H. Pacejka. Tyre modelling for use in vehicle dynamics studies. *SAE*, Technical Paper(870421), 1987. doi:10.4271/870421.

[64] M. Mizuno. Development of tire side force model based on magic formula with the influence of tire surface temperature. *Review of Toyota CRDL, Analysis and Control Methods for Improving Vehicle Dynamic Behavior*, 38(4):17–22, July-September 1996.

[65] Zhang C. Liu L. Ren, C. Variable structure control on active suspension of 4 dof vehicle model. *I.J. Information Engineering and Electronic Business*, Vol. 2:54–64, 2010.